A unit stream power model for the prediction of local scour

by

Neil Philip Armitage
BSc(Eng)(Natal), MSc(Eng)(Cape Town)

Dissertation presented for the degree of Doctor of Philosophy at the University of Stellenbosch. Promoter: Prof. Albert Rooseboom

Department of Civil Engineering
University of Stellenbosch

March 2002

Declaration of Candidate

I, the undersigned, hereby declare that the work contained in this dissertation is my own original work and that I have not previously in its entirety or in part submitted it at any university for a degree

Signature:

Date:

Abstract

Local scour is the erosion of a riverbed resulting from the flow of the river around an obstacle. It is a principal cause of failure of bridges and other hydraulic structures. Current design practice relies on the use of empirical formulae that are often extremely inaccurate, or on the use of physical models that are very expensive. Recent advances in the power of microcomputers have however made numerical simulation increasingly attractive. One obstacle to numerical simulation though is that there is no general agreement on the concept of incipient motion, that critical point at which motion – and hence scour – begins.

In this dissertation, the unit stream power model developed by Rooseboom (1992) is extended to handle the complex three-dimensional flow conditions that pertain close to the riverbed in the vicinity of an obstacle. The relationship between unit stream power (the dissipation function) and the Movability Number (the ratio of the shear velocity to the terminal settling velocity of the critical sediment particles) is clearly indicated. Since incipient motion is probabilistic in nature, a relationship was established between the Movability Number and the intensity of motion with allowance for bed-slope and relative depth. An extension of this work resulted in a new bed-load transportation equation that could be used to determine the rate of scour development. Physical modelling in a laboratory flume aided the selection of suitable critical conditions for the onset of scour.

The usefulness of the above-mentioned relationships was then demonstrated through the construction of a simple mathematical model of scour and deposition around a structure. This model was used in conjunction with commercially available computational fluid dynamics (CFD) software to predict the scour potential around typical engineering structures. Physical model data was obtained for four situations, and the measured scour was compared with that predicted by the numerical model. There was reasonable agreement between the different models and such differences as there were could be readily attributed to constraints on the numerical model, in particular the lack of a free-surface routine and the coarseness of the grid.

This dissertation has opened up a new method for the prediction of local scour that could be readily extended to include all types of scour. With the advent of increasingly fast computers, it could become a useful engineering tool that would assist engineers in the design of safe and cost-effective foundations for hydraulic structures.

Opsomming

Plaaslike uitskuring is die erosie van 'n rivierbed as gevolg van vloei verby 'n obstruksie. Dit is 'n belangrike oorsaak van die swigting van brûe en ander hidrouliese strukture. Bestaande ontwerppraktyk berus op empiriese vergelykings wat dikwels hoogs onakkuraat is, of op fisiese modelle, wat baie duur is. Numeriese simulasie het die afgelope tyd 'n al hoe meer aantreklike opsie geword danksy die snelle toename in die kapasiteit van mikro-rekenaars. 'n Struikelblok met numeriese simulasies is die gebrek aan konsensus oor die konsep van begin-van-beweging, daardie kritieke toestand waarby beweging en derhalwe uitskuring begin.

In hierdie proefskrif is die eenheidstroomdrywing model, ontwikkel deur Rooseboom (1992), uitgebrei om die komplekse drie-dimensionele vloeitoestande, wat teenaan die rivierbodem verby 'n obstruksie heers,te hanteer. Die verwantskap tussen Eenheid Stroomdrywing (Dissipasiefunksie) en die Beweeglikheidsgetal (verhouding tussen sleursnelheid en die ewewigvalsnelheid van die kritieke sedimentpartikels) is duidelik uitgewys. Aangesien begin van beweging probabilisties van aard is, is die verwantskap bepaal tussen die Beweeglikheidsgetal en die Intensiteit van Beweging, met voorsiening vir bodemhelling en relatiewe diepte. Verdere uitbreiding het gelei tot 'n nuwe bedvrag vervoervergelyking wat gebruik kan word om die tempo van uitskuring te bepaal. Kritieke toestande, waarby uitskuring begin, is met fisiese modelle in die laboratorium gekwantifiseer.

Die bruikbaarheid van bogenoemde verbande is gedemonstreer deur die ontwikkeling van 'n eenvoudige wiskundige model van uitskuring en afsetting rondom 'n struktuur. Hierdie model is saam met bestaande kommersiële sagteware vir vloeidinamika berekenings (CFD) ingespan om uitskuringspotensiaal rondom tipiese ingenieurstrukture te voorspel. Fisiese modelmetings van uitskuring vanaf vier uitlegte is vergelyk met die numeries voorspelde waardes. Bevredigende ooreenkoms is gevind en verskille kon geredelik gewyt word aan beperkings van die numeriese model, veral die gebrek aan ' n vryvlakroetine en die growwe maas.

Die proefskrif stel 'n nuwe metode vir die voorspelling van uitskuring daar wat geredelik uitgebrei kan word na ander vorms van uitskuring. Met die ontwikkeling van al vinniger rekenaars kan dit 'n nuttige hulpmiddel vir ingenieurs word om veilige en koste-doeltreffende fondamente in waterlope te ontwerp.

Contents

3. An overview of incipient motion

4. The full unit stream power equation

5. An overview of scour and deposition around selected structures

Part 2: The unit stream power model of scour and deposition

6. The unit stream power model

7. Selection of the criteria for incipient motion

Part 3: Numerical analyses

8. The CFD model

9. Numerical analyses

Figures

Tables

Notation

Symbol	Description	Normal units
a	Largest triaxial dimension of a sediment particle	(m or mm)
a_p	Projected area of a particle	(m^2)
a_r	Sediment reference level	(m)
a_1, a_2 etc	Constants	
A	Flow cross-sectional area	(m^2)
Al	Abutment alignment factor	
A_s	Constant associated with a boundary	
b	Intermediate triaxial dimension of a sediment particle	(m or mm)
b_p	Pier breadth	(m)
b_1, b_2	Arbitrary constants	
B	Constant associated with the condition of the boundary layer	
B_c	Width of a rectangular channel	(m)
B_f	Width of a rectangular laboratory flume	(m or mm)
B_r	Constant associated with a boundary of arbitrary roughness	
B_s	Constant associated with a sand boundary	
c	Shortest triaxial dimension of a sediment particle	(m or mm)
c_{bed}	Bed concentration	
C_D	Coefficient of drag	
C_L	Coefficient of lift	
CFD	Computational Fluid Dynamics	
CFX	CFD software (Version 4.3)	
d	Sediment diameter	(m or mm)
d_i	The median diameter of any particular size fraction	(m or mm)
d_s	Diameter of a sphere having the same surface area as a particular particle	(m or mm)
d_v	Diameter of a sphere having the same volume as a particular particle	(m or mm)
$d_{\%}$	Sediment diameter where % indicates the percentage of particles finer than the indicated value	(m or mm)
d_{50}	Median diameter ($= (d_{15.9} + d_{84.1}) / 2$)	(m or mm)
$\bar{d}$	Mean diameter ($= \sum p_i d_i / 100$)	(m or mm)
d_*	Dimensionless particle diameter ($= (\Delta g / \nu^2)^{1/3} d$)	

D	Hydraulic mean depth, hydraulic depth	(m)
DNS	Direct Numerical Simulation	
E	Specific energy	(J/kg)
f	Frequency of vortex shedding	(Hz)
F_D	Drag force (component)	(N)
$\mathbf{F_D}$	Drag force (vector)	(N)
$F_{D,cr}$	Critical drag force for any given slope	(N)
$F_{D,cr,0}$	Critical drag force for a horizontal slope	(N)
F_L	Lift force (component)	(N)
$\mathbf{F_L}$	Lift force (vector)	(N)
Fr	Froude Number ($= U / (gD)^{0.5}$)	
Fr_0	Densimetric Froude Number ($= U / ((\rho_s/\rho - 1)gd_{50})^{1/2}$	
g	Gravitational acceleration (≈ 9.81)	(m/s^2)
$\mathbf{g}$	Gravity vector	(m/s^2)
G	Abutment cross-section (geometric) factor	
i	Internal (thermal) energy	(J/kg)
I	Intensity of motion ($= m / Nt$)	(s^{-1})
k	Turbulent kinetic energy	
k-ε	A turbulence model	
k-ω	A turbulence model	
k_T	Coefficient of thermal conductivity	
k_r	Roughness height	(m)
k_s	Roughness height (sand)	(m)
k_β	Correction factor for a longitudinal slope	
k_γ	Correction factor for a transverse slope	
K_i	Correction factors for deviations from the ideal shape	
LDPE	Low-density polyethylene	
LES	Large Eddy Simulation	
ℓ_m	Prandtl "mixing length"	(m)
L_a	Length of the abutment normal to the dominant flow direction	(m)
m	Number of particle displacements during time t	
N	Total number of surface particles over a sample area	
n	Manning roughness coefficient	($s/m^{1/3}$)
$\mathbf{n}$	Normal vector (to the bed)	
n_b	Manning roughness coefficient for flume bed	($s/m^{1/3}$)
n_w	Manning roughness coefficient for flume walls	($s/m^{1/3}$)
p	Pressure	(Pa, N/m^2)

P	Wetted perimeter normal to the direction of flow	(m)
P_{av}	Average stream power dissipation per unit volume	(W/m^3)
P_i	Unit stream power input	(W/m^3)
P_r	Power required to keep a particle in suspension	(W/m^3)
P_t	Stream power dissipation per unit volume at any point = applied unit stream power	(W/m^3)
$P_{t(crit)}$	Critical applied unit stream power for scour	(W/m^3)
$P_{t(l)}$	Applied unit stream power in the linear layer	(W/m^3)
$P_{t(t)}$	Applied unit stream power in the log-law layer	(W/m^3)
PC	Personal Computer	
q_i	Heat flux component in the ith direction	(J/s)
$\mathbf{q}$	Heat flux vector	(J/s)
q_b	Unit bedload transport rate	(kg/m)
q_b^*	Dimensionless bedload parameter	
q_w	Unit discharge	(m^2/s)
Q	Flow rate	(m^3/s)
r	Ratio of the adjusted Movability Number to the theoretical Movability Number	
R	Hydraulic radius (= A / P)	(m)
R^2	Correlation coefficient	
RAM	Random access memory	
RANS	Reynolds averaged Navier-Stokes (equations)	
RNG	A turbulence model	
RSM	Reynolds Stress Model	
R_b	Effective hydraulic radius acting on the flume bed	(m)
Re	Reynolds Number (= ρUR / μ = UR / ν)	
Re_d	Particle fall Reynolds Number (= $v_{ss}d$ / ν)	
Re_r	Roughness Reynolds Number (= $u_* k_r$ / ν)	
Re_s	Roughness Reynolds Number for sand (= $u_* k_s$ / ν)	
Re_x	Local Reynolds Number (Ux / ν)	
Re_y	Wall Reynolds Number (= $u_* y$/ ν)	
Re_*	Particle Reynolds Number (= $u_* d$ / ν)	
s	Relative density (= ρ_s / ρ)	
S	Slope	(m/m)
S_E	Source of energy per unit volume per unit time	(J/(m^3.s))
S_0	Bed slope	(m/m)
S_f	Friction slope	(m/m)

T	Temperature	^{o}C, K
u	Component of velocity in x-direction	(m/s)
$\mathbf{u}$	Velocity vector	(m/s)
$\bar{u}$	Average component of velocity in x-direction	(m/s)
u'	Fluctuation about the mean of the velocity in x-direction	(m/s)
u_*	Shear velocity (= $(\tau_0 / \rho)^{0.5}$) (component)	(m/s)
u'_*	Virtual shear velocity (= $(\tau_{yx} / \rho)^{0.5}$)	(m/s)
$\mathbf{u}_*$	Shear velocity (vector)	(m/s)
u^+	Dimensionless velocity (= u / u_*)	
u_0	Effective velocity near a bed particle (component)	(m/s)
$\mathbf{u_0}$	Effective velocity near a bed particle (vector)	(m/s)
u_* / v_{ss}	Movability Number	
u'_* / v_{ss}	Virtual Movability Number	
$\mathbf{u}_* / \mathbf{v_{ss}}$	Movability Number "vector" – takes the direction of the $\mathbf{u}_*$ vector	
U	Average velocity (= Q / A)	(m/s)
U_c	Critical average flow velocity	(m/s)
UCT	University of Cape Town	
uPVC	Unplasticized polyvinyl chloride	
v	Component of velocity in y-direction	(m/s)
$\bar{v}$	Average component of velocity in y-direction	(m/s)
v'	Fluctuation about the mean of the velocity in y-direction	(m/s)
v_{ss}	Settling velocity	(m/s)
VLES	Very Large Eddy Simulation	
w	Component of velocity in z-direction	(m/s)
$\bar{w}$	Average component of velocity in z-direction	(m/s)
v'	Fluctuation about the mean of the velocity in z-direction	(m/s)
W^*	Bed load parameter	
$\mathbf{W}$	Weight vector	(N)
x	Horizontal distance from the origin in the direction of flow	(m)
$\mathbf{x}$	The position vector	(m)
y	Vertical height above the origin	(m)
y_*	Wall unit (= ν / u_*)	(m)

y^+	Dimensionless wall distance (= $y / y_* = Re_y$)	
y_s	Depth of the scour hole	(m)
Y	Depth – the vertical height between the lowest point of the channel section and the free surface	(m)
z	Horizontal distance from the origin normal to the direction of flow (transverse direction)	(m)
α_1, α_2	Constants in the incipient motion equations	
β	Longitudinal (streamwise) slope	(Degrees)
γ	Transverse slope	(Degrees)
δ	Thickness of the viscous sublayer	(m)
δ_l	Thickness of the laminar sublayer	(m)
δ_t	Thickness of the turbulent sublayer	(m)
Δ	Relative submerged density (= $(\rho_s - \rho) / \rho$)	
ε	Rate of viscous dissipation	
$\varepsilon_{(t)}$	Average turbulent kinematic viscosity of water ($\varepsilon_{(t)} = \mu_{(t)} / \rho$)	(Pa.s)
Γ	Relative blockage (= L_a / B_c)	
ζ	Height above some arbitrary datum	(m)
η	Ratio of applied unit stream power to unit power required to suspend a particle	
η_l	Ratio of applied unit stream power to unit power required to suspend a particle in the case of laminar boundary	
η_t	Ratio of applied unit stream power to unit power required to suspend a particle in the case of a turbulent boundary	
κ	Von Kármán "constant" (≈ 0.40 for clear water)	
θ	Shields' parameter	
θ_c	Critical Shields' parameter	
λ^+	Non-dimensionalised streak spacing (= $u_*\lambda / \nu$)	
μ	Dynamic viscosity of water	(Pa.s)
μ_b	Sum of the laminar and turbulent dynamic viscosities	(Pa.s)
$\mu_{(t)}$	Average turbulent dynamic viscosity of water	(Pa.s)
$\mu_{yx(t)}$	Turbulent dynamic viscosity of water associated with a shear stress of $\tau_{yx(t)}$	(Pa.s)
ν	Kinematic viscosity of water (= μ / ρ)	(m^2/s)
ρ	Density of water (≈ 1000)	(kg/m^3)
ρ_s	Particle density	(kg/m^3)
σ	Standard deviation	
σ_g	Geometric standard deviation	
τ_c	Critical bed shear stress for incipient motion	(Pa, N/m^2)

τ_0	Shear stress at the boundary	(Pa, N/m^2)
$\tau_{0,cr}$	Critical bed shear stress at any slope	(Pa, N/m^2)
$\tau_{0,cr,0}$	Critical bed shear stress on a horizontal bed	(Pa, N/m^2)
τ_{ji}	Shear stress in the i-direction on a plane with a normal orientated in the j-direction	(Pa, N/m^2)
$\tau_{ji(l)}$	Shear stress in the i-direction on a plane with a normal orientated in the j-direction as consequence of molecular viscosity	(Pa, N/m^2)
$\tau_{ji(t)}$	Shear stress in the i-direction on a plane with a normal orientated in the j-direction as a consequence of turbulent fluctuations	(Pa, N/m^2)
ϕ	Arbitrary scalar quantity	(Varies)
ϕ_r	Angle of repose	(Degrees)
Φ	Dissipation function (= P_t)	(W/m^3)
Φ_s	Measure of sediment size (= $\log_2$ (d) with d in mm)	
ψ	Slope correction factor	
ω	Turbulence coefficient	
1D	One-dimensional	
2D	Two-dimensional	
3D	Three-dimensional	

Acknowledgements

An investigation of this magnitude requires input from many sources. I gratefully acknowledge guidance and assistance from the following:

i) Prof Albert Rooseboom who ably guided me through this investigation. Time and time again, his years of accumulated experience and wisdom showed as he guided me through key aspects.

ii) Dr Howard Pearce of the University of Cape Town for his valuable advice concerning the numerical modelling, and his day to day assistance with computational problems. He also introduced me to many aspects of Computational Fluid Dynamics (CFD).

iii) The Water Research Commission of South Africa (WRC) for supporting the project. In particular, Mr Dawid van der Merwe, former Deputy Executive Director of the WRC for his positive and able leadership in the earlier phases of the project. Thanks are also due to Mr Hugo Maaren for stepping into the breach on Dawid's retirement.

iv) The Project Steering Committee who provided helpful support throughout. The complete committee was as follows:

Mr Dawid van der Merwe	–	WRC (Chairperson until 2001)
Mr Hugo Maaren	–	WRC (Chairperson from 2001)
Mr OCE Hempel	–	Committee Secretary
Ms Sue Matthews	–	Committee Secretary
Prof Albert Rooseboom	–	University of Stellenbosch
Prof Gerrit Basson	–	University of Stellenbosch
Prof Chris James	–	University of the Witwatersrand
Dr Pieter Wessels	–	Department of Water Affairs & Forestry

v) The University of Cape Town who made students and laboratory resources available and allowed me to spend considerable time on the project.

vi) Prof Garry Pender (formerly of the University of Glasgow, now at Heriot-Watt University, Edinburgh) and Dr Andrey Shvidchenko (University of Glasgow) provided much of the data on incipient motion.

vii) Prof Chris James (University of the Witwatersrand) provided the Harnett (1998) data on scour upstream of a weir.

viii) Dr Eric Valentine (University of Newcastle upon Tyne) and Dr Kourosh Babaeyan-Koopaei (formerly of the University of Newcastle upon Tyne, now of the University of Glasgow) provided laboratory data on scour and deposition around piers and abutments.

ix) The investigation would have taken twice as long had it not been for the assistance of a number of competent undergraduate and postgraduate (MSc(Eng)) students. They included:

Ms Caroline McGahey	–	All numerical (CFD) modelling
Ms Simone Lyons	–	Laboratory experimentation on sudden expansions
Mr John Offerman	–	Laboratory experimentation on sediment movement past vertical obstructions
Mr Denis Feuilloley (seconded from E.N.T.P.E. Lyon, France)	–	Laboratory experimentation on sudden contractions
Mr Alex Mitchell	–	Laboratory experimentation on scour around abutments
Mr Mark Midgley	–	Laboratory experimentation on scour around piers
Mr Ryan Lewis	–	Laboratory experimentation on the behaviour of sediment in uni-directional open channel flow
Mr Roberto Cavallaro	–	Laboratory experimentation on the behaviour of sediment oscillatory flow
Mr Songezo Sifumba	–	Laboratory experimentation on scour through sudden expansions

x) Messrs Eike von Guerard, Denis Botha, Charles Nicholas, Alton Siko and Hector Mafungwa provided laboratory and workshop assistance.

Neil Armitage PrEng, CEng
CAPE TOWN, 2001

Dedication

This thesis is dedicated to my darling wife Debbie and our three wonderful children: Jessica, Michael and Lauren. May the Lord God Almighty be close to you always.

Executive summary

In 1973, a national study of 383 bridge failures caused by catastrophic floods in the USA showed that around 25% involved pier damage and 72% abutment damage (Chang, 1973). Scour is not only the principal cause of failure of many bridges, it is also the principal cause of failure of countless other hydraulic structures. The opposite mechanism, deposition, is a cause of failure of many others. Together they are largely responsible for shaping the landmasses of the Earth.

Scour and deposition form part of the field of sediment transport, which in turn, is part of the field of fluid mechanics. As might be expected, a considerable body of literature has grown up dealing with this important subject. Yet, although the fluid mechanics of sediment transport is reasonably well understood, there is still no universally agreed design procedure that can cope with all the observed scour and deposition phenomena. Most methodologies place considerable reliance on the use of dimensional analysis and empirical formulae. Empirical formulae, however, have severe limitations. They usually only predict one parameter – the maximum scour depth – and the predicted value of this parameter varies over a large range depending on the formula that is used. Physical models are more reliable, provided that they are constructed at a sufficiently large scale. Physical models, on the other hand, are time consuming to construct and test, and are thus expensive.

In view of the above, increasing attention is being placed on the use of three-dimensional mathematical models for the estimation of scour and deposition. The ever-improving capability of computers and the increasing availability of powerful and flexible computational fluid dynamics (CFD) software have assisted this. Furthermore, the combination of a suitable three-dimensional model with appropriate CFD software promises to provide a greater insight into the scour and deposition processes than that currently provided by empirical equations or physical models. Ultimately, as computational power increases and mathematical modelling improves, it is likely to become the method of choice in design and analysis.

One problem, however, is that there is not even general agreement on the concept of incipient motion, that critical point at which motion – and hence scour – begins. It can be shown that there is always a statistical probability that a particle will move regardless of the flow conditions. The same comment can be made about the point at which deposition ceases. Deposition is not necessarily the opposite of scour since the

two processes can occur simultaneously, particularly under equilibrium conditions such as in the case of live-bed scour around an obstacle. Scour and deposition is the consequence of, and is affected by, a multitude of physical factors, one of the most significant being the structure of the boundary layer. Any unified theory of scour and deposition would have to explain the relationship between all of the various factors.

Incipient motion has been described in terms of flow velocity, bed shear stress and unit stream power. Traditionally, most emphasis has been placed on bed shear stress, but this is not necessarily the best parameter to use for the determination of scour and / or deposition. Various researchers (Ackers & White, 1973; Rooseboom, 1975 & 1992; Yang, 1972, 1973, 1976, 1979 & 1996) are convinced that stream power offers a sounder theoretical base for the understanding of incipient motion.

The objective of this thesis was to explore the use of the unit stream power method, as presented by Rooseboom (1992), to see whether this can be developed into a mathematical model that could provide and improved insight into the scour and deposition processes. The unit stream power method has a sound theoretical base and is one of the more flexible of the available approaches. The model should ultimately be capable of reflecting the link between all of the flow parameters – in particular those describing the boundary layer – and incipient motion. The model should thus have the potential to predict scour and deposition under a wide range of conditions through the use of Computational Fluid Dynamics (CFD) software running on a desktop personal computer (PC). To make the problem more tractable, this thesis concentrated on local clear-water scour in uniform, approximately spherical sand around structures of simple geometry

This thesis is broken into four parts. **Part 1** (Chapters 2 – 5) provides the literature review and theoretical background necessary for an understanding of the investigation. **Part 2** (Chapters 6 & 7) presents the proposed unit stream power model of scour and deposition. Numerical analyses using this unit stream power model are described in **Part 3** (Chapters 8 & 9). Some conclusions and recommendations for future work are included in **Part 4** (Chapters 10 & 11).

The findings were as detailed below.

i) Although incipient motion – the conditions under which sediment movement commences – can be described in terms of flow velocity, bed shear stress, and stream power, these parameters are related. The first and last parameters can

both be expressed in terms of the Movability Number (u_* / v_{ss}) where u_* is the shear velocity and v_{ss} is the settling velocity of the sediment particles in quiescent water. Meanwhile, since u_* is defined by Equation 2.13:

$$u_* = \sqrt{\frac{\tau_0}{\rho}} \tag{2.13}$$

where τ_0 is the bed shear stress and ρ is the density of water, the Movability Number is thus also proportional to the square root of the bed shear stress.

ii) Incipient motion is however something that is hard to define as it refers to some "threshold of motion" within what is actually a stochastic process. Analysis of sediment transportation data revealed that it is possible to link the "intensity of motion" to a Movability Number. This must be, however, adjusted for bed-slope and relative depth. The result is Equation 7.16 and Figure 7-3.

$$\frac{u_*}{v_{ss}} = \psi\left(0.2405 + 0.0066\ln(I) + 0.204\frac{d}{Y}\right) \tag{7.16}$$

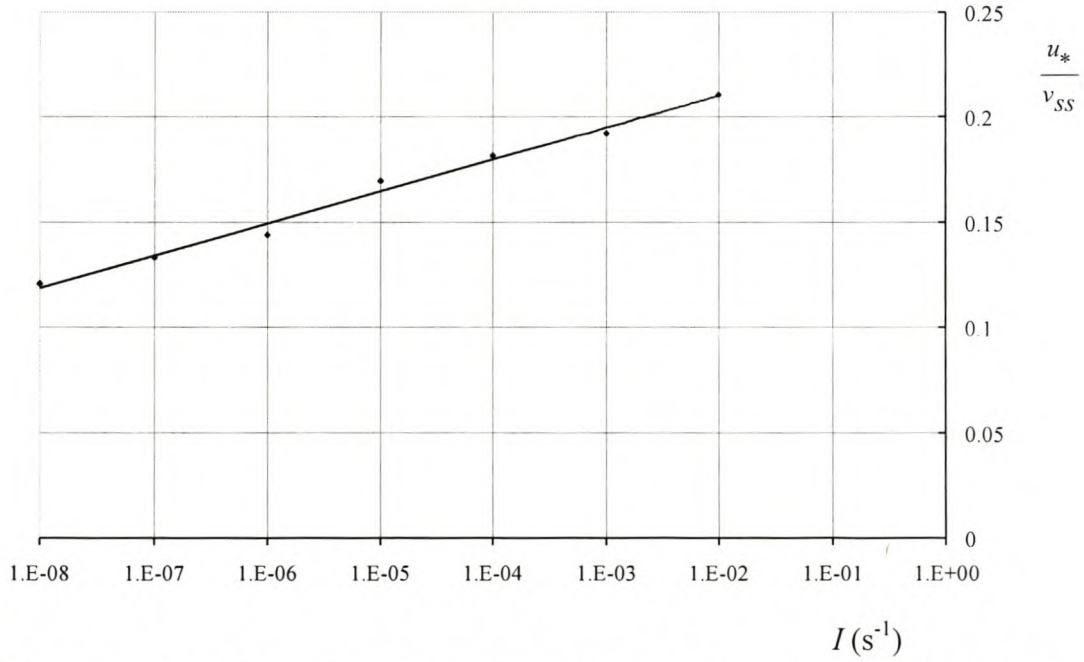

Figure 7-3: Variation of Movability Number with intensity of motion for a flat turbulent bed and zero relative roughness (Semi-logarithmic plot)

In Equation 7.16, I is the intensity of motion, d / Y is the relative depth (particle diameter divided by the water depth), and ψ is the slope correction factor given by Equation 6.18:

$$\psi = \sqrt{\cos\beta\left(1-\frac{\tan\beta}{\tan\phi_r}\right)\cos\gamma\left(1-\frac{\tan^2\gamma}{\tan^2\phi_r}\right)}^{1/2} \tag{6.18}$$

In Equation 6.18, β is the longitudinal bed-slope (in the direction of flow), and γ is the transverse bed-slope (normal to the direction of flow).

iii) Work carried out by Shvidchenko & Pender (2000) showed that the intensity of motion, I, can be directly equated to the dimensionless bedload parameter, q_b^*, i.e. Equation 7.12:

$$I = q_b^* \tag{7.12}$$

Equations 7.12 and 7.16 lead naturally to Equation 7.20, which could be used to determine the rate of scour:

$$q_b = \rho_s \sqrt{(s-1)gd^3}\, e^{\xi} \tag{7.20}$$

In Equation 7.20, q_b is the unit bedload transportation rate, ρ_s is the density of the sediment, s is the relative density of the sediment, g is gravitational acceleration, d is the diameter of the (uniform) sediment, and ξ is the exponent given by Equation 7.19:

$$\xi = \frac{1}{\psi}\frac{u_*}{v_{ss}} - 0.204\frac{d}{Y} - 0.2405 \tag{7.19}$$

iv) The analysis of transportation data revealed that there is no specific value of Movability Number at which movement can be said to have begun or ceased. For the purposes of the model presented in this thesis, however, Equations 7.21 and 7.22 can be used to describe the Movability Number criteria at which the intensity of motion becomes appreciable (taken to be at an intensity of motion

$I = 2 \times 10^{-5}$ s^{-1} in this thesis) on horizontal beds ($\psi = 1.00$). These equations are plotted in Figure 7-8:

$$\frac{u_*}{v_{ss}} \geq \frac{2.0}{Re_*} \quad \text{for } Re_* \leq 11.8 \text{ (laminar boundaries)} \tag{7.21}$$

$$\frac{u_*}{v_{ss}} = 0.17 \quad \text{for } Re_* > 11.8 \text{ (turbulent boundaries)} \tag{7.22}$$

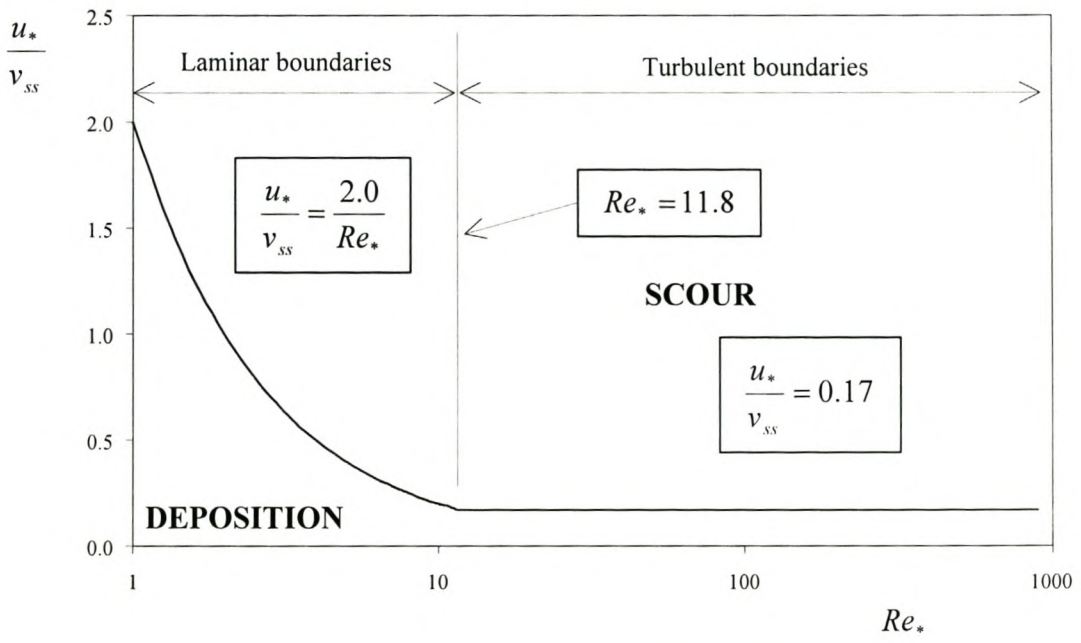

Figure 7-8: New criteria for predicting the onset of scour

If the bed is sloped, then Equation 6.17 is applicable:

$$\left.\frac{\mathbf{u}_*}{\mathbf{v}_{ss}}\right|_{\beta,\gamma} = \psi \left.\frac{\mathbf{u}_*}{\mathbf{v}_{ss}}\right|_{0} \tag{6.17}$$

In Equation 6.17 u_* / v_{ss} is the Mobility Number vector having the direction of the shear velocity.

Consideration of Equations 7.21 and 7.22 or Figure 7-8 reveals that relatively small changes in the flow conditions result in large changes in the intensity of motion.

v) Rooseboom (1992) showed that the unit stream power required to suspend a particle, P_r, could be related to the applied unit stream power, P_t. If η represents the ratio between the two, then this implies Equation 6.1:

$$P_t = \eta P_r \tag{6.1}$$

In Equation 6.1, P_t is the dissipation function, Φ, given by Equation 4.14:

$$\Phi = \tau_{ji} \frac{\partial u_i}{\partial x_j} \tag{4.14}$$

In Equation 4.14, τ_{ji} is the shear stress in the i-direction on a surface with a normal in the j-direction, u_i is the velocity component in the i-direction, and x_j indicates that the gradient is in the direction of the normal to the surface.

P_r is given by Equation 3.32:

$$P_r \approx (\rho_s - \rho) g v_{ss} \tag{3.32}$$

Closer examination of Equations 7.21 and 7.22 reveals that the ratio η is different for laminar boundaries, η_l = 1/6, and turbulent boundaries, η_t = 1/67. As a consequence, incipient motion can be described in terms of unit stream power as follows:

$$P_t \geq \frac{P_r}{6} \quad \text{for } Re_* \leq 11.8 \text{ (laminar boundaries)} \tag{7.24}$$

and,

$$P_t \geq \frac{P_r}{67} \quad \text{for } Re_* > 11.8 \text{ (turbulent boundaries)} \tag{7.25}$$

In the case of the unit stream power equations, correction for bed-slope can be made with the aid of Equations 6.19 or 6.20:

$$P_t = \psi^2 \eta_l P_r \quad \text{(Laminar boundaries)} \tag{6.19}$$

$$P_t = \psi^3 \eta_t P_r \quad \text{(Turbulent boundaries)} \tag{6.20}$$

The main drawback with the above is that unit stream power is a scalar variable, but the calculation of the longitudinal and transverse slopes demands a vector describing the direction of the flow.

vi) From the foregoing, a simple model of scour and deposition around a structure can be proposed (Section 6.4). The sediment transport through a hydraulic structure is determined mainly by the upstream and downstream conditions i.e. the supply and removal of sediment respectively. If the supply rate of sediment to the region around a structure exceeds the removal rate there is accretion at the structure. If the removal rate exceeds the supply rate there will be degradation. Sometimes, potential degradation in the vicinity of the structure is prevented by local conditions e.g. the structure may be founded on a rigid base.

Erosion and deposition around the structure will reach "equilibrium" at the point where the applied unit stream power, P_t, equals the value required for incipient motion. This is indicated by Equations 7.21 and 7.22, or 7.24 and 7.25 modified by Equations 6.17 or 6.19 and 6.20 if there is a non-zero bed-slope. If the unit stream power at the bed is greater than that required for incipient motion, there will be scour. If the unit stream power at the bed is less than that required for incipient motion, but the stream is conveying sediment, there will be nett deposition.

vii) McGahey (2001) tested out the proposed model with the flow parameters calculated with the aid of CFX Versions 4.3 and 4.4 using the k-ε turbulence model. The processor was a 667MHz Intel Pentium III processor (PC) with 256MB of RAM. The model appeared to give good results when applied to the prediction of scour upstream of a weir. The results were not as impressive when the model was applied to the prediction of scour around piers and abutments although the general scour pattern was clearly visible. This could be due in part to the free surface approximation that was implemented. Coding is now available that gives a better determination of the free surface, and that could lead to an improvement in the CFD modelling. The choice of the k-ε turbulence model also pays a role. The accuracy of the numerical model could be

improved through the use of Direct Numerical Simulation (DNS) of the Navier-Stokes equations. It is, however, likely to be a very long time before computers are generally available that are capable of adequately modelling the scour around engineering structures using DNS. The k-ε model is likely to be the best compromise for a while.

When the scour around a pier with a deformable boundary was modelled, the analysis showed that the final profile was approximately the equilibrium profile as determined by the theoretical model.

The unit stream power model presented in this thesis shows considerable promise for the prediction of scour and deposition, but extensive development will be required before the model will be able to solve the entire range of problems facing Engineers in this field.

Chapter 1
Introduction

In 1973, a national study of 383 bridge failures caused by catastrophic floods in the USA showed that around 25% involved pier damage and 72% abutment damage (Chang, 1973). In 1985, some 73 bridges were destroyed by floods in Pennsylvania, Virginia and West Virginia, while during the spring floods of 1987, 17 bridges in New York and New England were damaged or destroyed by scour (Hamil, 1999).

Scour is not only the principal cause of failure of many bridges, it is also the principal cause of failure of countless other hydraulic structures. The opposite mechanism, deposition, is a cause of failure of many others. Together they are largely responsible for shaping the landmasses of the Earth.

Scour and deposition form part of the field of sediment transport, which in turn, is part of the field of fluid mechanics. As might be expected, a considerable body of literature has grown up dealing with this important subject. Textbooks by, inter alia, Breusers & Raudkivi (1991), Chien & Wan (1999), Graf (1971, 1998), Hamil (1999), Hoffmans & Verheij (1997), Julien (1995), Raudkivi (1998), Van Rijn (1993), Vanoni (1975), Yalin (1972) and Yang (1996) have devoted considerable space to it. Hundreds of papers have appeared in journals. Yet, although the fluid mechanics of sediment transport is reasonably well understood, there is still no universally agreed design procedure that can cope with all the observed scour and deposition phenomena. Most methodologies place considerable reliance on the use of dimensional analysis and empirical formulae. Empirical formulae, however, have severe limitations. They usually only predict one parameter – the maximum scour depth – and the predicted value of this parameter varies over a large range depending on the formula that is used. Physical models are more reliable, provided that they are constructed at a sufficiently large scale. Physical models, on the other hand, are time consuming to construct and test, and are thus expensive. It is thus obvious that there is still considerable work to be done before this subject reaches maturity.

One problem, however, is that there is not even general agreement on the concept of incipient motion, that critical point at which motion – and hence scour – begins. It can be shown that there is always a statistical probability that a particle will move regardless of the flow conditions. The same comment can be made about the point at

which deposition ceases. Deposition is not necessarily the opposite of scour since the two processes can occur simultaneously, particularly under equilibrium conditions such as in the case of live-bed scour around an obstacle. Scour and deposition is the consequence of, and is affected by, a multitude of physical factors, one of the most significant being the structure of the boundary layer. Any unified theory of scour and deposition would have to explain the relationship between all of the various factors.

Incipient motion has been described in terms of flow velocity, bed shear stress and unit stream power. Traditionally, most emphasis has been placed on bed shear stress, but this is not necessarily the best parameter to use for the determination of scour and / or deposition. Various researchers (Ackers & White, 1973; Rooseboom, 1975 & 1992; Yang, 1972, 1973, 1976, 1979 & 1996) are convinced that stream power offers a sounder theoretical base for the understanding of incipient motion.

The objective of this thesis was to explore the use of the unit stream power method, as presented by Rooseboom (1992), to see whether this can be developed into a mathematical model that could provide an improved insight into the scour and deposition processes. The unit stream power method has a sound theoretical base and is one of the more flexible of the available approaches. The model should ultimately be capable of reflecting the link between all of the flow parameters – in particular those describing the boundary layer – and incipient motion. The model should thus have the potential to predict scour and deposition under a wide range of conditions through the use of Computational Fluid Dynamics (CFD) software running on a desktop personal computer (PC). To make the problem more tractable, this thesis concentrated on local clear-water scour in uniform, approximately spherical sand around structures of simple geometry.

The thesis is broken into four parts. **Part 1** (Chapters 2 – 5) provides the literature review and theoretical background necessary for an understanding of the investigation. **Part 2** (Chapters 6 & 7) provides further development of the unit stream power theory and presents the proposed model of scour and deposition. Numerical analyses using this unit stream power model are described in **Part 3** (Chapters 8 & 9). Some conclusions and recommendations for future work are included in **Part 4** (Chapters 10 & 11).

Chapter 2 discusses some key aspects of fluid mechanics; in particular the roles played by the boundary layer and coherent flow structures in the mobilisation of sediment.

Chapter 3 reviews incipient motion – the conditions under which the movement of sediment will commence. This is central to the scour and deposition processes, as the equilibrium profile for any particular flow condition – assuming that the supply of sediment is not limited – will be closely related to the conditions for incipient motion. The influences of various factors are described, as are the different types of motion. The concepts of "threshold of movement" and "pickup probability" are discussed. The different models of incipient motion are described with the main emphasis being placed on the stream power approach, as this is the one that appears to have the strongest theoretical backing. Since the conditions for incipient motion are clearly affected by the slope of the bed, some attention is therefore given to the factors that have been used to adjust the incipient motion parameters designed for flat beds.

Chapter 4 presents the mathematical derivation and definition of the unit stream power equation. This is placed firmly within the context of continuum mechanics, and the relationships between the unit stream power equation and the fundamental equations of fluid flow (for the conservation of mass, momentum and energy) clearly demonstrated. All of these equations are required for the numerical model.

The scour and deposition processes around selected engineering structures are described in **Chapter 5**. Physical and numerical models incorporating these selected structures are described in Chapter 9. This concludes **Part 1**.

The proposed unit stream power model for the prediction of scour and deposition is presented in **Chapter 6**. In view of the fact that channel beds are generally warped, a function is developed to correct the incipient motion criteria for bed slope. In the course of this development, the links between the three different approaches to incipient motion are indicated. Deposition is regarded as the opposite to scour with a critical incipient motion criteria marking the boundary between the two processes.

The probability of movement of any single particle can be directly linked to the intensity of motion – the simultaneous movement of a given number of particles over a given area of bed. In **Chapter 7**, intensity of motion is linked to the "Movability Number" for both laminar and turbulent boundaries. An intensity of motion, I, of

2×10^{-5} s^{-1} was chosen as marking the transition between scouring and depositing conditions in the context of clear-water scour around engineering structures. This is defined as the critical condition for scouring for the purposes of this thesis. Incipient motion is also expressed directly in terms of unit stream power. This chapter concludes **Part 2**.

A preliminary test of the theoretical model, presented in Chapters 6 & 7 was carried out using the CFD code, CFX, supplied by AEA Technology. **Chapter 8** summarises the way CFX was adapted for this purpose. This required, inter alia, describing the solution domain, modelling the boundary conditions, choosing the turbulence model, choosing the differencing scheme, coupling pressure to velocity, choosing the solution algorithm, and deciding between steady-state and transient analyses. The output was then interpreted in terms of the unit stream power equations and the "scour function".

Chapter 9 describes how the CFD model developed in Chapter 8 was applied to a number of test cases that had been previously been the subject of physical modelling. These included the scour upstream of a sharp-crested weir, the scour around a circular pier and a sharp-edged rectangular abutment situated within a rigid rectangular channel, and finally the scour and deposition around a circular pier situated in a regime channel with deformable boundaries. The results were sufficiently encouraging to suggest that the model has the potential to predict the scour and deposition around any structure. This concludes **Part 3**.

This thesis reaches the conclusion in **Chapter 10** that the unit stream power model presented indeed shows considerable promise for the prediction of scour and deposition. Considerable development will, however, be required before the model will be able solve the entire range of problems facing Engineers in this field (**Chapter 11**). This is an endeavour that will, no doubt, continue for a very long time to come!

Part 1

Literature Review
&
Theoretical Background

Chapter 2
An overview of boundary layer theory

2.1 Introduction

Scour and deposition are boundary phenomena – products of the interaction between the flow and the erodible boundaries. Ultimately they lead to shifts in the location of these boundaries. An understanding of some key aspects of boundary layer theory is thus important.

Forces are transmitted through the flow domain through shear stresses, which in turn are linked to viscosity and turbulence. This chapter thus commences with a brief overview of shear stress, viscosity and turbulence in fluids. The shear stresses also effect the velocity distribution resulting in the so-called "boundary layer" near the bed. The nature of the boundary layer and its interaction with bed roughness is described in some detail.

In the interests of simplicity, the theory is largely developed with reference to steady uniform flow in an infinitely wide rectangular channel. The chapter, however, concludes with an introduction to some of the so-called coherent flow structures that distort the flow parameters from their average values.

2.2 Viscosity, stress and turbulence in uni-directional flow

2.2.1 Viscosity

Define τ_{yx} (Pa) as the shear stress in the x-direction on a plane with its normal in the y-direction. The viscosity of a fluid is a measure of the rate of momentum transfer between adjacent regions as a result of the relative motion between them. If u is the horizontal component of the velocity at a point y above the bed, and μ is the "dynamic viscosity" then Newton's Law of Viscosity states (Prandtl, 1952):

$$\tau_{yx} = \mu \frac{\partial u}{\partial y} \tag{2.1}$$

Strictly speaking this equation applies only to laminar flow, in which case μ is a property of the fluid and results from the interchange of momentum at the molecular level. It is mainly a function of temperature, as increasing the temperature increases the movement of the molecules. In the case of liquids this increases the ability of the molecules to move past each other. The viscosity of a liquid thus decreases with increasing temperature. Viscosity also depends on pressure – but to a much lesser degree (in the case of a liquid). White (1991) presents the following empirical formula linking μ (Pa.s) to the temperature T (K) for water with an accuracy of ±1% over the range $273 < T\,(\mathrm{K}) < 373$:

$$\ln\frac{\mu}{0.00179} \approx -2.10 - 4.45\left(\frac{273}{T}\right) + 6.55\left(\frac{273}{T}\right)^2 \tag{2.2}$$

"Kinematic viscosity", ν, is defined in terms of the dynamic viscosity, μ, and the density of water, ρ, as:

$$\nu = \frac{\mu}{\rho} \tag{2.3}$$

Yang (1996) proposed the following empirical formula for ν (m^2/s) in terms of T (^oC) for water:

$$\nu = \frac{1.79 \times 10^{-6}}{(1.0 + 0.0337T + 0.000221T^2)} \tag{2.4}$$

2.2.2 Two simple turbulence models

In the case of turbulent flow, the stress is also increased as a result of large-scale interchange of particles – and hence momentum – between adjacent regions as a result of eddies. It is generally assumed that the total shear stress τ_{yx} on a horizontal plane at any point within the flow can be expressed as the sum of the stress due to molecular viscosity, $\tau_{yx(l)}$, and the stress due to turbulent fluctuations, $\tau_{yx(t)}$ (Yalin, 1972):

$$\tau_{yx} = \tau_{yx(l)} + \tau_{yx(t)} \tag{2.5}$$

The stress due to turbulent fluctuations is commonly calculated in one of two ways.

Let the instantaneous velocity components at a point be $u = \bar{u} + u'$ and $v = \bar{v} + v'$ in the x- and y-directions respectively, where the bar indicates the time average value and the prime indicates the fluctuating component. The "Reynolds' stress model" (e.g. Yalin, 1972; Schlichting, 1979; Massey, 1989; Chadwick & Morfett, 1998) expresses $\tau_{yx(t)}$ in terms of the fluctuating point velocity components u' and v' as follows:

$$\tau_{yx(t)} = -\rho\overline{u'v'} \tag{2.6}$$

Here, $\overline{u'v'}$ is the time average value of the product $u' \bullet v'$.

The "Prandtl eddy model" is based on the Prandtl "mixing-length theory" (Prandtl, 1925). By considering the order of magnitude of momentum transfer in a rotating "ball" of fluid, Prandtl determined that $\tau_{yx(t)}$ must be related to the velocity gradient and some "mixing length", ℓ_m. This led to the following expression (Prandtl, 1952; White, 1991; Versteeg & Malalasekera, 1995):

$$\tau_{yx(t)} = \rho \ell_m^{\,2} \left|\frac{\partial u}{\partial y}\right| \frac{\partial u}{\partial y} \tag{2.7}$$

In the vicinity of a solid boundary (but not so close that the turbulent fluctuations are dampened out – see later), Prandtl and Von Kármán determined that $\ell_m = \kappa y$ to give:

$$\tau_{yx(t)} = \rho \kappa^2 y^2 \left|\frac{\partial u}{\partial y}\right| \frac{\partial u}{\partial y} \tag{2.8}$$

κ is the so-called Von Kármán "constant", which is not a constant at all as it varies with, inter alia, the sediment concentration (Einstein & Chien, 1955) and possibly also the Reynolds Number, *Re* (French, 1994). For flows with low sediment concentration,

the Nikuradse (1933) data suggested that κ is approximately equal to 0.40. Rooseboom (1992) showed from the Prandtl "mixing-length theory" that its theoretical value is $1/(2\pi)^{0.5} \approx 0.40$. Other experimental data (e.g. Prandtl, 1952; Yalin, 1972; Versteeg & Malalasekera, 1995), however indicates that under certain circumstances, a more accurate value might be closer to $\kappa = 0.417$. Under extreme conditions e.g. high sediment concentrations, the value of κ can fall to as low as 0.20. Experimental data on the variation of κ with sediment concentration presented by Einstein & Chien (1954, 1955), Barton & Lin (1955), Vanoni & Nomicos (1959, 1960) and Einstein & Abdel-Aal (1972) is summarised by Basson & Rooseboom (1997). More information is given in Chien & Wan (1999).

The implication of Equation 2.8 is that a "turbulent viscosity" $\mu_{yx(t)}$, associated with the shear stress τ_{yx}, can be defined as follows:

$$\mu_{yx(t)} = \rho \kappa^2 y^2 \left| \frac{\partial u}{\partial y} \right| \tag{2.9}$$

Equation 2.5 can now be rewritten as follows (White, 1991):

$$\tau_{yx} = \left(\mu + \mu_{yx(t)}\right) \frac{\partial u}{\partial y} \tag{2.10}$$

2.2.3 The variation of shear stress with depth

The distribution of shear stress with depth is illustrated in Figure 2-1. It is easily shown (e.g. Yalin, 1972; Rooseboom, 1992; Yang, 1996) that, in the absence of any local disturbances, the shear stress τ_{yx} at any height y above the bed for steady, uniform flow within a wide channel with a bed-slope S_0 is given by:

$$\tau_{yx} = \rho g (D - y) S_0 \tag{2.11}$$

The shear stress is zero at the surface. It reaches a maximum, τ_0, at the bed where:

$$\tau_0 = \rho g D S_0 \tag{2.12}$$

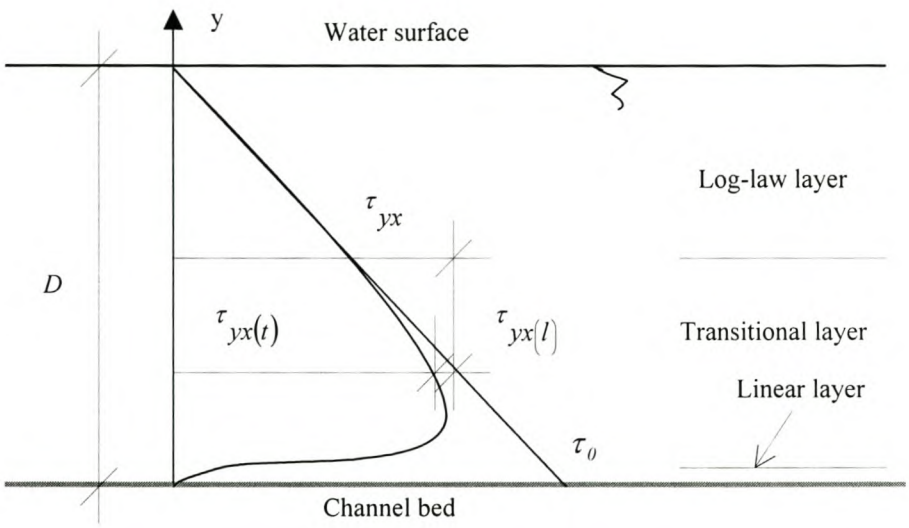

Figure 2-1: Typical shear stress distribution in a channel
(Vertical scale greatly distorted)

Close to the channel bed, the velocity gradient is large but the mixing length is small. As a consequence, $\tau_{yx(t)}$ is small because of the small mixing length, whilst $\tau_{yx(l)}$ is large because of the large velocity gradient. The latter thus makes the larger contribution to the total. Further away from the bed, however, the mixing length is large and that, plus the fact that $\tau_{yx(t)}$ is related to the square of the velocity gradient, means that turbulent shear stress dominates.

2.2.4 The variation of turbulence intensity with depth

The longitudinal and vertical "turbulence intensities" are defined as (Vanoni, 1975; Graf, 1998; Chien & Wan, 1999):

$$\frac{\sqrt{u'^2}}{u_*} \quad \text{and} \quad \frac{\sqrt{v'^2}}{u_*} \quad \text{respectively}$$

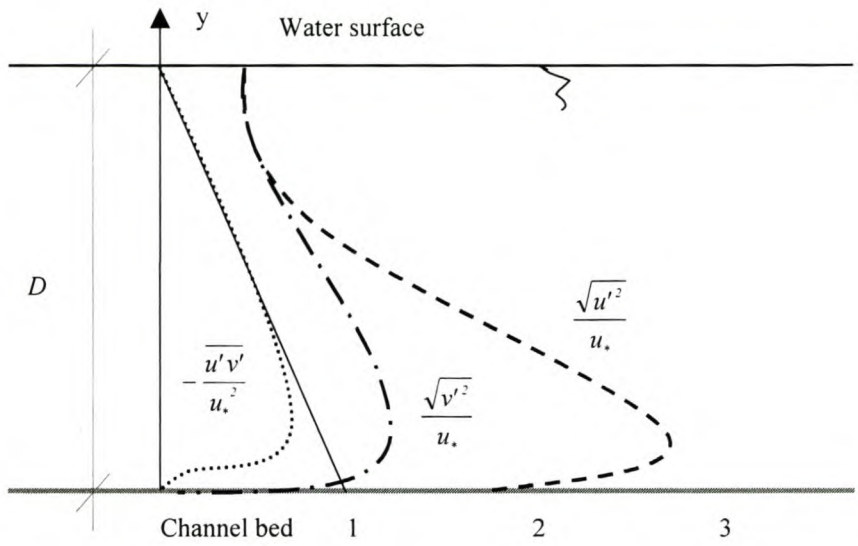

Figure 2-2: Schematic distribution of turbulence intensities
(After Graf, 1998 – y-axis not to scale)

The terms $\sqrt{u'^2}$ and $\sqrt{v'^2}$ are termed the "root mean square (r.m.s.)" values of the instantaneous velocity components and are a measure of the absolute turbulence in the x- and y-directions respectively.

The Reynolds stress (Equation 2.5), can also be expressed in a similar dimensionless form by dividing by $-\rho u_*^2$ to give:

$$\text{Reynolds Stress } (x\text{-}y \text{ plane}) = -\frac{\overline{u'v'}}{u_*^2}$$

Figure 2-2 is a schematic of the distribution of these three quantities when plotted against depth for steady uniform flow in a wide channel. According to Chien & Wan (1999), the turbulence intensity at the boundary is zero. It, however, increases rapidly to its peak value within a very small distance. According to Graf (1998), the longitudinal turbulence intensity approaches 1.8 in the inner boundary layer (see Section 2.3.3 for the definition of this), peaks at a value in excess of 2.0 a bit further away, and then falls back to a value of about 0.6 near the surface. The vertical turbulent intensity likewise reaches approximately 1.0 in the inner boundary layer before falling back to a value of about 0.6 near the surface. Near the boundary, therefore, it is clear that the turbulence is somewhat anisotropic i.e. not the same in all

directions. Far from the boundary, however, in the main flow region, the turbulence intensity is isotropic, lower, and essentially constant.

2.3 The boundary layer

2.3.1 Introduction

The region near the solid boundary is of particular interest since this is where the largest changes in the flow parameters are taking place and where sediment movement is initiated.

Ludwig Prandtl (1904) was the first to suggest that the flow near a boundary could be considered in two parts (Schlichting, 1979; Massey, 1989):

i) Near the boundary – in the so-called "boundary layer" – where the shear stresses are of prime importance.

ii) Remote from the boundary where (in general) velocity gradients are small and so the effect of viscosity is negligible.

In the case of open-channel flow, it could be argued that the entire flow depth is within the boundary layer, because everywhere the flow is affected by the presence of the boundary (French, 1994). On the other hand, the influence of the boundary is most keenly felt in the thin layer closest to it. To complicate matters further, the free surface also represents a boundary, albeit a (generally) moving one. One definition of the limit of the boundary layer is the point where the velocity is 99% of the free stream velocity. In open channel flow, however, there is a substantial velocity gradient at most points within the cross-section of the flow and the free stream velocity has no obvious interpretation. Secondary currents also play a role as they introduce transverse velocity components and help to depress the point of maximum velocity below the surface.

2.3.2 Definition of the wall units

To make the information universally applicable, quantities are generally expressed in a standard manner. If τ_0 is the shear stress at the wall and ρ is the density of the water, then the shear velocity, u_*, is defined as:

$$u_* = \sqrt{\frac{\tau_0}{\rho}} \approx \sqrt{gDS_0} \quad \text{(for steady, uniform flow in a wide channel)} \tag{2.13}$$

If μ and ν are the coefficients of dynamic viscosity and kinematic viscosity respectively, then the scaling distance from the wall, the so-called "wall unit", y_*, is defined as:

$$y_* = \frac{\mu}{\sqrt{\rho\tau_0}} = \frac{\nu}{u_*} \tag{2.14}$$

Assume that u is the average fluid velocity parallel to the boundary at a distance y from it. With the above two quantities, it is now possible to define a dimensionless velocity, u^+, and a dimensionless distance, y^+, as follows:

$$u^+ = \frac{u}{u_*} \tag{2.15}$$

and,

$$y^+ = \frac{y}{y_*} = \frac{u_* y}{\nu} = Re_y \tag{2.16}$$

As can be seen, the dimensionless distance, y^+, is in the form of a wall Reynolds Number, Re_y.

2.3.3 Description of the different layers

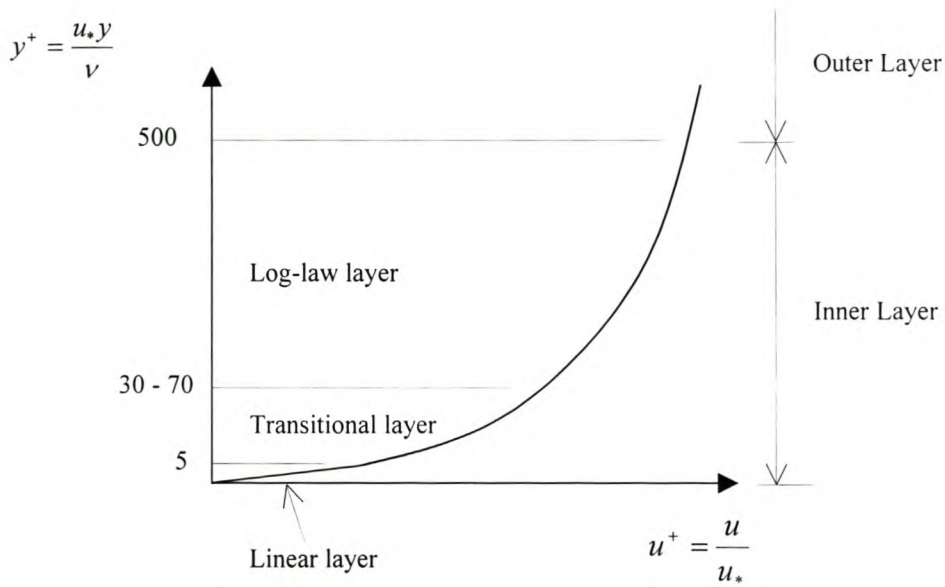

Figure 2-3: Schematic variation of velocity through the inner boundary layer

Close to the wall, in the inner boundary layer, the flow is dominated by viscous effects, and the mean flow velocity depends only on the distance from the wall, y, the fluid density, ρ, the viscosity, μ, and the wall shear stress, τ_0. Dimensional analysis (Yalin, 1972; Versteeg & Malalasekera, 1995) shows that:

$$u^+ = f\left(y^+\right) \tag{2.17}$$

Three different zones can be identified within the inner boundary layer (Figure 2-3):

i) The so-called "laminar" (Schlichting, 1979), "viscous" (Massey, 1989) or "linear" (Reynolds, 1974; Versteeg & Malalasekera, 1995) layer where:

$$u^+ = y^+ \quad \text{for} \quad y^+ < 5 \tag{2.18}$$

ii) The so-called "laminar-turbulent" (Schlichting, 1979), "transitional" (Yalin, 1972; Massey, 1989) or "buffer" (Reynolds, 1974) layer which starts at about $y^+ = 5$. The upper boundary is not very clear and is also dependent on the

nature of the boundary roughness (Yalin, 1972). For a plane sand boundary, the Nikuradse (1933) data seems to suggest $y^+ = 70$ (Yalin, 1972; Schlichting, 1979), although values of $y^+ = 30$ (Versteeg & Malalasekera, 1995) and $y^+ = 50$ (Reynolds, 1974) are also found in the literature.

There is no obvious relationship between u^+ and y^+ in the transitional layer and generally some curve is fitted to the data. Reynolds (1974) suggests several candidate curves that offer a smooth transition between the linear layer and the third layer – the log-law layer. Another tactic is to ignore the transitional layer altogether in which case the compromise border between the linear layer and the log-law layer lies somewhere between $y^+ = 11$ and $y^+ = 13$ (Yalin, 1972; Reynolds, 1974; Rooseboom, 1992). $y^+ \approx 11.8$ (Potter & Wiggert, 1997) is a commonly accepted value. Sometimes this theoretical border is deemed to indicate the extent of the "viscous sublayer" and its thickness given the symbol δ (Yalin, 1972).

iii) The "log-law layer" extends from the transitional layer up until about $y^+ = 500$ (Versteeg & Malalasekera, 1995) after which the boundary ceases to have such a great influence on the velocity profile. Here:

$$u^+ = \frac{1}{\kappa}\ln\left(y^+\right) + B \tag{2.19}$$

The value of the constant B depends on the nature of the channel, its relative roughness, and Re. Nikuradse (1933) experimentally determined the value of B to be about 5.5 for a channel with entirely laminar boundaries (Prandtl, 1952; Yalin, 1972; Reynolds, 1974, Schlichting, 1979). B can be thought of as the "slip" within the viscous layer interposed between the wall and the fully turbulent flow region (Reynolds, 1974). Alternatively, it can be viewed as a correction for the fact that the velocity according to the logarithmic velocity distribution is not zero right at the boundary (Rooseboom, 1992).

Equation 2.19 can also be expressed in terms of ordinary logarithms using the identity $\log_e x = 2.3026 \log_{10} x$. If $\kappa = 0.40$ and $B = 5.5$, then (Prandtl, 1952):

$$u^+ = 5.76(\log_{10} y^+) + 5.5 \tag{2.20}$$

The velocity distribution in the outer layer ($y^+ > 500$) also tends to be logarithmic, and, in the case of uni-directional flow in an open channel, the logarithmic distribution theoretically extends all the way to the surface (Yalin, 1972). In reality, however, secondary currents and local turbulence phenomena increasingly affect the velocity distribution as y^+ increases.

The general relationship between u^+ and y^+ (Equation 2.17) in the vicinity of a boundary is sometimes called the "law of the wall" (Schlichting, 1979; Versteeg & Malalasekera, 1995). The logarithmic relationship that describes the log-law layer, and to a certain extent the outer boundary layer (Equation 2.19), is sometimes termed the "universal velocity distribution law" (e.g. French, 1994) – although see Section 2.3.4 for a slightly different definition. Figure 2-4 shows the general velocity distribution for a completely laminar boundary when plotted using semi-logarithmic axes.

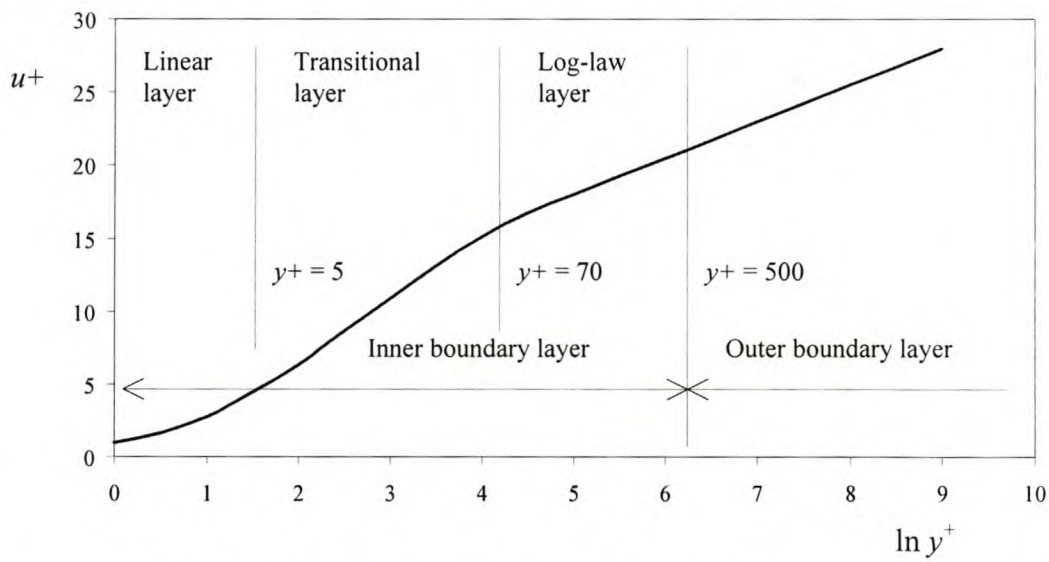

Figure 2-4: The logarithmic velocity distribution for a laminar boundary

(After Versteeg & Malalasekera, 1995)

It is important to remember that the inner boundary layer is usually extremely thin. A uniform depth of 1 m in an infinitely wide rectangular channel of slope 1:1000 would have a shear velocity u_* = 0.1 m/s, a linear layer thickness of about 0.05 mm, a transitional layer thickness of about 0.65 mm, and a log-law layer thickness of about

4.3 mm. Increasing the depth to 10 m and the slope to 1:100 results in a ten-fold decrease in these values. On the other hand, as the flow velocity reduces to zero, the inner boundary layer thickness tends to infinity.

2.3.4 The role of roughness

The role of roughness now needs to be discussed.

Assume that the roughness elements are small compared to the total fluid depth. If the absolute height of the roughness elements is k_s, then a dimensionless "roughness Reynolds Number", Re_s can be defined as follows:

$$Re_s = \frac{u_* k_s}{\nu} \tag{2.21}$$

The subscript s indicates that the roughness elements in this instance are sand grains.

There are three possible flow "regimes":

i) The roughness elements are completely buried within the linear layer ($Re_s < 5$). The fluid flows smoothly around and over the roughness elements without unduly disturbing the layers above. In this case, the velocity distribution depends only on the viscosity of the fluid, ν, and not on the size and nature of the roughness. The flow is said to be "hydraulically smooth" (Yalin, 1972; Schlichting, 1979) and the boundary "laminar" (Young et al., 1997).

ii) The roughness elements project deep into the log-law layer or the outer boundary layer ($Re_s > 70$). The velocity distribution now depends almost exclusively on the roughness height, k_s, and its shape, whilst the viscosity of the fluid no longer has a significant impact. The flow is said to be "rough" (Schlichting, 1979), "fully developed turbulent flow", or "rough turbulent flow" (Yalin, 1972) and the boundary "turbulent (Young et al., 1997).

iii) The roughness elements extend to somewhere between the linear layer and the log-law layer ($5 < Re_s < 70$). In-between the two extremes described in i) and

ii) above, the velocity distribution is dependent on both ν and k_s and is said to be in "transition" (Schlichting, 1979).

If the log-law is to serve for the three flow regimes then it has to be altered to take into account the roughness height k_s. Let B_s be a constant associated with a sand boundary. Define (Yalin, 1972; Schlichting, 1979):

$$u^+ = \frac{1}{\kappa} \ln \frac{y}{k_s} + B_s \tag{2.22}$$

where:

$$B_s = \frac{1}{\kappa} \ln \frac{u_* k_s}{\nu} + 5.5 \quad \text{for} \quad Re_s = \frac{u_* k_s}{\nu} < 5$$

and

$$B_s = 8.5 \quad \text{for} \quad Re_s = \frac{u_* k_s}{\nu} > 70$$

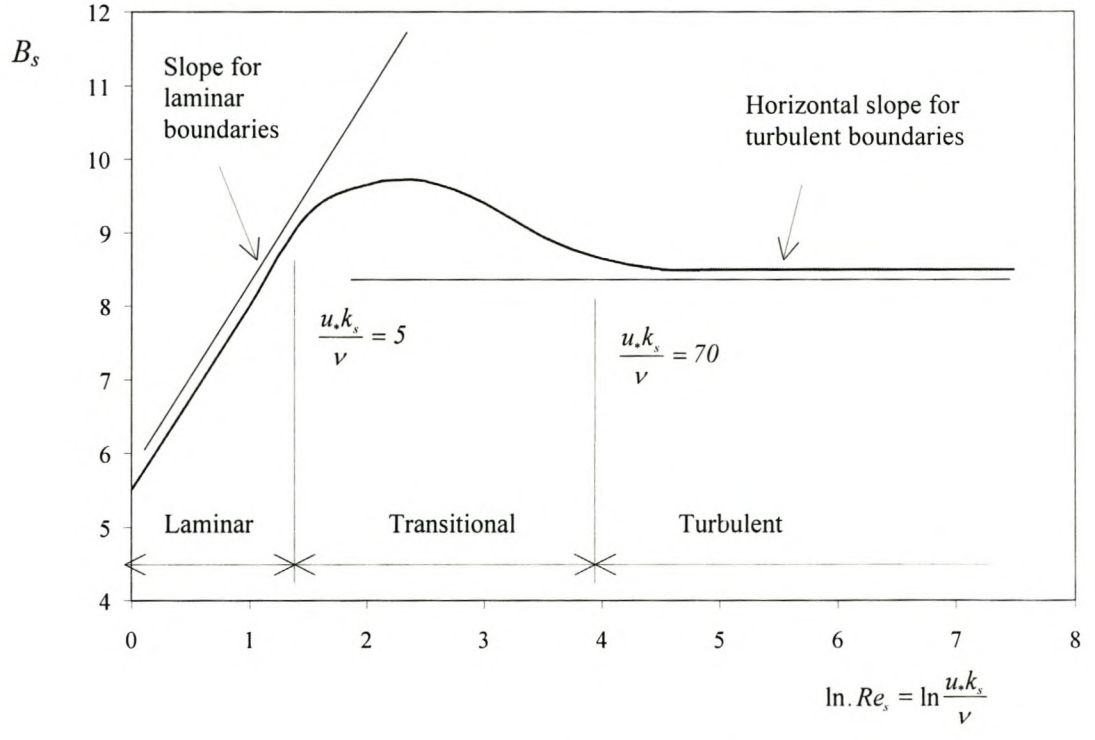

Figure 2-5: The variation of B_s with Re_s
(Adapted from Nikuradse, 1933; Yalin, 1972; and Schlichting, 1979)

When $Re_s < 5$, substitution of B_s into Equation 2.22 gives Equation 2.19 with $B = 5.5$. Values of Re_s between 5 and 70 can only be determined experimentally. Approximate values of B_s are shown in Figure 2-5 (Nikuradse, 1933).

A further refinement to the log-law is to incorporate B_s into the first term of Equation 2.22 through the substitution:

$$A_s = e^{\kappa B_s} \tag{2.23}$$

The log-law is now rewritten as:

$$u^+ = \frac{1}{\kappa} \ln \frac{A_s y}{k_s}$$

or:

$$u = \frac{u_*}{\kappa} \ln \frac{A_s y}{k_s} \tag{2.24}$$

In the case of a turbulent sand wall ($B_s = 8.5$), $A_s = 30.0$. A_s for rough sand walls has also been theoretically determined as equal to 30.1 by Simons and Sentürk (1977) and equal to 29.6 by Rooseboom (1992).

If the velocity distribution is assumed to be logarithmic all the way to the surface – which is approximately true for unidirectional flow in a wide channel – then the maximum velocity, u_{max}, is at the surface at a height, D, above the bed, and:

$$\frac{u_{\max}}{u_*} = \frac{1}{\kappa} \ln \frac{D}{k_s} + B_s \tag{2.25}$$

If Equation 2.22 is now subtracted from Equation 2.25:

$$\frac{u_{max} - u}{u_*} = -\frac{1}{\kappa} \ln \frac{y}{D} \tag{2.26}$$

To confuse matters slightly Equation 2.26 is also sometimes called the "universal velocity distribution law" (Yalin, 1972; Schlichting, 1979) (compare this equation with Equation 2.19 which is also given this name). It indicates that the dimensionless "velocity deficit" varies with the dimensionless height within the turbulent flow region in the same manner for any geometry of roughness (Yalin, 1972).

If the roughness elements have a different character from sand grains, e.g. asymmetrical sand dunes, then it is to be expected that although the form of the equations might be the same, the constant will change. Assume that Re_r is the dimensionless "Roughness Reynolds Number" for an arbitrary roughness geometry and B_r is the associated constant (Yalin, 1972). If k_r is the absolute height of the roughness elements, then:

$$Re_r = \frac{u_* k_r}{\nu} \tag{2.27}$$

Figure 2-6 compares a typical plot of B_r versus Re_r with that of B_s versus Re_s.

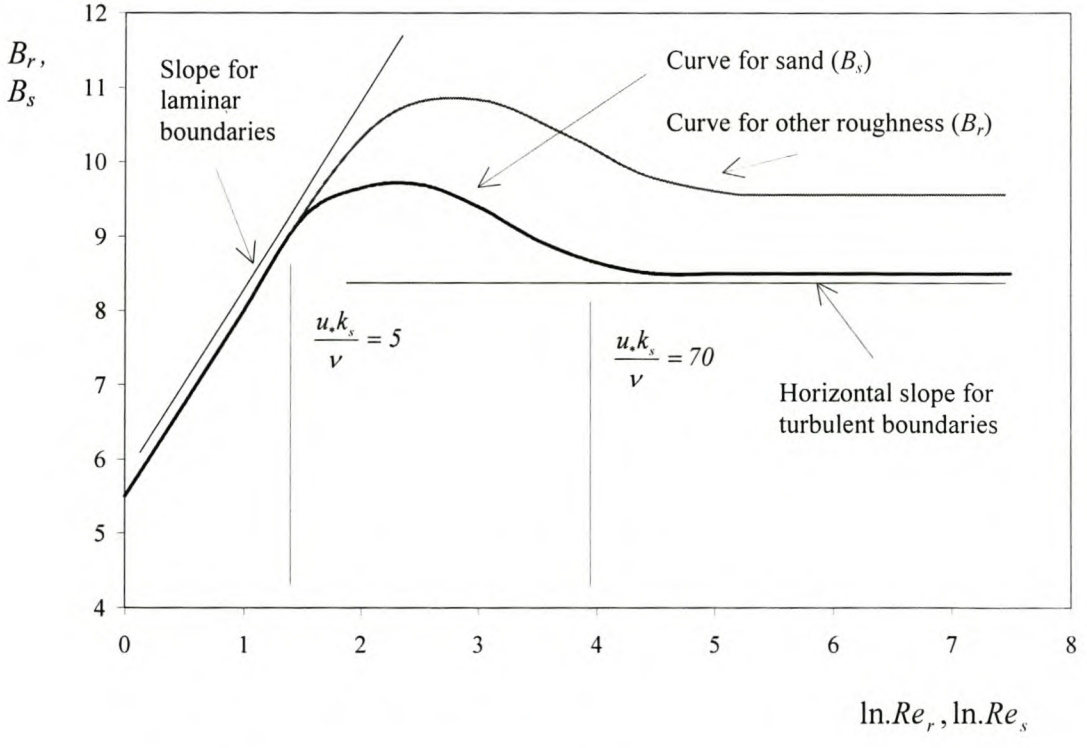

Figure 2-6: The variation of B_r with Re_r compared to B_s with Re_s
(Yalin, 1972)

It is readily apparent that there is no difference between the two curves for very small roughness heights. For large roughness heights, the two curves are parallel which implies that the new roughness can be expressed in terms of an equivalent sand roughness via the identity (Yalin, 1972):

$$k_s = k_r e^{-\kappa(B_r - B_s)} \tag{2.28}$$

In the transitional region between these two extremes there is no unique relationship between the two curves.

2.3.5 The development of boundary layers

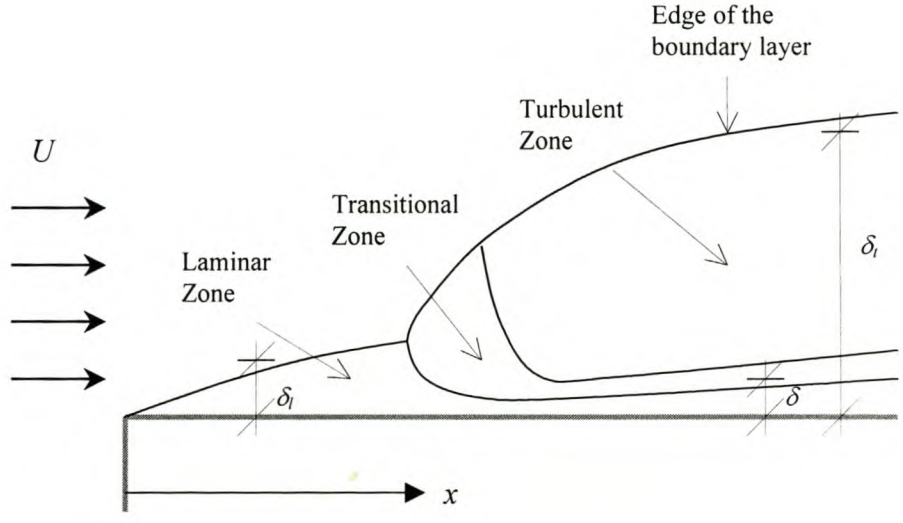

Figure 2-7: Schematic showing the growth of the boundary layer with length
(N.B. greatly exaggerated *y*-axis)

So far, the discussion on boundary layers has been limited to fully developed boundary layers on flat boundaries with a zero pressure gradient in steady flow. Before moving off the topic, mention should be made of some of general development of boundary layers on flat surfaces with negligible pressure gradients.

A boundary layer will develop with the introduction of each new surface into the flow. Furthermore, boundary layers can develop within other boundary layers

(French, 1994). The development of a boundary layer on a flat surface is illustrated schematically in Figure 2-7 (Massey, 1989; Potter & Wiggert, 1997; Chadwick & Morfett, 1998):

Assume that x is the distance from the start of the boundary layer. Define a "Local Reynolds Number", Re_x, such that:

$$Re_x = \frac{Ux}{\nu} \tag{2.29}$$

Initially the boundary layer is wholly laminar and its thickness, δ_l (from the boundary to a point where the velocity is 99% of the undisturbed velocity, U), may be estimated by the Blasius solution (French, 1994; Potter & Wiggert, 1997; Roberson & Crowe, 1997):

$$\delta_l = \frac{5x}{\sqrt{Re_x}} \tag{2.30}$$

The transition between the laminar and turbulent boundary layers generally takes place in the range $5 \times 10^5 < Re_x < 10^6$ (French, 1994). Assuming a free stream velocity U = 1 m/s would imply a laminar boundary layer from 0.5 to 1.0 m long. Doubling the free stream velocity to 2 m/s results in this distance being halved. A typical thickness is δ_l = 3.5 mm for $Re_x = 5 \times 10^5$ and x = 0.5 m.

The thickness of the turbulent boundary layer, δ_t, for $Re_x < 10^7$ is approximately given by (French, 1994; Potter & Wiggert, 1997; Roberson & Crowe, 1997):

$$\delta_t \approx \frac{0.37x}{Re_x^{0.2}} \tag{2.31}$$

Equation 2.31 is the time-average thickness of the turbulent layer. The instantaneous thickness typically varies between 40 – 120 % of this value (Potter & Wiggert, 1997).

Recall from Section 2.3.3 that the thickness of the viscous sublayer at the bottom of the turbulent boundary layer is approximately:

$$\delta \approx \frac{11.8\nu}{u_*} \tag{2.32}$$

Since u_* depends on the shear stress at the boundary τ_0 (Equation 2.13), which in turn depends on the velocity gradient (Equation 2.1), δ is also dependent on the distance from the beginning of the boundary layer. With distance, however, τ_0 trends to a fixed value dictated by Equation 2.12 and δ (for steady uniform flow in a wide channel) is then given by:

$$\delta \approx \frac{11.8\nu}{\sqrt{gDS_0}} \tag{2.33}$$

In general, the thickness of the boundary layer increases with increasing distance and fluid viscosity, and decreasing average velocity. Refer to Schlichting (1979) for details about more complex boundary layers.

2.4 Coherent flow structures and turbulence

"Big whirls have little whirls that feed on their velocity;
Little whirls have lesser whirls, and so on to viscosity."

(Attributed to E. G. Richardson by Reynolds, 1974
and to L. F. Richardson by Lugt, 1983)

2.4.1 Introduction

Up until now the theory has been largely developed with the assumption of steady uniform flow in a prismatic infinitely wide rectangular channel. Whilst many situations approximate this idealisation, the reality is that other factors usually play a role.

In most open channel flow situations, laminar flow only prevails in the region close to the boundary where eddying motion is damped out. Elsewhere the flow is characterised by turbulence for which the main driving mechanism is large scale

"whirls". Even in the laminar flow region, overlying turbulence makes its presence felt indirectly via the velocity gradient, and more directly through "sweeps", "ejections" and other types of "coherent flow structures". An additional complication arises with unsteady flow where the boundary is also subjected to inertial forces resulting from the acceleration or deceleration of the fluid. Unsteady flows are not explicitly considered in this investigation. Fortunately, in the many instances, flow rates change very slowly in time resulting in low inertial forces. Under these circumstances, the flow can be considered "quasi-steady".

Coherent flow structures (Ashworth et al., 1996) can be most conveniently divided into two groups:

i) Large-scale structures e.g. secondary currents, eddies, boils, whirlpools, turbidity currents.

ii) Small-scale structures e.g. streaks, hairpin vortices, bursts, sweeps, ejections, shear layers.

An overview of some of these structures is given below.

2.4.2 Large-scale coherent structures: Secondary currents

The terms "secondary current", "secondary flow" (Prandtl, 1952; Reynolds, 1974; French, 1994; Chadwick & Morfett, 1998), or "spiral flow" (Ven te Chow, 1959) refer to circulatory motion of the fluid around an axis which is parallel to the primary current or flow (French, 1994). Generally, secondary currents occur in turbulent flow when the isovels (the lines or contours of equal velocity) of the primary flow are not parallel to each other or the boundaries of the channel (Einstein & Li, 1958). They are also associated with cross-channel pressure gradients (Reynolds, 1974).

Reynolds (1974) identifies six types of secondary currents. Of these, *Types 1*, *2* and *4* are of the most interest here:

i) *Type 1 flows* occur in straight channels as a result of the increased stress and reduced velocity in the vicinity of the sidewalls. The situation is particularly complicated if compound channels are involved. See Figure 2-8.

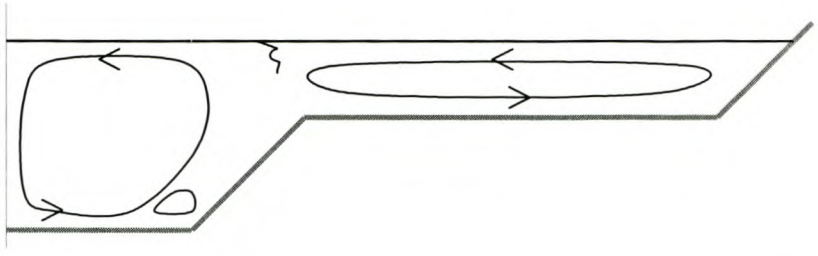

Figure 2-8: Typical secondary flow structures in compound channels
(After Wormleaton, 1996)

ii) *Type 2 flows* occur in curved channels. The faster moving flows near the channel surface results in a higher than average centrifugal force promoting a migration towards the outside bend (Chadwick & Morfett, 1998). Meanwhile, the super-elevation of the water surface gives rise to a radial pressure gradient that can only be balanced by a flow towards the inside of the bend along the bottom (Reynolds, 1974). See Figure 2-9.

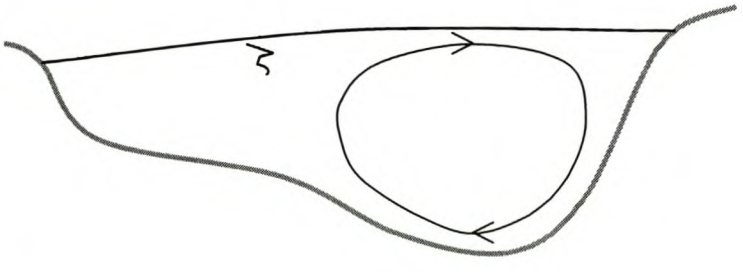

Figure 2-9: Typical secondary flow cell on a bend

iii) *Type 4 flows* result from the distortion of the boundary layer around protrusions into the flow. Complex separating and reattaching flows will be found in the wake, and also just ahead of the obstruction (Reynolds, 1974). This will be dealt with in much greater detail later on.

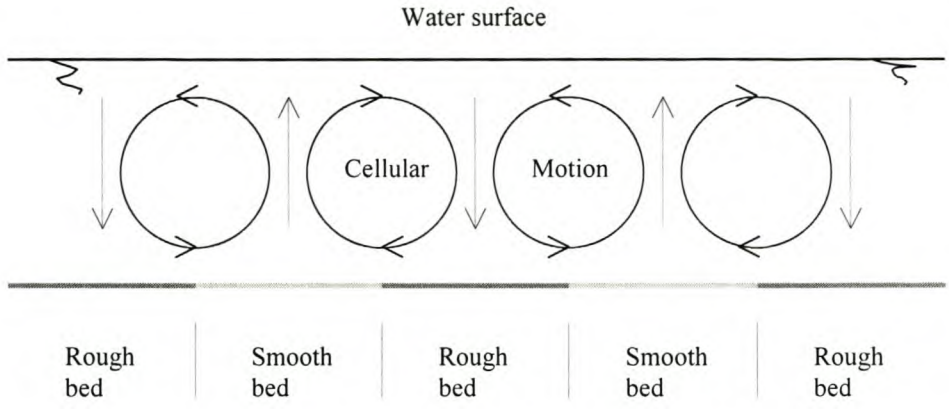

Figure 2-10: Schematic of cellular secondary currents
(After Tsujimoto & Kitamura, 1996)

Secondary currents can also develop from something as minor as a change in the bed roughness. Tsujimoto & Kitamura (1996) have shown that if a bed is comprised of alternately coarser- and finer-grained longitudinal strips, lateral flow cells tend to develop. These cells are particularly strong where the lateral wavelength of alternation of sorting is in the order of twice the flow depth. The flow is from the rough to the smooth region near the bed, returning near the surface. See Figure 2-10.

2.4.3 Small-scale coherent structures in the viscous sub-layer

Starting in 1956 and through the early 1960s, a series of experiments carried out at Stanford University demonstrated that there is far greater structure or order in turbulent boundary-layer flows than had been previously believed (Smith, 1996). According to Smith (1996), hairpin vortices play a major role in the interaction between the viscous and inviscid regions of the boundary layer, helping to focus and transfer vorticity from the wall layer into the main body of the fluid. Smith (1996) also describes the following coherent structures associated with the hairpin vortices:

i) Low-speed "streaks" are generated by the interaction of a passing streamwise or hairpin-like vortex with wall-region, and comprise a narrow wedge of low-speed fluid. This is illustrated in Figure 2-11.

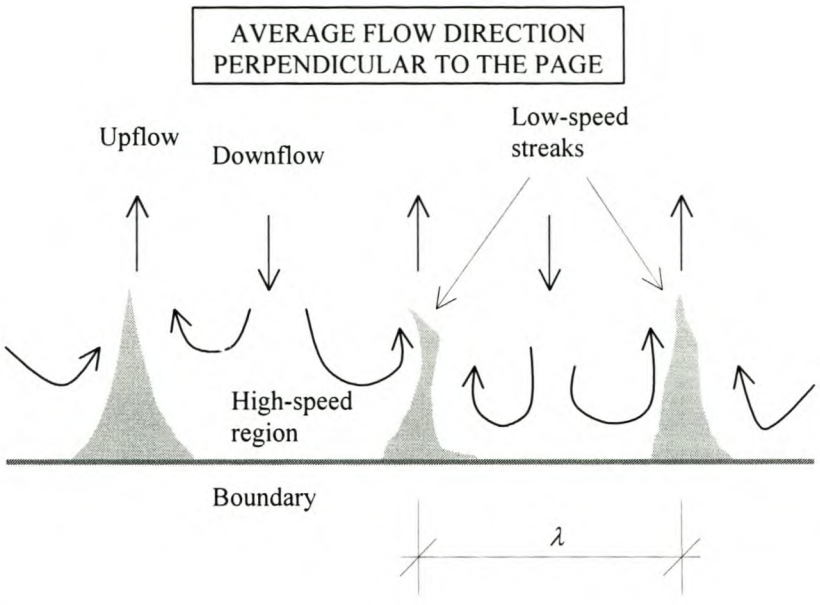

Figure 2-11: Schematic cross-section through the instantaneous velocity field (After Smith, 1996)

Although the streaks are unsteady and not uniformly distributed, it is possible to measure a mean spanwise streak spacing, λ, and to define a "non-dimensionalised streak spacing", λ^+, given by:

$$\lambda^+ = \frac{u_* \lambda}{\nu} \tag{2.33}$$

In the vicinity of a laminar boundary, λ^+ has a mean value of 100 over a wide range of Reynolds numbers, with individual values ranging between 50 and 300. The streamwise extent of the wall-layer streaks, expressed in terms of the local Reynolds number, is typically of the order of 600 – 1000 Re_x with x measured from the beginning of the streak. λ^+ tends to increase outside of the viscous sub-layer (Grass & Mansour-Tehrani, 1996).

In the case of a turbulent boundary, the spacing between the streaks depends on the wall roughness elements. For fully rough walls, Defina (1996) found that, if k_s is the height of the wall elements, then $\lambda / k_s \approx 4.5$.

ii) A "burst" is the local breakdown and ejection into the outer region of wall-layer fluid in the proximity of a low-speed streak. The ejection of fluid associated with the burst can result in the formation of one or more secondary hairpin-like structures in the immediate wake of the initial vortex. These structures typically have an inclination angle to the bed of about 14^{o} (Garcia et al., 1996).

Small scale coherent structures can also be described by means of a quadrant diagram (e.g. Ferguson et al., 1996; Shvidchenko & Pender, 2000). The quadrant diagram is constructed on the basis of the fluctuating velocity components. A sweep is a 4^{th} Quadrant event (positive u' and negative v'), whilst a burst / ejection is a 2^{nd} Quadrant event (negative u' and positive v'). This is illustrated in Figure 2-12:

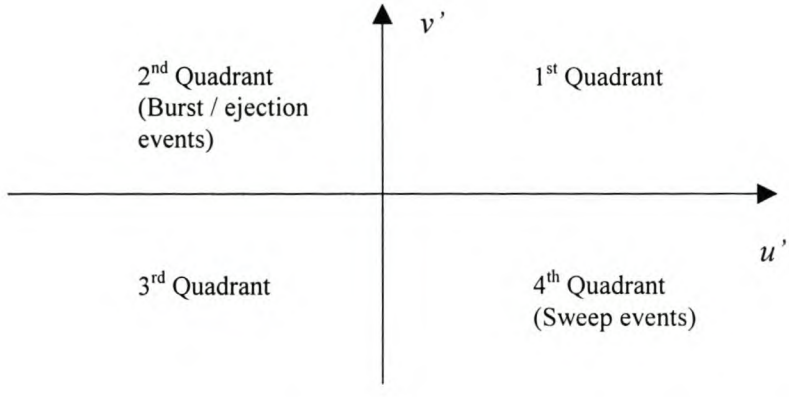

Figure 2-12: Quadrant diagram for small-scale coherent flow structures

2.4.4 Shear layers

In Section 2.2.3 it was noted that the shear stress at any point within a fluid could be expressed as the sum of the stress due to molecular viscosity and the stress due to turbulent fluctuations (Equation 2.5). The stress due to turbulent fluctuations is commonly calculated either by means of the Reynolds stress model (Equation 2.6), or by the Prandtl eddy model (Equations 2.7 & 2.8). The Reynolds stress model effectively says that a large turbulent shear stress is as a result of large local fluctuations in the velocity component. The Prandtl eddy model effectively says that a large turbulent shear stress is a result of large local velocity gradients.

Whichever model is used, the implication is that if there is something promoting large velocity fluctuations and consequently large velocity gradients in the flow, there will be high local turbulent shear stresses. All boundaries have this effect on the fluid, but uneven boundaries have a more significant effect than plane boundaries. Vortex shedding off the back of a dune, for example (Bennett & Best, 1996), is an ejection event that can give rise to very high local velocity fluctuations and thus high local turbulent shear stresses. These high turbulent shear stresses can effectively cut off the flow in the trough of the dune from that above the dune level. Such a zone of relatively high turbulent shear stresses is called a "shear layer". Sometimes, if the water is shallow enough, the shear layer can penetrate through the flow depth to the surface where it appears as a patch of disturbed water called a "boil". Such a shear layer is illustrated in Figure 2-13:

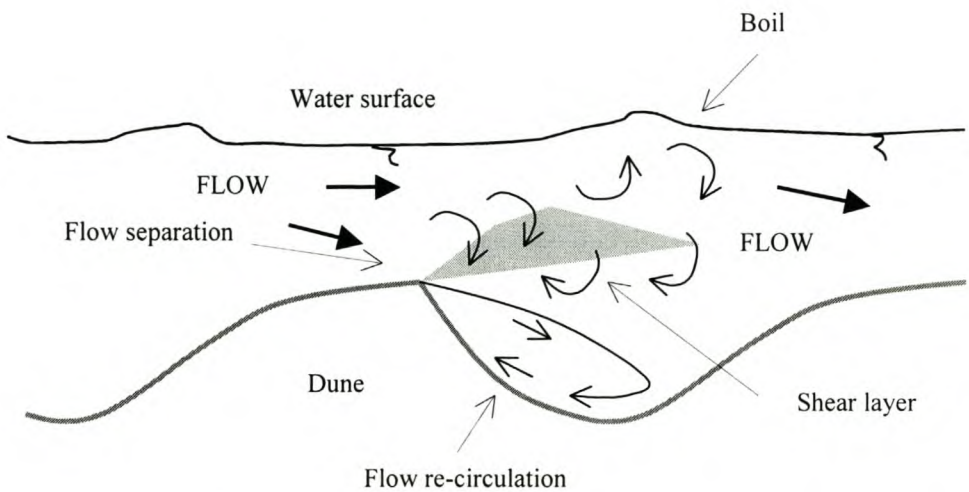

Figure 2-13: Schematic of a shear layer and boil combination over a dune
(After Bennett & Best, 1996)

2.5 Conclusions

It should have become obvious from the foregoing that the conditions under which sediment movement takes place are extremely complex.

It has been shown that the shear stress at any point within the flow field depends on both the viscosity and the velocity gradient – and both of these are variables. Viscosity depends on the temperature and turbulent fluctuations – which in turn depend on the proximity of the boundary and the velocity gradient. The sediment concentration and depth also affect shear stress. The turbulent intensity is anisotropic in the vicinity of the boundary – which is the zone of greatest interest.

In this chapter, considerable attention has been paid to the structure of the boundary layer and the implications this has for the interaction between the boundary surface and the overlying fluid flow. It was also noted that the boundary layer is not static, but varies according to local circumstances.

"Coherent structures" is a name given to identifiable vortical structures that exist within any flow field. They can be at both the macroscopic or microscopic layer. In either case they will influence the shape of the boundary layer and hence the shear stress at the boundary. In some instances, shear layers can develop which separate the flow field from the boundary leaving a semi-protected area next to it.

All of these factors make the prediction of the exact nature of the boundary layer extremely difficult. The nature of the boundary layer impacts on the movement of sediment. Attention must thus be turned to the interaction between the boundary layer and the individual sediment particles resting on the bed.

Chapter 3
An overview of incipient motion

3.1 Introduction

This chapter reviews incipient motion – the conditions under which the movement of sediment will commence. This is central to scour and deposition processes as the equilibrium scour / deposition profile for any particular flow condition – assuming that the supply of sediment is not limited – will be closely related to the conditions for incipient motion at the interface between the fluid and the sediments.

Incipient motion is extremely dependent on the physical characteristics of the sediments. Factors such as size, shape, uniformity, settling velocity, cohesiveness and the angle of repose all play a role. There are also different types of motion, which should be carefully distinguished.

An attempt is made in this chapter to identify all the forces that act on particles resting on the bed and to link these to the factors influencing the movement of any particular particle.

Incipient motion is an extremely ambiguous term as there is a statistical chance of particle movement no matter what the flow conditions. There is, therefore, some discussion on the concept of "threshold of movement" and "pickup probability".

Historically, there have been three primary models of incipient motion, each focusing on a different flow parameter – velocity, bed shear stress and stream power. These are described in some detail, although the main emphasis is placed on the stream power approach. The stream power model has not been explored as thoroughly as the other two – in particular the bed shear stress model. It does, however, show considerable promise as an alternative to them.

The conditions for incipient motion are clearly affected by the slope of the bed – both in the longitudinal and transverse directions. Some attention is therefore given to factors that have been used to adjust the incipient motion parameters as developed for flat beds to those that apply with slopes.

3.2 The physical characteristics of sediment

3.2.1 Size

The size of the particle is probably the most important parameter in defining incipient motion. Clearly smaller particles will generally be moved more easily by the flow than larger ones. It is generally assumed that sediment particles are reasonably spherical – although the reality, of course, could be very different. Some common definitions for the sediment diameter, d (Vanoni, 1975; Van Rijn, 1993; Yang, 1996; Raudkivi, 1998) are as follows:

i) Sieve diameter: the length of the side of a square sieve opening through which the particle will just pass.

ii) Nominal diameter: the diameter of a sphere of equal volume.

iii) Sedimentation diameter: the diameter of a sphere of the same density and the same settling velocity in the same fluid at the same temperature.

iv) Standard fall diameter: as for sedimentation diameter except that the sphere has a density of 2 650 kg/m^3, the liquid is quiescent distilled water of infinite extent, and the temperature is 24°C.

v) Triaxial dimensions: the length of the three orthogonal dimensions a, b and c where a is generally the longest dimension and c the shortest.

Since sediment dimensions cover a large size range, a logarithmic scale is often used for the classification of granular (sand) sediments. The "phi scale" is defined as:

$$\Phi_s = -\log_2(d) = -\frac{\log_{10}(d)}{\log_{10} 2} \quad (d \text{ in mm}) \tag{3.1}$$

The most common size description is that of the American Geophysical Union (Lane et al., 1947), which is summarised in Table 3-1.

Class	Size (mm)	Size (Φ_s)
Boulders	> 256	< -8
Cobbles	64 to 256	-6 to -8
Gravel	2 to 64	-1 to -6
Very coarse sand	1 to 2	0 to –1
Coarse sand	0.5 to 1.0	1 to 0
Medium sand	0.25 to 0.5	2 to 1
Fine sand	0.125 to 0.25	3 to 2
Very fine sand	0.062 to 0.125	4 to 3
Silt	0.004 to 0.062	8 to 5
Clay	0.00024 to 0.004	12 to 8
Colloids	< 0.0024	> 12

Table 3-1: Grain size classification (After Lane et al, 1947)

Clearly this classification system cannot be used for sediment particles that are not reasonably spherical.

3.2.2 Shape

Although sediments are not usually perfectly spherical, in the case of sand particles at any rate, abrasion in the natural transportation process does tend to round them. In fact, in the case of sand particles, the "roundness" of a particle is an indication of how far it has travelled. Since it is generally assumed that sediment particles are reasonably spherical, it is necessary to define a shape factor to take into account the deviation from the spherical. The most common shape factor is the Corey shape factor, defined as:

$$SF = \frac{c}{\sqrt{ab}} \tag{3.2}$$

In general, a shape factor of 1.0 would indicate a perfect sphere. Values falling below 1.0 would indicate increasing deviation from a perfect sphere. This generally works well, except that a cube also has a shape factor of 1.0! One way of overcoming this problem (Van Rijn, 1993) is to define d_s as the diameter of a sphere having the same

surface area as that of the particle, and d_v as the diameter of a sphere having the same volume as that of the particle, then:

$$SF = \frac{d_s c}{d_v \sqrt{ab}} \tag{3.3}$$

Naturally worn quartz particles typically have a shape factor of 0.7.

3.2.3 Uniformity

Sediment uniformity is the measure of the distribution of the particle sizes. Its determination is complicated by the measuring method. Since sediment size is commonly determined by sieve analysis, sediment uniformity is usually determined from frequency histograms depicting the percentage of material by mass passing one sieve diameter but retained on one size smaller. Statistical parameters such as the mean, standard deviation, skewness and kurtosis may be determined from this.

The most common definitions (Vanoni, 1975; Van Rijn, 1993; Yang, 1996; Raudkivi, 1998) are as follows:

i) Median diameter (d_{50}): The particle diameter that is exceeded by exactly 50% of the material by mass. If the size distribution is skewed, d_{50} is usually calculated from the average of the $d_{15.9}$ and $d_{84.1}$ values Yang, 1996):

$$d_{50} = \frac{d_{15.9} + d_{84.1}}{2} \tag{3.4}$$

ii) Mean diameter ($\bar{d}$): The arithmetic mean of the particle sizes. If d_i is the median diameter of any particular size fraction and p_i is the percentage by mass of that fraction then:

$$\bar{d} = \frac{\sum p_i d_i}{100} \tag{3.5}$$

iii) Standard deviation (σ): The standard deviation is generally defined (Friedman, 1962) as:

$$\sigma = \frac{\sum p_i \sqrt{d_i - \bar{d}^2}}{100} \tag{3.6}$$

Alternatively, d_{50} is substituted for $\bar{d}$.

iv) Geometric standard deviation (σ_g): Assuming that the particle size distribution is normally distributed – which is approximately true for well worked river sand – then the geometric standard deviation is defined as:

$$\sigma_g = \sqrt{\frac{d_{84.1}}{d_{15.9}}} = \frac{d_{84.1}}{d_{50}} = \frac{d_{50}}{d_{15.9}} = \frac{1}{2}\left(\frac{d_{50}}{d_{15.9}} + \frac{d_{84.1}}{d_{50}}\right) \tag{3.7}$$

If $\sigma_g < 1.3$, the sediment is considered to be uniform. Alternatively, if $\sigma_g > 1.3$, the sediment is considered to be non-uniform (Melville, 1997). This investigation focuses almost exclusively on uniform sediments.

There are many other definitions in connection with sediment uniformity, some of which are to be found in the references listed at the head of this section.

3.2.4 Settling velocity

The "settling velocity" of a particle – sometimes called the "fall velocity" – is generally defined as the terminal velocity of that fluid particle in an unbounded quiescent body of water. In general, it depends on the size, shape, surface-roughness and density of the particle, and on the density and viscosity of the fluid. Other factors that can also have an influence are the fluid turbulence, particle concentration, and the presence of boundaries. If the particle is less dense than the fluid, it will have a negative settling velocity – sometimes called a "rise velocity".

At the terminal velocity of the particle, the weight, buoyancy force and drag force are in equilibrium. If v_{ss} is the settling velocity, ρ_s the particle density, ρ the fluid density, and C_D the coefficient of drag, then (Raudkivi, 1998):

$$v_{ss} = \sqrt{\frac{4}{3}\frac{\rho_s - \rho}{\rho}\frac{gd}{C_D}} \tag{3.8}$$

C_D is a function of the particle shape and the "particle fall Reynolds Number" which is defined as:

$$Re_d = \frac{v_{ss} d}{\nu} \tag{3.9}$$

In general, C_D is high at low Re_d values, drops rapidly as Re_d increases up to about 10^3, after which it stays reasonably constant until about $Re_d = 10^5$. A typical value of C_D for a natural quartzitic sand in the range $10^3 < Re_d < 10^5$ is about 1.1 (Chien & Wan, 1998). For a perfect sphere it is about 0.45 over the same range (Massey, 1989).

Many researchers have attempted to fit curves to settling velocity data (e.g. Rubey, 1933; Schiller & Naumann, 1933; Kazanskij, 1981; Zhu & Cheng, 1993). One of the more recent attempts is that by Cheng (1997). Define the "relative submerged density, Δ" as:

$$\Delta = \frac{(\rho_s - \rho)}{\rho} \tag{3.10}$$

Define the "dimensionless particle diameter", d_*, as:

$$d_* = \left(\frac{\Delta g}{\nu^2}\right)^{1/3} d \tag{3.11}$$

The settling velocity of natural sand particles is then given approximately by:

$$v_{ss} = \frac{v\left(\sqrt{25+1.2d_*^2}-5\right)^{1.5}}{d} \tag{3.12}$$

Alternatively, the chart drawn up by the U.S. Inter-Agency Committee on Water Resources, Subcommittee on Sedimentation (1957) may be used. This may be found in any standard reference (e.g. Vanoni, 1975; Yang, 1996; Raudkivi, 1998; Chien & Wan, 1998). Chien & Wan (1998) also contains a detailed discussion on the variation in the settling velocity with various parameters.

The settling velocity of objects with unusual shapes must, of course, be determined experimentally.

3.2.5 Cohesiveness

Sediments can generally be classified into two different types:

i) Non-cohesive materials consist of individual particles, like sand, where the weight of the particles is the dominant force in determining transportability.

ii) Cohesive materials usually contain very fine particles – such as clay – that have a very high surface area to mass ratio. This relatively large surface area affords a greater opportunity for electro-chemical forces to bind the particles together into a coherent mass, whilst the impact of particle weight is relatively insignificant. Once, however, the electro-chemical bonds between cohesive particles have been broken down and the particles are carried into suspension, cohesive particles generally behave in much the same manner as non-cohesive materials (Vanoni, 1975).

This investigation will focus exclusively on non-cohesive particles, as they are easier to handle. The model that is developed in this thesis can, however, be extended for use with cohesive material by the addition of a factor accounting for the initial breaking of the electro-chemical bonds between the particles.

3.2.6 Angle of repose

The "angle of repose", ϕ_r, sometimes called the "angle of internal friction", is the maximum side-slope that can be sustained by sediment particles lying on the bottom or sides of a channel before sliding commences. It is largely a function of sediment size, shape and porosity (Van Rijn, 1993). In general, ϕ_r increases with increasing sediment size, increasing angularity (deviation from the spherical), and decreasing porosity (fraction of the sediment volume that is not occupied by the sediment material). There is a significant divergence in the published data on ϕ_r (Chien & Wan, 1998), but if the sediment is quartzitic sand, the values in Table 3-2 may be used for design purposes (Van Rijn, 1993):

Size (d_{50}) (mm)	**Angle of repose (ϕ_r)**	
	Rounded	**Angular**
≤ 1	30°	35°
5	32°	37°
10	35°	40°
50	37°	42°
≥ 100	40°	45°

Table 3-2: Angle of repose for quartzitic sand (Van Rijn, 1993)

Alternatively, ϕ_r may be read off the chart prepared by Lane (1953) (Chien & Wan, 1998). ϕ_r for any material other than quartzitic sand needs to be determined experimentally.

3.3 Types of motion

"Incipient motion", sometimes called "initiation of movement" or "threshold of movement", is the beginning of particle motion. That motion can be of one of several types:

i) Sliding.

ii) Rolling.

iii) Saltating (hopping).

iv) Suspension.

In general, sediment particles will roll or slide before they will saltate, and they will saltate before they are carried into suspension. There is, however, no clear-cut distinction between the four types of motion, and frequently all forms of motion occur simultaneously. Taken together, they constitute "sediment transport". Other commonly used definitions are "contact load", which refers to sediment that is moving continuously in contact with the boundary, i.e. sliding and rolling, and "bed load", which refers to the sediment which is moving in the close vicinity of the bed, i.e. sliding, rolling and saltating. The "suspended load" accounts for the remainder of the material.

The total load may also be divided up into the "bed sediment load" which refers to the particle sizes found in appreciable quantities in the shifting portions of the bed, and the "wash load" which refers to the particle sizes that are not found in appreciable quantities on the bed. The latter term is used because the material has presumably been "washed" down the river from somewhere else. Wash load is generally carried in suspension. Distinction is also generally made between the "sediment load" which refers to the material being transported, and the "sediment discharge" or "sediment transport" which refers to the rate of movement of the material (Vanoni, 1975).

In this investigation, the focus is not on sediment transport per se, but on the threshold at which sediment transport ceases and / or commences. It is this threshold that defines whether there will be scouring and / or deposition around a particular structure.

3.4 The forces acting on particles resting on the bed

Consider a typical particle resting on a bed (Figure 3-1).

It is immediately apparent that there are three main forces acting on an exposed particle: drag, lift and gravity. In addition to this, the particle is supported by neighbouring particles, and may, in turn, be supporting other neighbouring particles.

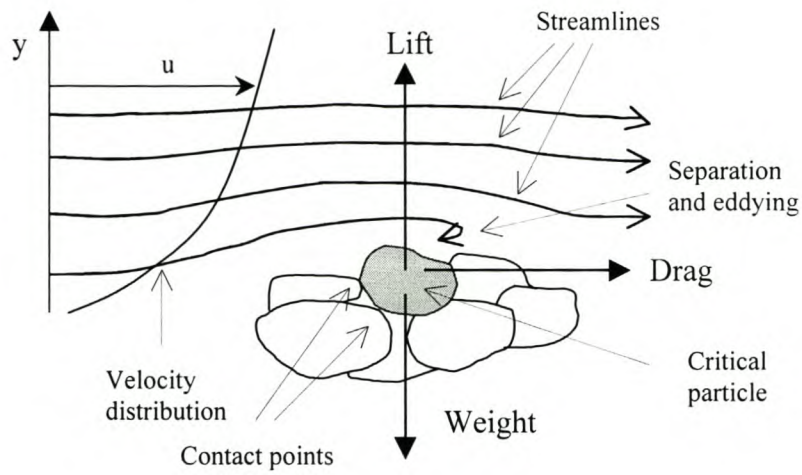

Figure 3-1: Forces on a sediment particle (horizontal bed)

The drag and lift forces represent the horizontal and vertical components respectively of the integrated shear stress and pressure forces acting on the particle.

The shear stress at any point on the particle surface, in turn, depends on the local velocity gradient in accordance with Equation 2.10 or one of its three-dimensional variants:

$$\tau_{yx} = \left(\mu + \mu_{yx(t)}\right)\frac{\partial u}{\partial y} \tag{2.10}$$

The shear stress acts tangentially to the surface in the direction of flow, and for this reason is sometimes called "surface drag". Despite its name, this surface drag can have components in both the horizontal and vertical (and transverse) directions.

The pressure force depends both on the depth and the local velocity in accordance with the Bernoulli Equation. It acts normal to the surface. If ζ is the height above some arbitrary datum, the Bernoulli equation reads:

$$\frac{p}{\rho g} + \frac{u^2}{2g} + \zeta = \text{Constant along the streamline} \tag{3.13}$$

In hydrostatic conditions, p is determined by the depth of water, Y, such that:

$$p = \rho g Y \tag{3.14}$$

Even in the absence of fluid motion, there is a net force on the particle, the "buoyancy force". The submerged weight acts in the vertical direction – vertically down if the particle is denser than water, vertically upwards if it is not. In the latter case, the particle, of course, tries to rise to the surface.

In hydrodynamic conditions, on the other hand, local increases in velocity lead to a corresponding decrease in the local pressure through Equation 3.13. The situation, however, is complicated by flow separation. Flow separation results in the formation of eddies which redistribute the pressure more uniformly over the separated surfaces. Usually this implies inadequate pressure recovery (Equation 3.13 breaks down). When the pressure forces are integrated over the entire surface of the particle, they can give rise to a resultant termed the "form drag". Once again, form drag may have horizontal and vertical (and transverse) components.

Assume that C_D is the coefficient of drag, C_L is the coefficient of lift, a_p is the projected area of the particle (which could be defined differently for drag and lift), and u_0 is the effective velocity near the bed particle. The drag force, F_D, and the lift force, F_L, are given by:

$$F_D = C_D a_p \frac{\rho u_0^{\,2}}{2} \tag{3.15}$$

$$F_L = C_L a_p \frac{\rho u_0^{\,2}}{2} \tag{3.16}$$

Chien & Wan (1998) present various options for the estimation of u_0.

The presence of the channel boundary means that velocity distribution is not linear. The lift forces are relatively large, whilst the drag force may not act through the centre of gravity of the particle

The particle Reynolds number, Re_* is defined as:

$$Re_* = \frac{u_* d}{\nu} \tag{3.17}$$

If $Re_* < 5$, the particle lies wholly within the linear layer (see Section 2.3.4). On the other hand, part of it may project into the transitional layer ($5 < Re_* < 70$), the log-law layer ($70 < Re_* < 500$), or even into the outer boundary layer ($Re_* > 500$). In other words, the particle could form part of a laminar boundary, a transitional boundary, or a turbulent boundary (Section 2.4.4).

If Re_* is less than about 3.5 (i.e. wholly within the linear layer), the flow tends to pass smoothly around the particle and surface friction is the main force, other than gravity or buoyancy, acting on the particle. Once Re_* increases beyond 3.5, however, separation commences behind the top of the particle and a wake is formed (Colebrook & White, 1937). Form drag then begins to take over as the dominant force on the particle (Chien & Wan, 1998).

Numerous researchers have made measurements of drag and lift forces. They include Einstein & El-Samni (1949), Yegiazapov (1960), Chepil (1958, 1961), the River Study Group, WIHEE (1965), Garde & Sethuraman (1969), Watters & Rao (1971), Cheng & Clyde (1972) and Coleman (1972). Their work is summarised in Chien & Wan (1998). According to Chien & Wan (1998), there are numerous discrepancies in the data depending on the shape, configuration, Re_*, position on the bed, method of measurement, choice of u_0 etc. In general, however:

i) There is a clear relationship between C_D and Re_* of a similar nature to that for a particle falling in a quiescent fluid.

ii) There is no clear relationship between C_L and Re_*.

iii) The fluctuation of the forces acting on particles exhibits a normal distribution (Einstein & El-Samni, 1949; Cheng & Clyde, 1972). The velocity fluctuations also tend to follow a normal distribution.

iv) The magnitudes of the lift and drag forces are much the same. The River Study Group, WIHEE (1965) came to the conclusion that, in general, drag is more important than lift for the initiation of particle motion. More recently, however, Allan and Frostick (1999) observed the entrainment of gravel particles using a digital video camera, and established that particles do not pivot around adjacent grains as would have been expected by drag-induced entrainment, but are entrained by vertical movement. They concluded that the most significant force at the time of entrainment was therefore lift, with drag only becoming significant once the particles were lifted clear of the bed. This observation was supported by visual observations made by Shvidchenko & Pender (2000).

3.5 Factors influencing the movement of any particular particle

The implication of the previous section is that, everything else being equal, there is a single combination of drag and lift acting on any particular particle. The likelihood of movement is however complicated by a number of factors:

i) The boundary is invariably uneven. Even in the absence of ripples and / or dunes, each particular particle is surrounded by other particles having their own unique size, shape, location and orientation. They all contribute to the flow regime around the particle under consideration. For example, the particle might rest in the turbulent wake cast off by an upstream particle, or be shielded by it. This becomes even more complicated in the presence of ripples and / or dunes where the location of the particle relative to the bed form becomes important. Motion is then generally initiated at the downstream end of the eddy region where the flow reattaches itself to the bed (Van Rijn, 1993).

ii) The particle will touch other particles at a number of points, called "contact points". Sometimes the particle will be supported by another particle, and the contact point represents a fulcrum around which rotation can potentially take place. At other times, the particle is supporting other particles that might prevent it from moving when movement would ordinarily have taken place. Alternatively, the close proximity of other particles hinders sliding.

iii) If the sediment is not uniform – and all natural sediments tend to be non-uniform to a certain extent – smaller particles on the surface of the bed might be preferentially swept away leaving a bed largely comprised of much coarser material that protects the underlying sediments. This process of bed coarsening is called "armouring".

iv) The particle will be subjected to various forms of coherent flow structures. The larger scale structures, such as secondary currents (see Section 2.4.2), are reasonably steady over short periods of time and may be regarded as part of the general flow over the particle. On the other hand, the smaller scale coherent structures, such as streaks, sweeps, bursts and hairpin vortices (see Section 2.4.3), are stochastic in nature and tend to subject individual particles to rapidly varying forces. Particle motions near the bottom have been found experimentally to take place in close association with turbulent bursting (e.g. Sumer & Oguz, 1978; Sumer & Deigaard, 1981; Grass, 1982; Cao, 1997).

v) If the particles are cohesive, the electro-chemical bonds between the particles have to be broken down – at least partially – before there is any movement.

vi) If more than one particle starts moving at a particular instant, they start to interact with the fluid and hence with each other. Some particles may even collide. This tends to create a force between the particles, perpendicular to the flow direction, called the "dispersive force". The momentum interchange between the slower moving particles close to the bed and the faster moving particles a small distance away gives rise to a "dispersive shear stress".

vii) Seepage into or out of the riverbed can give rise to "seepage pressure".

viii) The particle may be on a slope (longitudinal or transverse). This will tend to reduce the force required to move it (unless, of course, the flow direction is temporarily up the slope).

3.6 The threshold of movement

When the hydrodynamic force acting on a particle has reached a value that, if increased even slightly, it will put the particle into motion, "critical" or "threshold"

conditions are said to have been reached (Vanoni, 1975). The motion might however be of one or two particles only, several particles at a time, or involve general movement of the surface of the bed. Each level of movement will be associated with its own particular "critical" conditions. Kramer (1935) defined three intensities of motion near the critical or threshold condition (Vanoni, 1975):

i) "Weak movement" indicates that a few or several of the smallest particles are in motion in isolated spots in small enough quantities so as to allow the counting of those moving on 1 cm^2.

ii) "Medium movement" indicates the condition in which particles of mean diameter are in motion are too large to be countable. Such movement is no longer local in character. On the other hand, it is not yet strong enough to affect bed configurations and does not result in appreciable sediment discharge.

iii) "General movement" indicates the condition in which particles up to and including the largest are in motion, and movement is occurring in all parts of the bed at all times.

Alternatively, Shvidchenko & Pender (2000a, 2000b) define m as the number of particle displacements during the time interval t, and N as the total number of surface particles over the sample area. Then I, the intensity of motion (or transport intensity) is calculated from:

$$I = \frac{m}{Nt} \tag{3.18}$$

"Weak sediment transport" is now defined as $I = 10^{-4}s^{-1}$ (one of 10 000 surface particles is entrained every second. Visually this can be described as "occasional particle movement at some locations". "General movement", meanwhile, is defined as $I = 10^{-2}s^{-1}$ (one of 100 surface particles is entrained every second). Visually this can be described as "frequent particle movement at many locations".

Another strategy is that which was adopted by Shields (1936), who attempted to find the critical shear stress for the initiation of movement by extrapolating a graph of

observed sediment discharge versus shear stress to identify the value of zero sediment discharge.

3.7 The pickup probability

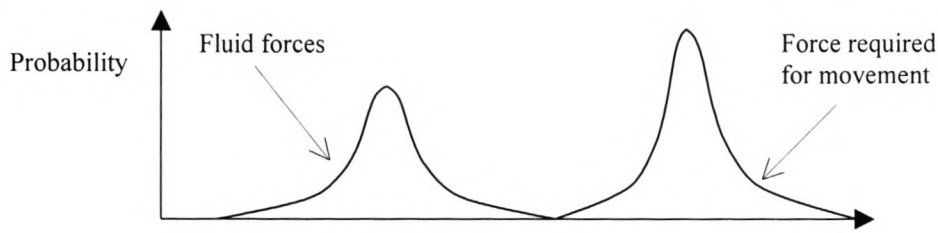

a) No motion

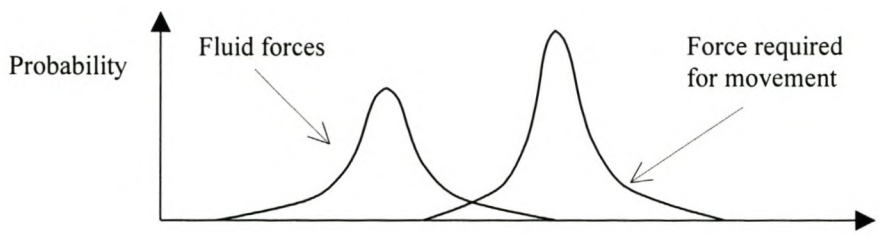

b) Incipient motion

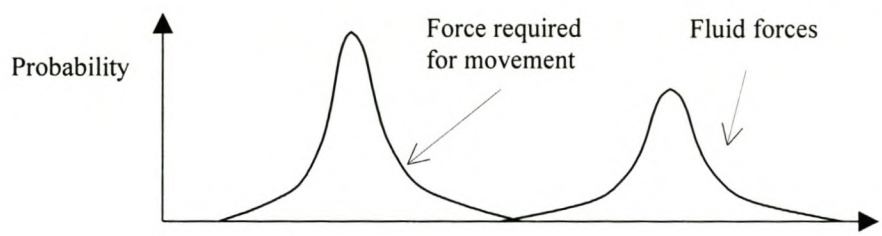

c) General motion

Figure 3-2: The stochastic approach to incipient motion
(Adapted from Grass, 1970 & Van Rijn, 1993)

The difficulty in defining a threshold below which there is definitely no movement has inevitably led researchers (e.g. Einstein, 1950; Grass, 1970; Engelund & Fredsoe,

1976; Fredsoe & Deigaard, 1992; Cheng & Chiew, 1998 & 1999) to define a "pickup probability". The essence of this approach is that the fluid forces applied to a particular particle are likely to be normally distributed around some mean value. At the same time, the force required to move the particle is also likely to be normally distributed around some other mean value for all particles in a similar situation. If the probability density function for the fluid forces overlaps the probability density function of the forces required to move a particle, there will be some movement on a scale indicated by the degree of overlap. Of course, if the former totally exceeds the latter, then there will be general movement of the whole surface of the bed. See Figure 3-2.

Treating the fluid forces and the response of particles to the fluid forces as a stochastic process obviously implies that, given adequate time, movement will occur somewhere on the bed of a channel almost irrespective of the flow rate. This is because there is always some probability that the forces acting on a particle will be large enough to move it (Van Rijn, 1993). For practical purposes, however, there must be some minimum overlap between the two probability density functions before there is a meaningful intensity of motion. The choice of this minimum is, however, likely to remain somewhat subjective.

3.8 Models of incipient motion

3.8.1 Introduction

The preceding discussion should have made it obvious that it is sometimes very difficult to predict when motion will take place. It is however necessary to do this for engineering purposes. In consequence, various simplified models of incipient motion have been developed. The essence of most of them is that there is a single flow-related parameter that plays the dominant role in determining whether there would be motion or not. The three flow-related parameters that are most often chosen are:

i) Velocity.

ii) Bed shear stress.

iii) Stream power.

3.8.2 Incipient motion in terms of flow velocities

Many researchers have tried to link incipient motion to some flow velocity because velocities are simple to visualise, convenient to use, and relatively easy to measure – particularly if it is the average velocity that is under consideration. Some of the better known investigations include Fortier & Scobey (1926), Hjulström (1935), Shamov (1952), Levy (1956), Knoros (1958), Li (1959), Goncharov (1962), Zeng & Wang (1963) and Vanoni (1975). All of the formulations, with the exception of Vanoni (1975), are summarised in Chien & Wan (1998). The data presented by Fortier & Scobey (1926), Hjulström (1935) and Vanoni (1975) are also to be found in many other standard text books e.g. Yang (1996), Raudkivi (1998).

The problem with the use of the average flow velocity as an indicator of incipient motion is that drag and lift forces are dependent on the velocity distribution rather than the average velocity. A deep channel will have smaller velocity gradients than a shallow channel for the same average velocity. In consequence, a higher average velocity will be required to promote sediment motion in a deep channel than an otherwise identical shallow channel. This was recognised many years ago by irrigation engineers who considered this when planning canal systems (Vanoni, 1975).

It clearly makes more sense to consider the local velocity in the vicinity of the sediment particle. Unfortunately, this is exceptionally difficult as the particles generally lie in regions of extremely high velocity gradients. Furthermore, it is difficult to determine the effective boundary location owing to the irregular roughness elements and the change in the nature of the boundary layer in the vicinity of the boundary. Chien & Wan (1998) gives numerous methods of determining the effective local velocity, but the results are mainly of theoretical interest.

Other researchers have based their formulations on the assumption that the local flow velocity is the driving force behind sediment movement, but have then used dimensional analysis to develop the final form of the equation. One example is that of Liu (1957). Liu came to the conclusion that the local velocity and hence the various drag coefficients were all functions of the particle Reynolds Number, Re_*. This enabled him to work out that there must be a unique relationship between the ratio of the shear velocity, u_*, to the particle settling velocity, v_{ss}, (what he termed the "movability number") and Re_*. The resulting curve does not, however, explicitly include the flow velocity – local or average. One of the most interesting features

about a plot of u_* / v_{ss} against Re_* is that it follows logically from considerations of stream power. See Section 3.8.4 for more discussion about this.

Yang (1973) also began his analysis from a consideration of the lift and drag forces due to the local velocity, and he also showed that Re_* is the most significant independent variable. The resulting formulation, however, was formulated in terms of a "dimensionless critical velocity", U_c / v_{ss} where U_c is the critical average flow velocity for incipient motion. The Yang (1973) formulation has been independently confirmed by Talapatra & Ghosh (1983), and by Govers (1987) using laboratory data, although Chien & Wan (1998) expressed some doubt about its applicability to natural rivers which have a much greater depth than laboratory flumes. According to Yang (1973) it is:

$$\frac{U_c}{v_{ss}} = \frac{2.5}{\log(Re_*) - 0.06} + 0.66 \quad \text{for} \quad 0 < Re_* < 70 \tag{3.19}$$

$$\frac{U_c}{v_{ss}} = 2.05 \quad \text{for} \quad Re_* > 70 \tag{3.20}$$

These two equations are plotted in Figure 3-3.

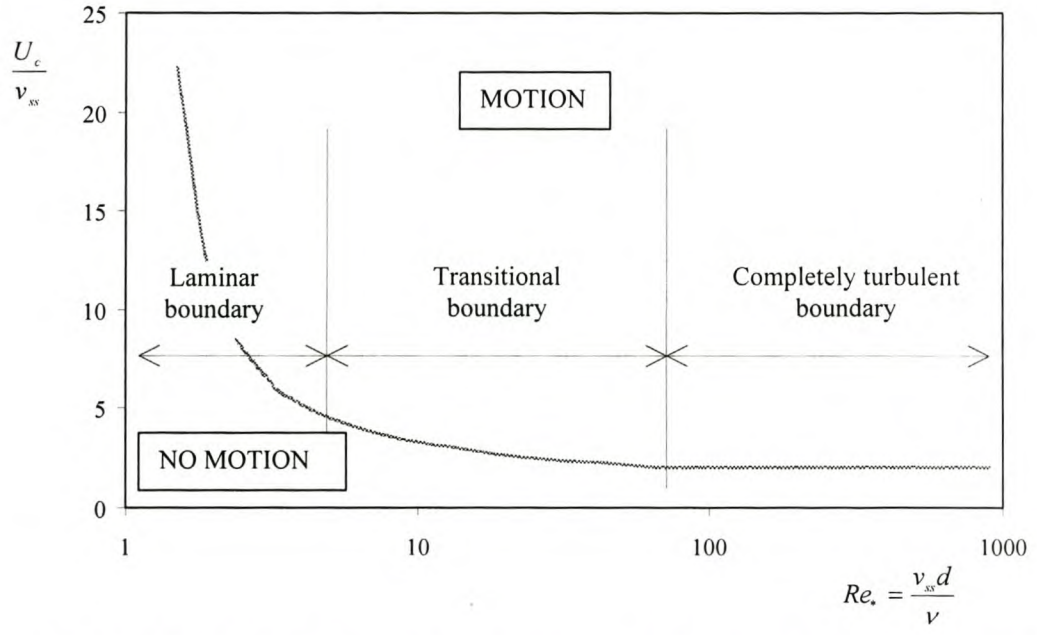

Figure 3-3: Relationship between dimensionless critical average velocity and the particle Reynolds number (After Yang, 1973)

From the foregoing, it is obvious that whilst there is a lot of theoretical support for the use of the local flow velocity to predict incipient motion, it is difficult to estimate. The average flow velocity, whilst easy to measure, is not a suitable parameter.

3.8.3 Incipient motion in terms of bed shear stress

One of the two or three most frequently cited references in sediment transport and river hydraulics is Shields (1936) (according to Kennedy, 1995). Using dimensional analysis, Shields determined that the drag force was a function of the particle diameter, the grain-shape factor, the bed form, the particle Reynolds number, Re_* and the bed shear stress, τ_0. Resistance to motion was assumed to depend only upon the form of the bed and the immersed weight of the particles (Raudkivi, 1998). From this, Shields deduced that the "dimensionless mobility factor", θ, often called the Shields' parameter, is a function of Re_* where θ is defined as:

$$\theta = \frac{\tau_0}{(\rho_s - \rho)gd_{50}} = \frac{\rho u_*^{\,2}}{(\rho_s - \rho)gd_{50}} \tag{3.21}$$

If τ_c is the critical bed shear stress for incipient motion, then the critical Shields parameter, θ_c, is given by:

$$\theta_c = \frac{\tau_c}{(\rho_s - \rho)gd_{50}} \tag{3.22}$$

To get around the difficulty of determining the point of incipience, Shields attempted to calculate the value of bed shear stress at which the extrapolated transport rate was zero. Other researchers have used different criteria. The envelope to most of the large amount of accumulated data is shown in Figure 3-4:

The large spread of data is an indication of the difficulty in defining incipient motion. Taylor (1971), Delft Hydraulics (1972), Graf & Pazis (1977), Unsöld (1982) and others have attempted to draw up families of curves that give some indication of the intensity of the incipient motion. See Vanoni, 1975; Van Rijn, 1993 and Raudkivi, 1998 for more details in this regard.

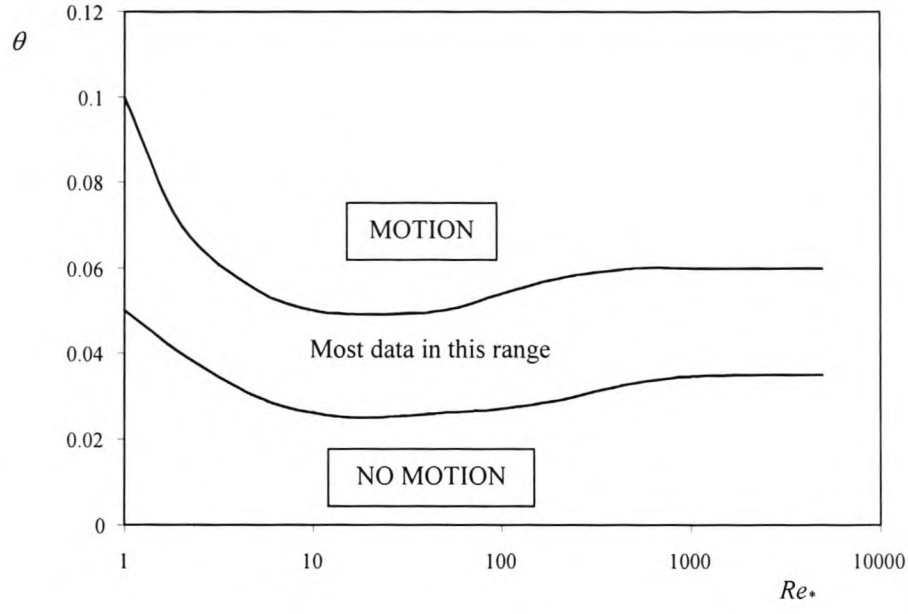

Figure 3-4: The Shields diagram for incipient motion (after Raudkivi, 1998)

Although the Shields diagram is probably the most commonly used method of determining incipient motion, it has many critics. Yang (1973), for example, lists seven factors against its use. Probably the most serious criticism is that the rate of sediment transport does not appear to be uniquely determined by the shear stress.

The Shields diagram has other drawbacks. The shear velocity appears on both axes, which requires trial and error solutions or the addition of curves to indicate the particle sizes. Bonnefille (1963) got around this by expressing θ in terms of the dimensionless particle size, d_* (Equation 3.11). See Van Rijn (1993) or Raudkivi (1998) for more details.

3.8.4 Incipient motion in terms of stream power

The movement of sediment – or water for that matter – requires the expenditure of energy. In open channel flow, the energy source is potential energy that is released as the water flows downhill. This energy gets dissipated into heat in the process of overcoming the internal friction of the flow or the friction associated with fluid / particle interaction (experienced by the particle in the form of lift and drag forces). Since the rate of energy dissipation – termed the "stream power" – is related to the

flow rate, it seems logical that the rate of sediment movement must also be linked to the stream power dissipation.

It is easily shown (e.g. Yang, 1996; Chien & Wan, 1998) that, for uniform flow with an average velocity U down a slope S_0, the average stream power per unit volume, P_{av}, is given by:

$$P_{av} = \rho g S_0 U \tag{3.23}$$

Bagnold (1960) was one of the first researchers to use unit stream power as an indicator of sediment motion. He found that a minimum "critical unit stream power" was required before sediment transport commenced.

A similar conclusion was arrived at by Yang (1972, 1973, 1976, and 1996) who also defined a "dimensionless unit stream power" given by:

$$\text{Dimensionless unit stream power} = \frac{US_0}{v_{ss}} \tag{3.24}$$

Ackers & White (1973) looked at stream power in a very different way. Following Bagnold (1966), they attempted to express sediment motion in terms of the stream power dissipation per unit area of channel bed. This, in turn, is proportional to the applied shear stress on the bed times the average velocity, i.e. $\tau_0 U$. From consideration of the work carried out on a sediment particle they were able to derive a "mobility number" that indicates whether the particle is likely to move. Significant transport only exists for mobility numbers above a certain critical value.

The problem with all of the above approaches is that they all involve the use of the average velocity, U, and hence look at unit stream power in terms of its average value down through the water column. Therefore, they are all strictly one-dimensional formulations. The fact of the matter is, however, that unit stream power dissipation varies greatly through the water column from zero at the surface to a maximum at the bed. A proper understanding of incipient motion can only come through examining what is happening on the bed. This was recognised by Rooseboom (1975 and 1992)

and his co-workers (Annandale, 1986; Le Grange & Rooseboom, 1993; Basson & Rooseboom, 1997).

It is easily shown (e.g. Rooseboom, 1992; Chien & Wan, 1998; Chapter 4) that the stream power dissipation per unit volume at any point in the water column for unidirectional flow, P_t, ignoring secondary turbulence components, is given by:

$$P_t = \tau_{yx} \frac{du}{dy} \tag{3.25}$$

Following the development in Rooseboom (1992), the shear stress, in the case of uniform flow down a wide channel, is approximately given by Equation 2.11:

$$\tau_{yx} \approx \rho g(D - y)S_0 \tag{2.11}$$

The velocity gradient, on the other hand, depends on whether the flow is laminar or turbulent. Very close to the boundary, the flow is always laminar. Here the velocity is given by Equation 2.18, which can be rewritten:

$$u = \frac{u_*^{\,2} y}{\nu} \tag{3.26}$$

For the linear layer in a deep, wide channel with steady uniform flow, $\tau_{yx} \approx \tau_0 \approx \rho g D S_0$ (Equation 2.12), whilst $u_* \approx \sqrt{g D S_0}$ (Equation 2.13).

Differentiating Equation 3.26 with respect to y and multiplying by $\tau_{yx} \approx \tau_0 = \rho u_*^{\,2}$ (Equation 2.13) gives the applied unit stream power in the linear layer, $P_{t(l)}$ (via Equation 3.25):

$$P_{t(l)} = \frac{\rho u_*^{\,4}}{\nu} \approx \frac{(\rho g D S_0)^2}{\mu} \tag{3.27}$$

In the turbulent zone of the inner boundary layer, the simplest expression for the velocity gradient is that supplied by the Prandtl mixing length theory (Prandtl, 1925).

From Equation 2.13, $\tau_0 = \rho u_*^2$. Noting that $\tau_{yx(t)} \approx \tau_0$ in the vicinity of the boundary, Equation 2.8 may thus be expressed in this zone as:

$$\frac{du}{dy} = \frac{u_*}{\kappa y} \tag{3.28}$$

Multiplying Equation 3.28 by $\tau_{yx} \approx \tau_0 = \rho u_*^2$ gives the applied unit stream power for the log-law layer, $P_{t(t)}$ (via Equation 3.25):

$$P_{t(t)} = \frac{\rho u_*^3}{\kappa y} \approx \frac{\rho (gDS_0)^{3/2}}{\kappa y} \tag{3.29}$$

Away from the boundary the situation gets a little more complicated as the assumption $\tau_{yx} \approx \tau_0$ no longer holds, whilst the velocity distribution is distorted by eddies and other coherent flow structures. What is clear, however, is that the stream power dissipation is a maximum at the bed and rapidly reduces with distance from it. At the surface it is zero ($\tau_0 = 0$ at the surface – see equation 2.11).

The unit stream power input, P_i, meanwhile, is given by Equation 3.23 with the point velocity u substituted for the average velocity U to give:

$$P_i = \rho g S_0 u \tag{3.30}$$

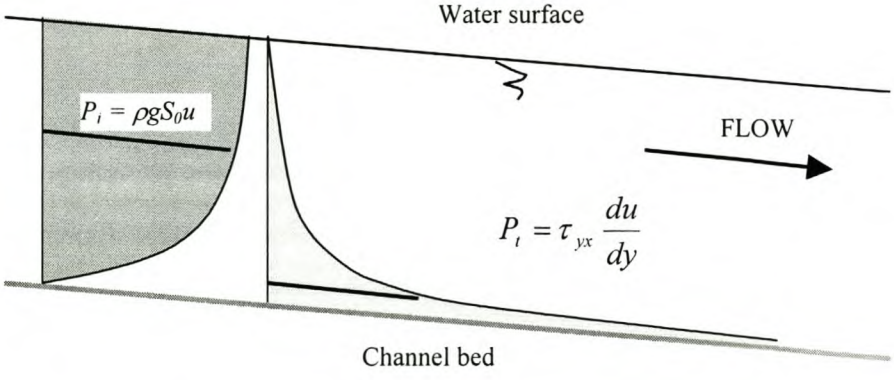

Figure 3-5: The relative distribution of stream power input and dissipation (Rooseboom, 1992)

The distribution of the point velocity – outside of the linear layer – is approximately logarithmic (see Equation 2.24) hence the distribution of the stream power input is also logarithmic. Figure 3-5 shows the relative distribution of the stream power input and stream power dissipation. The curve on the left represents the power input resulting from the release of potential energy as the water flows downstream. The curve on the right represents the power dissipated into heat in the process of overcoming shear stresses. The power input is greatest near the surface where the velocities are the greatest. On the other hand, the power dissipation is greatest near the bottom where the shear stresses and velocity gradients are the greatest. In effect, what is happening is that the faster moving particles near the surface are continuously "doing work" on the slower moving particles below, giving rise to a redistribution of power – an "energy cascade" – down the water column. To satisfy the law of conservation of power, the areas under the two curves must obviously be equal i.e.

$$\int_{y=0}^{y=D} \rho g S_0 u.dy = \int_{y=0}^{y=D} \tau_{yx} \frac{du}{dy}.dy \tag{3.31}$$

When a particle is lying on the bed, the dominant mechanism for movement will depend a lot on whether or not the particle projects through the linear layer into the turbulent layers above. In the turbulent layers, the instantaneous vertical velocities can be of the same order of magnitude as horizontal velocities (River Study Group, WIHEE, 1965; Watters & Rao, 1971). In the linear layer, turbulence is severely dampened, but instantaneous vertical velocities can nevertheless result from the adverse pressure gradients caused by overlying bursts. An "aerodynamic" lift force will also be present because of the velocity gradient over the top of the particle – irrespective of whether the particle forms part of a turbulent or a laminar boundary. Therefore, particles can always be momentarily lifted out of their place. Once a particle has been lifted clear of the limitations of movement imposed by neighbouring particles, the drag forces acting on it immediately sweeps it downstream.

The power required to keep a particle in suspension is similar to that which would be released if the particle were in free fall at terminal velocity (although there may be some small difference in the drag coefficient, C_D). The power per unit volume required to keep a particle in suspension, P_r, is thus given by:

$$P_r \approx (\rho_s - \rho) g v_{ss} \tag{3.32}$$

This, of course, implies that the instantaneous vertical velocities in the vicinity of a particle, v', must exceed the settling velocity, v_{ss}, of the particle from time to time.

Assume now that the flow will carry sediment if it can. The reason for this is because, by virtue of its greater density, a flow of sediment releases a greater quantity of energy into the system than a similar flow of water. The sediment therefore acts as a sort of lubricant. This lubricating quality is enhanced as the sediment concentration increases since the Von Kármán "constant", κ, decreases. A reduction in κ results in an increase in the velocity (see Equation 2.24). For a particle to be lifted out of its place in the bed matrix, the power dissipated on the particle must be equal to or greater than the power required to suspend it. In other words:

$$P_t \geq P_r \tag{3.33}$$

A particle need not necessarily be suspended by the flow to move. It could also roll, slide or saltate, i.e. move as bed load (see Section 3.3). Rooseboom (1992), however, suggested that the division between suspended load and bed load is artificial and unnecessary. Bed load could be considered as a highly concentrated suspended load moving very close to the bed. With this assumption, Equation 3.33 is altered to the following:

$$P_t \propto P_r \tag{3.34}$$

In Equations 3.33 and 3.34, P_t is determined from Equation 3.27 or Equation 3.29 depending on whether the particle is in the linear layer or the log-law layer respectively. P_r, which represents the power required to move (roll, slide, saltate or suspend), is given by Equation 3.32. It can thus be seen that in terms of this model, the mobility of a sediment particle is determined by the particle density, ρ_s, and settling velocity, v_{ss}. The settling velocity, in turn, may be calculated from (inter alia) Equation 3.8:

$$v_{ss} = \sqrt{\frac{4}{3}\frac{\rho_s - \rho}{\rho}\frac{gd}{C_D}} \tag{3.8}$$

3.8.4.1 Laminar boundaries

A particle wholly contained in the linear layer must be quite small. If $Re_d < 1$, then Stokes Law applies, in which case $C_D = 24/Re_d$ for perfect spheres or $C_D = 32/Re_d$ for natural sediment particles (Cheng, 1997). Re_d is defined by Equation 3.9. In the case of natural sediments, therefore, C_D is given by:

$$C_D = \frac{32\nu}{v_{ss}d} \tag{3.35}$$

Substituting Equation 3.35 into Equation 3.8 and squaring both sides yields:

$$v_{ss} = \frac{4}{3}\frac{(\rho_s - \rho)}{\rho}\frac{gd^2}{32\nu} \tag{3.36}$$

Meanwhile, the substitution of Equations 3.27 and 3.32 into Equation 3.34 yields:

$$\frac{\rho u_*^4}{\nu} \propto (\rho_s - \rho) g v_{ss} \tag{3.37}$$

Dividing both sides by v_{ss}^2 and rearranging:

$$\frac{u_*^2}{v_{ss}^2} \propto \frac{(\rho_s - \rho)}{\rho} g \frac{\nu}{v_{ss} u_*^2} \tag{3.38}$$

Substituting Equation 3.36 into right hand side of Equation 3.38 yields:

$$\frac{u_*^2}{v_{ss}^2} \propto \frac{24\nu^2}{u_*^2 d^2} \tag{3.39}$$

Taking the square root of both sides and noting the definition of the particle Reynolds Number, Re_* (Equation 3.17):

$$\frac{u_*}{v_{ss}} \propto \frac{4.9}{Re_*} \tag{3.40}$$

Rooseboom (1992) analysed incipient motion data presented by Grass (1970) and Yang (1973) and found that, in the case of laminar boundaries, the data appeared to fall along a curve described by:

$$\frac{u_*}{v_{ss}} = \frac{1.6}{Re_*} \tag{3.41}$$

Comparison of Equations 3.40 and 3.41 indicates that less applied stream power is required for incipient motion than that required for suspension. This is to be expected. The particles do not need to be suspended before motion commences e.g. they require less applied power for rolling. There is also a probabilistic element to incipient motion (see Section 3.7). Motion usually commences with bursting flow in the vicinity of particles than are abnormally sized, shaped and situated, not with average flow conditions over average particles. Bursts dissipate far more stream power than the average flow conditions. Section 3.6 highlights the fact that sediment motion can theoretically take place under any flow conditions. Considering a bed comprising many particles, it is the intensity of motion that is important, not the motion of a single particle. At this stage, it is convenient to describe the criterion for a given intensity of motion (laminar boundary) by an equation of the form:

$$\frac{u_*}{v_{ss}} = \frac{\alpha_1}{Re_*} \tag{3.42}$$

In Equation 3.42, α_1 is an empirical constant that needs to be measured. It is a function of the intensity of motion (I).

3.8.4.2 Turbulent boundaries

In the case of turbulent boundaries, the particles are much larger than the linear layer. If $Re_d > 1000$, then a typical value of C_D would be about 1.1 (Chien & Wan, 1998). Substituting this value into Equation 3.8 and squaring both sides yields:

$$v_{ss}^{\ 2} = \frac{4}{3}\frac{(\rho_s - \rho)}{\rho}\frac{gd}{1.1} \tag{3.43}$$

Meanwhile, the substitution of Equations 3.29 and 3.32 into Equation 3.34 yields:

$$\frac{\rho u_*^{\ 3}}{\kappa y} \propto (\rho_s - \rho) g v_{ss} \tag{3.44}$$

Dividing both sides by $v_{ss}^{\ 3}$ and rearranging:

$$\frac{u_*^{\ 3}}{v_{ss}^{\ 3}} \propto \frac{(\rho_s - \rho)}{\rho}\frac{\kappa g y}{v_{ss}^{\ 2}} \tag{3.45}$$

Equation 3.45 shows that the ratio u_* / v_{ss} – the Liu (1957) Movability Number – varies with depth. Assume that the critical value is at a height d above the bed (i.e. $y = d$), then substitute Equation 3.43 into Equation 3.45 and simplify:

$$\frac{u_*^{\ 3}}{v_{ss}^{\ 3}} \propto \frac{3.3\kappa}{4} \tag{3.46}$$

If $\kappa = 0.4$, then taking the cubic root of both sides yields:

$$\frac{u_*}{v_{ss}} \propto 0.69 = \text{constant} \tag{3.47}$$

In his analysis of the incipient motion data presented by Grass (1970) and Yang (1973), Rooseboom (1992) found that, in the case of turbulent boundaries, the data appeared to fall along the straight line described by:

$$\frac{u_*}{v_{ss}} = 0.12 \tag{3.48}$$

As for laminar boundaries, comparison of equations 3.47 and 3.48 indicate that less applied stream power is required for incipient motion than that required for suspension. In addition to the reasons given in Section 3.8.4.1, it should also be remembered that the applied stream power calculation has been made at a height of y above the bed. The applied stream power increases very rapidly as the bed is approached (see Figure 3-5), so this calculation could greatly underestimate the effective stream power acting to move the particle. At this stage, it is convenient to describe the criterion for a given intensity of motion (turbulent boundary) by an equation of the form:

$$\frac{u_*}{v_{ss}} = \alpha_2 \tag{3.49}$$

In Equation 3.49, α_2 is an empirical constant that needs to be measured.

3.8.4.3 Transitional boundaries

Rooseboom (1992) made no attempt to provide an analytical solution for the transitional region $1 < Re_d < 1000$, choosing instead to extrapolate Equations 3.41 and 3.48 to a common meeting point at $Re_* \approx 13$ (Figure 3-6). This falls within the region indicated for a transitional boundary layer as would be expected.

It is interesting to note that all three incipient motion models can be expressed in the form of a Movability Number. Equations 3.42 and 3.49 come from stream power. Since U_c can be expressed in terms of u_*, Equations 3.19 and 3.20 (velocity model) can be transformed into the form of a Movability Number. Section 6.3 shows how the bed shear stress model may also be expressed as a Movability Number.

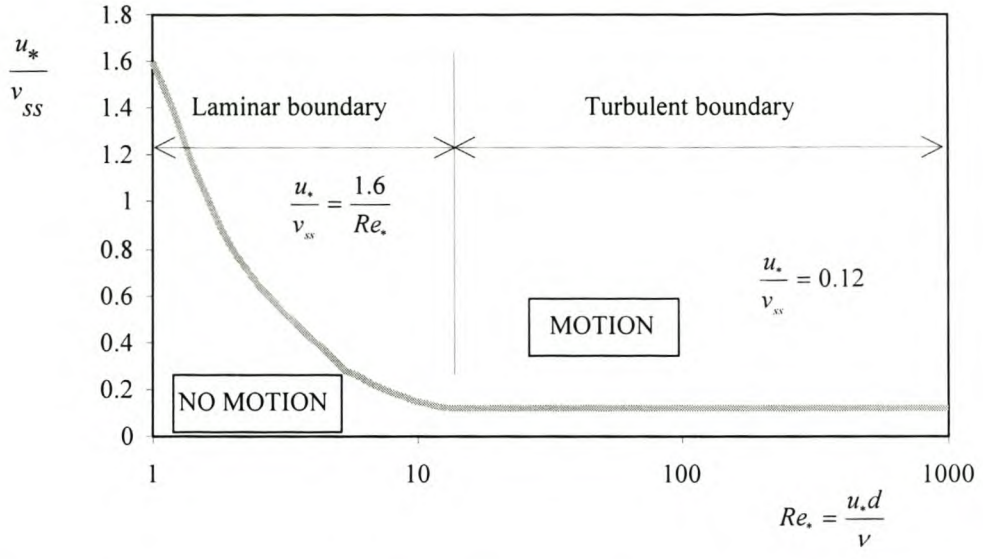

Figure 3-6: The Rooseboom diagram for incipient motion (Rooseboom, 1992)

3.9 Incipient motion on sloping beds

So far the discussion on incipient motion has been limited to that on flat (horizontal) beds. In reality, however, the streambed is rarely flat and the particles normally lie on a slope. Several references handle the changes in the incipient motion criterion with slope including Vanoni (1975), Van Rijn (1993), Chiew & Parker (1994), Yang (1996), and Chien & Wan (1998). Two different types of slope are generally defined:

i) A longitudinal or streamwise slope indicates a fall (or rise) of the bed in the direction of flow. Here it will be given the symbol, β (degrees). A fall in the direction of flow is regarded as a positive slope, a rise as a negative slope.

ii) A transverse slope indicates a fall of the bed in either direction normal to the flow direction. Here it will be given the symbol, γ (degrees).

In keeping with the established position of the Shields criterion for incipient motion, all of the above-mentioned references present formulae for the modification of the critical bed shear stress as a consequence of bed slope. As shown in Section 6.3, it is however possible to adapt these formulae for use with a Movability Number. Van Rijn (1993) derives the incipient motion criteria for a slope in terms of the drag force,

F_D, on the particle. Comparison of Equation 3.15 with Equation 3.16 indicates that the drag force and the lift force, F_L are closely related both with each other and with the effective velocity near the particle, u_0. If $F_{D,cr}$ is the critical drag force for any given slope, $F_{D,cr,0}$ is the critical drag force for a horizontal bed, ϕ_r is the angle of repose of the sediment and β is the longitudinal slope (Van Rijn, 1993; Chiew & Parker, 1994), then:

$$\frac{F_{D,cr}}{F_{D,cr,0}} = k_\beta = \frac{\sin(\phi_r - \beta)}{\sin\phi_r} = \cos\beta\left(1 - \frac{\tan\beta}{\tan\phi_r}\right) \tag{3.50}$$

Since the bed shear stress is proportional to the drag force, this is equivalent to saying that the critical bed shear stress at any longitudinal slope, $\tau_{0,cr}$, is related to the critical bed shear stress on a horizontal bed, $\tau_{0,cr,0}$, by:

$$\tau_{0,cr} = k_\beta \tau_{0,cr,0} \tag{3.51}$$

The validity of Equation 3.51 has been demonstrated experimentally by Whitehouse & Hardisty (1988) and Chiew & Parker (1994) except in the case of adverse slopes where the equation tends to underestimate the critical shear stress (Chiew & Parker, 1994).

The transverse slope, γ, is handled in the same way except this time (Van Rijn, 1993):

$$\frac{F_{D,cr}}{F_{D,cr,0}} = k_\gamma = \cos\gamma\sqrt{1 - \frac{\tan^2\gamma}{\tan^2\phi_r}} \tag{3.52}$$

and,

$$\tau_{0,cr} = k_\gamma \tau_{0,cr,0} \tag{3.53}$$

According to Van Rijn (1993), Leiner (1912) was the first to propose Equation 3.52. For a combination of a longitudinal and transverse slope:

$$\tau_{0,cr} = k_\beta k_\gamma \tau_{0,cr,0} \tag{3.54}$$

3.10 Conclusions

The following conclusions can be drawn in connection with incipient motion:

i) There is an enormous variation in the size, shape, and location of natural non-cohesive particles. There is also an enormous variation in the fluid forces being brought to bear on individual particles at any point in time. It is thus to be expected that the incipient motion is a highly stochastic process.

Reference	Criterion for incipient motion	Remarks
Bagnold (1966)	$\frac{u_*}{v_{ss}} > 1$	Suspension.
Van Rijn (1984)	$\frac{u_*}{v_{ss}} > \frac{4}{d_*}$ $\frac{u_*}{v_{ss}} > 0.4$	Suspension with $1 < d_* \leq 10$, $d = d_{50}$. Suspension with $d_* > 10$, $d = d_{50}$.
Raudkivi (1998)	$0.17 < \frac{u_*}{v_{ss}} < 0.5$ $0.5 < \frac{u_*}{v_{ss}} < 1.7$ $\frac{u_*}{v_{ss}} > 1.7$	Bed-load. Saltation. Suspension.
Julien (1995)	$\frac{u_*}{v_{ss}} > 0.2$ $\frac{u_*}{v_{ss}} > 2.5$	Turbulent water flow over turbulent boundaries. Inception of suspension. Dominant suspended load.
Rooseboom (1992)	$\frac{u_*}{v_{ss}} = \frac{1.6}{Re_*}$ $\frac{u_*}{v_{ss}} = 0.12$	Incipient motion, laminar boundary ($Re_* < 13$). Incipient motion, turbulent boundary ($Re_* > 13$).

Table 3-3: Criteria for motion in terms of Movability Number
(After Chanson, 1999 and Rooseboom, 1992)

ii) Since incipient motion is so highly stochastic, the various published critical parameters for incipient motion cannot be compared without the probability of movement also being indicated. A convenient way of doing this is through the use of the concept of the "intensity of motion, I" (Shvidchenko & Pender, 2000a & 2000b). This is a measure of the rate of particle movement on the surface of the channel bed.

iii) All three popular models of incipient motion; the velocity approach, the bed shear stress approach, and the stream power approach can be expressed in terms of the Movability Number (u_* / v_{ss}). This makes this parameter an extremely attractive one to use in the prediction of incipient motion.

iv) The unit stream power model of incipient motion as presented by Rooseboom, 1992 and his co-workers deserves further consideration.

Various published criteria for motion on a flat bed expressed in terms of the Movability Number, u_* / v_{ss}, are presented in Table 3-3.

Chapter 4
The full unit stream power equation

4.1 Introduction

This chapter looks at the mathematical derivation and definition of the full unit stream power equation. This is placed firmly within the context of continuum mechanics and the relationships between the unit stream power equation and the fundamental equations of fluid flow (for the conservation of mass, momentum and energy) clearly demonstrated. All of these equations are required for the numerical model (see Chapter 8). In the interests of simplicity, all equations are expressed in the differential form.

4.2 Fundamental assumptions

4.2.1 Water as a continuum

Water can be regarded as a continuum. This means that the molecular structure and the molecular motions of the fluid are ignored and its behaviour is described in terms of the macroscopic properties: velocity, pressure, density and temperature, together with their space and time derivatives. This can easily be justified by the observation that a volume as small as 1 $(\mu m)^3$ of water contains some 3×10^{10} molecules.

4.2.2 The co-ordinate system

Consider a small element of fluid with sides δx, δy and δz (Figure 4-1). To fit in with the usual convention for uni-directional flow, the x-axis is assumed to be a horizontal axis in the dominant direction of flow, whilst the y-axis is assumed to be in the vertical direction. The z-axis is thus in the transverse direction.

The fluid properties: density, pressure, temperature and velocity are assumed to be concentrated at the centre of the element at the position $\mathbf{x}(x, y, z)$. These properties are functions of time and space i.e. $\rho(x, y, z, t)$, $p(x, y, z, t)$, $T(x, y, z, t)$ and $\mathbf{u}(x, y, z, t)$.

The components of the velocity vector **u** are u, v, and w in the x, y and z directions respectively.

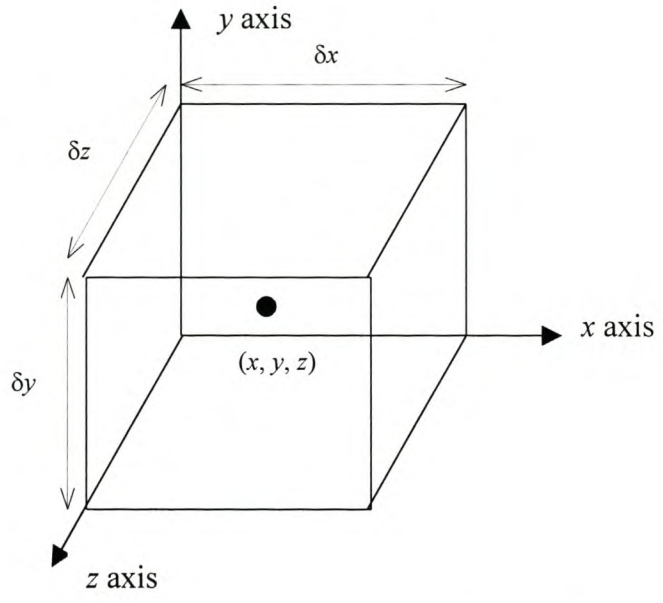

Figure 4-1: Definition sketch for a fluid element

The element under consideration is assumed to be sufficiently small so that the fluid properties at the faces can be expressed sufficiently accurately by the first two terms of a Taylor series expansion.

4.2.3 The conservation laws of physics

Fluid flow is described by the conservation laws of physics (Versteeg & Malalasekera, 1995):

i) The mass of a fluid is conserved.

ii) The rate of change of momentum equals the sum of the forces on a fluid particle (Newton's Second Law).

iii) The rate of change of energy is equal to the sum of the rate of heat addition to and the rate of work done on a fluid particle (First Law of Thermodynamics).

These laws may be applied to any fluid control volume.

4.2.4 The forces acting on fluid particles

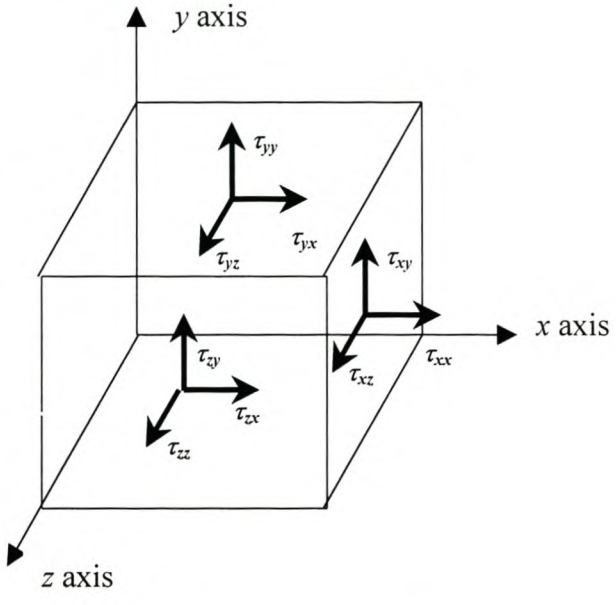

Figure 4-2: The viscous stress components acting on a fluid element

Two different types of forces act on fluid particles (Versteeg & Malalasekera, 1995):

i) **Surface forces**, e.g. pressure and viscous forces.

ii) **Body forces**, e.g. gravitational, centrifugal, Coriolis and electromagnetic forces.

The contributions due to the body forces are frequently lumped together as "source terms" whilst the contributions due to the surface forces are considered separately.

Of the surface stresses, pressure p is a normal stress. The nine viscous stress components τ_{ji} acting on a fluid element (or particle) are shown in Figure 4-2. The suffices i and j indicate that the stress component acts in the i-direction on a surface with a normal in the j-direction.

4.2.5 The difference between elements and particles

There are two ways of looking at fluid motion (see, for example, Sumer, 1973; White, 1991; Young et al., 1997). The first alternative is to analyse the flow through an element that is fixed in space. This is the more common approach as the interest is usually in the variation of the physical properties at a fixed point in space rather than those associated with a moving point. It is often termed the Eulerian approach. It gives rise to the so-called "conservation", "conservative" or "divergence" forms of the governing equations of fluid flow (Versteeg & Malalasekera, 1995). The other alternative is to track the physical properties of a fluid particle as it moves through space. This is often termed the Lagrangian approach. It gives rise to the so-called "non-conservation" or "non-conservative" form of the governing equations of fluid flow. Both approaches will be used here although the Eulerian approach is the more useful in the context of engineering design.

The momentum and energy conservation laws both make statements regarding the changes of properties of a fluid particle (Versteeg & Malalasekera, 1995). Any property, ϕ, of a particle (per unit mass) is usually a function of its position $\boldsymbol{x}(x, y, z)$ and time t. The rate of change of any property ϕ of a particle with respect to time, $D\phi/Dt$, is called the "total", "substantive" (Versteeg & Malalasekera, 1995), "material", "particle" (White, 1991), or "absolute" (Chanson, 1999) derivative. It is defined as:

$$\frac{D\phi}{Dt} = \frac{\partial \phi}{\partial t} + \frac{\partial \phi}{\partial x}\frac{dx}{dt} + \frac{\partial \phi}{\partial y}\frac{dy}{dt} + \frac{\partial \phi}{\partial z}\frac{dz}{dt} \tag{4.1}$$

Since a fluid particle follows the flow, $dx/dt = u$, $dy/dt = v$ and $dz/dt = w$, and therefore:

$$\frac{D\phi}{Dt} = \frac{\partial \phi}{\partial t} + u\frac{\partial \phi}{\partial x} + v\frac{\partial \phi}{\partial y} + w\frac{\partial \phi}{\partial z} = \frac{\partial \phi}{\partial t} + \mathbf{u} \bullet grad\ \phi = \frac{\partial \phi}{\partial t} + \mathbf{u} \bullet \nabla \phi \tag{4.2}$$

Note that $D\phi/Dt$ defines the rate of change of a property ϕ per unit mass. This must be multiplied by the density ρ to obtain the rate of change of the property ϕ per unit volume.

The rate of change of a property ϕ per unit volume for an element is given by:

$$\rho \frac{\partial \phi}{\partial t} = \rho \frac{D\phi}{Dt} - \rho \, (\mathbf{u} \bullet grad \, \phi) \tag{4.3}$$

In other words, the rate of increase of ϕ of a fluid element per unit volume is equal to the rate of increase of ϕ for a fluid particle (moving through the element) per unit volume, minus the net rate of flow of ϕ out of the fluid element per unit volume.

4.3 The mass conservation (continuity) equation

It is readily shown (e.g. Streeter, 1948; Versteeg & Malalasekera, 1995) that the three-dimensional mass conservation (continuity) equation describing the vector field at any point in an incompressible fluid is:

$$\frac{\partial u}{\partial x} + \frac{\partial v}{\partial y} + \frac{\partial w}{\partial z} = div \, \mathbf{u} = \nabla \bullet \mathbf{u} = 0 \tag{4.4}$$

4.4 The momentum and Navier-Stokes equations

Newton's second law states that the rate of change of momentum of a fluid particle equals the sum of the forces on the particle.

Define a momentum source $\mathbf{S_M}$ to represent the effect of body forces on a particle per unit volume per unit time. The x-components of the forces due to the pressure p and the axial shear stresses τ_{xx}, τ_{yx} and τ_{zx} are shown in Figure 4-3:

Similar diagrams could be constructed for the y- and z-components.

According to Versteeg & Malalasekera (1995), the rates of increase of x-, y- and z-momentum per unit volume of the fluid particle are then given by the following set of equations:

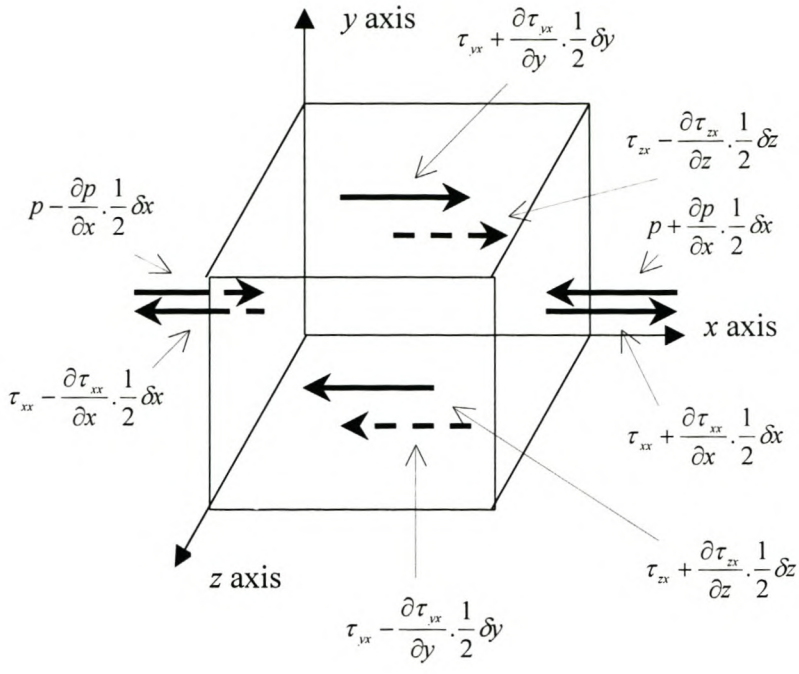

Figure 4-3: The surface forces acting on a fluid particle in the *x*-direction

$$\rho \frac{Du}{Dt} = \frac{\partial(-p + \tau_{xx})}{\partial x} + \frac{\partial \tau_{yx}}{\partial y} + \frac{\partial \tau_{zx}}{\partial z} + S_{Mx} \tag{4.5a}$$

$$\rho \frac{Dv}{Dt} = \frac{\partial \tau_{xy}}{\partial x} + \frac{\partial(-p + \tau_{yy})}{\partial y} + \frac{\partial \tau_{zy}}{\partial z} + S_{My} \tag{4.5b}$$

$$\rho \frac{Dw}{Dt} = \frac{\partial \tau_{xz}}{\partial x} + \frac{\partial \tau_{yz}}{\partial y} + \frac{\partial(-p + \tau_{zz})}{\partial z} + S_{Mz} \tag{4.5c}$$

The sign associated with pressure is opposite to that associated with the normal viscous stress because the usual sign convention takes a tensile stress to be the positive normal stress. Pressure, which by definition is a compressive normal stress, must therefore be a negative stress.

S_{Mx}, S_{My} and S_{Mz} are the x-, y- and z-components of the source term representing the contribution due to the body forces. If gravity is the only body force, $S_{Mx} = 0$ and $S_{Mz} = 0$, whilst $S_{My} = -\rho g$. Alternatively, $\mathbf{S_M} = \rho\mathbf{g}$ where $\mathbf{g}$ is the gravity vector.

In a Newtonian fluid the viscous stresses are proportional to the rates of deformation. If the fluid is also incompressible, these stresses are:

$$\tau_{xx} = 2\mu\frac{\partial u}{\partial x} \qquad \tau_{yy} = 2\mu\frac{\partial v}{\partial y} \qquad \tau_{zz} = 2\mu\frac{\partial w}{\partial z}$$

$$\tau_{xy} = \tau_{yx} = \mu\left(\frac{\partial u}{\partial y} + \frac{\partial v}{\partial x}\right) \qquad \tau_{xz} = \tau_{zx} = \mu\left(\frac{\partial u}{\partial z} + \frac{\partial w}{\partial x}\right) \qquad \tau_{yz} = \tau_{zy} = \mu\left(\frac{\partial v}{\partial z} + \frac{\partial w}{\partial y}\right) \tag{4.6}$$

Substituting for the body force and the viscous stresses, Equations 4.5a to 4.5c inclusive can now be rewritten in indicial notation (White, 1991) as:

$$\rho\frac{D\mathbf{u}}{Dt} = \rho\mathbf{g} - \nabla p + \frac{\partial}{\partial x_j}\left[\mu\left(\frac{\partial u_i}{\partial x_j} + \frac{\partial u_j}{\partial u_i}\right)\right] \tag{4.7}$$

This is the Navier-Stokes equation for an incompressible Newtonian fluid. Note that, in general, the viscosity, μ, varies with temperature, pressure and position.

4.5 The energy equations and unit stream power

4.5.1 The first law of thermodynamics

The first law of thermodynamics states that the rate of change of energy of a fluid particle is equal to the rate of heat transfer to the fluid particle plus the rate of work done on the particle (Versteeg & Malalasekera, 1995).

The rate of work done on a fluid particle by surface forces is equal to the product of the force and the velocity component in the direction of the force.

4.5.2 Heat transfer to a fluid particle

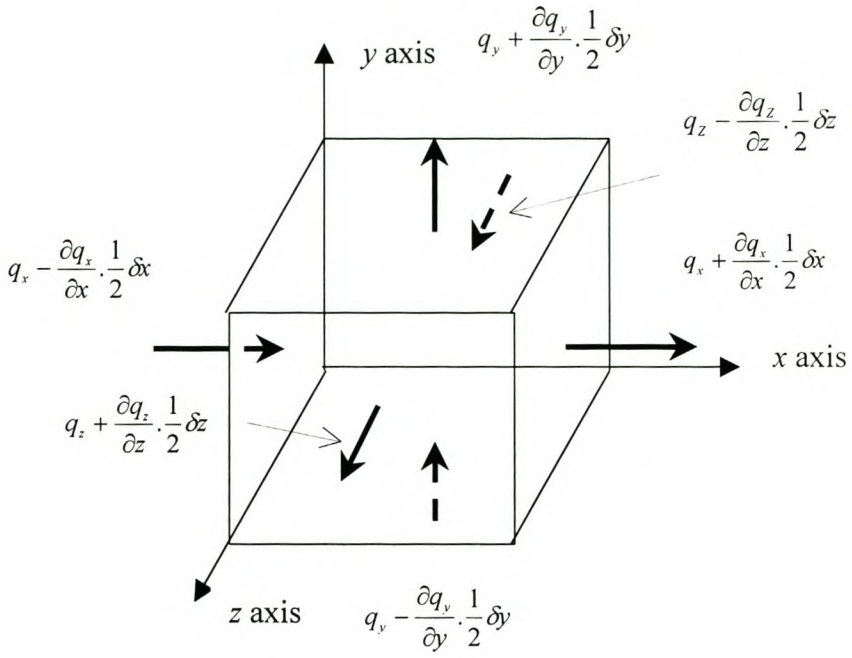

Figure 4-4: The heat transfer to a fluid particle

The heat flux vector **q** has three components q_x, q_y and q_z (Figure 4-4). The total rate of heat added to the fluid particle per unit volume due to heat flow across its boundaries (Versteeg & Malalasekera, 1995) is:

$$-\frac{\partial q_x}{\partial x} - \frac{\partial q_y}{\partial y} - \frac{\partial q_z}{\partial z} = -div\ \mathbf{q} \tag{4.8}$$

According to Fourier's law of heat conduction:

$$q_x = -k_T \frac{\partial T}{\partial x} \qquad q_y = -k_T \frac{\partial T}{\partial y} \qquad q_z = -k_T \frac{\partial T}{\partial z}$$

where k_T is the coefficient of thermal conductivity. This can be written in vector form as follows:

$$\mathbf{q} = - k_T \, grad \, T \tag{4.9}$$

Equations 4.8 and 4.9 can be combined to give the total rate of heat addition to the fluid particle due to heat conduction across the particle boundaries:

$$- div \, \mathbf{q} = div \, (k_T \, grad \, T) \tag{4.10}$$

4.5.3 The rate of change of specific energy of a fluid particle

The specific energy E of a fluid is generally defined as the sum of its internal (thermal) energy i, its kinetic energy $(u^2 + v^2 + w^2)/2$, and its gravitational potential energy. However, the gravitational potential energy may also be regarded as a body force that does work on the fluid particle as it moves through the gravity field. This body force then provides a source of energy S_E per unit volume per unit time.

With $E = i + (u^2 + v^2 + w^2)/2$, the rate of change of energy of the fluid particle per unit volume (Versteeg & Malalasekera, 1995) is given by:

$$\rho \frac{DE}{Dt} = -div \, (p\mathbf{u}) + \frac{\partial(u\tau_{xx})}{\partial x} + \frac{\partial(u\tau_{yx})}{\partial y} + \frac{\partial(u\tau_{zx})}{\partial z} + \frac{\partial(v\tau_{xy})}{\partial x} + \frac{\partial(v\tau_{yy})}{\partial y}$$

$$+ \frac{\partial(v\tau_{zy})}{\partial z} + \frac{\partial(w\tau_{xz})}{\partial x} + \frac{\partial(w\tau_{yz})}{\partial y} + \frac{\partial(w\tau_{zz})}{\partial z} + div \, (k_T \, grad \, T) + S_E \tag{4.11}$$

4.5.4 The rate of change of kinetic energy of a fluid particle

The (mechanical) kinetic energy component may be obtained separately by multiplying the x-momentum equation (4.5a) by the velocity component u, the y-momentum equation (4.5b) by the velocity component v, and the z-momentum equation (4.5c) by w, and adding the results together. The resulting equation for the rate of change per unit volume of kinetic energy of a particle (Versteeg & Malalasekera, 1995) is:

$$\rho \frac{D\left[\frac{1}{2}\left(u^2+v^2+w^2\right)\right]}{Dt} = -\mathbf{u}\bullet grad\, p + u\left(\frac{\partial \tau_{xx}}{\partial x}+\frac{\partial \tau_{yx}}{\partial y}+\frac{\partial \tau_{zx}}{\partial z}\right)$$

$$+v\left(\frac{\partial \tau_{xy}}{\partial x}+\frac{\partial \tau_{yy}}{\partial y}+\frac{\partial \tau_{zy}}{\partial z}\right)+w\left(\frac{\partial \tau_{xz}}{\partial x}+\frac{\partial \tau_{yz}}{\partial y}+\frac{\partial \tau_{zz}}{\partial z}\right)+\mathbf{u}\bullet \boldsymbol{S}_M \qquad (4.12)$$

In other words, the rate of change of the kinetic energy of a fluid particle depends on the energy lost in doing work against the pressure gradient plus the energy gained from the work done through the shear gradient plus the work done by the body force (gravity).

4.5.5 The rate of change of internal energy of a fluid particle

The equation for the rate of change of the internal energy for a fluid particle may now be obtained by subtracting Equation 4.12 from Equation 4.11 (Versteeg & Malalasekera, 1995). Note that *div* **u** = 0 for an incompressible fluid, and if gravity is the only body force, $S_E = \mathbf{u}\bullet\mathbf{S_M} = -\rho g v$ giving S_E - $\mathbf{u}\bullet\mathbf{S_M} = 0$. The resulting equation is:

$$\rho \frac{Di}{Dt} = \tau_{xx}\frac{\partial u}{\partial x}+\tau_{yx}\frac{\partial u}{\partial y}+\tau_{zx}\frac{\partial u}{\partial z}+\tau_{xy}\frac{\partial v}{\partial x}+\tau_{yy}\frac{\partial v}{\partial y}+\tau_{zy}\frac{\partial v}{\partial z}+\tau_{xz}\frac{\partial w}{\partial x}+\tau_{yz}\frac{\partial w}{\partial y}+\tau_{zz}\frac{\partial w}{\partial z}$$

$$+ div\,(k_T\, grad\, T) \qquad (4.13)$$

In the case of an incompressible fluid, $i = cT$ where c is the specific heat of the fluid. This implies that the rate of change in the internal energy of a fluid particle is determined by the shearing on the particle surfaces plus the inflow of internal energy from outside the particle owing to the temperature gradient.

The effects due to viscous stresses in the internal energy equation may be replaced by the "dissipation function", Φ (White, 1991; Versteeg & Malalasekera, 1995). In other words, using indicial notation:

$$\Phi = \tau_{ji} \frac{\partial u_i}{\partial x_j} \tag{4.14}$$

In the case of an incompressible Newtonian fluid, simple algebra and the use of the shear stress relationships given in Equations 4.6 (White, 1991; Versteeg & Malalasekera, 1995) yield:

$$\Phi = \mu_b \left\{ 2\left[\left(\frac{\partial u}{\partial x}\right)^2 + \left(\frac{\partial v}{\partial y}\right)^2 + \left(\frac{\partial w}{\partial z}\right)^2 \right] + \left(\frac{\partial u}{\partial y} + \frac{\partial v}{\partial x}\right)^2 + \left(\frac{\partial u}{\partial z} + \frac{\partial w}{\partial x}\right)^2 + \left(\frac{\partial v}{\partial z} + \frac{\partial w}{\partial y}\right)^2 \right\} \tag{4.15}$$

where μ_b is the sum of the laminar and turbulent viscosities. In indicial notation (White, 1991):

$$\Phi = \mu_b \left(\frac{\partial u_i}{\partial x_j} + \frac{\partial u_j}{\partial x_i} \right) \frac{\partial u_i}{\partial x_j} \tag{4.16}$$

Yang & Song (1979) have developed similar expressions to Equations 4.14, 4.15 and 4.16 from a consideration of the Reynolds modification of the Navier-Stokes equations of motion for incompressible fluids. In the case of gradually varied steady open channel flows for which the Froude number is not too large, they give:

$$\Phi = \frac{1}{2} \rho \left(\nu + \varepsilon_{(t)}\right) \left(\frac{\partial u_i}{\partial x_j} + \frac{\partial u_j}{\partial x_i} \right)^2 \tag{4.17}$$

Here, $\varepsilon_{(t)}$ is the average turbulent kinematic viscosity defined in terms of the average turbulent dynamic viscosity, $\mu_{(t)}$, as follows:

$$\varepsilon_{(t)} = \frac{\mu_{(t)}}{\rho} \tag{4.18}$$

Noting that the total kinematic viscosity is the sum of the viscous and turbulent kinematic viscosities, it is easily shown that Equation 4.17 can be rewritten as Equation 4.15 or 4.16 with μ_b representing the total coefficient of viscosity.

Equation 4.13 may now be rewritten as follows:

$$\rho \frac{Di}{Dt} = \Phi + div\,(k_T\, grad\, T) \tag{4.19}$$

The rate of change of the internal energy of a fluid element is obtained by combining Equations 4.3 and 4.19 to give:

$$\rho \frac{\partial i}{\partial t} = \Phi + div\,(k_T\, grad\, T) - \rho\,(\mathbf{u} \bullet grad\, i) \tag{4.20}$$

Since $i = cT$:

$$\rho \frac{\partial i}{\partial t} = \Phi + div\,(k_T\, grad\, T) - \rho\,(\mathbf{u} \bullet grad\, cT) \tag{4.21}$$

In other words, in the case of a fixed element, internal energy can also be transported into or out of the element by the flow of fluid through it.

4.5.6 The energy source

Equations 4.11, 4.12 and 4.13 (or 4.19) represent the rate of change of the total, kinetic, and internal energy respectively per unit volume of a fluid particle. Note that whilst Equation 4.13 equals zero in the case of steady uniform flow, Equations 4.12 and 4.14 can only be zero if the fluid is at rest. This is because all fluid motion expends energy.

What is the energy source? Well, in the case of open channel flow, it is ultimately the body force, gravity. Each fluid particle releases potential energy at a rate of $-\mathbf{u} \bullet \boldsymbol{S}_M =$

$-\rho g v = \rho (\boldsymbol{g} \bullet \boldsymbol{u})$ as it moves through the gravitational field. Along the way, however, energy may be transferred between internal energy and kinetic energy.

4.6 The definition of applied unit stream power

Power is defined as the rate of change of energy. Equations 4.13 (or 4.19) and 4.21 thus represent the power output per unit volume of a fluid particle and an element respectively. The dissipation function, Φ, is that component involved in maintaining motion. This motion can be purely that of the fluid, or it can be of a fluid / solid mixture. The other components describe the transportation of internal energy through the system via the thermal gradient or through fluid motion.

If the fluid can be regarded as isothermal, then:

$$\rho \frac{Di}{Dt} = \rho \frac{\partial i}{\partial t} = \Phi \tag{4.22}$$

In keeping with previous work in this field (e.g. Rooseboom, 1992; Le Grange & Rooseboom, 1993; Basson & Rooseboom, 1997; Rooseboom & Le Grange, 2000), Φ will hereinafter be called the "applied unit stream power" and given the symbol P_t. The letter P is a reminder that it is a power term. The subscript t is a reminder that the power is used to overcome the shear stresses (t being a substitute for τ). In other words:

$$P_t = \Phi = \tau_{ji} \frac{\partial u_i}{\partial x_j} \tag{4.23}$$

In the metric system, $P_t = \Phi$ has the units Watt per cubic metre (W/m^3).

When Equation 4.23 is applied to steady uni-directional flow, i.e. steady flow down an infinitely wide rectangular prismatic channel of small slope, most of the terms disappear to give:

$$P_t \approx \tau_{yx} \frac{\partial u}{\partial y} \tag{4.24}$$

as before.

4.7 Conclusions

This chapter gives the derivation of the fundamental equations of fluid motion: the conservation of mass, momentum and energy respectively. These are required for the construction of the numerical model (Chapter 8). It shows that the applied unit stream power is the rate of loss of internal energy of a fluid particle per unit volume as the particle overcomes viscous stresses. It is identical to the dissipation function, Φ. The applied unit stream power is hereinafter given the symbol, P_t.

Chapter 5
An overview of scour and deposition around selected structures

5.1 Introduction

This thesis is concerned about the development of a mathematical model for the prediction of scour and deposition. The proposed model will be presented in Chapters 6 and 7. A preliminary test of this model was carried out by modelling the local clear-water scour associated with three typical engineering structures: upstream of a sharp-crested weir, around circular piers, and around a vertical sharp-edged abutment. This work is described in Chapters 8 and 9.

This Chapter seeks to describe the different observed types of scour, before going on to describe the complex flow and scour patterns that are commonly associated with the above-mentioned structures. These will have to be replicated by the mathematical model. Some commonly used scour formulae are presented, as are some recent efforts to model scour through numerical computation.

5.2 Types of scour

5.2.1 Introduction

Scour is generally categorised into three main types (e.g. Breusers & Raudkivi, 1991; HEC-18, 1995; Raudkivi, 1998):

i) General scour.

ii) Constriction scour.

iii) Local scour.

Hoffmans & Verheij (1997), however, only have two main categories: general scour and local scour, but general scour is further broken down into four sub-categories:

i) Overall degradation.

ii) Constriction scour.

iii) Bend scour.

iv) Confluence scour.

The fundamental difference between general scour and local scour is that whilst general scour is caused by long-term uni-directional velocity gradients in the vicinity of the bed, local scour is largely a consequence of vortex formation and dissipation. Based on this definition, the scour due to bends and confluences can be classified under both categories.

In this study, only the local scour around engineering structures was modelled, and therefore this will be the main focus of this chapter.

5.2.2 General scour

According to Hoffmans & Verheij (1997), the time scale for general scour is normally longer than the time scale for local scour. Four sub-categories are identified:

i) "Overall accretion or degradation" occurs as a river adjusts to changes in the water or sediment flow. The changes may be natural or as a result of human interference. Examples of changes include:

   a) Flow-rate variations.

   b) The construction of flood embankments, flood detention basins, wetlands, weirs or dams.

   c) Dredging.

   d) The clearance of riverine vegetation.

   e) Inter-basin water transfers.

f) Meander cut-offs.

Overall accretion or degradation can affect long reaches of rivers extending over many kilometres and taking place over periods of many years (De Vries, 1975).

There cannot be accretion without a sediment supply. If there is suspended sediment, it will tend to settle out if the flow conditions drop below the critical values for incipient motion, although the deposition process may take a very long time and very fine particles may stay in suspension indefinitely in the form of colloids. Sediment will also tend to settle out if the concentration of suspended sediment is in excess of the stream flow capacity.

There cannot be degradation if the in-situ "sediments" cannot be mobilised (e.g. rock). Mobilisation of sediments can only commence once incipience (see Chapter 3) is reached.

The absence of accretion or degradation does not necessarily indicate that there is no scour or deposition. It merely indicates that scour and deposition are in equilibrium. In many cases, this equilibrium is a "dynamic equilibrium" where scour and deposition proceed at the same rate.

ii) "Constriction scour" is a special, localised, case of overall degradation. It occurs when the channel is confined, and results in the lowering of the bed level across the confined channel. It is readily ascribed to the increased flow velocity in the constricted section.

iii) "Bend scour" occurs in response to the large coherent flow structures / secondary currents that are set up whenever the flow is forced to follow a curved path (see Section 2.4.2). These secondary currents result in increased local velocities in the vicinity of the bed on the outside of the bend. The resulting scour can result in the local depth being up to twice the average flow depth (Hoffmans & Verheij, 1997). Meanwhile, on the inside of the bend, reduced local velocities can result in deposition. To complicate the issue further, shallow and deep sections can alternate round the bend and for a short distance downstream as the river profile continually over-adjusts to the spiral flow phenomena (Hoffmans & Verheij, 1997).

iv) "Confluence scour" occurs when two branches of a river meet. Invariably, the flow rates, slopes, sediment transport and the angle of approach relative to the downstream channel will be different for the two branches. These factors result in complicated secondary flow patterns with associated scour and deposition downstream of the confluence.

This investigation will not look at general scour in any further detail.

5.2.3 Local scour

Local scour results from the effect of a structure on local flow patterns. It is superimposed on the general scour. It is normal to differentiate between two types of scour: clear-water scour, and live-bed scour.

"Clear-water scour" occurs in the absence of general scour. In other words, the flow conditions in the general vicinity of the structure (but not close to the structure) are below the critical conditions for incipient motion. All sediment movement thus occurs directly as a result of the altered flow conditions caused by the presence of the structure. An exception is made in the case of wash-load that might have been transported over considerable distances (Raudkivi, 1998).

"Live-bed scour" occurs in the presence of general scour and is superimposed on it. In this case, the flow conditions in the general vicinity of the structure are above the critical conditions for incipient motion. Whilst clear-water scour can theoretically reach static equilibrium, live-bed scour can only reach dynamic equilibrium when the rate of sediment entering the scour hole equals the rate of sediment leaving it. A further complication is that river beds are not generally flat, but usually consist of bed-forms, such as ripples or dunes, that migrate downstream as sediment is eroded from the upstream face and deposited on the downstream face.

A typical plot showing the scour depth versus time for the two types of scour is given in Figure 5-1. It will be noted that the scour hole develops much more rapidly in the case of live-bed scour, but the gross dimensions of the scour hole never reach equilibrium as they are affected by the passage of bed-forms.

This investigation will focus almost exclusively on clear-water scour. Not only is it easier to analyse than live-bed scour, it also results in the larger scour hole, which is particularly important from the perspective of engineering design.

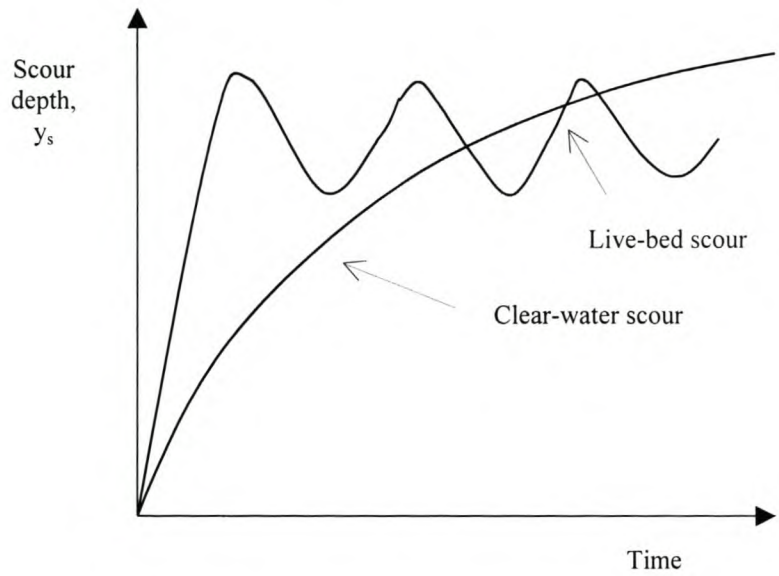

Figure 5-1: Scour depth as a function of time

5.3 Weirs

The flow over a weir is essentially two-dimensional (2D) in the vertical plane (over the central section). This makes it a convenient structure to analyse first. Piers and abutments, on the other hand, cause the formation of complex three-dimensional (3D) flow patterns. In this investigation, the emphasis will be placed on the movement of sediment upstream of the weir rather than downstream of the weir. To further simplify the problem, only weirs with vertical upstream faces will be considered.

In general, sediment would be expected to deposit on the upstream side of a weir, whilst the channel downstream of the weir is vulnerable to scour if not adequately protected. This is illustrated in Figure 5-2:

Scouring downstream of a weir is a complex problem that has attracted the attention of many investigators. Information on this subject may be found in Breusers & Raudkivi (1991), French (1994), Hoffmans & Verheij (1997), and Raudkivi (1998).

On the other hand, there is very little literature on the deposition patterns upstream of weirs.

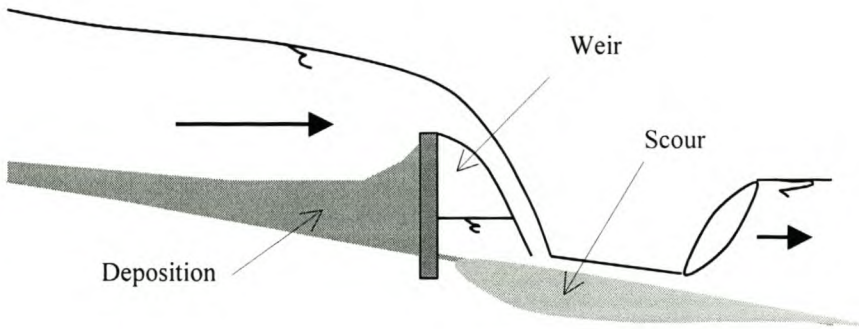

Figure 5-2: Typical scour and deposition patterns around a weir

Experiments carried out in a 0.37 m wide rectangular laboratory flume (Harnett, 1998) clearly show that the equilibrium sediment profile upstream of the weir is curved with a minimum reduced level close to, but not at, the weir face. Upstream of this point of maximum scour depth, the sediment profile becomes parallel to the water surface. Downstream of this point, the sediment abruptly rises up the front face of the weir, occasionally reaching the lip and spilling over the top. It can be deduced that the sediment transport capacity of the flow was initially at a maximum at the point of maximum scour depth.

5.4 Piers

5.4.1 Introduction

Piers and abutments (which will be considered in Section 5.5) are structures where, as a consequence of the vertical velocity distribution upstream, the flow is fully three-dimensional (3D). There is an almost overwhelming amount of literature dealing with the scour around piers and abutments. There is an obvious reason for this – it is a major engineering problem.

In view of the fact that the flow around an abutment behaves, to a certain extent, like the flow around one side of a pier, piers will be considered first.

5.4.2 The flow patterns around a cylindrical pier

It is normal for the scour around piers and caissons (hereinafter called simply "piers") to be described in terms of the deviation from that for cylindrical piers (e.g. Breusers & Raudkivi, 1991; HEC 18, 1995; Hoffmans & Verheij, 1997; Raudkivi, 1998; Graf, 1998). The maximum scour depth is generally achieved with clear-water scour in a uniform sediment (Figure 5-1). Non-uniform sediments tend to limit scour depths as a consequence of armouring. The three-dimensional mathematical model was thus initially developed for clear-water scour in a uniform non-cohesive sediment.

The flow around a cylindrical pier is extremely complex. Figure 5-3 shows a schematic diagram of the flow around a cylindrical pier with a fully developed scour hole.

Four distinct flow patterns can be identified:

i) The "bow wave" is caused by the sudden deceleration of the oncoming flow. The rise in height at the leading face of the pier corresponds to the velocity head of the oncoming flow that is a maximum at the surface. The flow is forced up and back onto itself to form a bow wave or "roller".

ii) The rise in pressure on the leading face of the pier (termed the "stagnation pressure") decreases with the square of the velocity of the oncoming flow i.e. it decreases from top to bottom. This results in a partial reversal of the normal pressure gradient that provides the driving mechanism for a vertical "downflow". The maximum velocity of the downflow in vertical section, according to experimental data by Ettema (1980) and Raudkivi (1986), is situated between 0.05 and 0.02 times the pier breadth, b_p, upstream of the pier, being closer to the pier near the bed than at the surface. The velocity of the downflow also increases in magnitude towards the bed in the vertical section. If no scour is present, the maximum velocity is approximately 40% of the average oncoming velocity, U. This velocity increases to approximately $0.8U$ as the scour depth increases past $2b_p$ (Breusers & Raudkivi, 1991; Raudkivi, 1998). This relatively high velocity flow directed at the base of the pier acts as a sort of water jet that helps to initiate and maintain the scouring process (Graf, 1998). The increased pressure on the leading face of the pier also helps to provide the necessary force for the acceleration of the flow around the sides.

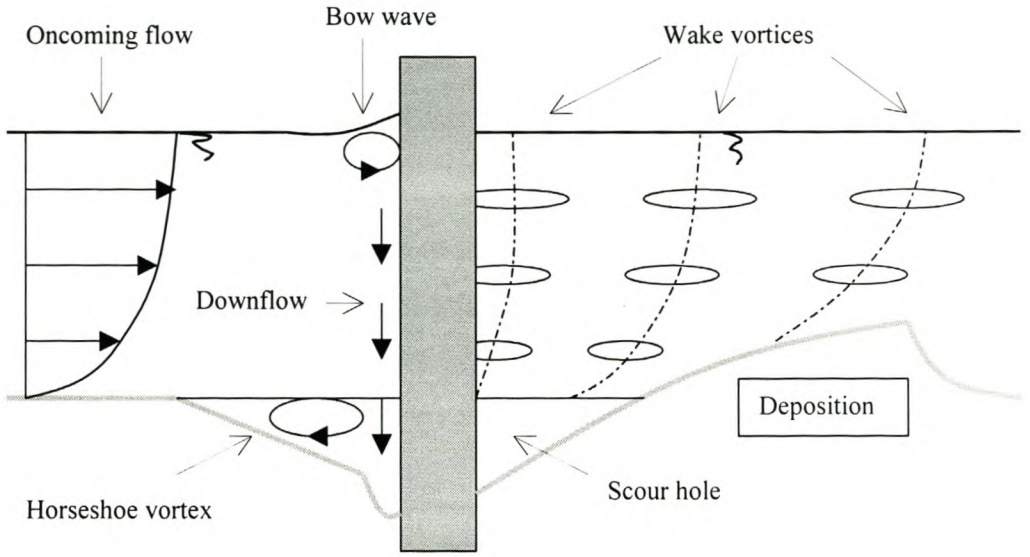

a) Centreline profile

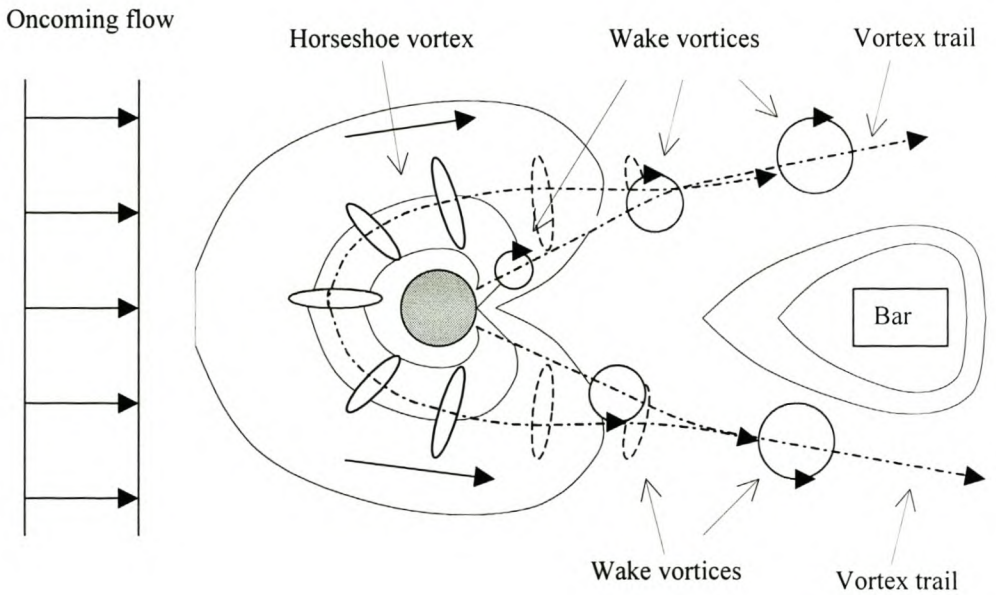

b) Plan

Figure 5-3: Flow patterns around a cylindrical pier
(After Breusers & Raudkivi, 1991; Hoffmans & Verheij, 1997; Raudkivi, 1998)

iii) Once a scour hole begins to form, flow separation at the upstream rim results in the formation of a lee eddy that rotates in the opposite direction to the bow roller. This lee eddy is called the "horseshoe vortex" owing to its distinctive shape: it wraps itself around the front half of the pier and extends a few pier diameters downstream on either side before losing its identity and becoming part of the general turbulence. According to Raudkivi (1998), the vorticity of the horseshoe vortex is quite small and its main role in the scouring process comes about through its interaction with other flow structures. For example, it pushes the maximum downflow velocity within the scour hole closer to the pier.

iv) Flow separation around the sides of the pier results in the formation of "wake vortices" that alternately separate from the two sides to form a Von Kármán vortex street. Near the bed, these vortices interact with the horseshoe vortex and, with their vertical low-pressure centres, lift sediment from the bed like miniature tornadoes (Raudkivi, 1998). The frequency, f, of the vortex shedding is indicated by the Strouhal Number, St:

$$St = \frac{fb_p}{U} \approx 0.2 \tag{5.3}$$

5.4.3 The development of the scour hole

According to Breusers & Raudkivi (1991), scour hole development commences at the sides of the cylinder with the two holes rapidly propagating upstream around the perimeter of the cylinder to meet on the centreline. The eroded material is transported downstream by the flow. Soon after the commencement of scouring, a shallow groove, concentric with the front portion of the cylinder, is formed by the downflow. This groove often has near-vertical faces with a sharp upper edge. The downflow is turned 180° in the groove, and the resulting upward flow is deflected by the horseshoe vortex up the scour hole slope. The sand in the region around the rim collapses into the groove from time to time in order to return the slope angle to the angle of repose of the bed material. Sand particles in the groove are lifted by the upflow into the region of the horseshoe vortex where they are either deposited on the slope or transported into and through the wake region. They tend to deposit in the region

between the two vortex trails to form a bar. As the scour approaches its equilibrium depth, the groove becomes shallower and can disappear altogether.

Zanke (1978) has distinguished four phases in the evolution of a scour hole: an initial phase, a development phase, a stabilisation phase, and an equilibrium phase (Hoffmans & Verheij, 1997). It sometimes takes several days for clear-water scour to reach equilibrium (Raudkivi, 1998).

If the sand is fine, ripple formation tends to reduce the maximum scour depth (Raudkivi, 1998).

Live-bed scour is complicated by the passage of bed forms past the pier. The equilibrium depth is thus generally defined as the time-averaged scour depth. It is generally less for live-bed scour than clear-water scour (Raudkivi, 1998). Live-bed scour also tends to reach equilibrium much faster than clear-water scour – commensurate with the higher sediment transportation capacity of the flow.

5.4.4 Factors influencing the depth of the scour hole

The most significant parameter, from the point of view of engineering design, is the scour depth, y_s, which is usually a maximum at or near the pier. As a consequence, most research effort has been directed toward the determination of this single parameter. However, the complicated flow patterns that exist around piers have led many researchers to resort to the use of dimensional analysis in their effort to determine the parameters affecting y_s.

The effectiveness of dimensional analysis is dependent on the choice of the dependent parameters. The following parameters are of importance (Breusers & Raudkivi, 1991; Hoffmans & Verheij, 1997; Raudkivi, 1998; Melville & Chiew, 1999):

i) Flow: acceleration of gravity (g), fluid density (ρ), kinematic viscosity (ν), flow depth (Y), shear velocity (u_*), mean velocity (U).

ii) Bed material: representative diameter (d e.g. d_{50} or $\bar{d}$) sediment density (ρ_s), geometric standard deviation (σ_g), critical average flow velocity (U_c), shape

factor (*SF*), gradation of the bed material, surface packing, cohesion of the material etc.

iii) Pier: diameter / breadth (b_p), and in the case of non-cylindrical piers, the shape and alignment of the pier, pier grouping.

iv) Time: actual time (t), time for equilibrium scour to develop (t_e).

The dimensionless Π-groups depend very much on the initial choice of variables. For a cylindrical pier situated in a non-cohesive uniform sediment of constant density and typical shape factor, the depth of the scour hole, y_s, relative to the breadth of the pier, b_p, can be expressed (Breusers & Raudkivi, 1991; Raudkivi, 1998) as:

$$\frac{y_s}{b_p} = f\left(\frac{Ub_p}{\nu}, \frac{U^2}{gb_p}, \frac{Y}{b_p}, \frac{d}{b_p}\right) \tag{5.4}$$

or,

$$\frac{y_s}{b_p} = f\left(\frac{u_* b_p}{\nu}, \frac{u_*^2}{\Delta g b_p}, \frac{Y}{b_p}, \frac{d}{b_p}\right) \tag{5.5}$$

Alternatively, Melville & Chiew (1999) express the "relative scour depth", y_s/b_p as:

$$\frac{y_s}{b_p} = f\left(\frac{U}{U_c}, \frac{Y}{b_p}, \frac{d}{b_p}, \frac{t}{t_e}\right) \tag{5.6}$$

In other words, the relative scour depth is a function of the "flow intensity", the "flow shallowness", the "sediment coarseness" and the "time ratio".

According to Melville & Chiew (1999), the local scour depth in uniform sediment increases almost linearly with flow intensity to a maximum at the threshold velocity (the "threshold peak"). It then decreases a little before increasing again to a second peak at about the transition flat bed stage of sediment transport on the channel (the "live-bed peak") (Figure 5-4a).

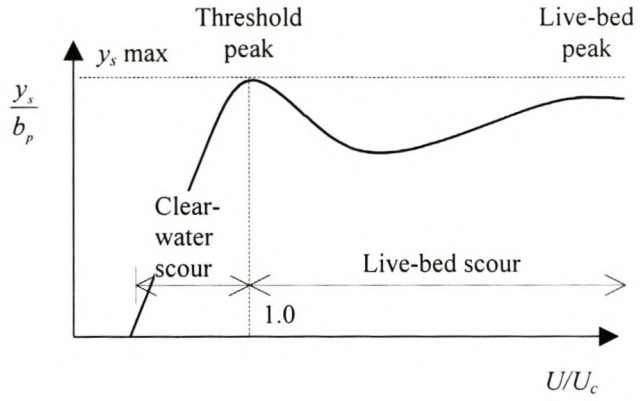

a) Variation with the flow intensity

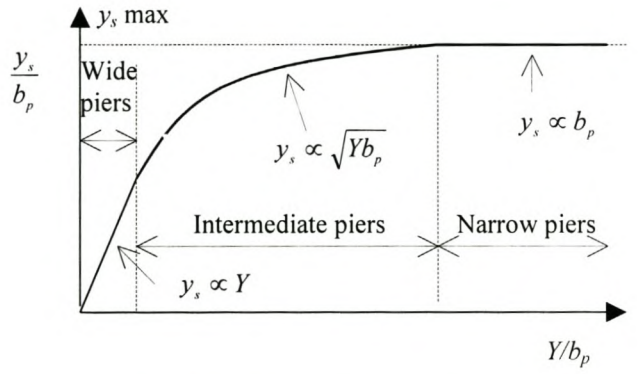

b) Variation with flow shallowness

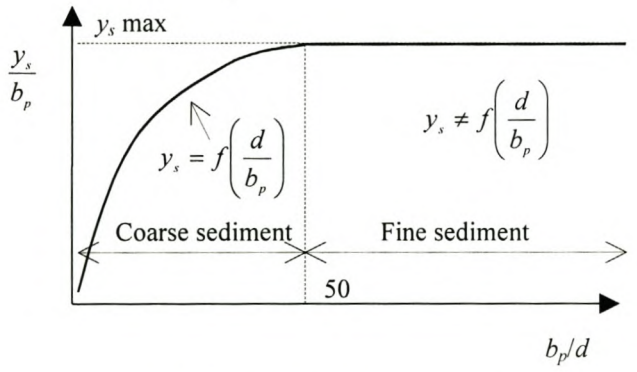

c) Variation with sediment coarseness

Figure 5-4: Factors affecting the relative scour depth around a pier
(After Melville & Chiew, 1999)

As long as the surface roller and horseshoe vortex are sufficiently far apart that they do not affect one another, scour depth is unaffected by any reduction in the flow depth. If, however, they are close together, since the two vortices rotate in opposite directions, they interfere with each other and the scour depth is reduced. For shallow flows (or very wide piers), the scour depth is directly proportional to the flow depth (Melville, 1997) (Figure 5-4b).

In the case of uniform sediments, local scour depths are unaffected by sediment size unless the sediment is relatively coarse. If, however, $d/b_p < 50$, the scour depth is reduced because the grains are large compared with the groove excavated by the downflow and proportionately more energy is dissipated there (Ettema, 1980; Melville & Chiew, 1999) (Figure 5-4c).

The variation of the relative scour depth with time is a little more complicated as, according to Melville & Chiew (1999), the equilibrium time depends on the same parameters as the relative scour depth. Define the equilibrium time scale, t^*, as:

$$t^* = \frac{Ut_e}{b_p} \tag{5.7}$$

Then,

$$t^* = \frac{Ut_e}{b_p} = f\left(\frac{U}{U_c}, \frac{Y}{b_p}, \frac{d}{b_p}\right) \tag{5.8}$$

Melville & Chiew (1999) then proceed to describe the relationship between the scour depth and time for each of the dimensionless Π-groups indicated in Equation 5.8. Hoffmans & Verheij (1997) also list several equations that can be used to estimate the development of scour with time.

The first two terms in Equations 5.4 and 5.5 are effectively the pier Reynolds number and pier Froude number respectively. Note the different definitions of these two parameters in these two equations. An analysis of field data by Johnson (1995) seems to indicate that the scour depth is not that sensitive to these two parameters although Shen et al. (1969) use a Reynolds number in their pier-scour equation. Hancu (1971), Jain & Fischer (1979) and HEC-18 (1995), meanwhile, all use Froude numbers in their scour depth equations. Table 5-1 gives a list of some of the better known scour-

depth equations. More extensive summaries of the various scour-depth equations can be found in Johnson (1995), Babaeyan-Koopaei (1996) and Hoffmans & Verheij (1997). Comparisons of the accuracy of the various different scour-depth equations have been made by, inter alia, Hopkins et al. (1980), Jones (1983) and Johnson (1995).

A glance at the formulae presented in Table 5-1 reveals that there is a general consensus that scouring around piers generally commences at $U \approx 0.5U_c$. Chiew (1995) however has recorded scour at $U = 0.3U_c$.

The difference between measured and estimated scour depths can be as much as an order of magnitude (Johnson, 1995). The enormous amount of uncertainty inherent in the prediction of the scour depth has prompted some researchers to propose a single figure for design purposes, e.g. Neill (1973) and Ettema (1990) who proposed y_s/b_p = 1.5, and y_s/b_p = 2.4 respectively.

Reference	Scour-depth formula	Remarks
HEC-18 (1995) (Alternatively called the Colorado State University, CSU, equation)	$y_s = 2.0YK_1K_2K_3\left(\frac{b_p}{Y}\right)^{0.65} Fr^{0.43}$	K_1, K_2, K_3 = Factors for pier nose shape, flow angle of attack and bed condition respectively. $Fr = \frac{U}{\sqrt{gY}}$ The limiting values of y_s/Y are: 2.4 for $Fr \leq 0.8$ and 3.0 for $Fr >$ 0.8
Melville & Sutherland (1988)	$y_s = K_1K_dK_yK_\alpha K_sb_p$	$K_1, K_d, K_y, K_\alpha, K_s$ = Factors to account for the flow-intensity, sediment size, flow-depth, pier alignment and pier-shape respectively.

Table 5-1a: Commonly used pier scour depth equations
(After Johnson, 1995)

Reference	Scour-depth formula	Remarks
Breusers et al. (1977)	$y_s = b_p f K_1 K_2 \left[2\tanh\left(\frac{Y}{b_p}\right)\right]$	K_1, K_2 = Factors for pier nose shape and flow angle of attack respectively. $f = 0$ for $U/U_c \le 0.5$ $f = 2U/U_c - 1$ for $0.5 < U/U_c \le 1$ $f = 1$ for $U/U_c > 1$
Jain & Fischer (1979)	$y_s = 2.0 b_p (Fr - Fr_c)^{0.25}\left(\frac{Y}{b_p}\right)^{0.5}$ for $(Fr - Fr_c) > 0.2$ $y_s = 1.85 b_p Fr_c^{0.25}\left(\frac{Y}{b_p}\right)^{0.5}$ for $(Fr - Fr_c) < 0.2$	$Fr_c = \frac{U_c}{\sqrt{gY}}$ For $0 < (Fr - Fr_c) < 0.2$, use the larger of the scour depths calculated from the two equations
Laursen & Toch (1956)	$y_s = 1.35 b_p^{0.7} Y^{0.3}$	As described by Neill (1964)
Larras (1963)	$y_s = 1.05 b_p^{0.75}$	Live-bed scour only
Hancu (1971)	$y_s = 2.42 b_p \left(\frac{2U}{U_c} - 1\right)\frac{U_c^2}{g b_p}$ for $0.05 \le \frac{U_c^2}{g b_p} \le 0.6$	$U_c = 1.2\sqrt{\frac{g d_{50}(\rho_s - \rho)}{\rho}}\left(\frac{Y}{d_{50}}\right)^{0.2}$ For clear water scour, $\left(\frac{2U}{U_c} - 1\right) = 1$ Equation does not apply for: $\frac{U}{U_c} \le 0.5$
Shen et al. (1969)	$y_s = 0.00022\, Re^{0.619}$	Clear-water scour only, $Re = \frac{U b_p}{2\nu}$

Table 5-1b: Commonly used pier scour depth equations (cont.)

(After Johnson, 1995)

5.4.5 The shape of the scour hole

The shape of the scour hole around a single cylindrical pier in a uniform flow with its foundation in a uniform bed material has been studied by a number of researchers including Dargahi (1987), Olsen & Melaaen (1993), and, indirectly, by Dey et al. (1995). A typical scour hole profile is shown in Figure 5-3.

Dargahi (1987) schematised the plan section of a fully developed cylindrical pier scour hole into a semi-circle on the upstream side and half of an ellipse (cut along the minor axis) on the downstream side. The semi-circle has a radius of about $2b_p$ measured from the centre of the pier, provided that the flow depth is at least $3b_p$. The length of the scour in the downstream direction is in the order of $5b_p$. According to Hoffmans & Verheij (1997), the average upstream slope is approximately equal to the angle of repose, ϕ_r, being a little steeper in the groove close to the pier and a little flatter outside of this. The average downstream slope is about $\phi_r/2$. The deepest point of the scour hole is usually in the vicinity of the leading face of the pier, but at times it can be found at an angle of up to 60^o on either side of the front face (Chiew, 1995).

5.4.6 Computational modelling of local scour around a pier

In view of the rapid improvement in the computational power of digital computers, it is becoming increasingly attractive to attempt to model scour numerically. The work of Olsen & Melaaen (1993) is of particular interest to this investigation. They computed the geometry of a scour hole around a circular pier with the aid of a numerical model. A finite-volume method was used to solve the non-transient Navier-Stokes equations for the three-dimensional flow field on a general non-orthogonal grid. The k-ε turbulence model was used to solve for the Reynolds-stress term. The flow field gave the shear stress on the boundaries, which in turn was used to estimate the sediment concentration for the bed elements. The diffusion / convection equation for the sediment concentration was then solved, and changes in the bed elevation were calculated from continuity. A new flow field was then calculated using the modified bed, and the above sequence repeated until the depth of the calculated scour hole was identical to that measured in a separate physical model study. Once the scour depth was correct, the shape of the computed scour hole compared quite well with that measured in the physical model.

Inspired by work of Olsen & Melaaen (1993), Richardson & Panchang (1998) used the FLOW-3D computational fluid dynamics software (Sicilian et al., 1987) to model the flow field past a circular pier for which physical model results were available. Three steady-state flow conditions were modelled: with the initial flat bed, the intermediate scour hole, and the equilibrium scour hole respectively. All of the boundaries were rigid i.e. no free surface or scour routines were employed. The shape of the scour hole was approximated by a frustum of a cone. The computed flow velocities were broadly in agreement with the laboratory observations. Particle tracking showed that sediment movement through the scour holes was also much as expected. Each simulation required approximately 168 hours of CPU time on a desktop SUN workstation.

Olsen & Kjellesvig (1998) improved substantially on the Olsen & Melaaen (1993) study. The Reynolds averaged transient Navier-Stokes equations were used with the k-ε turbulence model to predict the water flow. The location of the water surface was calculated by extrapolating the pressure from the inner cells to the water surface. The pressures in the surface cells were then compared to fixed reference located on the downstream boundary. If there were any discrepancies between the two values, the water surface was adjusted accordingly. The sediment transport was calculated using the convection-diffusion equation for sediment concentration except for the cells closest to the bed. In these cells, the bed concentration, c_{bed}, was calculated using a formula presented by Van Rijn (1987):

$$c_{bed} = 0.015 \frac{d_{50}^{0.7}}{a_r} \frac{\left[\frac{\tau_0 - \tau_c}{\tau_c}\right]^{1.5}}{\left[\frac{(\rho_s - \rho)g}{\rho \nu^2}\right]^{0.1}} \tag{5.9}$$

In Equation 5.9, a_r is a reference level that was set to 5% of the water depth in this study. The critical bed shear stress, τ_c, was adjusted for sloping beds using a formula presented by Brooks (1963). The level of the bed was then adjusted for the next time step (100 seconds). The height of the cells was continuously adjusted in proportion to the height difference between the bed and the water surface.

The flow field for a stationary solution with a horizontal non-moving bed and water surface seemed to give realistic looking velocity vector and bed shear stress fields. The same problem was then run with the sediment concentration calculation procedure adjusting the location of the bed and the water surface after each time step. The scour hole and bar developed much as expected although it took an IBM-370 workstation nine weeks to simulate 208 hours of scour hole development. The maximum scour depth was obtained after about 104 hours. The depth was of the same magnitude as those predicted by four different empirical equations.

It should be noted that grid and the time-step were relatively large. As a consequence, the model did not identify the wake vortices. A coarser grid gave a significantly smaller scour hole that also indicated the sensitivity of the analysis to mesh size. The shape of the scour hole was very sensitive to the angle of repose. The speed of the scour development was dependent on the empirical parameters in Equation 5.9, which means that it is impossible to tell how well the numerical model predicted the development of the scour hole without resort to confirmation from some sort of physical modelling.

In spite of the above-mentioned reservations, the work carried out by Olsen and his co-workers clearly points the way forward for the numerical computation of local scour.

5.5 Abutments

5.5.1 Introduction

There are a large number of different structures that encroach into the channel flow from one or both sides. Spur dikes are built out from the bank of a river to deflect the main river current away from an erodible bank. Guide banks are built around structures such as road embankments to protect them from erosion (Breusers & Raudkivi, 1991). Bridge crossings are often made shorter by locally reducing the width of the river with the aid of approach embankments and abutments that extend across the floodplain into the main channel. In all cases, groynes, dikes, guide banks and abutments (hereinafter called simply "abutments") are horizontal constrictions in the flow that promote three-dimensional flow patterns in a similar manner to piers (Hoffmans & Verheij, 1997).

There are many different abutment shapes. To simplify analysis, however, it is usual to describe the scour around each abutment shape in terms of the deviation from that measured for a vertical, sharp-edged, "plate" abutment (e.g. Breusers & Raudkivi, 1991; Hoffmans & Verheij, 1997; Raudkivi, 1998). All abutments, of course, have a finite thickness, but a vertical-wall abutment can be regarded as equivalent to a "plate" abutment if the length of the abutment normal to the dominant flow direction, L_a, is at least five times the width of the abutment (Hoffmans & Verheij, 1997).

5.5.2 The flow patterns around a vertical plate abutment

The general flow patterns around a vertical plate abutment are depicted in Figure 5-5. To a degree, the flow pattern around an abutment is similar to the flow around one half of a pier. In both cases there is a bow wave (or roller), an associated downflow, a horizontal vortex near the base, and wake vortices that are shed rhythmically from the side of the structure (c.f. Section 5.4.2).

There are, however, important differences. Piers do not generally reduce the channel flow section to any great degree. Abutments, on the other hand, frequently restrict the horizontal width of the channel by a substantial amount. This results in an increased average flow velocity through the remaining open section, and consequential increase in the possibility of scour in that region. Scour resulting from the reduced width of the flow-section is generally termed "constriction scour", but it can be readily seen that it is a special case of general scour.

Another difference is the "principal" vortex that is the equivalent of the horseshoe vortex in piers. Except in the case of very short abutments, the principal vortex does not generally remain closely attached to the structure, but usually commences from a point somewhat upstream. It lies along the boundary between the fast-moving upstream flow section and the "dead" water trapped in the corner between the abutment and the sidewalls or banks of the channel. Often a secondary, counter-rotating vortex is induced by the principal vortex immediately upstream of it. The flow acceleration into the funnel marked by the principal vortex helps to make this vortex extremely strong and, as a consequence, the maximum scour depth usually occurs immediately upstream of the end of the structure (Hoffmans & Verheij, 1997).

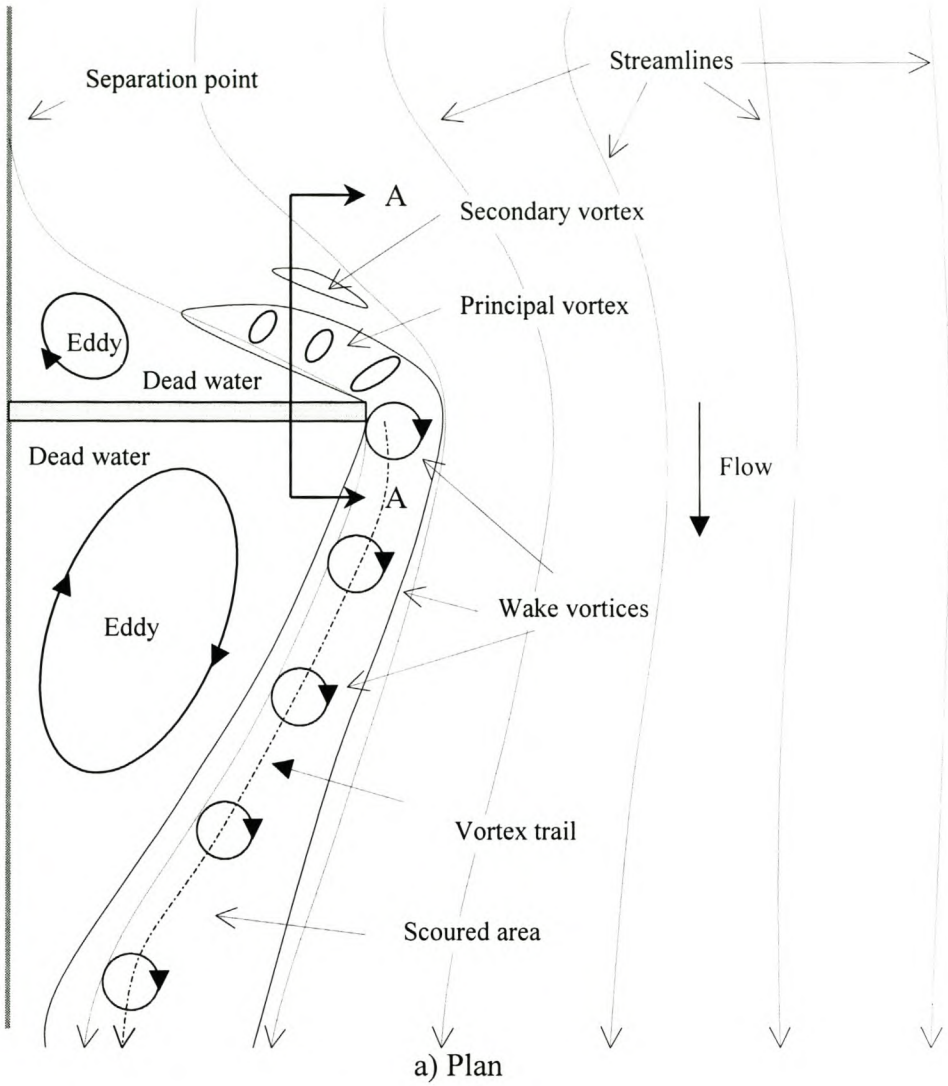

a) Plan

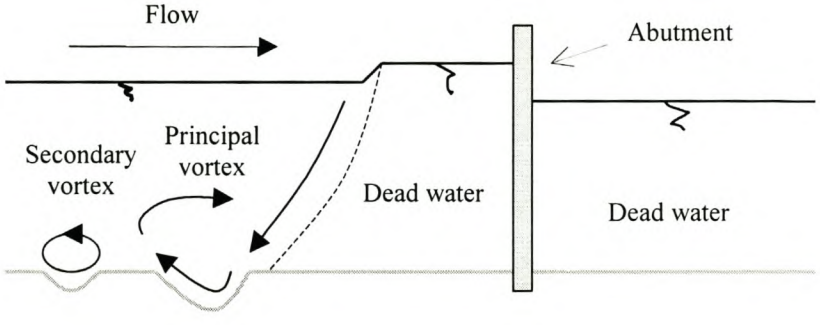

b) Section A-A

Figure 5-5: Flow patterns around an abutment

(After Breusers & Raudkivi, 1991; Hoffmans & Verheij, 1997; Raudkivi 1998)

Downstream of the structure, wake vortices, shed from the end of the abutment, travel along the boundary between the main flow channel and a second "dead" water region before dying out into general turbulence. The flow eventually re-attaches itself to the banks of the channel some way downstream of the structure.

Although the two "dead" water regions are hydraulically separated from the main channel by the principal vortex and the vortex trail respectively, very strong eddies can be induced in them through the shearing along the boundary. Under certain circumstances, these eddies can cause the formation of local scour holes.

In general, the scour hole around the abutment develops in a similar manner to that around a pier (Section 5.4.3), except that there is no sharp-edged groove in the vicinity of the structure.

5.5.3 Factors influencing the depth of the scour hole

Let the shape of the abutment be represented by a parameter *Sh*, its alignment by another parameter *Al*, and the effects of lateral distribution of flow and the cross-sectional shape of the approach channel by a third parameter *G*. Then, according to Melville (1992), the maximum equilibrium scour depth at an abutment can be written as:

$$y_s = f(\rho, \nu, U, Y, \rho_s, d, \sigma_s, L_a, Sh, Al, G, g) \tag{5.10}$$

Assuming constant relative density of the sediment and the absence of viscous effects, dimensional analysis yields:

$$\frac{y_s}{L_a} = f\left(\frac{U^2}{gd}, \frac{Y}{L_a}, \frac{d}{L_a}, \sigma_g, Sh, Al, G\right) \tag{5.11}$$

or,

$$\frac{y_s}{Y} = f\left(\frac{U^2}{gd}, \frac{L_a}{Y}, \frac{d}{L_a}, \sigma_g, Sh, Al, G\right) \tag{5.12}$$

It will be noted that, in the first instance, the scour depth is normalised with the abutment length, whilst in the second instance, it is normalised with the flow depth.

The particle Froude number, U^2/gd, can also be written in terms of the flow intensity, U/U_c. As with piers, the maximum scour depth coincides with $U/U_c = 1.0$. In view of the fact that abutments are usually very long compared with the sediment size, the sediment coarseness seldom plays a meaningful role in the determination of the scour depth. The scour depth is reduced with non-uniform sediments. In abutments other than a thin plate abutment in a rectangular channel, allowance has to be made for the shape, alignment and approach geometry.

Kwan (1988) measured the velocity field around a relatively short (i.e. small L_a/Y ratio) wing-wall abutment. He found that the downflow-associated primary vortex is primarily responsible for the scour hole development – a similar conclusion to that for piers. He also showed that the flow pattern was relatively unaffected by changes in the approach flow depth – again a similar conclusion to that for piers. Other observations were that the primary vortex and downflow are confined predominantly within the scour hole beneath the original bed level, and that the maximum downflow was of the same magnitude regardless of the flow depth. Kwan thus concluded, for short piers, scour depth scales with abutment length (Melville, 1992) and Equation 5.11 is appropriate.

In the case of relatively long abutments, however, Melville (1992) showed that the scour depth scales with the flow depth, and Equation 5.12 is more appropriate. In-between these two extremes, the equilibrium scour depth is affected by both the abutment length and the flow depth.

In the special case of a thin vertical plate abutment projecting at 90° from the bank in a rectangular channel with a uniform sand bed, Melville (1992) gives the maximum equilibrium scour depth as:

$$y_s = 10Y \text{, for } \frac{L_a}{Y} \geq 25 \text{ (“long” abutments)} \tag{5.13}$$

$$y_s = 2\sqrt{YL_a}\text{, for } 1 < \frac{L_a}{Y} < 25 \text{ (“intermediate” abutments)} \tag{5.14}$$

$$y_s = 2L_a\text{, for } \frac{L_a}{Y} \leq 1 \text{ (“short” abutments)} \tag{5.15}$$

Melville (1992) goes on to note that the well-known Laursen equations (Laursen & Toch, 1956; Laursen 1958, 1962, 1963) for the above-mentioned situation can be simplified to:

$$y_s \approx 1.93\sqrt{YL_a} \tag{5.16}$$

The explanation for the relationship between the equilibrium scour depth and the relative length is easily made by analogy with piers. With “short” abutments, with a relatively deep flow depth, the strength of the principal vortex is closely related to the flow section blocked by the structure, i.e. its length. “Long” abutments, on the other hand, have relatively shallow flow depths that result in interference between the surface roller and the horseshoe vortex. Furthermore, part of the flow approaching the abutment is deflected parallel to the upstream abutment face and is therefore ineffective in generating downflow ahead of the abutment. The depth is thus dependent only on the flow depth and is independent of the abutment length (Kandasamy, 1989; Melville, 1997).

In view of the complexity of the flow patterns around abutments, the dimensional approach to the assessment of scour depth has been a very popular one. Apart from Melville (1992, 1995, and 1997), other publications have included Garde et al. (1961), Liu et al. (1961) and Froehlich (1989). Alternatives to the dimensional approach include the regime approach (e.g. Ahmad, 1953), where the scour depth is related to the increased discharge intensity at the abutment, and an analytical or semi-empirical approach (e.g. Laursen, 1963; Gill, 1972; Lim, 1997; Lim & Cheng, 1998).

Lim (1997) provides a typical example of an analytical / semi-empirical approach to the determination of the equilibrium scour depth. At time t = 0, it is assumed that conditions in the approach channel are clear water while those in the vicinity of the

abutment are live-bed owing to the local flow constriction. As the scour develops, the scour hole increases in size until it eventually reaches a maximum at the equilibrium scour condition. At equilibrium, the lateral side slope of the scour hole is at an angle between 22° and 26°, with the maximum depth at the end of the abutment. The entire flow of the main channel blocked by the abutment and reaching to the end of the scour hole is assumed to pass through the gap between the end of the abutment and the end of the scour hole. An assumption concerning the velocity distribution allows the estimation of the shear velocity, that in turn is compared with the Shields criterion for incipient motion. After some manipulation, the following expression is obtained:

$$\frac{y_s}{Y} = 0.9\left\{\theta_c^{-0.375} Fr_o^{0.75}\left(\frac{d_{50}}{Y}\right)^{0.25}\left[0.9\left(\frac{L_a}{Y}\right)^{0.5}+1\right]\right\}-2 \tag{5.17}$$

In this expression, θ_c is the critical Shields parameter (Equation 3.22), and Fr_o is the "densimetric Froude number", given by:

$$Fr_o = \frac{U}{\sqrt{\left(\frac{\rho_s}{\rho}-1\right)gd_{50}}} \tag{5.18}$$

Considering only the maximum clear-water scour condition with a thin plate vertical abutment, Equation 5.16 can be simplified to:

$$y_s = 1.8\sqrt{YL_a} \tag{5.19}$$

It can be seen that Equation 5.19 is similar to Equations 5.14 and 5.16. It should also be noted that all three equations are appropriate for intermediate length abutments only. Fortunately, many abutments fall into this category.

Reference	Scour-depth formula	Remarks
Melville (1997)	$y_s = K_y K_I K_d K_s K_\theta K_G$	K_y, K_I, K_d, K_s, K_θ, K_G = factors for the depth size, flow intensity, sediment size, abutment shape, abutment alignment and channel geometry respectively. See Equations 5.12 – 5.14 inclusive for flat plate abutments.
Laursen (1963)	$\frac{L_a}{Y} = 2.75\frac{y_s}{Y}\left[\left(\frac{y_s}{12Y}+1\right)^{7/6}-1\right]$	For abutments that do not extend over the over-bank region
Liu et al. (1961)	$y_s = 2.15Y\left(\frac{L_a}{Y}\right)^{0.4} Fr^{0.33}$	Increase by 30% for maximum scour depth.
Ahmad (1953)	$y_s = 2K_p K_s K_\alpha K_\eta\left[\frac{q_w}{(1-\Gamma)}\right]^{2/3} - Y$	K_p, K_s, K_α, K_η = factors for the influence of the channel bed, shape of the structure, abutment alignment and porosity respectively. m = L_a/B_c = relative blockage.
Froehlich (1989)	$\frac{y_s}{Y} = 2.27K_I K_2\left(\frac{L_a}{Y}\right)^{0.43} Fr^{0.61}+1$	K_I, K_2 = factors for abutment shape and abutment alignment respectively.
Richardson et al. (1990) (or HEC-18, 1995)	$y_s = 4\mathrm{Y}Fr^{0.33}\frac{K_I}{0.55}$	K_I = factor for abutment shape. For use with long abutments, $L_a/Y > 25$.
Garde et al. (1961)	$y_s = Y\left(\frac{KFr^n}{\alpha}-1\right)$	K = coefficient, n = exponent, $K, n = f(C_D)$, α = opening ratio = $((B-b)/B)$
Dietz (1969)	$y_s = \frac{\omega q_w}{U_c} - Y$	ω = turbulence coefficient. (See Hoffmans & Verheij for guidance on this).

Table 5-2: Commonly used abutment scour depth equations

A large number of equations have been developed for the determination of the maximum equilibrium scour depth around abutments. A most extensive summary is to be found in Przedwojski et al. (1995). Other, shorter, summaries are to be found in Babaeyan-Koopaei (1996), Hoffmans & Verheij (1997), and Raudkivi (1998). A few of the better-known equations are listed in Table 5-2. It will be noted that the upstream Froude number is a popular parameter for the determination of the equilibrium scour depth. An assessment of the relative accuracy of some of the more popular equations is to be found in Hoffmans & Verheij (1997).

It can take a considerable time for a scour hole to reach equilibrium – particularly in the riverine environment where high flows are not generally maintained for long periods. Information on the development of scour with time is to be found in Hoffmans & Verheij (1997).

Scour depths can reach very great depths – particularly when the abutment causes considerable blockage of the river cross-section. Scour depths in excess of 50 m have been observed in the lower Meghna River upstream of Chandpur (Hoffmans & Verheij, 1997).

5.5.4 Computational modelling of local scour around an abutment

There have been many attempts to construct a numerical model for the flow around abutments. Zaghlou & McCorquodale (1973) developed a model capable of simulating the flow around spur-dikes by solving the Helmotz vorticity equation and a Poisson-type equation. The model was not however experimentally verified. More recently, Tingsanchali & Maheswaran (1990) modelled the flow around a groyne using the 2D depth-averaged TEACH model developed by Gosman & Pun (1973) and later modified by Rodi et al. (1981). This utilises a hybrid finite difference scheme and an iterative method to solve the governing equations of flow and turbulence transport. A correction factor was incorporated into the k-ε model to improve the agreement between the computed and experimental data of the velocities and streamline pattern in the vicinity of the groyne tip. A further 3D correction factor helped to improve the prediction of bottom shear stresses. Molls & Chaudhry (1995), using another code that also utilised the 2D depth-averaged equations, obtained similar results for the same problem.

Biglari & Sturm (1998) also used a 2D, depth-averaged, k-ε model – this time for the prediction of the flow around bridge abutments situated in compound channels. Clear water equilibrium maximum scour depths near the upstream corner of the abutment face were then estimated using an empirically determined relationship between the dimensionless scour depth and the excess velocity ratio. Although this method satisfactorily explained the general relationship between measured values of equilibrium scour depth and the different abutment lengths and discharges tested, there were shortcomings. Biglari & Sturm concluded that more work was needed to identify the influence of additional local hydraulic variables that could only be predicted accurately by 3D numerical turbulence models. Additional criticisms are that the method only predicts the maximum equilibrium scour depth, and it is likely that the empirical relationship between the dimensionless scour depth and the excess velocity ratio will change for different abutment arrangements and flow conditions.

Ouillon & Dartus (1997) appear to have been the first to publish work on the 3D modelling of the flow around a groyne. They used a Reynolds solver with the SIMPLE algorithm and the k-ε turbulence model. The porosity method was used to track the free surface. They did not attempt to model scour hole development. Instead, by comparing the computed bed shear stress with the critical bed shear stress for a particular problem that had been previously been the subject of a physical model investigation, Ouillon & Dartus were able to identify potential scour and deposition zones with reasonable accuracy.

It is no surprise that work on the development of a numerical model for the computational of local scour around abutments has lagged behind that for piers. The additional plane of symmetry through the centreline of a circular pier greatly reduces the computational effort required for success.

5.6 Conclusions

It is readily apparent that it is difficult to predict the scour and deposition around structures. Scour profiles are extremely sensitive to a multitude of parameters such as the geometry of the structure, changes in the flow rate, local constrictions, and the presence of bends and confluences etc. Even when the focus is placed solely on structures of simple shape in ideal conditions, there are a large number of formulae

giving widely disparate estimates for something as seemingly easy to measure as the equilibrium scour depth. Almost all of the available formulae are empirical in nature.

In view of the above, there is an increasing move towards the development of numerical models that will compute scour hole formation. One of the best attempts so far is the one developed by Olsen & Kjellesvig (1998) for modelling the development of local scour around a circular pier (Section 5.4.6). The fact that it took nine weeks to simulate the scour hole development clearly demonstrates the limitations placed on this type of research by the speed of the machines currently available. A further restriction was the empirical relationship used for the determination of the sediment concentration at the bed.

There is clearly a need for additional work to be carried out in this field. It could be particularly useful if the model used to predict incipient motion on the channel bed was also suitable for the estimation of sediment transport. The unit stream power model developed by Rooseboom (1992) has the potential to do just this. It could be used in conjunction with a suitable computational fluid dynamics model to predict the sediment movement in any situation. This investigation aimed to show how it could be adapted to predict local scour.

Part 2

The unit stream power model of scour and deposition

Chapter 6
The unit stream power model

6.1 Introduction

This chapter presents the unit stream power model for the prediction of scour and deposition that was developed as part of this investigation. The link between the applied unit stream power and incipient motion is described. An overview of incipient motion was given in Chapter 3. In this chapter the focus is on the link between incipient motion and unit stream power as presented by Rooseboom (1975 and 1992) and his co-workers.

In view of the fact that channel beds are generally warped, a function is developed to correct the incipient motion criteria for bed slope. In the course of this development, the links between the three different approaches to incipient motion are indicated.

It concludes with a theoretical model describing scour and deposition in terms of unit stream power. Deposition is regarded as the opposite to scour with the incipient motion criteria marking the boundary between the two processes. The aim is that this model will form the basis for the development of new software that will eventually be capable of predicting all scour and deposition given the requisite boundary conditions.

This chapter and the next (Chapter 7 on the selection of the criteria for incipient motion) represent the main contributions of this thesis. Incipient motion criteria provide the key in defining the equilibrium scour conditions where the rate of scour equals the rate of deposition.

6.2 The link between applied unit stream power and incipient motion

Table 3-3 presents various criteria for incipient motion based on the shear velocity / settling velocity ratio (hereinafter called Movability Number after Liu, 1957). This velocity ratio varies over the range 0.12 to 2.5 – a very large range. Closer examination, however, suggests that three categories of incipient motion are described or could be inferred:

i) Rolling and / or sliding commences at a very low Movability Number in the order of 0.12 – 0.2.

ii) Saltation (which can be considered as the beginning of suspension) commences at a moderate Movability Number in the order 0.4 – 0.5.

iii) General suspension commences at high Movability numbers above 1.0.

The wide range of values is indicative of the difficulties that are encountered in describing the threshold of movement (see Section 3.6).

For a particle to be lifted out of its place in the bed matrix, the power dissipated on the particle must be, at least momentarily, equal to or greater than the power required to suspend the particle. This implies Equation 3.33:

$$P_t \geq P_r \tag{3.33}$$

On the other hand, less power is required to roll the particle. Assuming that the average unit stream power required to roll a particle is some constant fraction, η, of the power required to suspend it, then:

$$P_t = \eta P_r \tag{6.1}$$

If the Rooseboom expressions are redeveloped with the equality expressed in Equation 6.1, then Equation 3.42 for the laminar boundary case becomes:

$$\frac{u_*}{v_{ss}} = \eta_l^{1/2} \frac{\alpha_1}{\mathrm{Re}_*} \tag{6.2}$$

Here η_l is the "power fraction" for a laminar boundary.

Similarly, Equation 3.49 for the turbulent boundary case becomes:

$$\frac{u_*}{v_{ss}} = \eta_t^{1/3} \alpha_2 \tag{6.3}$$

Here η_t is the power fraction for a turbulent boundary.

With the various assumptions listed in Section 3.8.4, $\alpha_1 \approx 4.9$ and $\alpha_2 \approx 0.69$ for particle suspension from the bed. Assuming further that the Rooseboom (1992) criteria for incipient motion are accurate, this implies that, at this point:

$$4.9\eta_l^{1/2} \approx 1.6 \text{ (laminar boundary)}$$

or,

$$\eta_l \approx 0.11 \approx \frac{1}{9} \tag{6.4}$$

and,

$$0.69\eta_t^{1/3} \approx 0.12 \text{ (turbulent boundary)}$$

or,

$$\eta_t \approx 0.0053 \approx \frac{1}{190} \tag{6.5}$$

A relatively higher unit stream power value is required to roll a particle lying wholly within the viscous sub-layer (laminar boundary condition) compared with one that projects into the log-law layer (turbulent boundary condition). This is to be expected. Velocity fluctuations are severely damped in the viscous layer.

In Sections 3.6 and 3.7, it was mentioned that the movement of particles on the bed is stochastic in nature and there is no defined threshold below which motion cannot take place. In other words, it is necessary to take into account the intensity of motion (or transport intensity). The discrepancies between the different incipient motion criteria given in, inter alia, Table 3.3, thus probably reflect different interpretations of the critical intensity of motion below which movement could be said to have effectively ceased. A different intensity of motion implies a different unit stream power requirement. If, for example, it is assumed that the Raudkivi (1998) criterion for incipient rolling motion ($u_* / v_{ss} \geq 0.17$) applies to a turbulent boundary, the power fraction for rolling on that type of boundary is increased to $\eta_t \approx 0.015 \approx 1/67$. Treating the Julien (1995) criterion for the inception of "suspension" (regarded here as simply incipient motion i.e. rolling) in the same manner ($u_* / v_{ss} \geq 0.2$), increases the power fraction to $\eta_t \approx 0.024 \approx 1/41$.

With all the above-mentioned assumptions, it appears as though, whichever criterion is chosen, some particles will start moving over a turbulent boundary once the average applied unit stream power is 0.5 – 2% of the power required for particle suspension. For a laminar boundary, the minimum average applied unit stream power required for motion increases to about 10% of the power required for particle suspension.

One problem with the above analysis is the fact that the applied unit stream power increases rapidly as the boundary is approached since the velocity gradient increases rapidly in this region (the shear stress also increases, but generally much more gradually). In Section 3.8.4 the applied unit stream power was calculated on a turbulent boundary with $y = d$ in Equation 3.29:

$$P_{t(t)} = \frac{\rho u_*^{\ 3}}{\kappa y} \tag{3.29}$$

In Equation 3.29, the two main variables are $P_{t(t)}$ and y. Assume that rolling commences with suspension (the particle is then "pushed" over neighbouring particles by the drag force that also operates on the particle). In this scenario, $\eta_t = 1.0$ and the average unit stream power resulting in the suspension of the particle is to be found at $y = d/190$, $d/67$ or $d/41$ depending on whether the Rooseboom (1992), Raudkivi (1998) or Julien (1995) criteria are used.

The problem with this alternative approach is that it assumes that the particle is standing in isolation on a flat boundary in a flow that is turbulent right down to this hypothetical boundary. The truth is that the particle is generally sitting within a matrix formed by surrounding particles so the "boundary" is not very well defined. Also, the log-law layer gives way to the transitional layer and the linear layer in the close proximity of the particles making Equation 3.29 invalid in this region. Even if there were no transitional layer or linear layer, the zero point of the log-law layer would not coincide with the hypothetical boundary (see Section 2.3.3). Furthermore, the argument collapses in the case of a laminar boundary as the average applied unit stream power in the linear layer is approximately constant (Equation 3.38).

It is most likely that the critical conditions for incipient motion with respect to unit stream power (at any given intensity of motion) can be described as follows:

i) The average unit stream power causing the initial movement of a particle is to be defined at a position below its highest point.

ii) The instantaneous unit stream power associated with the movement of a particular particle is considerably higher than the average – being associated with a turbulent burst or some other form of coherent flow structure. Even in the case of a laminar boundary, turbulent bursts in the immediate vicinity can temporarily raise the instantaneous unit stream power dissipation within the linear layer.

iii) A particle does not require sufficient applied unit stream power for suspension before it will move. It is likely that the first form of motion will be rolling.

At the present moment, little is known about the actual unit stream power distribution in the vicinity of a particle that is about to commence movement. In view of this, it will simply be assumed that incipient motion on a turbulent boundary occurs at a fixed fraction (η_i) of the average unit stream power at the point $y = d$.

Suspension requires that $\eta \geq 1.0$. This implies, for a turbulent boundary, that $u_* / v_{ss} \geq 0.69$. Bearing in mind that this refers to the average value and that the effective unit stream power operating on a particle could momentarily be much larger, it is easy to understand why particles commence saltation in the range $0.4 < u_* / v_{ss} < 0.5$. Once lifted out of position, however, the unit stream power in the vicinity of the particle rapidly drops (see Figure 3-5) and the particle falls back onto the bed.

General suspension requires $u_* / v_{ss} >> 0.69$, and this is seen to be the case.

6.3 The influence of bed-slope

The sensitivity of the critical drag force – or bed-shear stress – to bed slope is described in Section 3.9. What is now required is the adaptation of Equations 3.51, 3.53 and 3.54 for use with the Movability Number (u_* / v_{ss}) and the critical applied unit stream power. This means that incipient motion must first be defined in physical terms for a horizontal bed. It also means that the Movability Number must be expressed in vector form. Following the approach suggested by Van Rijn (1993), the following assumptions are made (see Figure 6-1):

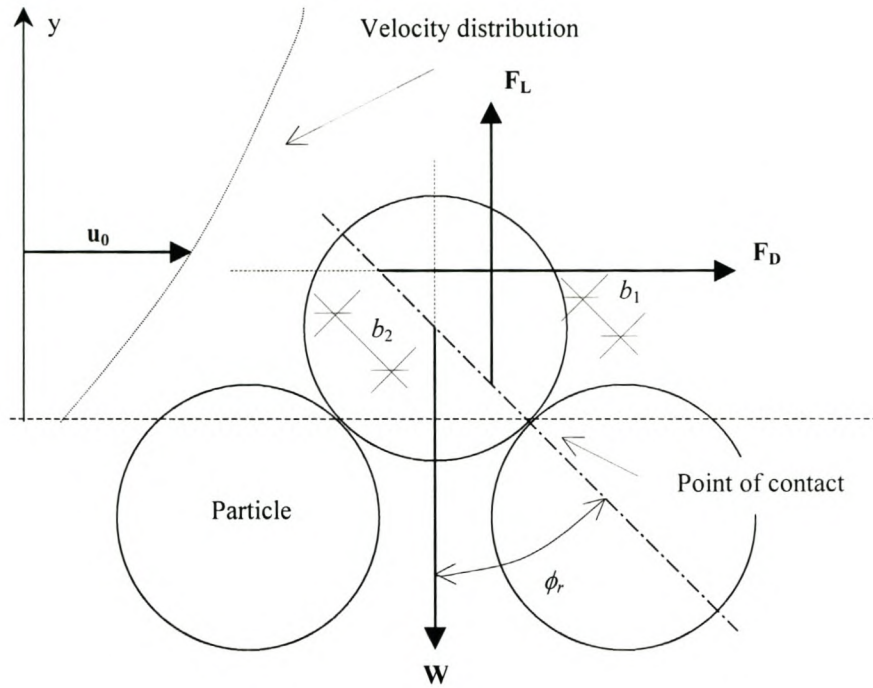

Figure 6-1: The forces on a particle resting on a horizontal bed
(After Van Rijn, 1993)

i) The pivot angle equals the angle of repose, ϕ_r.

ii) The critical particle is almost spherical and thus has a submerged weight of:

$$\mathbf{W} = \frac{a_1 \pi}{6}(\rho_s - \rho)\mathbf{g}d^3 \tag{6.6}$$

The constant a_1 accounts for the variation in the shape of the particle from that of a sphere ($a_1 = 1.0$ for a spherical particle).

iii) The lift force on the critical particle, $\mathbf{F_L}$, is some ratio, a_2, of the drag force, $\mathbf{F_D}$:

$$\mathbf{F_L} = a_2 \mathbf{F_D} \tag{6.7}$$

iv) Following from above and considering Equations 3.15 and 3.16:

$$\mathbf{F_L} = \frac{C_L}{C_D}\mathbf{F_D} \tag{6.8}$$

v) The effective velocity, u_0, acting on the critical particle is some ratio, a_3, of the shear velocity, u_*:

$$\mathbf{u}_0 = a_3\mathbf{u}_* \tag{6.9}$$

vi) The three forces (**W**, $\mathbf{F_D}$ and $\mathbf{F_L}$) act on the particle in the positions and directions shown in Figure 5-6.

The particle will roll when:

$$\mathbf{F_D}\left(\frac{d}{2} + b_2\right)\cos\phi_r + \mathbf{F_L}b_1\sin\phi_r = \mathbf{W}\frac{d}{2}\sin\phi_r$$

$$\left[\left(\frac{d}{2} + b_2\right)\cos\phi_r + \frac{C_L}{C_D}b_1\sin\phi_r\right]\mathbf{F_D} = \mathbf{W}\frac{d}{2}\sin\phi_r$$

Since b_1 and b_2 are both fractions of $d/2$, whilst $\sin\phi_r$ and $\cos\phi_r$ are constants, the whole of the expression contained within the square brackets can be expressed as some ratio, $1/a_4$, of $d.\cos\phi_r/2$ giving:

$$\frac{1}{a_4}\frac{d}{2}\cos\phi_r.\mathbf{F_D} = \mathbf{W}\frac{d}{2}\sin\phi_r$$

Hence,

$$\mathbf{F_D} = a_4\mathbf{W}\tan\phi_r \tag{6.10}$$

According to Van Rijn (1993), White (1940) was the first to present this result.

Now, from Equation 3.15:

$$\mathbf{F_D} = C_D a_p \frac{\rho \mathbf{u_0}^2}{2} \tag{3.15}$$

Hence,

$$\mathbf{F_D} = C_D \frac{\pi d^2}{4} \frac{\rho}{2} a_3^{\,2} \mathbf{u_*}^2 \tag{6.11}$$

Combining Equations 6.10, 6.6 and 6.11:

$$\mathbf{u_*}^2 = \frac{a_1 a_4}{a_3^{\,2}} \tan\phi_r \left[\frac{4}{3} \frac{(\rho_s - \rho)}{\rho} \frac{\mathbf{g} d}{C_D} \right] \tag{6.12}$$

Examination of Equation 3.8, however, reveals that the expression in square brackets represents $v_{ss}^{\,2}$, therefore:

$$\frac{u_*}{v_{ss}} = \frac{\sqrt{a_1 a_4 \tan\phi_r}}{a_3} = \text{constant} \tag{6.13}$$

The expression for shear velocity, u_*, is not bolded in Equation 6.13 because the Movability Number, u_* / v_{ss}, does not generally take the directions of the two velocity vectors, $\mathbf{u_*}$ and $\mathbf{v_{ss}}$ into account.

According to Section 3.8.4, incipient motion over a turbulent boundary for a given intensity of motion is governed by Equation 3.49:

$$\frac{u_*}{v_{ss}} = \alpha_2 \tag{3.49}$$

It is immediately apparent that Equation 6.13 is identical to Equation 3.49 with the constant equal to α_2, i.e.:

$$\alpha_2 = \frac{\sqrt{a_1 a_4 \tan \phi}_r}{a_3} \tag{6.14}$$

In the case of laminar boundaries, Section 3.8.4 indicates that incipient motion for a given intensity of motion is governed by Equation 3.42:

$$\frac{u_*}{v_{ss}} = \frac{\alpha_1}{Re_*} \tag{3.42}$$

It is convenient at this point to assume that, by extension, the constant α_1 can be expressed as:

$$\alpha_1 = \frac{\sqrt{a_1 a_4 \tan \phi_r}}{a_3} Re_* \tag{6.15}$$

If the Movability Number, u_* / v_{ss}, is expressed as a vector, $\mathbf{u}_* / \mathbf{v}_{ss}$, having the same direction as that of the shear velocity, a comparison of Equations 3.15, 6.9, 6.12, and 6.13 indicates that the Mobility Number varies with the drag force, $\mathbf{F_D}$, in the following manner:

$$\frac{\mathbf{u}_*}{\mathbf{v}_{ss}} \alpha \sqrt{\mathbf{F}_D} \tag{6.16}$$

If this is the case then the variation of the velocity ratio with a longitudinal bed slope, β, and transverse bed slope, γ, with respect to the direction of the shear velocity vector, $\mathbf{u}_*$, is (c.f. Equation 3.54):

$$\left.\frac{\mathbf{u}_*}{\mathbf{v}_{ss}}\right|_{\beta,\gamma} = \psi \left.\frac{\mathbf{u}_*}{\mathbf{v}_{ss}}\right|_{0} \tag{6.17}$$

with (from Equations 3.50 and 3.52):

$$\psi = \sqrt{k_\beta k_\gamma} = \sqrt{\cos\beta\left(1-\frac{\tan\beta}{\tan\phi_r}\right)\cos\gamma\left(1-\frac{\tan^2\gamma}{\tan^2\phi_r}\right)}^{1/2} \tag{6.18}$$

The subscript 0 here refers to a horizontal bed.

Equation 6.18 is similar to the expression for the critical velocity presented in Chiew & Parker (1994) for a longitudinal slope only.

Comparison of Equations 6.1, 6.2, 6.3 and 6.17 indicates that the slope correction factor, ψ, can be used with the unit stream power equations for turbulent and laminar boundaries in the following manner:

$$P_t = \psi^2 \eta_l P_r \quad \text{(Laminar boundaries)} \tag{6.19}$$

$$P_t = \psi^3 \eta_t P_r \quad \text{(Turbulent boundaries)} \tag{6.20}$$

The main drawback with using unit stream power directly in this application is that unit stream power is a scalar quantity, but the calculation of the longitudinal and transverse slopes demands a vector describing the direction of flow. As with the Movability Number, this can be achieved through the use of the shear force vector, $\mathbf{u}_*$. Alternatively, in view of the fact that the Movability Number can be related to the unit stream power and vice verse, the Movability Number can be used as a stand in for unit stream power (c.f. Rooseboom, 1992). This was the course that was followed in this investigation.

If critical bed shear stress is being used as the criterion, then from Equation 3.51:

$$\tau_{0,cr} = \psi^{1/2} \tau_{0,cr,0} \tag{6.21}$$

The value of $\tau_{0,cr,0}$ would be determined from Shields' diagram (e.g. Figure 3-4).

Comparison of Equations 6.17 and 6.21 indicates the nature of the difference between the Movability Number and bed shear stress approaches to incipient motion. The bed shear stress is effectively a measure of the drag force on the particle. The drag force meanwhile is proportional to, inter alia, the square of the effective velocity. The effective velocity is proportional to the shear velocity. Hence, the critical Movability number may be related to the square of the critical bed shear stress as was demonstrated by Egiazaroff (1957, 1965) (in Vanoni, 1975):

$$\theta_c = \frac{4}{3C_D}\left(\frac{u_*}{v_{ss}}\right)^2 \tag{6.22}$$

In the above equation, θ_c is the critical Shields parameter, and C_D is the coefficient of drag on a single particle.

6.4 The unit stream power model for the prediction of scour and deposition

One of the aims of this thesis was to extend the unit stream power model developed by Rooseboom (1992) and others to the point where it could ultimately be used for the prediction of scour and deposition. This model has the advantage that it accounts for sediment transport and is also readily adaptable for numerical solution. It is appropriate at this juncture to put forward the proposed mechanism of scour and deposition that formed the basis of the remainder of the investigation:

i) The sediment transport through a hydraulic structure is determined mainly by the upstream and downstream conditions i.e. the supply and removal of sediment respectively. If the supply rate of sediment to the region around a structure exceeds the removal rate there is accretion at the structure. If the

removal rate exceeds the supply rate there will be degradation. Sometimes, potential degradation in the vicinity of the structure is prevented by local conditions e.g. the structure may be founded on a rigid base.

ii) In general, erosion and deposition around the structure will reach equilibrium at the point where the applied unit stream power, P_t, equals the power required for incipient motion. The applied unit stream power is defined as the dissipation function, Φ. The threshold for incipient motion depends on, inter alia, the size, shape, uniformity, density, settling velocity, cohesiveness and the angle of repose of the sediment. It depends on the hydraulic characteristics of the bed (laminar, transitional, rough) and the bed-slope. Incipient motion is also stochastic in nature i.e. certain particles at random will commence movement before there is general movement of the bed. There is no clear line demarcating the commencement of movement, and as a consequence, the critical intensity of motion has to be defined before the incipient motion parameters can be determined. This will be discussed further in Chapter 7. With cohesionless sediments, the angle of repose of the sediment is generally the limiting slope of the bed (the exception being an adverse slope).

iii) Sediment motion generally commences with rolling at the point $P_t = \eta P_r$, where η is some fraction between 0 and 1. This fraction tends to be much larger for laminar boundaries ($\eta_l \approx 0.1$ or 10%) than for turbulent boundaries ($\eta_t \approx 0.01$ or 1%). If the bed is not horizontal, then the unit stream power requirement for incipient motion must be multiplied by a factor (ψ) to account for the longitudinal (β) and transverse (γ) slopes respectively.

iv) If the applied unit stream power at the bed is greater than that required for incipient motion, there will be scour. If the unit stream power at the bed is less than that required for incipient motion, but the stream is conveying sediment, there will be deposition. This implies that deposition is the exact opposite of scour with the border between the two being defined by the incipient motion criteria (laminar or turbulent). This is not a view that is held by all researchers. For example, Hjulström (1935) divided his plot of average velocity versus grain size into erosion, transportation and sedimentation zones. Midgley (2000) and Mitchell (2000), however, carried out experiments as part of this investigation (Chapter 9). The experiments indicated that there was no significant difference

between the scour zones formed by scouring pre-existent sand compared with the scour zones defined by the absence of deposition of sand sprinkled into the flow slightly higher upstream. Once again, attention should be paid to the fact that there is no clear distinction between erosion and deposition. It is difficult to determine at exactly what point there is sufficient motion at the bed for scouring to take place and deposition to cease, i.e. even in the case of clear-water scour, there is a flow zone where there is both scouring and deposition.

In view of the complex nature of the flow patterns around engineering structures (Chapter 5), computational fluid dynamic (CFD) software was used for the analyses carried out in this investigation. The unit stream power dissipation within the flow field, and the Movability Number on the boundaries were computed for various scour situations measured in the laboratory (Chapters 8 & 9). This showed the potential that the above-mentioned model has for the prediction of scour and deposition.

6.5 Conclusions

This chapter shows that incipient motion – here defined as the nominal boundary between scour and deposition – may be expressed in terms of a fixed fraction of the applied unit stream power for a given intensity of motion. It may also be expressed in terms of the Movability Number. Examination of the laboratory data gathered by various researchers indicates that a particle situated on a laminar boundary will move when it is subjected to an applied stream power value of approximately 10% of the unit stream power value required for suspension. If the particle is situated on a turbulent boundary, the applied stream power requirement drops to approximately 1% of the unit stream power required for suspension. This discrepancy is as a consequence of the different nature of the linear boundary layer compared with the log-law layer.

The boundary between scour and deposition conditions is somewhat blurred owing to the fact that incipient motion is a stochastic process. As the Movability Number / applied unit stream power / bed shear stress increases so does the probability of movement – until such time there is general movement.

A slope correction factor has been derived that will correct the critical conditions for incipient motion for bed-slopes (both longitudinal and transverse). This slope correction factor can be used with all three measures of incipient motion.

A unit stream power model for the prediction of scour and deposition has also been derived. CFD software is required for the computation of the flow parameters in view of the complex nature of the flow around structures situated in open channel flow.

Chapter 7
Selection of the criterion for incipient motion

7.1 Introduction

Chapter 3 provided an overview of incipient motion. It was noted in that chapter that there is no clearly defined lower limit for motion – the probability of movement simply reduces to an insignificant level once the flow parameters decrease below some minimum. Three flow parameters are commonly linked to incipient motion: velocity, bed shear stress, and stream power. A comparison of the implications of the three flow parameters indicated that the ratio of the shear velocity to the settling velocity (u_* / v_{ss}), called the Movability Number in this investigation, is a good indicator of incipient motion.

Table 3-3 reveals that different researchers have determined different incipient motion criteria based on the use of the Movability Number. Whilst considerable work has been carried out by various researchers into establishing the relationship between the bed shear stress and the intensity of motion / probability of movement (Shvidchenko & Pender, 2000a & 2000b), nothing equivalent appears to be available for the critical Movability Number. It is important to know this relationship for design purposes.

The probability of movement of any single particle can be directly linked to the intensity of motion – the simultaneous movement of a given number of particles over a given area of bed. In Section 3.6, the intensity of motion was described both visually (Kramer, 1935), and numerically (Shvidchenko & Pender, 2000a & 2000b). The Shvidchenko & Pender definition is given by Equation 3.19:

$$I = \frac{m}{Nt} \tag{3.19}$$

Here I is the intensity of motion (s^{-1}), m is the number of particle displacements during a time interval t, and N is the total number of surface particles under observation.

This chapter attempts to answer four questions:

i) What is the link between the Movability Number and the intensity of motion?

ii) How can the rate of scour be calculated from the Movability Number?

iii) For the purposes of the numerical model (to be described in Chapters 8 & 9), what is a suitable intensity of motion and associated Movability Number that would describe the point at which scouring effectively commences?

iv) What are the associated values of α_1 and α_2 in Equations 3.42 and 3.49?

Shvidchenko & Pender (2001) provided the author with 529 measurements of sediment transport over turbulent boundaries made by eight researchers including themselves. The Movability Number and the intensity of motion were calculated for each data point. Corrections had to be made to the data to account for the effects of the flume sidewalls, the bed slope and the relative roughness. A curve was then fitted through the adjusted data linking Movability Number to intensity of motion thereby providing an answer to the first question. The equation of this curve was then rearranged so as to provide a new bedload transportation equation that offers a method of calculating the rate of scour and thereby answering the second question. This work includes some of the most significant findings of this thesis. It is described in Section 7.2

Experimental measurements were made in the laboratory of the incipient motion of different sized particles representing laminar and transitional boundaries. The intensity of motion could not be measured with the available equipment so the effective commencement of scouring was determined through visual observation and personal judgement. The Movability Number and the particle Reynolds Number were calculated for each data point after applying sidewall and bed slope corrections. The values of α_1 and α_2 in Equations 3.42 and 3.49 were then adjusted so that the two equations described the lower limit of the data in the transitional zone. Equation 3.49 then allowed an intensity of motion to be assigned to the effective commencement of scouring. This provided answers to the third and fourth questions. The work is described in Sections 7.3 and 7.4.

The main conclusions to this chapter are contained in Section 7.5.

7.2 The turbulent boundary data

7.2.1 Introduction

Measurements of sediment transport over turbulent boundaries made by eight different researchers was used to try and establish the links between the Movability Number and the intensity of motion, and the Movability Number and the rate of scour. The data was that used by Shvidchenko & Pender (2000) and was kindly supplied to the author by them (Shvidchenko & Pender, 2001).

In Section 2.3.4, a turbulent boundary layer, with sand as the boundary material, was defined as having a roughness Reynolds Number, Re_s, of greater than 70, where Re_s is defined by Equation 2.21:

$$Re_s = \frac{u_* k_s}{\nu} \tag{2.21}$$

Bed-forms will not be considered in this investigation. Following general convention, the height of the roughness elements, k_s, will be set equal to the particle diameter, d. Under these circumstances, the roughness Reynolds Number is identical to the particle Reynolds Number, Re_*, defined by Equation 3.18:

$$Re_* = \frac{u_* d}{\nu} \tag{3.18}$$

7.2.2 Data

The data, which may be found in full in Appendix A, included both experimental measurements made by Shvidchenko & Pender (2001) as well as data collected by them from other sources. A summary of the data is presented in Table 7-1:

Source	d (mm)	B_f (mm)	Y (mm)	S_0 (m/m)	Fr
Shvidchenko & Pender (2000)	1.5 – 12.0	300	6 – 136	0.0019 – 0.0287	0.17 – 1.18
Casey (1936)	2.46	400	27 – 219	0.0012 – 0.0051	0.42 – 0.89
Bogardi & Yen (1939)	6.85	300 & 823	40 – 74	0.0141 – 0.0148	0.96 – 1.23
Ho (1939)	6.01	400	109 – 174	0.0034 – 0.005	0.64 – 0.83
Paintal (1971)	2.5, 7.95 & 22.2	914	29 – 203	0.0012 – 0.0096	0.43 – 1.10
Ikeda (1983)	6.5	4000	135 – 313	0.0024 – 0.0054	0.78 – 1.09
Bathurst et al. (1984)	11.5, 22.2 & 44.3	600	44 – 254	0.005 – 0.07	0.79 – 2.21
Graf & Suszka (1987)	12.2 & 23.5	600	94 – 245	0.005 – 0.025	0.77 – 1.26

Table 7-1: Summary of sediment transport data for turbulent boundaries
(After Shvidchenko & Pender, 2000a & 2000b)

In Table 7-1, d is the median sand diameter, B_f is the width of the flume, Y is the depth, and S_0 the bed slope. The sediment was gravel that could be considered reasonably uniform in each instance. The particle Reynolds Number, Re_*, was high, averaging about 1100 and never dropping below 36. The boundary can thus be considered as completely turbulent over the entire data range. In all, there were 529 data points of which those obtained by Shvidchenko & Pender (2000a & 2000b) made up 56% (297).

7.2.3 Sidewall correction

Since all of the data was obtained from laboratory flumes, a correction was required to remove the influence of the sidewalls. The method that was adopted was the one followed by Shvidchenko & Pender (2000a & 2000b).

The Manning roughness coefficient of the glass sidewalls, n_w, was assumed to be 0.010. The Strickler (1923) relationship was used to estimate the Manning roughness coefficient of the gravel bed, n_b (with d in metres):

$$n_b = 0.048 d^{1/6} \tag{7.1}$$

The Manning roughness coefficient of the combined bed and sidewalls was then estimated from:

$$n = \frac{\left(B n_b^{3/2} + 2Y n_w^{3/2}\right)^{2/3}}{P^{2/3}} \tag{7.2}$$

Here P is the total wetted perimeter:

$$P = B + 2Y \tag{7.3}$$

The effective hydraulic radius operating on the bed, R_b, was then determined from:

$$R_b = R\left(\frac{n_b}{n}\right)^{3/2} \tag{7.4}$$

Here, R is the actual hydraulic radius given by:

$$R = \frac{BY}{(B + 2Y)} \tag{7.5}$$

The shear stress at the bed, τ_0, is then given by a modified version of Equation 2.12 with R_b substituted for D, and the friction slope, S_f, substituted for the bed slope, S_0 (uniform flow):

$$\tau_0 = \rho g R_b S_f \tag{7.6}$$

7.2.4 Conversion to Movability Number

Once the values of bed shear stress, τ_b, had been obtained, these were converted to shear velocity, u_*, using Equation 2.13 with τ_b substituted for τ_0:

$$u_* = \sqrt{\frac{\tau_0}{\rho}} \tag{7.7}$$

The Cheng (1997) equation (Equation 3.12) was used to determine the settling velocity, v_{ss}, of the sediment:

$$v_{ss} = \frac{\nu\left(\sqrt{25 + 1.2d_*^2} - 5\right)^{1.5}}{d} \tag{3.12}$$

Here, the dimensionless particle size, d_*, is given by Equation 3.11:

$$d_* = \left(\frac{\Delta g}{\nu^2}\right)^{1/3} d \tag{3.11}$$

The relative submerged density, Δ, is given by Equation 3.10:

$$\Delta = \frac{(\rho_s - \rho)}{\rho} \tag{3.10}$$

The kinematic viscosity, ν, is estimated by the Yang (1996) formulation:

$$\nu = \frac{1.79 \times 10^{-6}}{(1.0 + 0.0337T + 0.000221T^2)} \tag{2.4}$$

Adjustment needs to be made for the bed slope. This is carried out with the aid of Equation 6.18:

$$\psi = \sqrt{\cos\beta\left(1-\frac{\tan\beta}{\tan\phi_r}\right)\cos\gamma\left(1-\frac{\tan^2\gamma}{\tan^2\phi_r}\right)}^{1/2} \tag{6.18}$$

In this equation, β is the longitudinal slope, γ is the transverse slope, and ϕ_r is the angle of repose. Here, γ is zero (no transverse slope). The angle of repose, ϕ_r, depends on the particle size and its angularity (Table 3-2). A curve was fitted to the mean values of each of the two sets of angles quoted in Table 3-2 for rounded and angular particles respectively (taken to the nearest whole number) for particle sizes between 1 and 50 mm:

$$\phi_r = 32.4d^{0.047} \tag{7.8}$$

In Equation 7.8, d is in mm and ϕ_r is in degrees.

The effective flat bed Movability Number may then be determined as:

$$\left.\frac{u_*}{v_{ss}}\right|_b = \frac{1}{\psi}\left.\frac{u_*}{v_{ss}}\right|_{\text{calculated}} \tag{7.9}$$

7.2.5 Estimation of the intensity of motion

Shvidchenko & Pender (2000a & 2000b) not only counted the number of particle displacements during a given time interval, they also measured the sediment transport rate per unit width along the bed, q_b, associated with the intensity of motion. This was then expressed in terms of the dimensionless bedload parameter:

$$q_b^* = \frac{q_b}{\rho_s\sqrt{(s-1)gd^3}} \tag{7.10}$$

Here, s is the "relative density" given by:

$$s = \frac{\rho_s}{\rho} \tag{7.11}$$

The Shvidchenko & Pender (2000a & 2000b) data showed that:

$$I = q_b^* \tag{7.12}$$

This equality allows any measured bedload transport rate to be expressed in terms of the intensity of sediment motion. It means that the data collected by the other researchers and measured in terms of unit sediment transport rate can also be included in the data set for this exercise.

It should be noted that Equation 7.12 is not dimensionally homogeneous (I generally has the units s^{-1} whilst q_b^* is dimensionless). The intensity of motion, I, can also, however, be understood as the probability that a particle in a bed area of length equal to the average length of displacement of a grain after detachment and unit width will start moving in any given second (Shvidchenko & Pender, 2000a).

7.2.6 Correction for relative roughness

At this point, an analysis of the complete data set showed that there was a general relationship between the intensity of motion and the Movability Number, but there was also considerable scatter (Figure 7-1). Furthermore, it seemed as though the Movability Number appears to increase slightly with increasing bed-slope. Shvidchenko & Pender (2000a) noted that the bed shear stress (which is related to the Movability Number) also appeared to increase with bed-slope. An increase in bed-slope (bearing in mind that a positive bed-slope is defined as a slope that falls in the direction of flow) should however lead to a decrease in the critical bed shear stress, not vice versa. The reason for the discrepancy is that all of the data comes from experiments carried out in laboratory flumes. In consequence, the water depths in the various experiments all tend to decrease with increasing slope, giving rise to an increasing "relative roughness" – sometimes to as much as $d / Y = 0.5$ where d is the median diameter of the particle and Y is the average depth. Correction had therefore to be made for relative roughness.

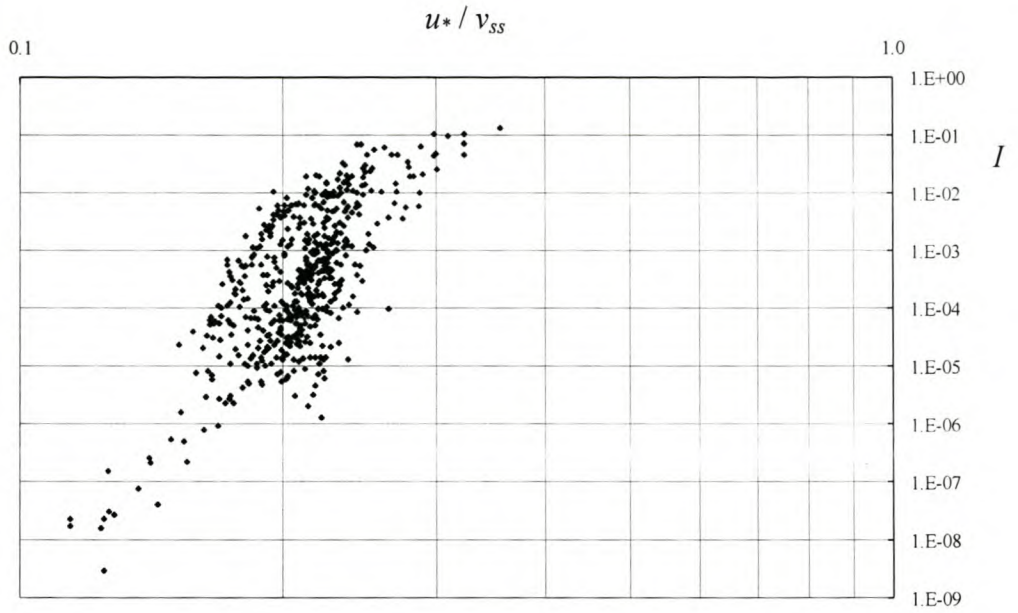

Figure 7-1: Intensity of motion versus Movability Number prior to correction for relative roughness (Log scales on both axes)

The correction for relative roughness was made as follows:

i) The following whole-number intensities of motion were selected: $I = 10^{-2}$, 10^{-3}, 10^{-4}, 10^{-5}, 10^{-6}, 10^{-7}, 10^{-8} s^{-1}.

ii) Data with intensity of motion between 0.3 and 3 times a particular whole number selected from the list given in i) above was deemed to have that whole number intensity of motion. The values 0.3 and 3 were selected because they roughly represent the median point between two whole numbers on a logarithmic (Base 10) scale.

iii) The data associated with each intensity level was then plotted on a graph of Movability Number versus relative roughness (e.g. Figure 7-2). A straight line was fitted through the data and extrapolated to zero relative roughness. A few high outliers (generally with $d / Y > 0.3$) were eliminated as they tended to distort the data.

iv) The extrapolated values of the Movability Number (zero relative roughness) were then plotted against the intensity of motion (Figure 7-3).

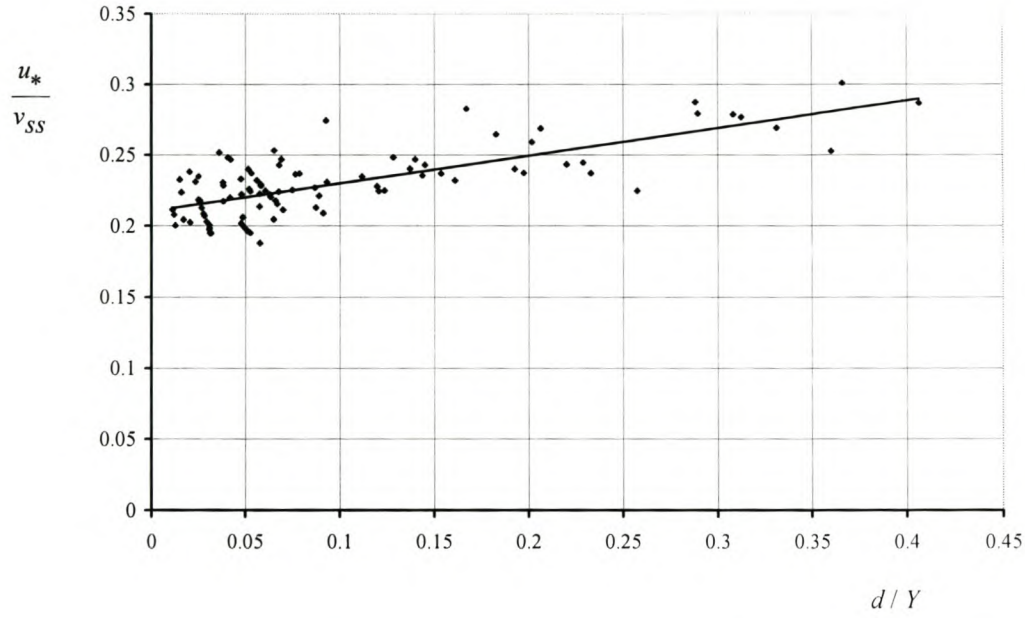

Figure 7.2: Example of a plot of Movability Number versus relative roughness ($I = 10^{-2}$ s^{-1})

I (s^{-1})	Data points	Gradient	Intercept	R^2
10^{-8}	5	-0.0003	0.1208	-
10^{-7}	6	0.0855	0.1331	0.0917
10^{-6}	12	0.3112	0.1438	0.4767
10^{-5}	79	0.2256	0.1696	0.6116
10^{-4}	140	0.1980	0.1814	0.4365
10^{-3}	142	0.2041	0.1924	0.4472
10^{-2}	99	0.1948	0.2106	0.5502

Table 7-2: The relationship between relative roughness and Movability Number for different intensities of motion

Table 7-2 gives the gradient and intercept of the straight-line relationship linking the relative roughness to the velocity ratio for different intensities of motion. The equation reads:

$$\left.\frac{u_*}{v_{ss}}\right|_{I,\beta=\gamma=0} = \text{Gradient}\left(\frac{d}{Y}\right) + \text{Intercept} \tag{7.13}$$

It can be seen from Table 7-2 that there was considerable scatter of the data, particularly with low intensities of motion. The mean gradient for the four highest intensities ($I = 10^{-5}$ to 10^{-2}) is 0.204.

The reason for the increased velocity ratio requirement with high relative roughness is easy to explain with reference to the applied power equation for unidirectional flow (Equation 3.36):

$$P_t = \tau_{yx}\frac{du}{dy} \tag{3.25}$$

The shear stress, τ_{yx}, decreases approximately linearly from the bed to the surface. The velocity gradient, du / dy is inversely proportional to distance from the bed. In consequence, the applied power decreases very rapidly away from the bed in accordance with Figure 3-5. For a bed with a large relative roughness, d / Y, the effective applied power value will be reached at some point above the theoretical bed. The theoretical applied power at the bed will thus be much larger than the effective applied power at the time where the particle begins to move.

7.2.7 New intensity of motion equation

A plot of the intercept values from Table 7-2 versus the intensity of motion gives the relationship between the Movability Number and intensity of motion for a flat bed with zero relative roughness (i.e. deep water). These values appear to fall on a straight line with semi-logarithmic axes (Figure 7-3):

The equation of the line fitted to the data points ($R^2 = 0.9893$) is:

$$\frac{u_*}{v_{ss}} = 0.0066\ln(I) + 0.2405 \tag{7.14}$$

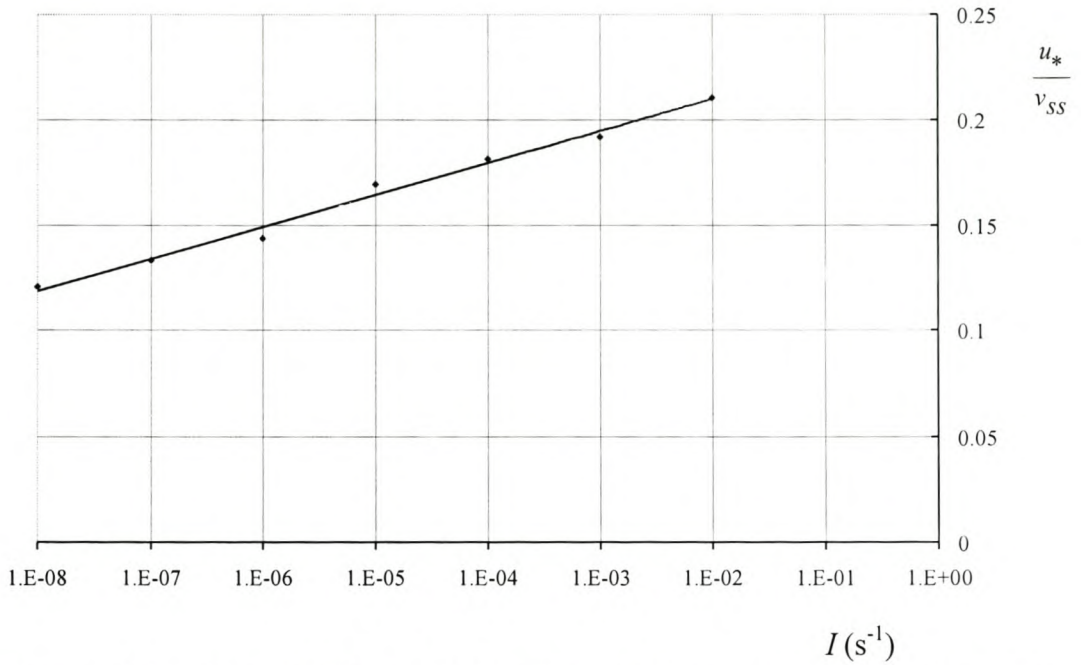

Figure 7-3: Variation of Movability Number with intensity of motion for a flat turbulent bed and zero relative roughness (Semi-logarithmic plot)

This equation can be compared with the data set after the latter has been adjusted for slope and relative roughness as follows:

$$\left.\frac{u_*}{v_{ss}}\right|_{\frac{d}{Y}=\beta=\gamma=0} = \frac{1}{\psi}\left.\frac{u_*}{v_{ss}}\right|_{\text{measured}} - 0.204\left.\frac{d}{Y}\right|_{\text{measured}} \tag{7.15}$$

This is presented as Figure 7.4.

It will be noted from Figure 7-4 that there is still considerable scatter – particularly at the low intensities of motion where there was little data, and accurate data was probably difficult to obtain. The scatter could have been reduced a little by using the relative roughness gradient associated with a particular intensity of motion, instead of using the average gradient for the complete data set.

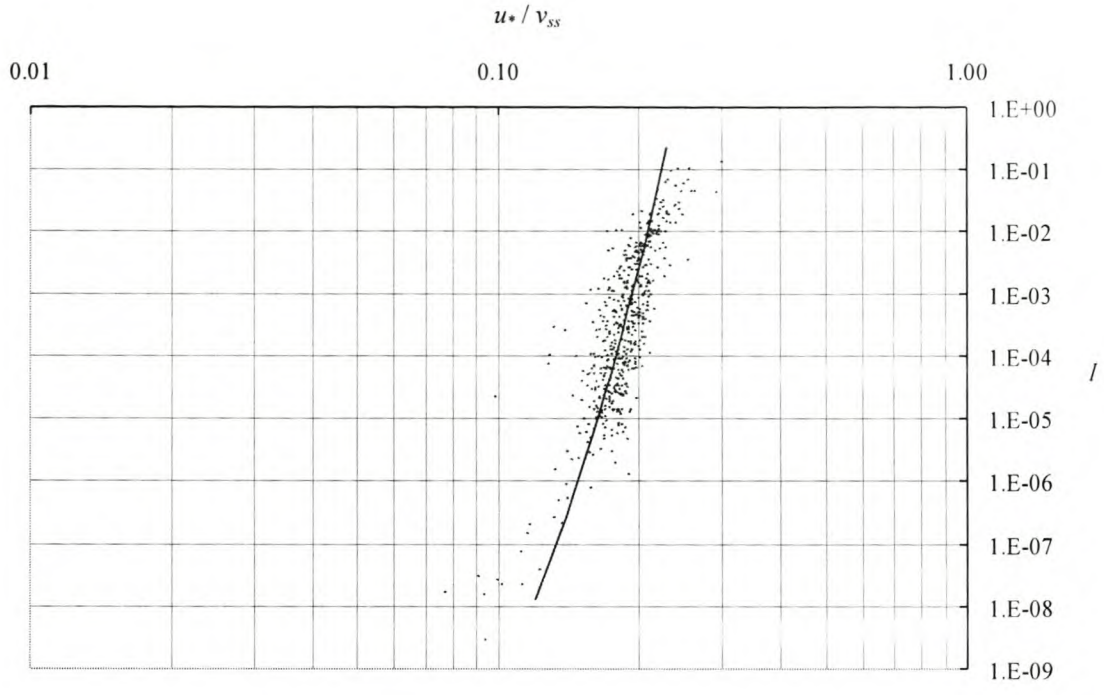

Figure 7-4: Comparison of new intensity of motion equation for turbulent boundaries with adjusted data set

Shvidchenko & Pender (2000a & 2000b) noted that the critical bed shear stress appeared to decrease with the particle Reynolds Number, Re_*, for large values of Re_*. This is contrary to the currently accepted view that the critical bed shear stress is constant for rough turbulent flow. To check this, the Movability Numbers of the data were adjusted in accordance with Equation 7.15 and the resulting values divided by the theoretical Movability Number for a flat bed and zero relative roughness (Equation 7.14) to give a new ratio, r. Perfect agreement would result in $r = 1.00$. These values were then plotted against Re_* to give Figure 7-5:

Figure 7-5 serves two purposes:

i) It shows that the Movability Number associated with a particular intensity of motion appears on a turbulent boundary seems to stay reasonably constant with the Particle Reynolds Number for turbulent boundaries. This is in accordance with the conventional presentations of the Liu (1957) diagram.

ii) It shows that the new intensity of motion equation (Equation 7.14), once adjusted for bed-slope and relative roughness (Equation 7.15), is a good

predictor of the critical Movability Number for a wide range of intensities of motion. The error appears to be less than about 20%.

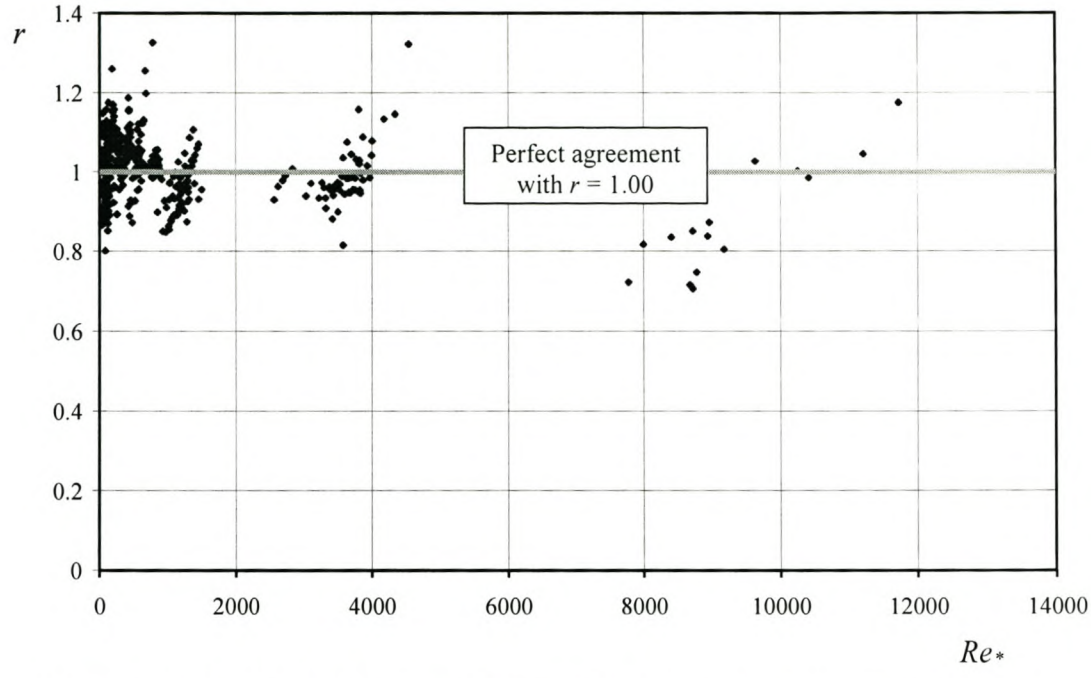

Figure 7-5: Ratio of the adjusted Movability Number to the theoretical Movability Number versus the particle Reynolds Number

The final equation for intensity of motion can now be written as follows:

$$\frac{u_*}{v_{ss}} = \psi\left(0.2405 + 0.0066\ln(I) + 0.204\frac{d}{Y}\right) \tag{7.16}$$

With ψ given by Equation 6.18:

$$\psi = \sqrt{\cos\beta\left(1-\frac{\tan\beta}{\tan\phi_r}\right)\cos\gamma\left(1-\frac{\tan^2\gamma}{\tan^2\phi_r}\right)}^{1/2} \tag{6.18}$$

All symbols having their usual meanings.

7.2.8 New bedload transportation equation

There is a corollary to the above. Shvidchenko & Pender (2000) showed that $I = q_b^*$ (Equation 7.12). Equation 7.16 may therefore be rewritten:

$$\frac{u_*}{v_{ss}} = \psi\left(0.2405 + 0.0066\ln\left(q_b^*\right) + 0.204\frac{d}{Y}\right) \tag{7.17}$$

Rearrangement of Equation 7.16 to make q_b^* the subject yields:

$$q_b^* = e^{\xi} \tag{7.18}$$

The exponent, ξ, is given by:

$$\xi = \frac{1}{\psi}\frac{u_*}{v_{ss}} - 0.204\frac{d}{Y} - 0.2405 \tag{7.19}$$

In Equation 7.19, u_* and v_{ss} may be estimated from Equations 2.13 and 3.12 respectively:

$$u_* = \sqrt{\frac{\tau_0}{\rho}} \approx \sqrt{gDS_0} \tag{2.13}$$

$$v_{ss} = \frac{\nu\left(\sqrt{25 + 1.2d_*^2} - 5\right)^{1.5}}{d} \tag{3.12}$$

The unit bedload transport rate, q_b, may then be determined from:

$$q_b = \rho_s\sqrt{(s-1)gd^3}\,e^{\xi} \tag{7.20}$$

Equation 7.20 offers a method of calculating the rate of scour with the sediment moving in the direction of the fluid flow. Along any particular streamline, the overall rate would be limited by the minimum unit bedload transport rate. Scour or deposition would then have to take place to satisfy conservation of sediment mass. Such an analysis was not however attempted in this investigation.

Equation 7.20 should also be suitable for the computation of sediment transport over a turbulent bed where bed-load is the dominant form of movement.

7.3 The laminar / transitional boundary data

7.3.1 Introduction

Section 7.2 clearly shows that the intensity of motion over a turbulent boundary depends on a number of factors including bed-slope, relative roughness, and intensity of motion. In the process, a link was established between the Movability Number and the intensity of motion, and an expression was developed for the computation of the scour rate.

Two further questions remain to be answered: what is a suitable intensity of motion (and associated Movability Number) that would describe the point at which scouring effectively commences, and what are the associated values of α_1 and α_2 in Equations 3.42 and 3.49? Furthermore, all the results reported on in Section 7.2 have come from turbulent boundary layers. Some consideration therefore needs to be given to incipient motion over the laminar and transitional boundaries that are extremely common with sediment in the sand range and smaller. A decision was thus made to carry out experimental measurements of incipient motion over laminar and transitional boundaries in the hydraulics laboratory at the University of Cape Town. This enabled a direct comparison with the incipient motion criteria used in two of the physical models (Midgley, 2000 and Mitchell, 2000). The determination of incipient motion in all these instances relied on visual observation and personal judgement. The intensity of motion could not, in any case, be measured with the available equipment.

7.3.2 Experimental apparatus

The measurements were carried out in the 18 m long, 610 mm wide tilting flume situated in the hydraulics laboratory at the University of Cape Town (UCT) (See Figure 7-6). Water is supplied to the flume via a constant head tank through a 150 mm diameter steel pipe into a steel stilling basin and thence into the flume. The flume has a 610 mm wide glass floor and 550 mm high glass walls. At the downstream end of the flume, the water flows over an adjustable tailgate into the under-floor channels, from whence it is returned to the header-tank via two large sump pumps. A butterfly valve on the inlet pipe controls the flow rate. The water depth can also be adjusted with the aid of the tailgate.

For the purposes of these measurements, the flow rate was estimated with the aid of a removable 90° V-notch weir that was installed immediately downstream of the flume inlet. The effective range of this weir was from 1 – 20 *l*/s. Depth measurement was made with the aid of a Vernier Depth Gauge located along the centreline of the flume. Although the gauge could be read to the nearest 0.1 mm, difficulties in determining the exact location of the vertex of the weir meant that the depth reading could have been up to 1 mm out of true. This translates to an effective measurement error of about 5% at the lower flows, decreasing to about half this value at the higher flows.

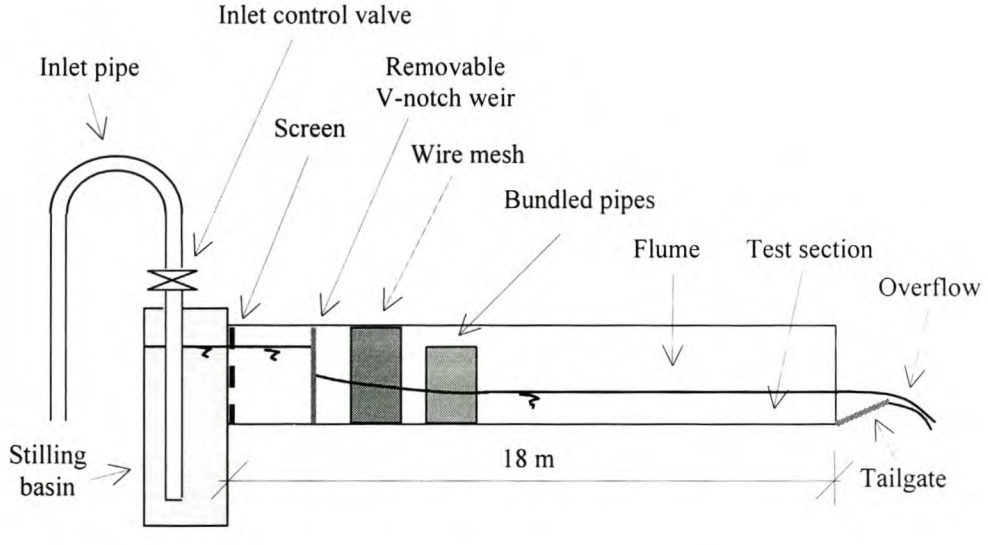

Figure 7-6: Schematic long-section through the UCT 610 mm flume

Turbulence emanating from the discharge of the V-notch weir was reduced through the following means:

i) Sheets of wire mesh were placed parallel to the flow immediately downstream of the weir.

ii) A flow guide, comprising 150 mm long lengths of 20 mm diameter LDPE irrigation pipe tightly bundled together and orientated in the direction of the flow, was placed downstream of the wire mesh.

These measures were sufficient to ensure relatively straight streamlines in the remainder of the flume.

The measurement of the depth of water downstream of the flow guide was also performed by means of a Vernier Depth Gauge.

7.3.3 Experimental procedure

The flume was levelled to eliminate bed-slope as a parameter. The following experimental procedure was then followed:

i) A quartzitic sand fraction, passing one mesh size but retained on the mesh one size smaller, was spread evenly along the bed of the flume downstream of the flow guide with the aid of a custom designed sand spreader that ran on rails above the flume. The level of the sand surface was then measured with a Vernier Depth Gauge at a point 4 m upstream of the tailgate (sufficiently far that the streamlines were, for all intents and purposes, parallel to the bed, although, of course, the flow was gradually varied not uniform).

ii) The tailgate was closed and the flume flooded – taking care not to disturb the sand-bed. The water temperature was measured.

iii) The flow rate was increased to the maximum to be used for that sand fraction.

iv) The tailgate was slowly lowered until motion was detected on the bed over the test section. The level of the water surface was then measured with the same

Vernier Depth Gauge that was used to measure the sand-bed level. The flow rate was slowly decreased by about 2 *l*/s.

v) Steps iv) and v) were repeated until the flow had reduced to about 2 *l*/s. Once the final water level measurement had been made, the water temperature was noted, and the flume was cleaned ready for the next set of measurements.

41 measurements were made in all. The experimental range is indicated in Table 7-3. The data is summarised in Appendix B.

The flume was not equipped for the measurement of the sediment transport rate, and it proved to be very difficult to judge the point of incipience with any degree of consistency. This is clearly shown on a plot of the Movability Number versus the particle Reynolds Number (Figure 7-7). The fact that each data set appears to be spread along a diagonal is largely as a consequence of shear velocity appearing on both axes.

d (μm)	Q (l/s)	Y (mm)	Re_*	Fr
150 – 300	2.1 – 12.3	20.6 – 83.7	1.66 – 1.99	0.27 – 0.37
300 – 425	2.1 – 19.9	19.0 – 112.6	4.08 – 5.06	0.24 – 0.49
425 – 500	4.1 – 20.0	19.6 – 111.1	7.46 – 11.41	0.28 – 0.78
500 – 600	2.3 – 19.8	14.0 – 106.3	9.63 – 13.27	0.30 – 0.73
600 - 850	2.2 – 11.9	14.7 – 70.7	10.48 – 13.17	0.33 – 0.65

Table 7-3: Summary of the incipient motion data for laminar boundaries

7.3.4 Data processing

The main purpose of the physical experiments was to establish a suitable intensity of motion / Movability Number that would describe the point at which scouring effectively commences, and to determine the associated values of α_1 and α_2 in Equations 3.42 and 3.49. In Section 7.2, use was made of the Manning Equation to determine the effective hydraulic radius operating on the bed, R_b. The Manning equation was not developed for use with laminar and transitional boundaries. In these

regions, the Manning roughness coefficient, n, is a function of Reynolds Number (laminar boundaries) or both Reynolds Number and roughness (turbulent boundaries). There are more accurate ways of determining the influence of the different boundaries on the flow. Nevertheless, for the sake of continuity, the experimental data was analysed in a similar way to that previously described for turbulent boundaries (Section 7.2). This means that the estimate for n will be increasingly in error as the particle Reynolds Number, Re_*, reduces. In the region where transitional boundaries give way to turbulent boundaries the error is, however, small. The value of n is used to correct the hydraulic radius for the influence of the sidewall (Equation 7.4) and to determine the local friction slope, S_f for use in the determination of the bed shear stress (Equation 7.6). Other points to note:

i) The Manning roughness value, n, was determined using the maximum diameter of the sand fraction under consideration.

ii) The local friction slope was determined from the Manning equation. The average velocity, U, was determined by continuity.

iii) The critical conditions for movement were determined by consideration of the minimum diameter of the sand fraction under consideration. It seemed probable that the finer sand fractions will move before the coarser fractions assuming no armouring. Since the sand fractions were reasonably uniform, there was no reason to expect significant armouring. Visual observation appeared to bear out these suppositions.

The data was then plotted on a graph of the Movability Number versus the particle Reynolds Number (Figure 7-7).

7.4 Discussion

7.4.1 Critical Movability Numbers

On several occasions throughout the dissertation, it has been pointed out that particle motion can theoretically take place under any flow conditions (c.f. Section 3.7). For the purposes of the numerical model, it is however necessary to define a lower limit below which particle movement effectively ceases. In terms of the incipient motion

model developed throughout this dissertation, this means that values have to be chosen for the empirical coefficients, α_1 and α_2 in Equations 3.42 and 3.49:

$$\frac{u_*}{v_{ss}} = \frac{\alpha_1}{Re_*} \tag{3.42}$$

$$\frac{u_*}{v_{ss}} = \alpha_2 \tag{3.49}$$

Three factors guided the selection of these two coefficients:

i) Considering all the data collected in Section 7.3, the Movability Number never dropped below 0.257. This suggests a value of α_2 much higher than the value of 0.12 proposed by Rooseboom (1992) (Section 3.8.4) should be used for the determination of the critical conditions for scouring.

ii) The numerical modelling (described in Chapters 8 & 9) gave the best results with $\alpha_2 \approx 0.17$. This is identical to the value proposed by Raudkivi (1998) (see Table 3-3).

iii) The practical division between laminar and boundary conditions could not be determined from the data. A particle Reynolds Number, Re_*, of 11.8 is often used as the practical division between laminar and turbulent boundaries (e.g. Potter & Wiggert, 1997). It was also the division used by the computer program employed in the numerical analyses. This value was thus selected as the (somewhat arbitrary) division between laminar and turbulent boundary conditions.

Selection of $Re_* \approx 11.8$ as the division between laminar and turbulent boundaries, and $\alpha_2 \approx 0.17$ (Raudkivi, 1998; numerical modelling) automatically implies $\alpha_1 = 2.0$. Substitution of this value into Equation 3.42 gave a curve that seemed to loosely define the lower limit of the laminar boundary data in the transitional region. As Re_* reduces, the fit is not so good, but this is the zone in which the Manning roughness coefficient is increasingly in error.

The two new equations marking the division between scour and deposition are thus:

$$\frac{u_*}{v_{ss}} = \frac{2.0}{\mathrm{Re}_*} \tag{7.21}$$

$$\frac{u_*}{v_{ss}} = 0.17 \tag{7.22}$$

They are plotted in Figure 7-7 together with the data on laminar and transitional boundaries.

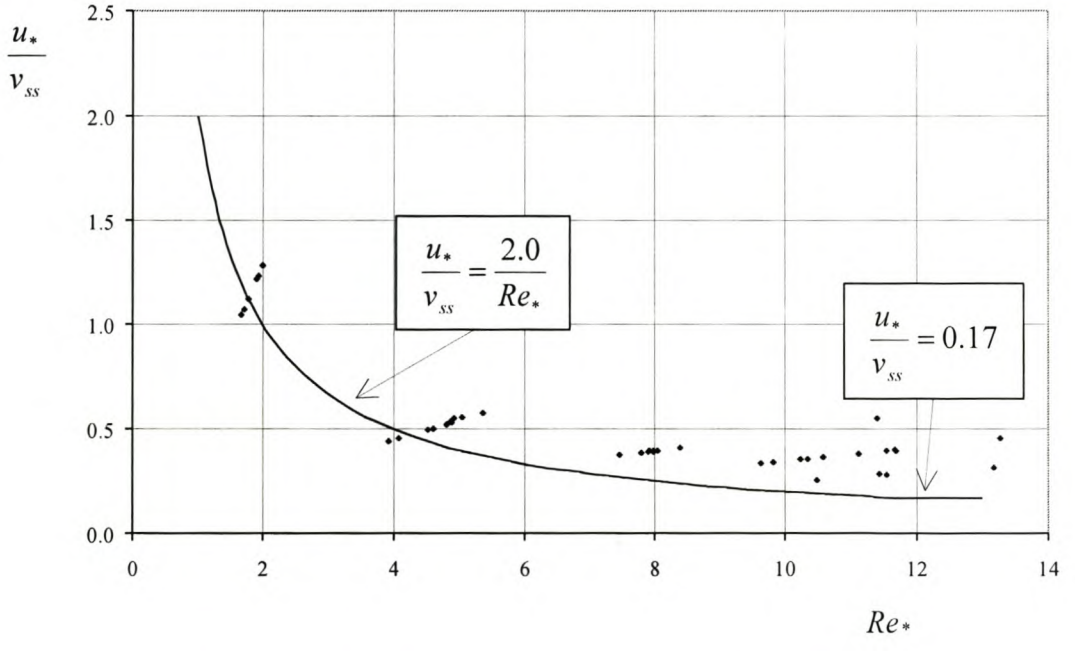

Figure 7-7: Variation of Movability Number with particle Reynolds Number for laminar and transitional boundaries

From Equation 7.14 and Figure 7-3, it can be seen that the scour criterion for turbulent boundaries is $I \approx 2 \times 10^{-5}$ s^{-1}. This could be described as "weak" or perhaps "very weak" movement in accordance with the Kramer (1935) definitions. Shvidchenko & Pender (2000a & 2000b) used $I \approx 10^{-4}$ s^{-1} for their definition of incipient motion. Parker et al (1982) introduced a bed load parameter:

$$W^* = \frac{q_b^*}{\theta} \tag{7.23}$$

and suggested a value of $W^* = 0.002$ as a reference transport rate corresponding to threshold conditions. According to Shvidchenko & Pender (2000a), this corresponds to $I \approx 3 \times 10^{-5}$ s^{-1}. In view of this $I \approx 2 \times 10^{-5}$ s^{-1} seems reasonable. By extension, this also applies to the commencement of scouring over laminar and turbulent boundaries.

In the course of the experimental work, it was noticed that there appeared to be a fine line between very weak movement and general movement. Inspection of Equation 7.14 or Figure 7-3 shows that increasing the Movability Number by only 24% (from 0.169 to 0.210) increases the intensity of motion by a factor of 500 (from 2×10^{-5} to 10^{-2}). A 9% increase in Movability Number increases the intensity of motion by a factor of 10. The use of a single equation to distinguish between a scouring condition and a depositing condition simplifies the design process. The evidence of both the experimental and numerical work (Chapter 9) suggests that Equations 7.21 and 7.22 are a good indication of the division between the two conditions where clear-water scour is involved. It should however be noted that this, somewhat subjective, selection of the critical Movability Number might not be appropriate under different circumstances.

7.4.2 Critical unit stream power

From Section 6.2, incipient motion on a laminar bed is given by:

$$\frac{u_*}{v_{ss}} = \eta_l^{1/2} \frac{\alpha_1}{Re_*} \tag{6.2}$$

For incipient motion on a turbulent bed:

$$\frac{u_*}{v_{ss}} = \eta_t^{1/3} \alpha_2 \tag{6.3}$$

where η_l and η_t are the appropriate values in the equation:

$$P_t = \eta P_r \tag{6.1}$$

With $\alpha_1 = 2.0$ and $\alpha_2 = 0.17$, $\eta_l \approx 0.167 \approx 1/6$ and $\eta_t \approx 0.015 \approx 1/67$. The conditions for scouring can therefore be described in terms of the unit power required for the suspension of a particle as follows:

$$P_t \geq \frac{P_r}{6} \quad \text{for } Re_* \leq 11.8 \tag{7.24}$$

and,

$$P_t \geq \frac{P_r}{67} \quad \text{for } Re_* > 11.8 \tag{7.25}$$

As before, scour commences once:

$$P_t \geq P_r \tag{3.33}$$

$$P_r = (\rho_s - \rho) g v_{ss} \tag{3.42}$$

7.5 Conclusions

The objective of Chapter 6 was the selection of criteria for incipient motion. The main problem was that sediment motion could theoretically occur in any flow state. This was resolved by reference to the Shvidchenko & Pender (2000) definition of intensity of motion. Other issues included bed-slope and relative roughness.

Data supplied by Shvidchenko & Pender (2001) for turbulent boundaries was reprocessed in such a manner that the bed-slope and relative roughness could be accounted for in an equation that linked intensity of motion with a critical Movability Number. This was expressed as Equation 7.14. It was shown that the critical

Chapter 8
The CFD model

8.1 Introduction

Computational Fluid Dynamics (CFD) is the analysis of systems involving fluid flow, heat transfer and associated phenomena such as chemical reactions by means of computer-based simulation (Versteeg & Malalasekera, 1995). Many commercial codes are now available. A preliminary test of the theoretical model, presented in Chapters 6 & 7, was carried out using the CFD code, CFX, supplied by AEA Technology. CFX was designed to handle a variety of fluid problems ranging from multiphase flows in chemical reactors to the drag forces associated with spherical balls suspended in air.

Two versions of CFX were used in this investigation. Most of the work was carried out using Version 4.3 (CFX, 1999). This version was not necessarily the most suitable code for this particular application – for example, it does not include a free-surface routine. It was selected because it was the code that had the greatest technical support at the University of Cape Town during the period of the investigation. Version 4.4 (CFX, 2001) became available towards the end of the investigation, and this was used for the last of the analyses (deformable boundaries around a pier). Although a free-surface routine was available in Version 4.4, it was not used, as this would have introduced unnecessary additional complexity to the model at a very late stage. The simplified treatment of the free surface proved sufficient to adequately prove the efficacy of the theoretical model.

McGahey (2001), a MSc (Eng) student working under the supervision of the author, made the requisite modifications to the program and operated it.

The purpose of this chapter is to summarise the way CFX was used to predict scour and deposition using the unit stream power model developed in the previous chapters. This required, inter alia, describing the solution domain, modelling the boundary conditions, choosing a turbulence model, choosing a differencing scheme, coupling pressure to velocity, choosing the solution algorithm, and deciding between steady-state and transient analyses.

Part 3

Numerical analyses

for $Re_* > 11.8$, and is depicted graphically in Figure 7-8. In terms of unit stream power, the criteria are given by Equations 7.24 & 7.25.

Movability Number does not appear to vary with the particle Reynolds Number for turbulent boundaries. The linkage between intensity of motion and the dimensionless bedload parameter also allowed for the development of an equation that could be used to predict the rate of scour. It may also be suitable for the estimation of sediment transport over a turbulent bed where bedload is the dominant form of movement. Additional data gathered for flow with laminar and transitional boundaries was combined with the data for turbulent boundaries and used to help determine the values of α_1 and α_2 in Equations 3.42 and 3.49 that describe the effective commencement of scour.

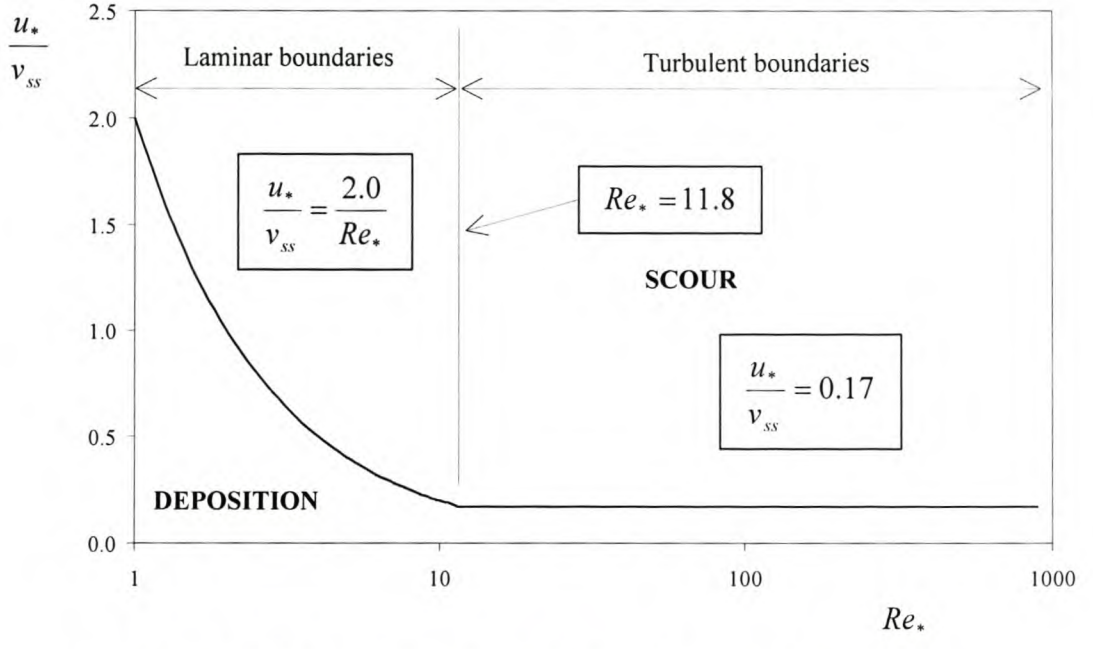

Figure 7-8: New criteria for predicting the onset of scour

Experiments carried out in the laboratory as part of this investigation (Section 7.3, Chapter 9) show that the intensity of motion appears to vary widely over a relatively small range of Movability Numbers (or unit stream power). The Movability Number (and unit stream power) is closely related to the flow depth. Thus the transition from a situation of no scour (and potential deposition) to general scour tends to take place over a very narrow range of flow depths. For simplicity sake, an intensity of motion of $I = 2 \times 10^{-5}$ s^{-1} was taken as the boundary between the cessation of scour and the commencement of scour for the purposes of the theoretical model proposed by this thesis (clear-water scour only). This leads to the new scour criteria being defined in terms of the Movability Number by Equation 7.21 for $Re_* \leq 11.8$, and Equation 7.22

Once the program was running, the output had to be interpreted. This was carried out with the aid of the unit stream power equation and a function that was termed the "scour function".

The results of the numerical analyses are described in Chapter 9.

8.2 The main elements of CFX

Like all commercial CFD codes, CFX has three main elements:

i) Pre-processor,

ii) Solver, and

iii) Post-processor.

8.2.1 Pre-processor

The pre-processor is an input interface where the user specifies (Versteeg & Malalasekera, 1995):

i) The geometry of the computational domain.

ii) The mesh. Optimal computational efficiency is achieved by using small volumes in the regions where the gradients are large, and large volumes in the areas where they are small.

iii) The physical and chemical phenomena to be modelled.

iv) The fluid properties.

v) The boundary conditions.

vi) The solution control parameters.

8.2.2 Solver

The solver reads the input files from the pre-processor, and then processes the data by applying numerical techniques in the following way (Versteeg & Malalasekera, 1995):

i) The governing equations of fluid flow are integrated over all the finite control volumes of the solution domain.

ii) CFX is a "Finite Volume" code. This means that the computational domain is divided into non-overlapping fluid elements called fluid "volumes". To simplify the computation, the properties of each of these volumes are represented by the values at the centre point (called the "node"). The program relates the properties at each node to those surrounding it via finite difference approximations of the conservation laws of fluid motion (see Chapter 4).

iii) The algebraic equations are then solved using an iterative method.

8.2.3 Post-processor

The post-processor is the output interface where the user specifies the presentation of the data. In the case of CFX, this includes:

i) The domain geometry.

ii) The mesh.

iii) Vector plots (e.g. of point flow velocities).

iv) Colour-coded contour plots of scalars (e.g. pressure, unit stream power, or the magnitude of the point velocities).

8.3 Describing the solution domain

8.3.1 Creating the geometry

The first step in numerical analysis involves the identification and description of a suitable flow domain for solution. Real flow in real channels may exhibit an inter-related variety of gradually and rapidly varied flow phenomena. There may be flow separation around obstacles; there may be waves on the surface; there may be coherent flow structures at both the microscopic and macroscopic level. Whilst CFD is theoretically capable of modelling all of these phenomena, it is not possible with the computer hardware currently available to model all of them simultaneously without making major simplifying assumptions.

The first restriction that had to be placed on the numerical model was to limit, as far as was reasonably possible, the extent of the channel that was to be modelled. The length of channel, both upstream and downstream of the obstacle, was made relatively short. Where there was symmetry e.g. on either side of a circular pier placed in the centre of a rectangular channel, only one of the symmetrical portions was modelled. This meant that the boundary conditions, particularly on the inflow and outflow faces, had to be chosen with care so that they accurately represented the key influences of the upstream and downstream flow phenomena. This topic will be discussed in further detail in Section 8.4.

The solid boundaries were modelled as follows:

i) Rectangular blocks were adequate for representing the boundary elements of the rectangular channels, the weirs, and the abutments. The structures had, in any case, been expressly chosen to facilitate modelling in this manner.

ii) Arcs were used to create solid segments, which were then linked together to form cylinders.

iii) Splines were fitted through the co-ordinates of uneven surfaces such as the channel bed in loose boundary situations. These were then linked together to form one side of the requisite boundary volumes.

8.3.2 Meshing the domain

Once a decision had been made on the geometry of the flow domain, it had to be divided up into finite volumes ("cells") by means of a two- or three-dimensional mesh. Increasing the number of cells decreases their average size which, as previously mentioned, increases the accuracy, but at the cost of increased computational time. It can also result in the creation of data files that are too large for the post-processor to handle. Fortunately, CFX Version 4.3 offers the option of biasing the mesh in such a way that the mesh is finer in the areas of large velocity gradients than in the areas of small velocity gradients.

There are two main regions where large velocity gradients are to be found: near the solid boundaries; and in the areas where flow separation might lead to large-scale eddies.

i) The applied unit stream power increases exponentially with decreasing distance from a solid boundary until the viscous sub-layer is reached. It was thus important that the boundary cells were made smaller than the viscous sub-layer thickness, δ (see Section 2.4). This thickness was deemed to be determined by a value of $y^+ = Re_y = 11.8$, where y^+ is given by Equation 2.16:

$$y^+ = \frac{y}{y_*} = \frac{u_* y}{\nu} = Re_y \tag{2.16}$$

The shear velocity, u_*, was not, however, initially known. It had to be estimated from a preliminary run of the computational problem using a fairly coarse mesh. Since CFX has shear stress as a possible output, the shear stress at the boundary could be determined from the boundary shear stress, τ_0, using Equation 2.13:

$$u_* = \sqrt{\frac{\tau_0}{\rho}} \tag{2.13}$$

If the boundary was turbulent (see Section 2.4.4), then the cell size also had to be smaller than the roughness height, k_s (see Figure 8-1).

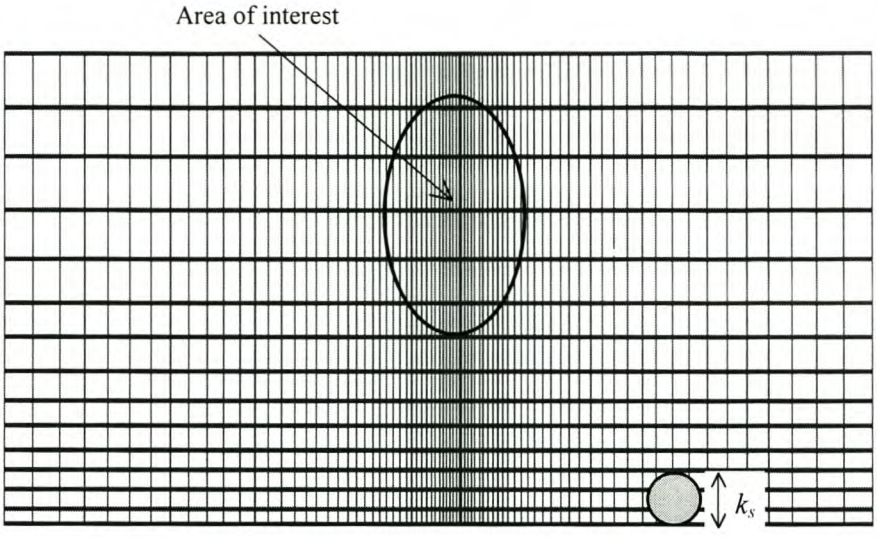

Figure 8-1: Typical example of mesh refinement
(McGahey, 2001)

ii) The cell size was also reduced in the regions where eddies might be expected – usually downstream of a flow separation.

8.4 Modelling the boundary conditions

8.4.1 Inflow face

The inflow face had to be carefully programmed in view of the restricted length of the computational model which allowed very little room for the development of the typical steady uniform flow profiles (see Section 8.3.1). As a first step, the velocity was increased logarithmically with distance from a solid boundary. This is typical of real flows in the log-law layer (see Section 2.3.3), and is a reasonable approximation outside of this (Section 2.3.4). Care was taken to ensure that the integrated flow over the input face equalled the total flow that was being modelled.

The flux generated by the above-mentioned velocity profile was then routed through a uniform section of channel using a fairly coarse mesh so as to get the boundary values of the turbulent kinetic energy, k, and rate of viscous dissipation, ε, into the correct range. The procedure was verified by comparing the velocity distribution obtained from the model with that measured by Fujisaki et al. (1999) for a long rectangular

channel. There is more discussion on the role of k and ε in the section on "the choice of turbulence model".

8.4.2 Outflow face.

Care also had to be taken with the specification of the outflow face. To simplify matters, the velocity was increased linearly from the bed to the surface. Obviously, mass continuity had to be satisfied. The pressure field was computed from upstream conditions.

It was important to ensure that the outflow boundary was sufficiently removed from the area of interest so that the flow conditions at the outflow did not have a significant impact there.

8.4.3 Symmetrical faces

Symmetrical faces can be modelled in CFX. A symmetrical face is one where one side is the mirror image of the other. Computationally it means that all fluxes are tangential to the face in the boundary cells abutting the plane of symmetry. It is an extremely useful way of reducing the number of cells in the flow domain and it was typically used with two-dimensional flows and with the flow around symmetrical structures (e.g. circular piers).

8.4.4 The free surface

CFX Version 4.3 does not have a free-surface routine. The free-surface routine in CFX Version 4.4 was not used as this version only became available at the end of the investigation and the routine would only have increased the complexity of the program without adding substantial value to the output.

In the absence of a free-surface routine, the following alternatives were considered:

i) The free surface was modelled as a plane of symmetry. The drawback with this approach is that it distorted the turbulent viscosity ($\mu_{(t)}$) distribution. This is

unacceptable in a unit stream power model because unit stream power is a function of the turbulent viscosity.

ii) The free surface was modelled through the specification of an air pocket of fixed thickness between the water and a rigid lid (c.f. Ouillon & Dartus, 1997; Soltiropoulos & Ventikos, 1996). The velocity of the air was made equal to that of the water surface and its pressure set at atmospheric. The problem with this approach was that convergence difficulties were encountered as soon as an obstacle was introduced.

iii) The free surface was modelled as a moving wall. The velocity of this moving wall was set equal to that of the topmost layer of water. This approach gave the best results and was adopted for the analyses. The only place where there were noticeable distortions in the model output was in the surface layers. Since the aim of the investigation was the prediction of scour and deposition on the bed of the channel, this distortion was ignored.

In all three cases, the free surface profile had to be estimated and fixed by the user using one-dimensional analyses.

8.4.5 The walls

All solid surfaces fell under this category. A "no-slip" condition was specified for all wall surfaces, as was a logarithmic wall function for the water velocity. If specification of the logarithmic wall function led to computational problems, linear or quadratic functions were used in its place.

There were two types of wall boundary:

i) "Rigid" boundaries usually had surfaces that were either planes or arcs that were (at least partly) parallel to the principal axes. The surface could be specified as "laminar" or "turbulent". If the latter, then the height of the roughness elements, k_s, was made equal to the sediment diameter, d. A sensitivity analysis showed that, however, roughness did not appear to have any impact on the results for the test cases.

ii) "Loose" boundaries, for the purposes of this investigation, included all those boundaries that were allowed to undergo deformation in the laboratory. No capability was written into the CFX coding allowing for the progressive deformation of the boundary as the computation proceeded. Instead, an attempt was made to model the final deformed surface. A procedure to develop the final deformed surface iteratively from the initial surface will be discussed in Section 10.3. Strictly speaking, therefore, all the boundaries considered in this investigation were "rigid". In computer terminology, the approach that was adopted here, where interim solutions do not directly impact on, and possibly alter, the boundary conditions, is called an "uncoupled" model. The alternative is a "coupled" model where there is an interaction between the wall geometry and the flow field, which while desirable, is much more computationally demanding.

In this investigation, the main difference between a "rigid" boundary and "loose" one lay in the modifications to the incipient motion criteria that had to be made as a consequence of the variation in the bed-slope. Whilst this did not impact directly on the simulation of any particular boundary layout, it was the key to the acceptance of the final profile. How this was handled will be discussed in detail in Section 8.10.

8.5 The choice of turbulence model

8.5.1 Introduction to turbulence modelling

Turbulence modelling is one of the most complex aspects of CFD. Turbulent flow is characterised by high frequency velocity and pressure fluctuations over a wide range of length and time scales. Direct numerical simulation (DNS) of turbulent flow using the full Navier-Stokes equations (see Section 4.4) requires a mesh size smaller than about 10 μm and a time step smaller than about 10 μs. Analysis of most open channel flow problems of practical interest using DNS requires computers many orders of magnitude faster than those currently available (Speziale, 1991).

CFD modellers have reduced the problem of unacceptably high computational loads by approximating the turbulent processes in a number of ways. One way is to model the turbulent eddies as individual units, inferring the small-scale turbulent process from the behaviour of the larger scale eddies. These types of models are called large

eddy simulation (LES) or very large scale eddy simulation (VLES) models. Clearly the larger the size of the eddy, the greater the degree of approximation.

Even LES and VLES are computationally intensive. The most common computational methods thus approximate the Navier-Stokes equations with the so-called Reynolds averaged Navier-Stokes equations (RANS). In essence this involves the expression of the various fluid parameters (e.g. velocity and pressure) as the sum of mean and fluctuating components (see the Reynolds stress model in Section 2.2.2). The revised equations can be solved through the estimation of the turbulent (eddy) viscosity.

There are numerous ways of estimating the eddy viscosity. Some of the more common ones are:

i) Assume a constant eddy viscosity (a zero equation model).

ii) The Prandtl eddy model. This model links the eddy viscosity to a length scale (a one-equation model).

iii) The k-ε model. This model introduces equations for the transport of kinetic energy and the rate of viscous dissipation. These are then used to approximate the length and velocity scales – which are in turn used to determine the eddy viscosity. These so-called transport equations contain a number of empirically derived constants that are applicable to certain situations. It is a two-equation model.

iv) The algebraic stress model. This model introduces transport equations for each of the six Reynolds stresses (a six-equation model).

There are many other similar models that perform well under various circumstances. Unfortunately, no universal model has been developed that is applicable to all situations (Chen et al., 1996). It is therefore common for commercial CFD codes to offer a range of turbulence models. The modeller must then choose the one that is the most appropriate for their situation.

8.5.2 Turbulence models supported by CFX

CFX Version 4.3 offers the following turbulence models:

i) The k-ε model.

ii) The Low Reynolds Number k-ε model.

iii) The Low Reynolds Number k-ω model. ω is the "turbulence frequency" (Wilcox, 1993).

iv) The RNG model (for very high Reynolds Number flows).

v) The differential stress model.

vi) The algebraic stress model.

vii) The differential flux model.

The last two mentioned models are termed Reynolds Stress Models (RSMs). They are supposedly more accurate than, for example, the k-ε and k-ω models, but are more computationally intensive.

8.5.3 The choice of turbulence model

The decision on the choice of turbulence model was made after comparing the performance of the various options in CFX with the Cellino & Graf (2000) data. Cellino & Graf (2000) provided data on the variation of the velocity and the Reynolds stresses with depth for a two-dimensional, sediment-laden flow over bedforms fixed at 2 and 3 degrees respectively (Figure 8-2).

Comparison of the variation of the relative velocity (Figure 8-3) and of the relative shear stress (Figure 8-4) with the relative depth indicated that only the algebraic stress model (denoted in the figures as RSM) and the k-ε models provided reasonable predictions of these parameters. Of the two, the k-ε model appeared to be the better and this was the one that was selected.

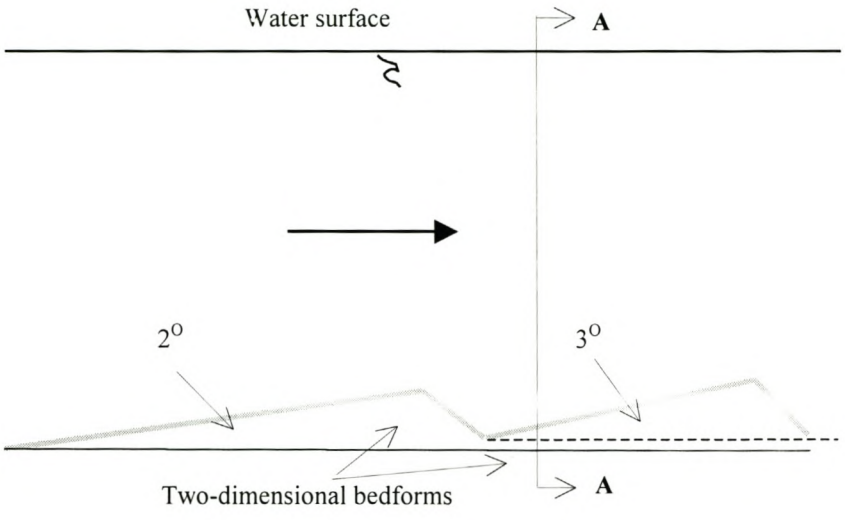

Figure 8-2: The Cellino & Graf (2000) 2D bedforms
(McGahey, 2001)

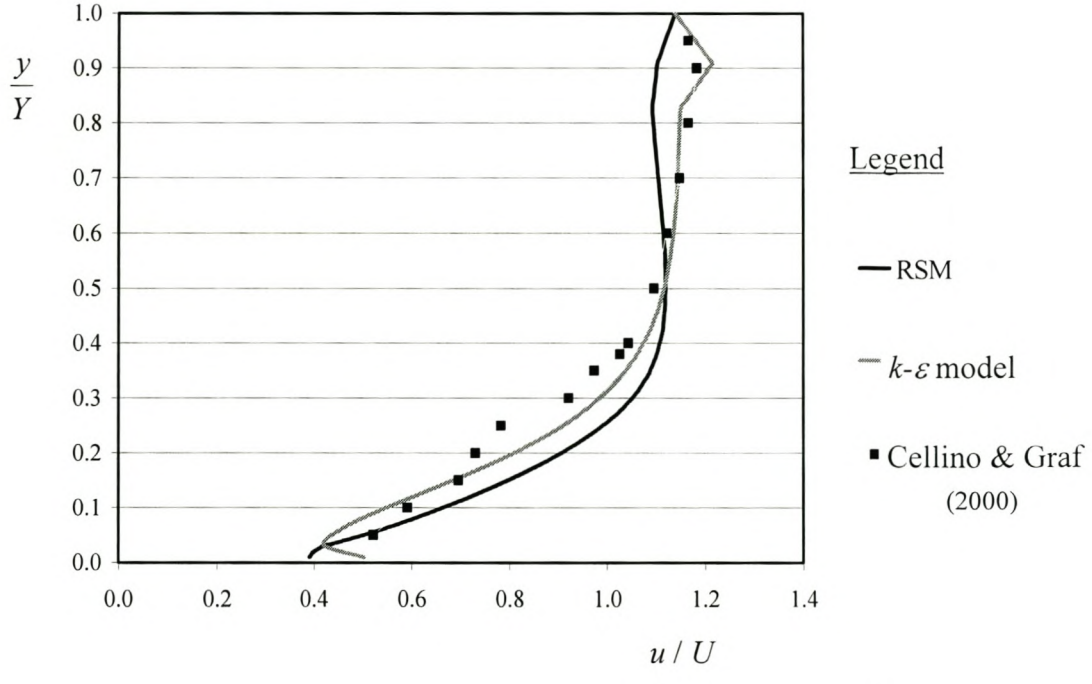

Figure 8-3: Cellino & Graf (2000) – Relative velocity versus relative depth
(McGahey, 2001)

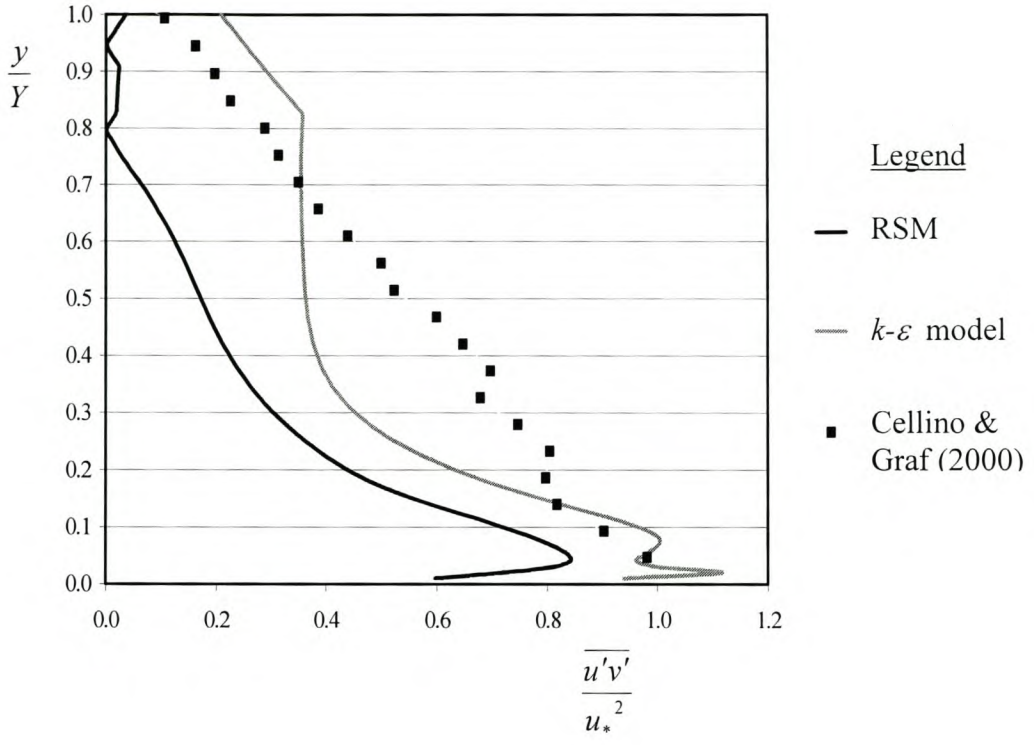

Figure 8-4: Cellino & Graf (2000) - Relative shear stress versus relative depth
(McGahey, 2001)

8.6 The choice of a differencing scheme

The integral equations can be discretised as soon as the governing equations have been adapted to incorporate the turbulence equation. This involves the substitution of finite-difference type approximations for the terms in the integral equations representing flow processes such as convection and diffusion (Versteeg & Malalasekera, 1995). This result is a system of non-linear algebraic equations.

As might be expected, different systems of equations are appropriate for different turbulence models and different situations. CFX Version 4.3 supports the following differencing schemes:

i) Upwind (1st order accurate).

ii) Higher Order Upwind (2nd order accurate).

iii) Central (2nd order accurate).

iv) Hybrid (1st order accurate).

v) QUICK (3rd order accurate for advection, 2nd order accurate for diffusion).

vi) CCCT (3rd order accurate for advection, 2nd order accurate for diffusion).

vii) CONDIF (2nd order accurate).

viii) MUSCL (3rd order accurate).

The choice of differencing scheme was made after comparing the results obtained with each of the schemes with the benchmark results for a lid-driven cavity provided by Ghia et al. (1982). As a consequence of this study, the QUICK scheme was implemented for the velocity and pressure terms, but the Upwind or Hybrid schemes were used for modelling the turbulent kinetic energy and rate of dissipation terms.

8.7 Pressure-velocity coupling

Once the governing equations have been discretised to form a system of non-linear algebraic equations, it becomes necessary to ensure that velocity and pressure are correctly coupled. This is usually performed with the aid of a staggered grid for the velocity components, whilst the other flow variables are solved for and stored at the original nodal points. A number of algorithms have been developed for this purpose. Those supported by CFX Version 4.3 include:

i) SIMPLE.

ii) SIMPLEC.

iii) PISO.

iv) Non-iterative PISO.

The default option in CFX Version 4.3 is the SIMPLEC algorithm, which is the one that was used unless there were convergence difficulties. Under those circumstances, SIMPLE or PISO were used.

8.8 The solution algorithm

The system of algebraic equations can be solved once the pressure correction has been applied. Owing to their non-linearity, they need to be solved iteratively, both individually (the inner iteration) and as a system (the outer iteration). The solvers available in CFX Version 4.3 are:

i) Line relaxation (LINE SOLVER).

ii) Preconditioned conjugate gradients (ICCG).

iii) Full field Stone's method (STONE).

iv) Block Stone method (BLOCK STONE).

v) Algebraic multi-grid (AMG).

vi) General version of the algebraic multi-grid (GENERAL AMG).

In this investigation, BLOCK STONE was generally used for velocity, ICCG or AMG for pressure, and LINE SOLVER for turbulent kinetic energy and rate of viscous dissipation.

The stopping criteria for the iterations can be defined in terms of:

i) Number of iterations.

ii) Number of time-steps (for transient problems).

iii) Mass source tolerance on a residual.

The third option was the one that was generally used.

8.9 Choosing between steady state and transient analyses

In many situations, e.g. converging flow problems with constant – or reasonably constant – flow rates, numerical analysis can be undertaken assuming steady state. In other words, the solution is independent of time. Flow fields that vary with time, whether as a consequence of flow separation or unsteady flow rates, theoretically require transient analyses. Most scour and deposition problems fall into the second category because they are commonly associated with flow separation.

The problem with transient analyses is that they introduce another degree of complexity. The flow has to be solved over the entire domain for each time interval, and the time intervals have to be relatively short to ensure numerical stability. This dramatically increases the computational load.

Transient analyses were attempted for two situations: the modelling of scour and deposition around an abutment in a rectangular channel, and around a pier in a rectangular channel. In both cases, the flow separates around the structure and forms a vortex trail. This vortex trail is partly responsible for sediment movement downstream of the structure. Care had to be taken to ensure that the mesh in the vicinity of the expected vortex trail was much smaller than the size of the vortices. CFX Version 4.3 offers either Implicit (backward) or Crank-Nicolson (central) time-differencing schemes. These can be made either linear (first-order) or quadratic (second-order) – although the CFX manual advised against the simultaneous use of the Crank-Nicolson scheme with quadratic time differencing. The default option of Implicit / linear time differencing was selected and no convergence problems were encountered.

Either fixed or adaptive time stepping may be specified in CFX Version 4.3. Adaptive time stepping allows automatic control of the time step as long as convergence is achieved, thus allowing the program to speed up the time stepping if possible. In this investigation, a combination of the two was used: the problem was initially run with fixed time steps; then stopped and continued with adaptive time steps.

In spite of computer runs in excess of 24 hours, no vortex street was ever observed and the solution converged towards the steady-state solution. It was eventually concluded that the use of a moving-wall boundary in place of the free surface

probably suppressed the formation of the vortex street. Fortunately, the main area of interest was in the vicinity of the structures where the solution looked reasonably accurate.

Once the decision had been made to ignore the influence of the vortex street on scour and deposition, transient analyses could be abandoned and the problems analysed using steady-state simulation only. This decision will have to be reviewed once a suitable free-surface routine is in use.

8.10 Determining the potential for scour or deposition

8.10.1 Basic criteria

In the context of this investigation, the criteria for determining the potential for scour and deposition on a flat bed in terms of the Movability Number are laid out in Section 7.4 and summarised in Figure 7-8. The equations are:

$$\frac{u_*}{v_{ss}} \geq \frac{2.0}{Re_*} \quad \text{for } Re_* \leq 11.8 \tag{7.21}$$

and

$$\frac{u_*}{v_{ss}} = 0.17 \quad \text{for } Re_* > 11.8 \tag{7.22}$$

A Movability Number higher than the indicated value indicates a potential for scour. A Movability Number lower than the indicated value indicates a potential for deposition. Clearly, scour and deposition will only take place in the presence of loose sediment on the channel bed (scour) or in suspension (deposition).

If the channel bed is sloped, then these values have to be adjusted using the slope correction factor:

$$\psi = \sqrt{k_\beta k_\gamma} = \sqrt{\cos\beta\left(1 - \frac{\tan\beta}{\tan\phi_r}\right)\cos\gamma\left(1 - \frac{\tan^2\gamma}{\tan^2\phi_r}\right)}^{1/2} \tag{6.18}$$

The link between the critical Movability Number and the critical applied unit stream power at the bed is described in Section 6.2.

8.10.2 Implementation of slope correction

If the channel bed is sloped, then these values have to be adjusted using the slope correction factor ψ.

The computation of ψ was carried out at follows:

i) The cells adjacent to the boundary cells were identified (the boundary cells could not be used for this exercise since the velocities in the boundary cells were set to zero – the "no-slip" condition).

ii) The velocity vector **u** for each adjacent cell was obtained.

iii) The normal vector **n** for each adjacent cell was obtained (on the side closest to the boundary).

iv) Since **u** must be parallel to the bed in the adjacent cells, the longitudinal (streamwise) slope, β, can be determined from:

$$\beta = \arctan\left(\frac{-v}{\sqrt{u^2 + w^2}}\right) \tag{8.3}$$

where u, v and w are the x, y and z components of the velocity vector **u**. In the case of downflow adjacent to a structure, u and w were exceptionally small relative to v, and β was set equal to $\pm 90^{O}$. Clearly scour is not an issue here.

v) The transverse slope, γ, was obtained from the slope of the transverse vector **t** formed from the cross-product of **u** and **n**:

$$\mathbf{t} = \mathbf{u} \times \mathbf{n} \tag{8.4}$$

Then,

$$\gamma = \left| \arctan\left(\frac{t_y}{\sqrt{t_x^{\,2} + t_z^{\,2}}} \right) \right| \tag{8.5}$$

where t_x, t_y and t_z are the x, y and z components of the transverse vector **t**. The absolute value is taken because γ is always positive.

The value of the function ψ could then be determined from Equation 6.16.

8.10.3 Determination of the scour potential

In practice, the method selected for the determination of the potential for scour or deposition depended on the problem. Although either the critical Movability Number or the critical unit stream power value could be used, it soon became apparent that the latter was very sensitive to cell size and thus the critical Movability Number was often a more reliable measure. For more complex problems it was often convenient to subtract the computed Movability Number / unit stream power at the boundary from the critical values to produce a "scour potential":

$$\text{Scour potential (Movability Number)} = \Omega = \left.\frac{u_*}{v_{ss}}\right|_{\text{computed}} - \psi \left.\frac{u_*}{v_{ss}}\right|_{\text{critical}} \tag{8.6}$$

or,

$$\text{Scour potential (unit stream power)} = \Omega_p = P_t\big|_{\text{computed}} - \psi\eta P_r\big|_{\text{critical}} \tag{8.7}$$

A positive scour potential indicated a propensity to scour, whilst a negative scour potential indicated a propensity to deposit. The magnitude of the scour potential indicated the approximate degree of this propensity. Obviously the value of the scour potential obtained from Equation 8.6 was different from that obtained from Equation 8.7.

In theory, the boundaries could be warped in response to the scour potentials. In practice, this would have meant continuously recreating the geometry and the mesh in

an iterative manner. This would have been extremely time consuming and a decision was taken to model only the initial and final profiles in this current, developmental, phase.

8.11 Conclusions

A numerical model for the prediction of scour and deposition was constructed using CFX Version 4.3 as the main vehicle. Along the way, however, it became apparent that there were some difficulties in using this program. Some issues were:

i) The construction of the flow geometry – which was extremely tedious for the more complex problems.

ii) The particular care and judgement that had to be paid to the meshing of the domain.

iii) The correct inflow and outflow boundary conditions were critical.

iv) The lack of a proper free-surface routine was a major handicap.

v) The available turbulence models were very limited in their capacity to model the flows of interest in this investigation.

vi) The model was incapable of identifying transient phenomena.

As is always the case with CFD, the computer that was used was very limited in both speed and memory (256 MB of RAM together with a 667 MHz Intel Pentium III processor). There is, however, continuous improvement in this regard.

A flow diagram describing the computational procedure followed in this investigation is attached as Appendix C.

Chapter 9
Numerical analyses

9.1 Introduction

The scour model developed in Part 2 (Chapters 6 & 7) was used to model the scour potential associated with certain weirs, piers and abutments. The work was carried out by McGahey (2001), a MSc (Eng) student working under the supervision of the author, using CFX Version 4.3 & 4.4 CFD software in the manner described in Chapter 8. Some theoretical background on the scour around these three types of structures was provided in Chapter 5. The numerical model was applied to data supplied from various physical models.

The first example that was modelled was the scour potential upstream of a weir using data supplied by Harnett (1998). As the flow over a weir is essentially 2D it was the simplest of the situations to model. Two situations were considered: prior to the commencement of scour, and after scour equilibrium had been reached.

The flow around piers and abutments, on the other hand, is 3D and extremely complex. Initially, therefore, the scour problem was simplified by modelling the scour potential in channels of rectangular cross-section with uniform quartzitic sand as the sediment. Two BSc (Eng) students working under the supervision of the author supplied data on the scour of a thin layer of sand around a circular pier (Midgley, 2000) and a vertical sharp-edged abutment (Mitchell, 2000).

Finally, the investigation was extended to loose boundaries by modelling data gathered by Babaeyan-Koopaei (1996) on the scour around a circular pier situated in a "self-formed channel". As with the weir, two situations were considered: prior to the commencement of scour, and after scour equilibrium had been reached.

As will be seen, the results were sufficiently encouraging to suggest that the model has the potential to predict the scour and deposition around any structure.

9.2 Scour upstream of a weir

9.2.1 Physical modelling (Harnett, 1998)

Harnett (1998) measured equilibrium scour profiles in uniform sands upstream of a sharp-crested vertical weir. The apparatus used for the tests was a tilting flume, 9 m long and 370 mm wide with wooden floors and 650 mm high glass walls. All flow measurements were done with the aid of a V-notch weir mounted at the end of the flume. Depth measurements were obtained with the aid of Vernier Depth Gauges located along the centreline of the flume.

The sand used in the Harnett (1998) experiments was uniform sized silica (quartzitic) sand sieved into three fractions. The sand parameters are summarised in Table 9-1.

d_{50} (mm)	v_{ss} (m/s)	P_r (W/m^3)	$P_{t\,(crit)}$ (W/m^3)
0.84	0.09	1 457	21.7
1.05	0.11	1 781	26.6
3.00	0.27	4 370	65.2

Table 9-1: Summary of the Harnett (1998) sand parameters

The flume was set up to give a 50 mm fall over the 6.38 m distance between the upstream entrance and the vertical weir (a rectangular wooden block). The sediment was then placed in the wedge between the entrance and the weir in such a way that the top of the sediment layer was horizontal and flush with the invert of the weir (Figure 9-1a)). Water was slowly introduced from the upstream entrance until the sediment had been properly saturated. The discharge was then gradually increased to the test values. Five test discharges were used: 3.5 *l*/s, 5 *l*/s, 7.5 *l*/s, 8.5 *l*/s, and 10 *l*/s. Since there were three sediment sizes, and each was tested for all five flow rates, there were 15 tests in all. The flows were maintained until equilibrium was reached – usually after some 35 hours (Figure 9-1b)).

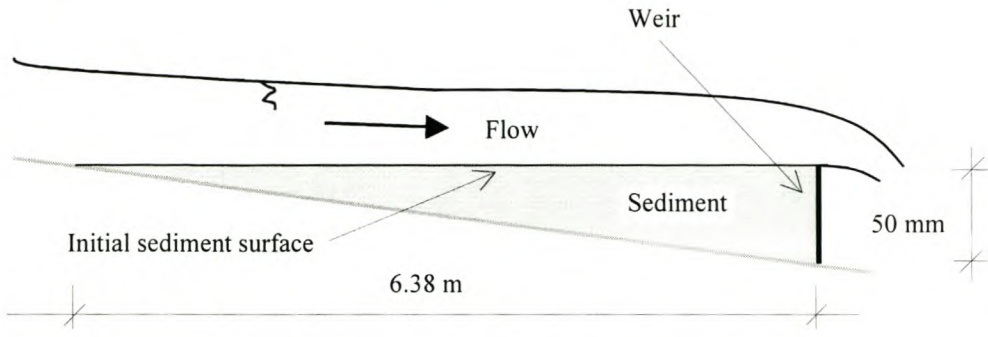

a) Initial profile

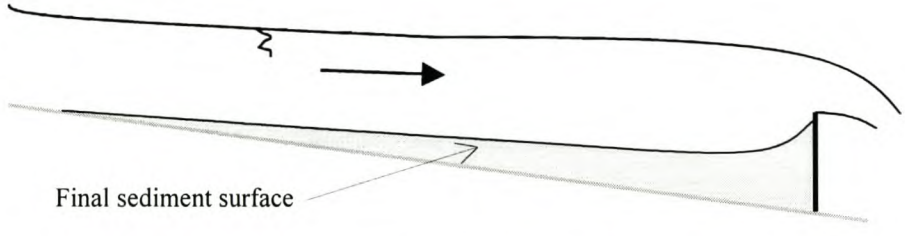

b) Final profile

Figure 9-1: Typical views of the sediment profiles upstream of a weir in the Harnett (1998) experiments

9.2.2 Numerical modelling (McGahey, 2001)

McGahey (2001) only modelled one of the Harnett (1998) tests. The example she used involved sand with a median diameter of 0.86 mm and a flow rate of 3.5 *l*/s. Both the initial state – subjected to the flow but before scour – and the final scoured state were modelled (Figure 9-2). The model was made two-dimensional by giving the flow domain a width of one cell and imposing a symmetry condition on the sidewalls (see Section 8.4.3). The unit stream power equation for two-dimensional flow may be derived from Equation 4.23 by setting all terms referring to the *z*-axis to zero:

$$P_t = \tau_{xx}\frac{\partial u}{\partial x} + \tau_{xy}\frac{\partial v}{\partial x} + \tau_{yx}\frac{\partial u}{\partial y} + \tau_{yy}\frac{\partial v}{\partial y} \tag{9.1}$$

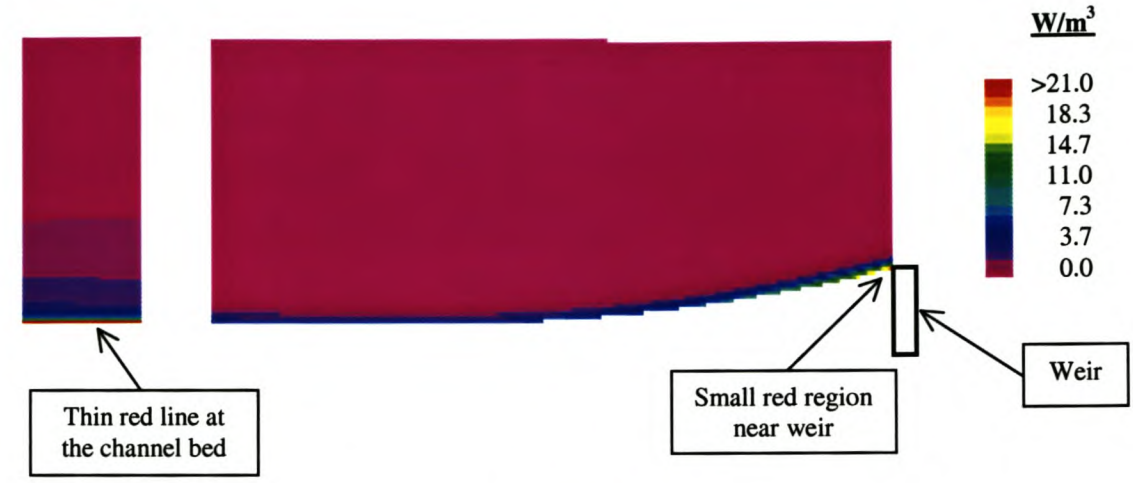

a) Initial State b) Eroded State

Figure 9-2: Typical unit stream power contours associated with scour upstream of a weir (McGahey, 2001)

The boundary condition in this particular test was ascertained as being turbulent ($Re_d > 11.8$). The applied unit stream power requirement for scour on a turbulent bed is given by Equation 7-25:

$$P_t \geq \frac{P_r}{67} \tag{7.25}$$

where,

$$P_r = (\rho_s - \rho) g v_{ss} \tag{3.32}$$

In this instance, $P_r \approx 1\ 457$ W/m^3, so $P_t \geq 21.7$ W/m^3 for scour. It can be seen from Figure 9-2 that initially the entire bed of the flume was subjected to $P_t > 21$ W/m^3 and thus erosive conditions. After a period of time, however, the bed eroded to a new equilibrium profile where $P_t > 21$ W/m^3 only over a very short distance immediately upstream of the weir. It should be noted that the bed-slope correction factor was not applied to this particular example. An adverse slope increases the critical unit stream power for scour.

The problem with this approach is that P_t increases very rapidly as the boundary is approached (Figure 3-5). The CFX model could not compute P_t exactly on the boundary (a finite volume code can only compute values at cell centres and a boundary cannot be a cell centre). P_t had thus to be calculated at some distance off the theoretical boundary (typically 0.5 mm prototype scale). This did not always give realistic results. It soon became apparent that the use of Movability Numbers made the scour condition on the boundary much easier to determine.

Define u_*' as the "virtual shear velocity" where:

$$u_*' = \sqrt{\frac{\tau_{yx}}{\rho}} \tag{9.2}$$

Now define a "virtual Movability Number", u_*' / v_{ss}, that varies throughout the water column. This is depicted in Figure 9-3 for both the initial and eroded states.

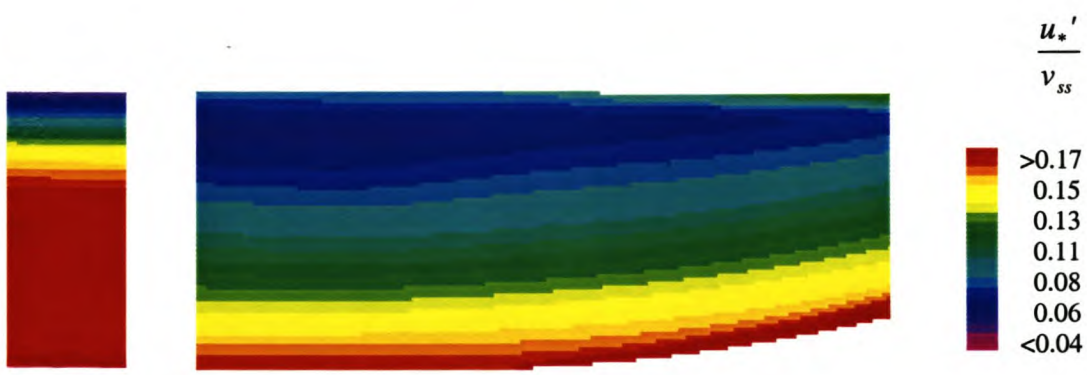

a) Initial State b) Eroded State

Figure 9-3: Typical virtual Movability Number contours for the Harnett (1998) experiments (McGahey, 2001)

It is immediately apparent that the scour profile is defined by a Movability Number in the order of 0.17 (at the boundary, $u_*' = u_*$). This is in accordance with the critical conditions for scour proposed in Section 7.4.1 (it was used to help define this value).

9.3 Circular pier situated in a rigid rectangular channel

9.3.1 Physical modelling (Midgley, 2000)

The physical modelling was carried out in the UCT 610 mm flume (previously described in Section 7.3.2) by Midgley (2000) (Figure 9-4). The flume was levelled to eliminate bed-slope as a parameter. A 45 mm diameter circular pier, supported by specially constructed brackets from above, was installed in the test section. Initially, the glass bottom of the flume was free of sediment. Uniform quartzitic sand was introduced into the flow from upstream and allowed to deposit on the bottom of the flume around the pier, usually leaving a sediment-free area in the vicinity of the structure. Once equilibrium had apparently been reached, the sediment and water supplies were cut off and the "scour" profile around the pier measured.

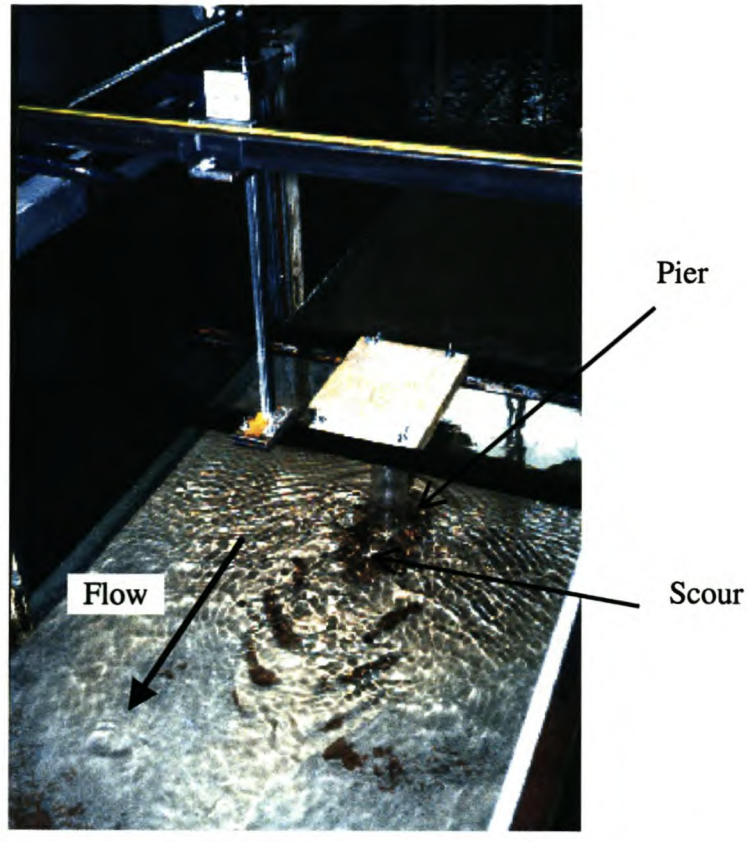

Figure 9-4: View of one of the Midgley (2000) pier experiments

Five sediment size ranges were used. Their details are summarised in Table 9-2. The critical applied power conditions for scour (e.g. $P_{t(crit)}$) were based on the largest particle size in the range and turbulent boundary conditions. It became apparent from the numerical analysis that shear velocities are greatly increased in the turbulent zone around a structure. This raises the Re_d over that which would pertain in uniform flow conditions, and thus the boundaries were turbulent in this region.

d (μm)	v_{ss} * (mm/s)	P_r (W/m^3)	$P_{t\,(crit)}$ (W/m^3)
150 – 300	48.3	782	11.7
300 – 425	70.8	1 150	17.0
425 – 500	82.9	1 340	20.0
500 – 600	97.8	1 580	23.6
600 – 850	130.0	2 100	31.4

* The settling velocity was calculated using Equation 3.12 and the maximum d

Table 9-2: Details of the sediment used in the Midgley (2000) and Mitchell (2000) experiments

The boundary was laminar in the scoured region around the structure. This was not of great concern because friction losses at a boundary are relatively small compared to viscous losses in rapidly varied flow, and it was the edge of the scoured region that was the focus of attention, not the interior. It proved to be convenient to deposit the sediment onto the initially laminar, glass bed. A separate experiment showed that there was no significant difference in the scour shape between this and the one obtained by scouring an initially sediment-covered bottom.

Midgley used the five different sediment sizes together with three different flow velocities (7.69 *l*/s, 9.31 *l*/s and 11.1 *l*/s) and three different Froude Numbers (0.20, 0.25, and 0.30). There were thus 45 measurement scour profiles in all.

9.3.2 Numerical modelling (McGahey, 2001)

McGahey (2001) applied the numerical model to the case: d = 500 – 600 μm, Q = 7.69 *l*/s, Fr = 0.20 (Y = 74.4 mm). A typical velocity vector plot for one depth is depicted in Figure 9-5. The unit stream power contours in the bottom 550 μm of the flow depth (the average height of the sediment) are depicted in Figure 9-6a), whilst the Movability Number contours are depicted in Figure 9-6b).

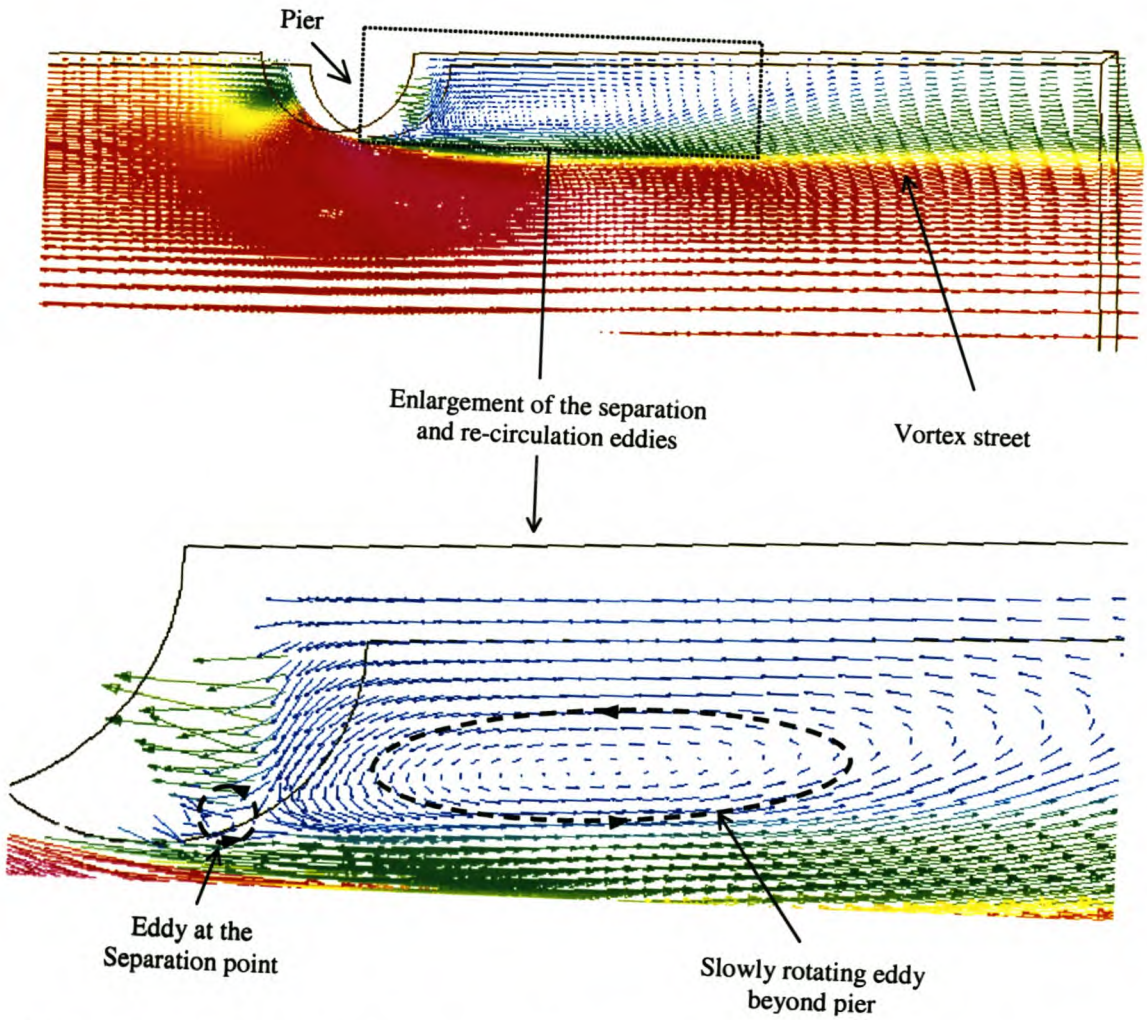

Figure 9-5: Typical velocity vector plot for the flow around a pier (rigid bed) (McGahey, 2001)

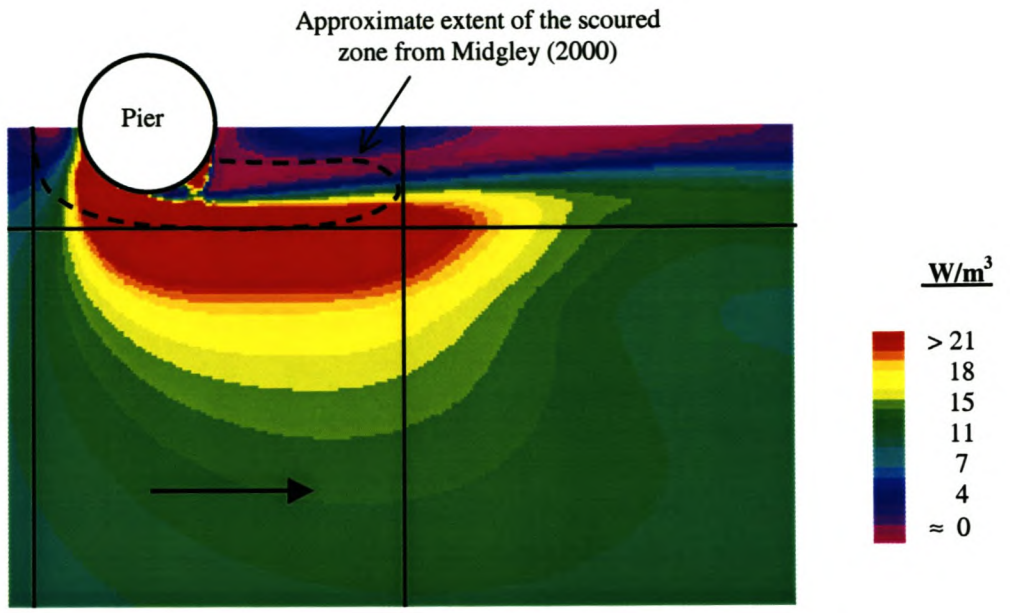

a) Unit stream power plot (next to the bed)

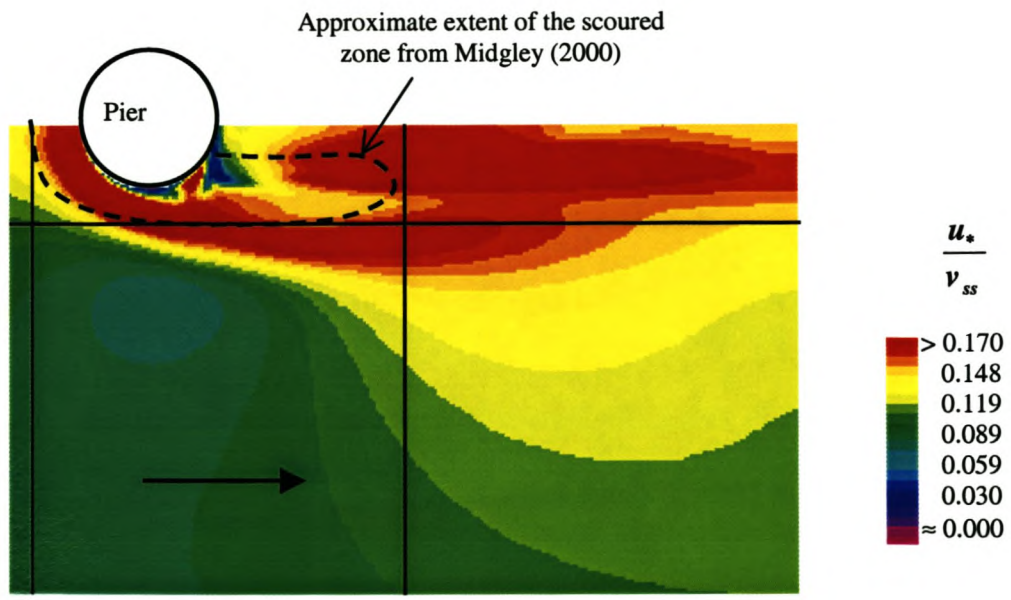

b) Movability Number plot

Figure 9-6: Typical scour zone around a pier
(d = 500 – 600 µm, Q = 7.69 *l*/s, Fr = 0.20) (McGahey, 2001)

The velocity vector plot (Figure 9-5) may be compared with the description of the typical flow patterns around a pier contained in Section 5.4.2. The plot indicates a vertical downflow along the leading face of the pier (not shown in Figure 9-5). It shows the wake vortex that forms in the separation zone to the side and slightly to the rear of the pier. It even shows a re-circulation region downstream of the pier roughly along the line of the expected Vortex Street. Since there is no scour hole, there is no lee eddy. Since the free surface was modelled by a moving boundary (Section 8.4.4) which tends to suppress free vortices (Section 8.9), it is unlikely that a Vortex trail would have been evident even if a transient analysis had been undertaken instead of the actual steady-state analysis.

The predicted scour area is shown in red in both the unit stream power plot (Figure 9-6a)) and the Movability Number plot (Figure 9-6b)). The former seems to predict the approximate extent of the scour zone, but in the wrong place. The predicted scour zone is shifted backwards and outwards relative to the measured scour zone. The latter correctly predicts the scour zone upstream of the pier, but once again, it suggests that the scour zone should be displaced outwards a little more downstream of the pier. Furthermore, it predicts scour in the lee of the pier in what is usually a deposition zone (see Section 5.4.3).

It is quite possible that these anomalous results can be largely explained by the use of a moving, essentially flat, boundary for the free surface. The flat surface boundary suppresses the formation of the bow roller thereby reducing the strength of the downflow. This will reduce the unit stream power at the base of the leading edge of the pier – as observed. It also distorts the flow patterns in the lee of the pier. In this region, the water surface would be expected to drop owing to the acceleration of the flow around the sides of the pier. Keeping the free surface artificially elevated increases the pressure on the bed, which in turn increases the local shear stresses and forces the high-speed separated jet further away. This is exactly as observed.

What is not so easy to explain is why the unit stream power plot (Figure 9-6a)) shows a deposition zone in the lee of the pier (correctly), whilst the Movability Number plot (Figure 9-6b)) shows a scour zone in the same place (incorrectly). This is possibly because unit stream power is computed using Equation 4.16:

$$P_t = \Phi = \mu_b \left(\frac{\partial u_i}{\partial x_j} + \frac{\partial u_j}{\partial x_i} \right) \frac{\partial u_i}{\partial x_j} \tag{4.16}$$

If the unit stream power is small, it is because the velocity gradients are small. Smaller than normal velocity gradients could result from an artificially level free surface. The Movability Number, however, is directly proportional to the shear velocity, which in turn is calculated with the aid of Equation 2.13:

$$u_* = \sqrt{\frac{\tau_0}{\rho}} \tag{2.13}$$

If the shear stress at the bed, τ_0, is being kept artificially high by, for example, a high free surface, this will raise the Movability Numbers accordingly. The two effects thus have opposite effects on the two ostensibly equivalent measures that might explain the discrepancy between them.

Another reason why the scour prediction is poor in the separated zone in the lee of the pier is because the k-ε turbulence model that was used for this analysis is only an approximation of the real situation. The error increases with the degree of turbulence.

9.4 Rectangular abutment situated in a rigid rectangular channel

9.4.1 Physical modelling (Mitchell, 2000)

Mitchell (2000) carried out the physical modelling in a custom made flume constructed within the concrete wave basin situated in the UCT hydraulics laboratory (Figure 9-7 and 9-8). The flume was 8 m long, 820 mm wide and 650 mm high. The walls were constructed of brick and were plastered and painted with a waterproofing sealant. Cement slurry was placed on the concrete floor and covered with glass sheets to provide a smooth level surface.

Water was supplied to one side of the basin via a constant head tank through a 160 mm diameter uPVC pipe. It was regulated with the aid of a gate valve on the end

of this inlet pipe. This side of the basin was separated from the remainder by a baffle wall designed to reduce wave action. The water was then discharged over a 90° V-notch weir into the flume. Rubble placed below the V-notch weir reduced the turbulence emanating from the weir. This was followed by a flow guide comprising 150 mm long lengths of 20 mm LDPE irrigation pipe tightly bundled together and orientated in the direction of the flow. The water was discharged from the flume via a 300 x 300 m sluice gate situated in a sump located at the end. From here, the water was returned to the header tank via two large sump pumps. The water depth could be regulated with the aid of the sluice gate.

An orifice plate equipped with a mercury filled manometer and located on the inlet pipe allowed coarse adjustment of the flow via the gate valve. The estimation of the flow rate was however made with the aid of the V-notch weir. Depth measurements were made with the aid of a Vernier Depth Gauge located along the centreline of the flume. The Vernier Depth Gauge was mounted on a bracket that slid on two parallel rails that were levelled and bolted to the top of the two walls. Since the depth readings were probably only accurate to the nearest 1 mm, the flow measurement error was probably in the order of 5%.

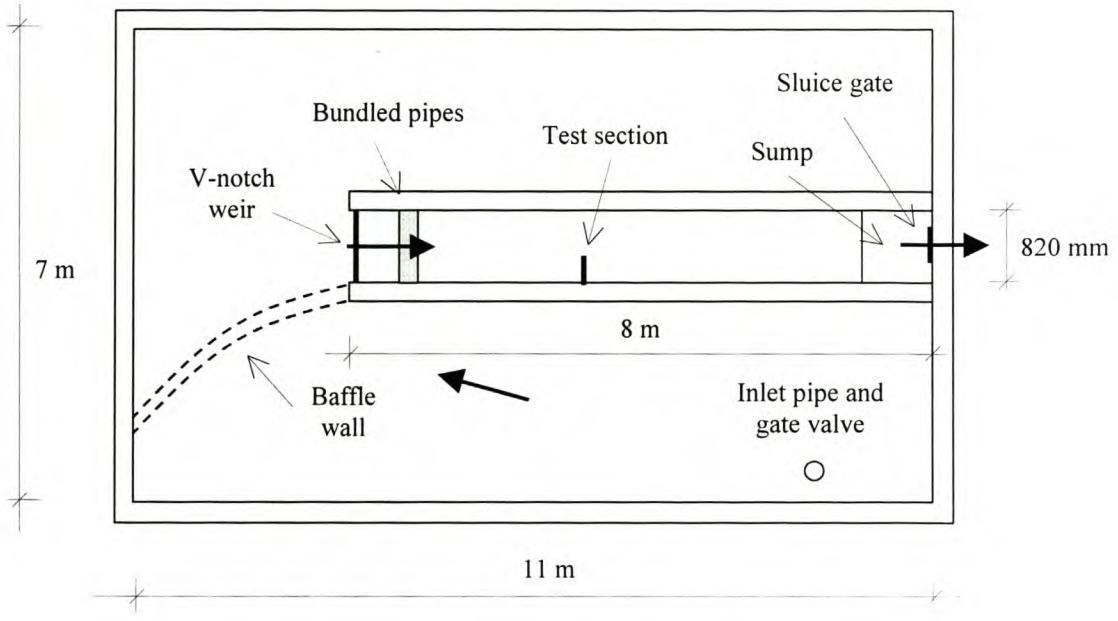

Figure 9-7: Plan of the UCT 820 mm flume

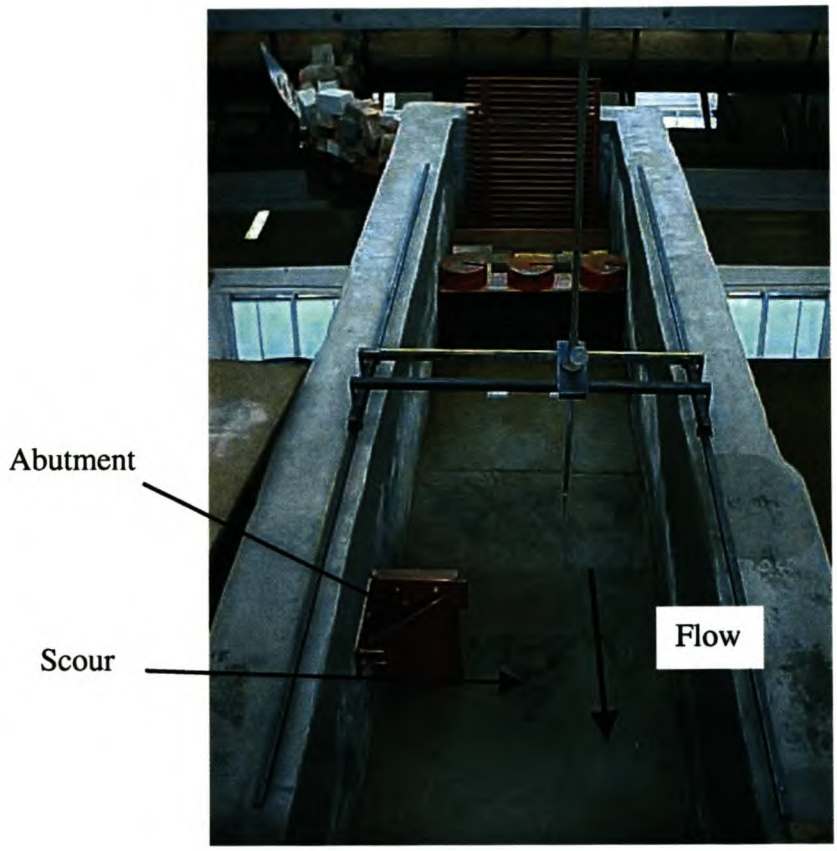

Figure 9-8: View of the apparatus used for the Mitchell (2000) abutment experiments

The abutment was made out of a rectangular piece of wood 300 mm high, 220 mm wide and 35 mm thick. The wood was painted with a waterproof varnish to stop it from warping. It was held in place at the top by a steel frame, which in turn was bolted rigidly into the wall. Silicone sealant was used to fill the gap between the abutment and the flume bottom and side.

Mitchell (2000) followed the same general procedure as Midgley (2000) (Section 9.3.1) with the slight difference that this time the sand was laid uniformly over the glass bottom prior to the commencement of the test. The same sediment was used (Table 9-2). The flow was then allowed to scour the sand until equilibrium had apparently been reached, when the flow was cut off and the "scour" profile around the abutment measured. A separate experiment showed that there was no significant difference in the scour shape between this and the one obtained by introducing the sand into the flow from upstream and allowing it to deposit on the bottom of the

flume around the abutment. One difference, however, was that there was very little deposition in the lee of the abutment in the latter instance, but this was because the presence of the abutment cut off the source of sediment.

As with Midgley (2000), Mitchell (2000) carried out 45 measurements using five different sediment sizes together with three different flow rates (10.2 *l*/s, 14.2 *l*/s and 16.5 *l*/s) as well as three different Froude Numbers (0.07, 0.09 and 0.13).

9.4.2 Numerical modelling (McGahey, 2001)

McGahey (2001) applied the numerical model to the case: d = 500 – 600 μm, Q = 10.2 *l*/s, Fr = 0.13 (Y = 100.0 mm). A typical velocity vector plot for one depth is depicted in Figure 9-9. The unit stream power contours in the bottom 550 μm of the flow depth (average height of the sediment) are depicted in figure 9-10a), whilst the Movability Number contours are depicted in Figure 9-10b).

The velocity vector plot (Figure 9-9) may be compared with the description of the typical flow patterns around an abutment contained in Section 5.5.2. As with the pier, it shows the wake vortex that forms in the separation zone to the side and slightly to the rear of the leading edge of the abutment. It shows the re-circulation region downstream of the abutment in the dead water zone. As there is no scour hole, the principal vortex, which forms in the scour hole upstream of the abutment, is not evident. Since the free surface was modelled by a moving boundary (Section 8.4.4) which tends to suppress free vortices (Section 8.9), the Vortex trail is only indicated by the separation streamlines emanating from the edge of the abutment.

The predicted scour area is shown in red in both the unit stream power plot (Figure 9-10a)) and the Movability Number plot (Figure 9-10b)). Both plots seem to predict the approximate location of the scour zone, but not the full extent. Since it is possible that the Mitchell (2000) test did not completely reach equilibrium (the average run length was in the order of 3 hours), it is also possible that a better fit would have been obtained if the run time had been extended. Away from the area of interest, there is some deviation between the two plots, particularly in the area near the wall downstream of the abutment where the Movability Number plot indicates a much higher scour potential that suggested by the unit stream power plot. Once again, this is possibly as a consequence of distortion caused by the modelling of the free-surface boundary condition (moving, essentially flat, boundary).

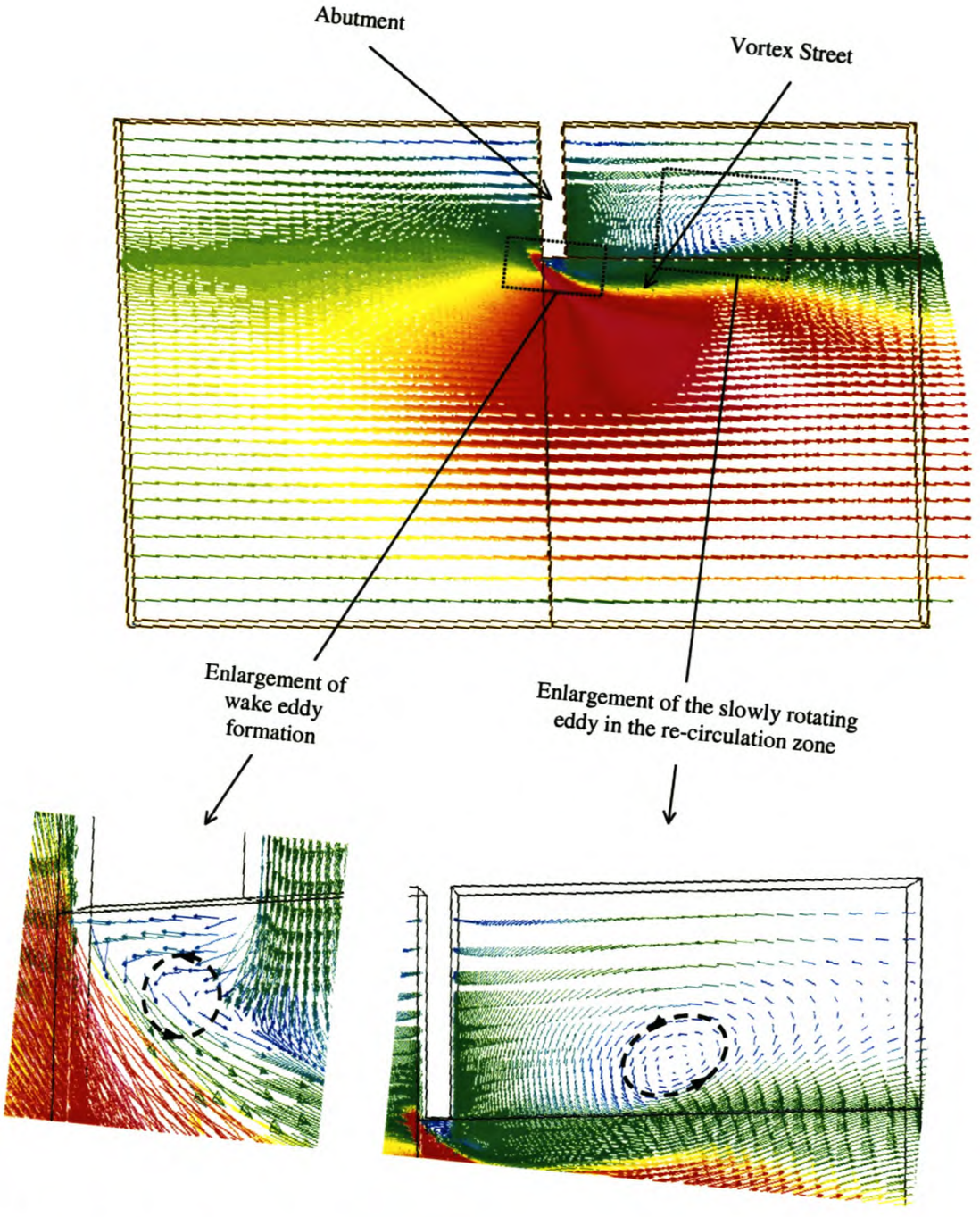

Figure 9-9: Typical velocity vector plot for the flow around an abutment (rigid bed) (McGahey, 2001)

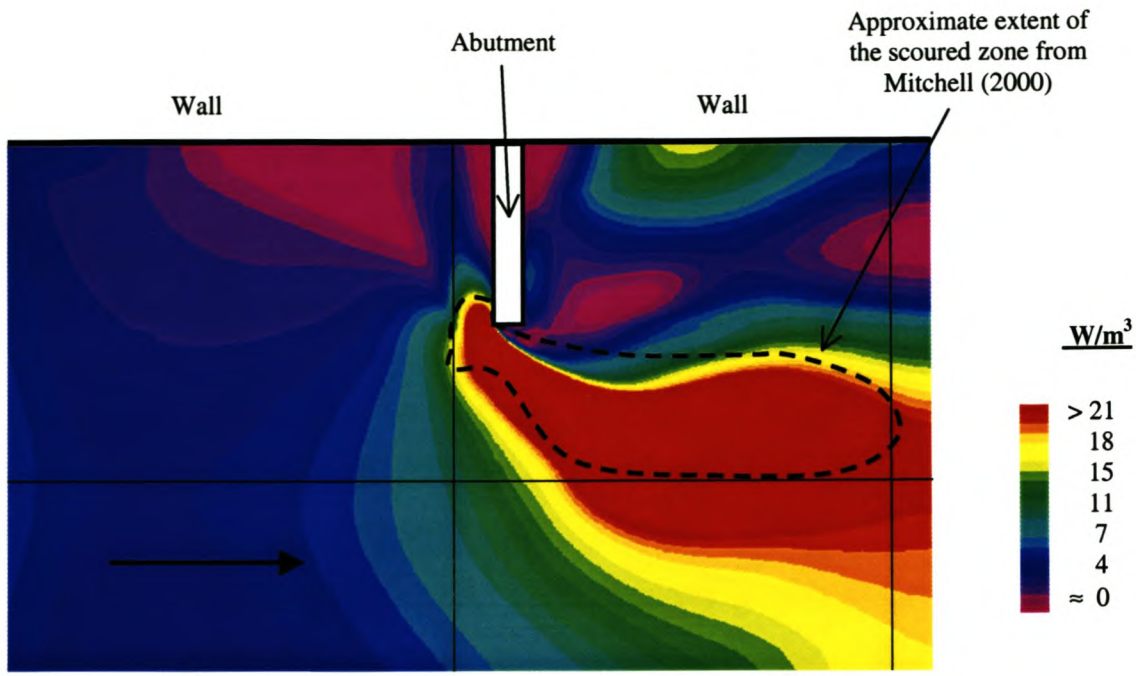

a) Unit stream power plot (next to the bed)

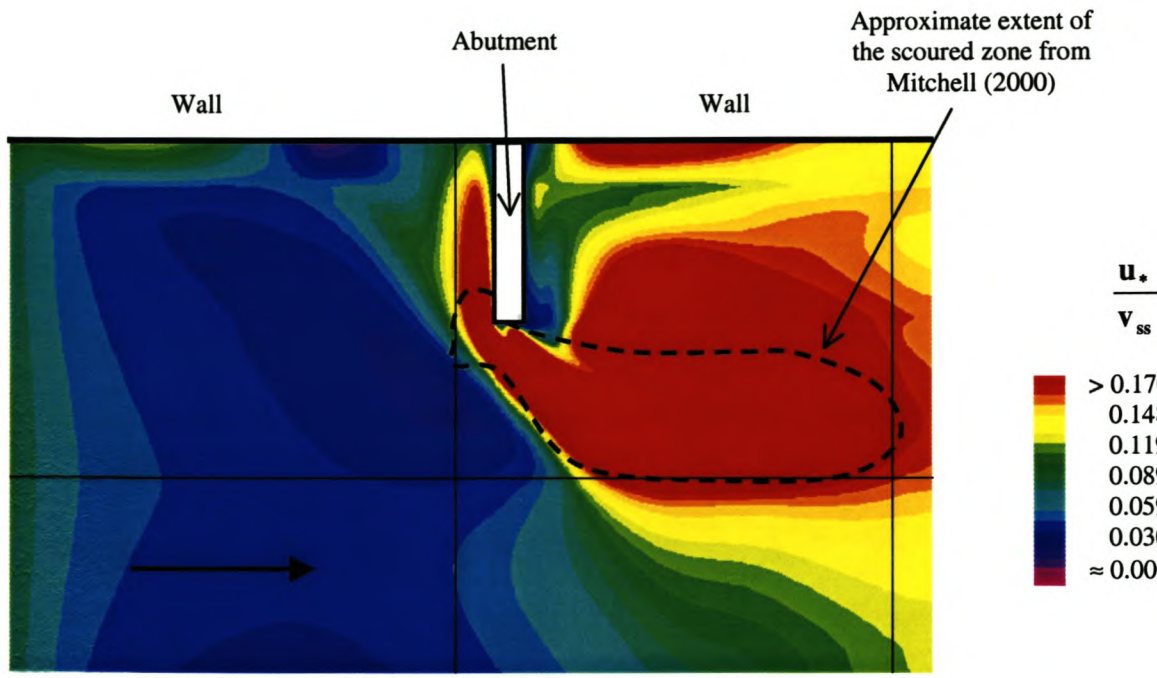

b) Movability Number plot

Figure 9-10: Typical scour zone around a pier
(d = 500 – 600 µm, Q = 10.2 *l*/s, Fr = 0.13) (McGahey, 2001)

9.5 Circular pier situated in a channel with loose boundaries

9.5.1 Physical modelling (Babaeyan-Koopaei, 1996)

Babaeyan-Koopaei (1996) measured equilibrium scour profiles in uniform sands around piers and abutments at the University of Newcastle upon Tyne, UK. The apparatus used for the tests comprised a 22 m long by 2.5 m wide flume. It was partially filled with quartzitic sand having a particle mean diameter, d_{50}, of 1 mm. The surface was smoothed off.

The tests were conducted in so-called "regime channels". A trapezoidal channel was cut along the centre-line of the flume. A fixed discharge was then passed down the channel until it had formed itself into a stable section (Figure 9-11). The structure was then carefully located near the middle of the flume and subjected to the same discharge until such time that equilibrium conditions had been reached (Figure 9-12).

Figure 9-11: A typical self-formed (regime) channel (Babaeyan-Koopaei, 1996)

Figure 9-12: An example of equilibrium scour around a pier group
(Babaeyan-Koopaei, 1996)

9.5.2 Numerical modelling (McGahey, 2001)

McGahey (2001) modelled one of the Babaeyan-Koopaei (1996) tests (Test No. 38B). This involved a single 48 mm diameter circular pier located in the centre of the regime channel. The discharge was 2.5 *l*/s, the average water depth was 129.5 mm, and the average velocity was 0.301 m/s. The maximum water depth adjacent to the pier was 55.6 mm. A half-section of the channel was modelled in both its initial (regime channel) and final (scour channel) states. Only the Movability Number calculations were made in this instance in the interests of saving time.

The particle settling velocity was not measured experimentally. The estimated settling velocity of 0.129 m/s was taken as the mean of the values obtained from Equations 3.8 and 3.12.

In general, the critical Movability Number for a sloped bed is determined from:

$$\left.\frac{u_*}{v_{ss}}\right|_{\beta,\gamma} = \psi \left.\frac{u_*}{v_{ss}}\right|_0 \tag{6.17}$$

where the subscripts β and γ refer to the longitudinal and transverse slopes respectively, and the subscript 0 refers to incipient scouring conditions on a flat bed (Equations 7.21 and 7.22 or Figure 7-8).

The slope correction factor, ψ, is given by:

$$\psi = \sqrt{\cos\beta\left(1-\frac{\tan\beta}{\tan\phi_r}\right)\cos\gamma\left(1-\frac{\tan^2\gamma}{\tan^2\phi_r}\right)}^{1/2} \tag{6.18}$$

The scour potential (Movability Number) is equal to the difference between the Movability Number calculated by the program, and the critical Movability Number calculated from Equation 6.15:

$$\Omega = \left.\frac{u_*}{v_{ss}}\right|_{computed} - \left.\frac{u_*}{v_{ss}}\right|_{critical} \tag{8.6}$$

The scour potential indicates the extent to which the flow is trying to scour the bed (positive value) or deposit on it (negative value). A zero scour potential indicates that the flow neither wants to scour or deposit i.e. the bed is in equilibrium with the flow at that point.

Figure 9-13 shows the Movability Numbers calculated by the program in the vicinity of the pier prior to the commencement of scour. The values are in the range 0.2 to 0.4 at a nominal height of 0.5 mm above the bed. Since the critical Movability Number

for incipient motion over a turbulent boundary (as is the case here) is 0.17, erosive conditions are indicated. The results were plotted using the program IDL (2000).

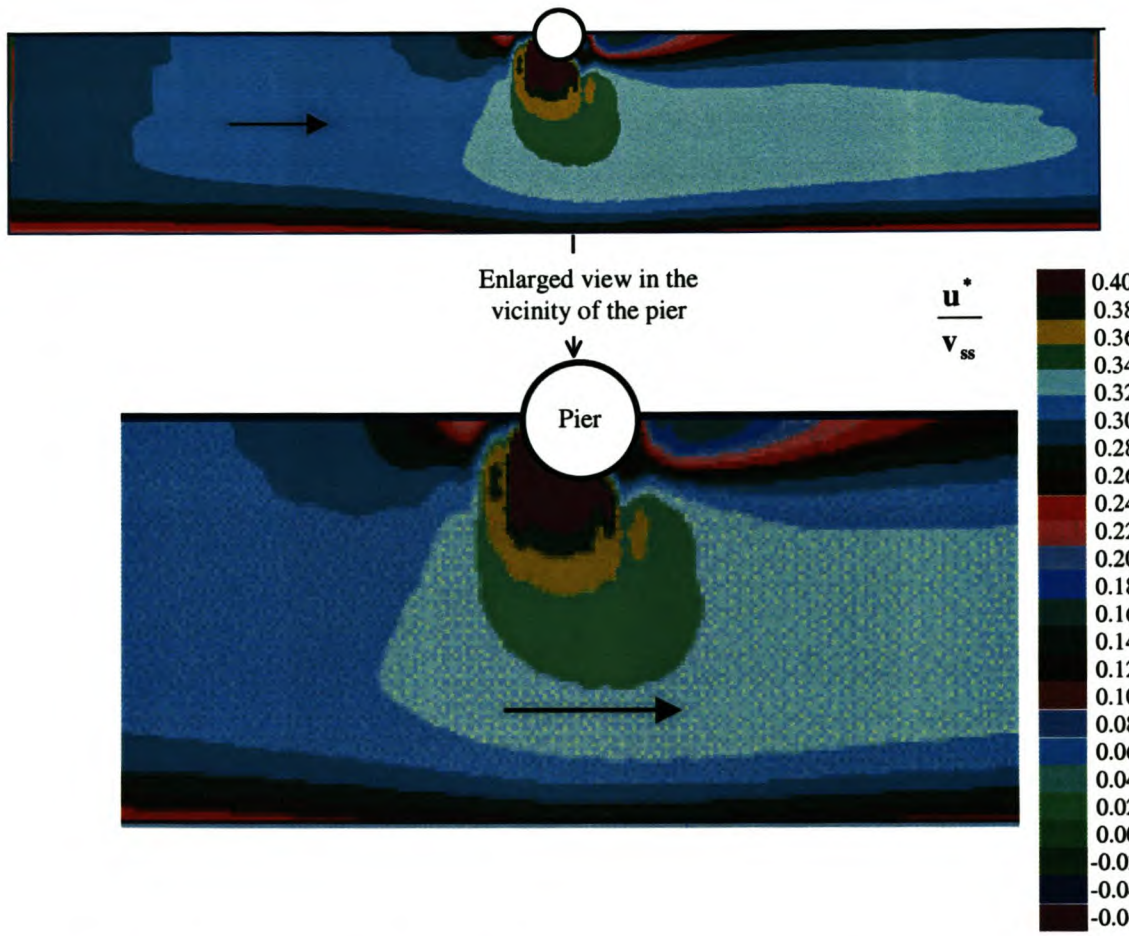

Figure 9-13: The Movability Number distribution in the vicinity of a pier before the development of local scour (McGahey, 2001)

Figure 9-14 shows the same flow condition, but this time showing the scour potential. Most of the values fall in the range 0.1 to 0.25 indicating erosive conditions. The values are highest in the vicinity of the pier, indicating the greatest scour potential in this region.

Ideally, the scour potential could be used to indicate the probable deformation of the boundary. This would be an iterative procedure with the scour potentials being determined for the proposed new boundary. The final solution would be obtained once all scour potentials were close to zero. In CFX Versions 4, this can not be

automated. A new geometry would have to be determined for each iteration by the operator. In this instance, only the initial and final scour developments were modelled.

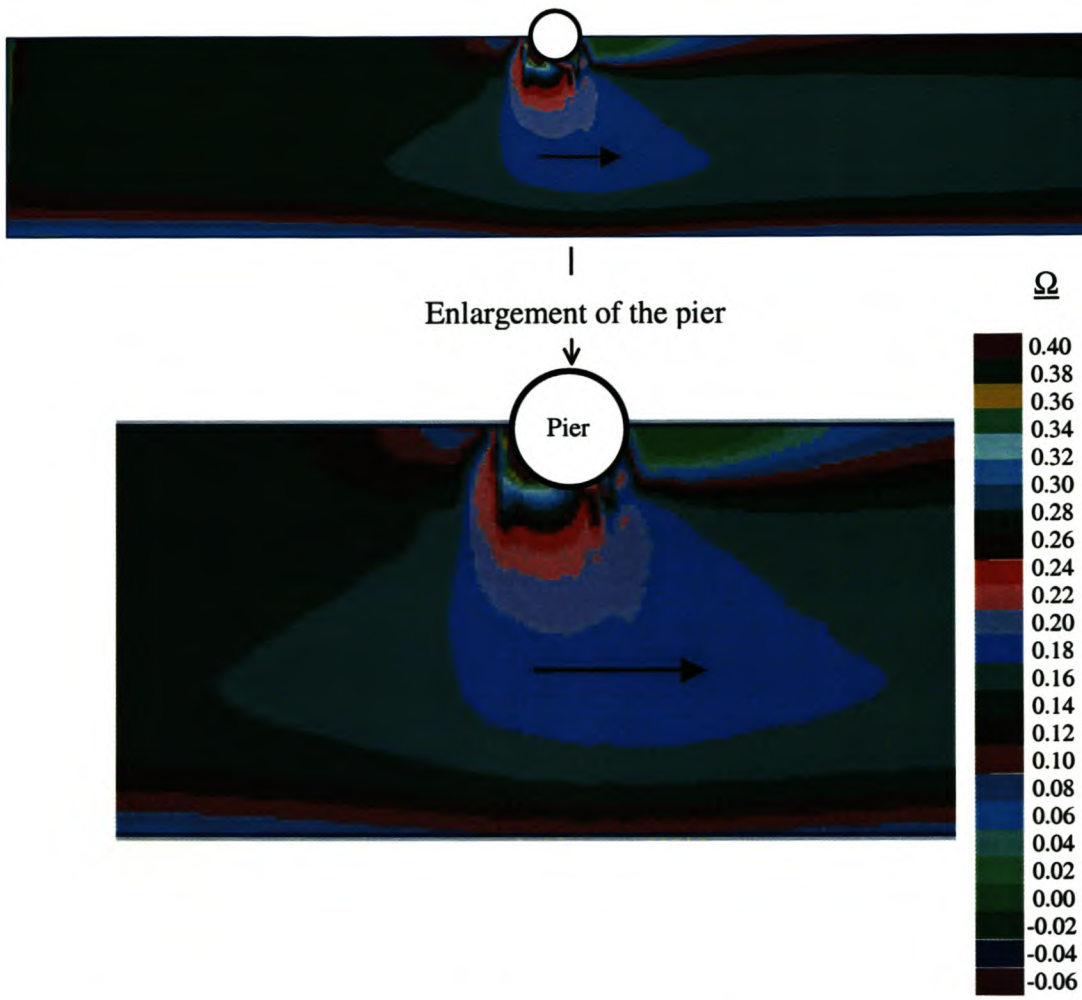

Figure 9-14: The scour potential distribution in the vicinity of a pier before the development of local scour (McGahey, 2001)

Figure 9-15 depicts a 3D view of the scoured channel. Figure 9-16 depicts the elevation of the bed in the physical model and the CFD model on a cross-section through the centreline. Figure 9-17 depicts the elevation of the bed in the physical model and the CFD model on a long-section through the centreline. The profile in the CFD model is created through best-fit smooth curves through spot-heights measured in the physical model. The result is a slight deviation between the two profiles.

Figure 9-18 depicts the associated Movability Numbers. It is immediately apparent that the Movability Numbers are generally much lower than they were previously, typically in the range 0.2 to 0.4.

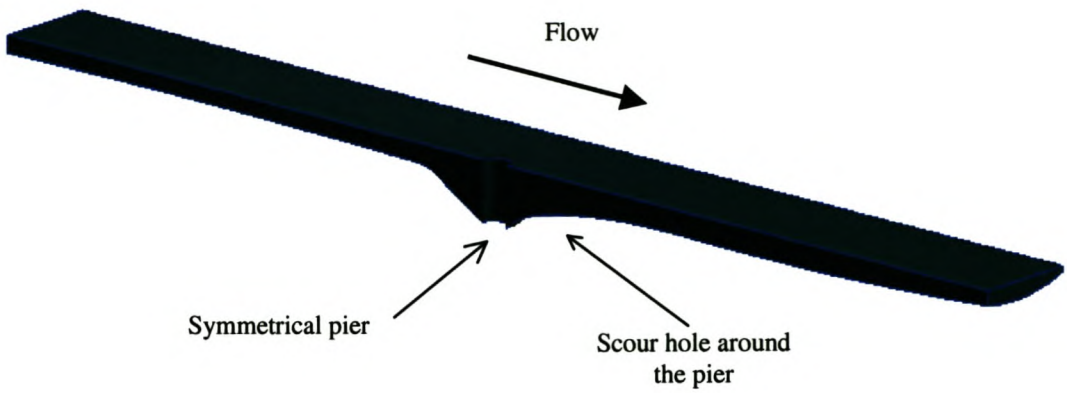

Figure 9-15: 3D view of the scoured channel around a pier (McGahey, 2001)

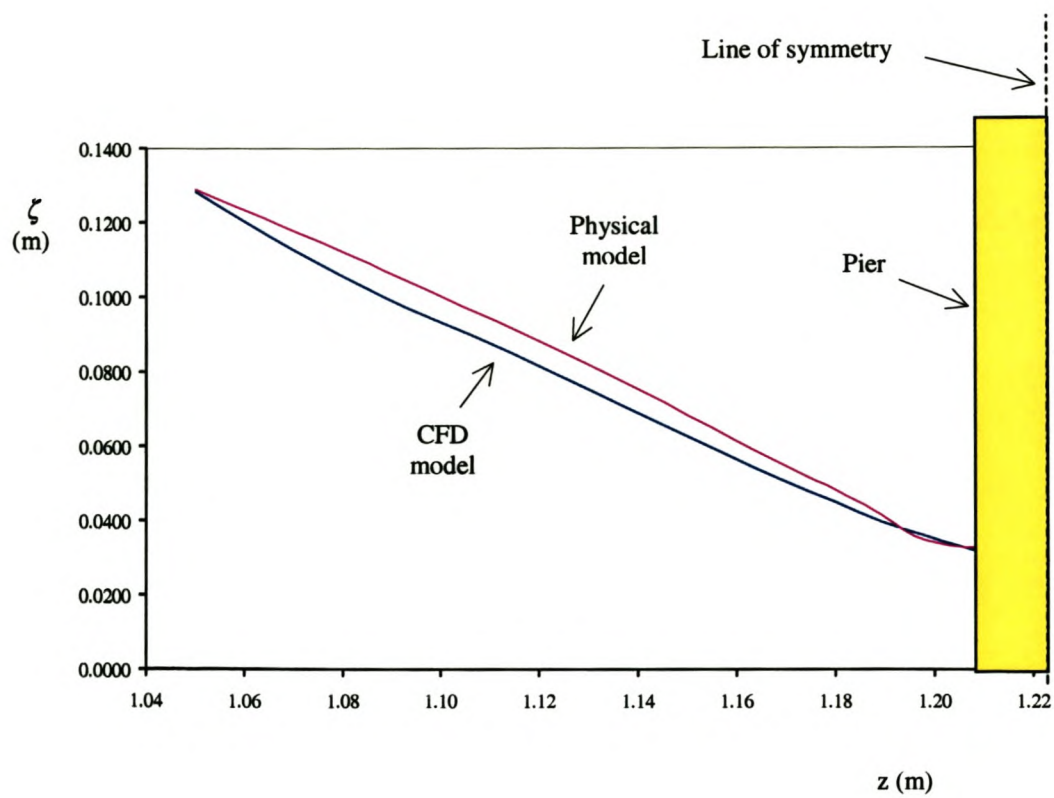

Figure 9-16: The elevation of the bed in the physical model and the CFD model on a cross-section through the centreline (McGahey, 2001)

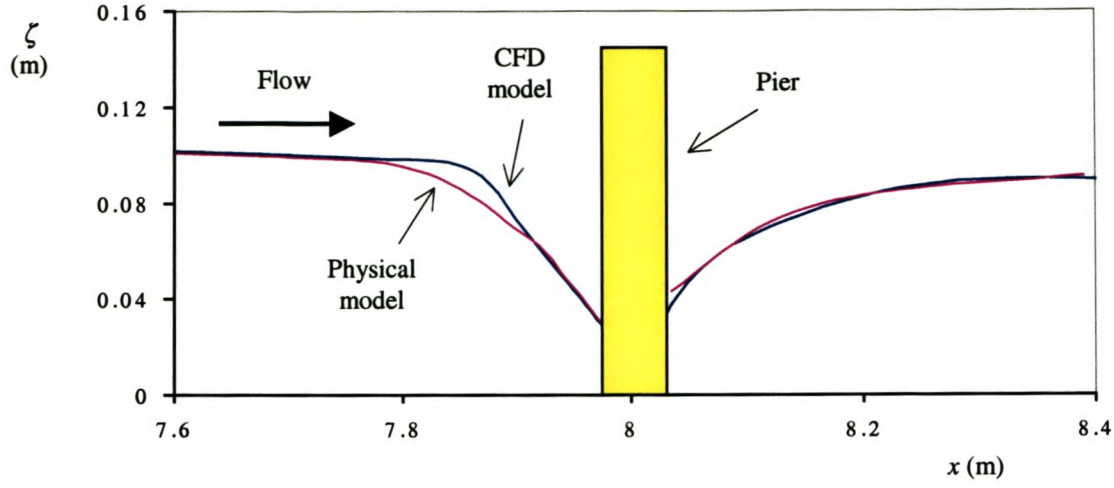

Figure 9-17: The elevation of the bed in the physical model and the CFD model on a long-section through the centreline (McGahey, 2001)

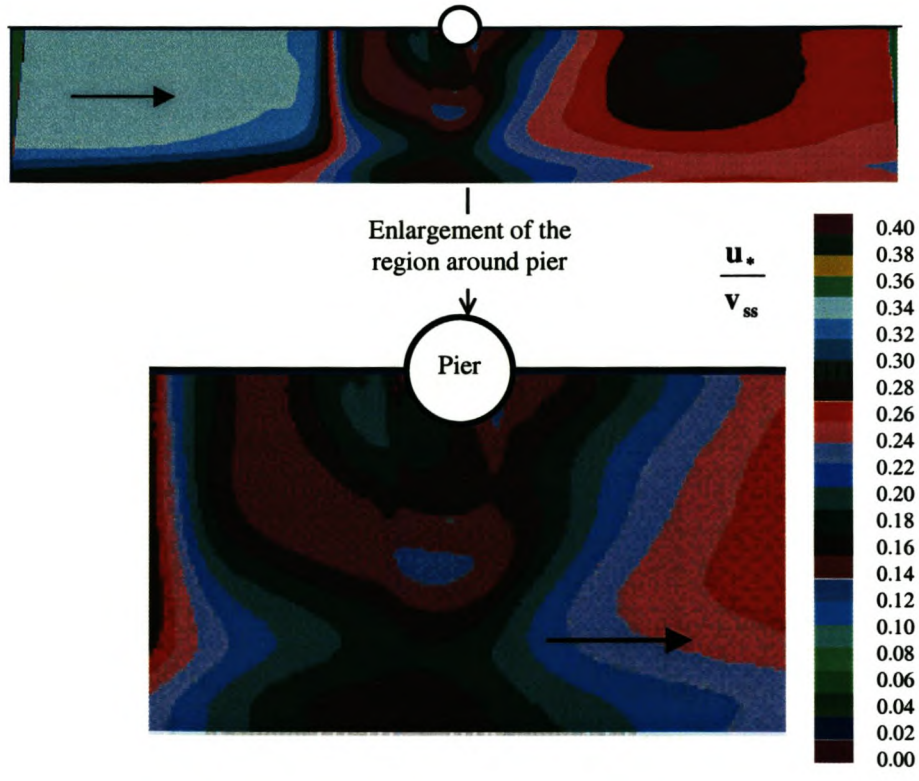

Figure 9-18: Movability Number distribution in the vicinity of a pier after the development of local scour (McGahey, 2001)

Figure 9-19 depicts the scour potential over the scoured boundary. The values fall in the range -0.04 near the scour hole to 0.06 further away. This indicates that the profile is approximately in equilibrium with the flow. Since the CFD bed profile is an approximation of the physical model profile, it is possible that a more accurate rendition would have improved the result.

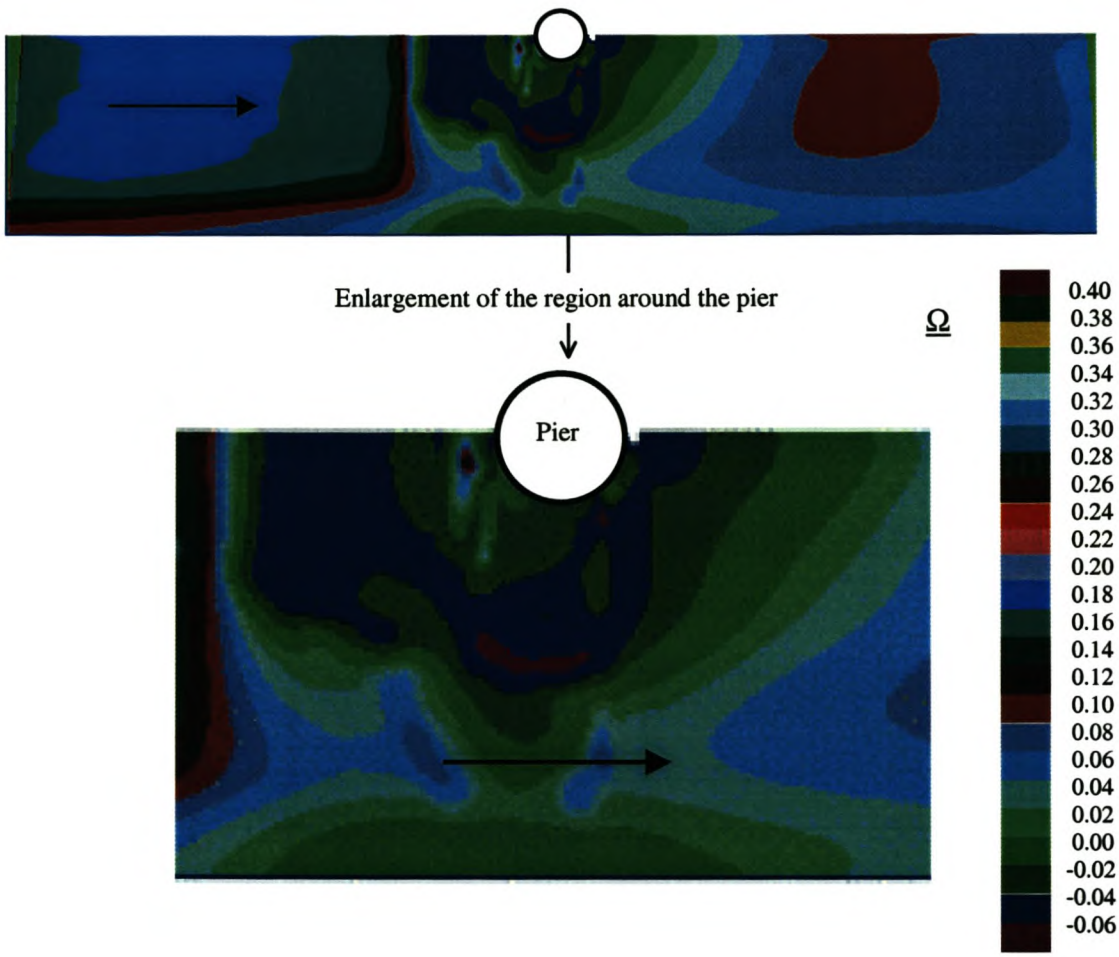

Figure 9-19: The scour potential distribution in the vicinity of a pier after the development of local scour (McGahey, 2001)

9.6 Comparison with previous numerical models

Sections 5.4.6 and 5.5.4 summarise the published attempts to model the local scour around piers and abutments respectively. It should be noted that it was never the intention of this study to provide a "state of the art" computer program to predict local scour. This would have taken far more time and resources than was available. Rather, the purpose of the numerical modelling was to help validate the scour model developed in Chapters 6 and 7, and show how this scour model could be used to predict the scour around several common obstacles. In spite of this, much was achieved within the limitations of the software (CFX Version 4.3) and the machine (667 MHz Intel Pentium III with 256 MB of RAM). A brief comparison between the achievements of published models and this study follows.

9.6.1 Local scour around a pier

Richardson & Panchang (1998) only managed to model the flow field and likely sediment movement through pre-determined scour geometries. This was similar to what was achieved in this study except that here the scour potential is also indicated.

Olsen & Melaaen (1993) showed how the scour potential determined from one run could be used to modify the geometry of the bed for the next. This procedure was later automated (Olsen & Kjellesvig, 1998). The improved program also automatically determined the free surface. This is extremely impressive and far more than what was achieved in this study, but it should be noted that this took extensive development and a single run required nine weeks on an IBM-370 workstation.

9.6.2 Local scour around an abutment

Most published work describes only 2D modelling of the flow around an abutment (Zaghlou & McCorquodale, 1973; Tingsanchali & Maheswaran, 1990; Molls & Chaudhry, 1995; Biglari & Sturm, 1998). Only Ouillon & Dartus (1997) report on 3D flow modelling such as was achieved here. As with the present study, scour profiles were not directly determined, but in some cases the scour potential could be inferred from the flow parameters at the bed. It is clear that the work reported here is on a par with that described in the literature.

9.7 Conclusions

The theoretical model which was developed in Part 2 (Chapters 6 & 7) was used to model the scour potential in four test cases:

i) Upstream of a weir.

ii) Around a pier situated in a rigid rectangular channel.

iii) Around an abutment situated in a rigid rectangular channel.

iv) Around a pier installed in a regime channel with deformable boundaries.

In the first and last cases, both initial (before scour) and final (after scour) profiles were modelled. The situations were of increasing complexity from a 2D problem (the weir), through to a 3D problem incorporating deformable boundaries. In each case, a physical model was available to act as a comparison.

In three of the four cases, there appeared to be considerable agreement between the scour predicted by the numerical model and that measured by the physical model. The exception was case (ii) – scour around a pier situated in a rigid rectangular channel. In this example, scour was predicted in the lee of the pier when Movability Numbers were calculated, whilst unit stream power and the physical model indicated deposition. This could have been due to the fact that the water surface was modelled as a plane whereas in reality there is a drawdown of the water surface behind the weir. This level water surface could have the effect of increasing the Movability Numbers whilst reducing the unit stream power in this zone.

Both Movability Numbers and unit stream power generally proved to be suitable for modelling although in the last situation that was modelled, the pier situated in a deformed bed, only Movability Numbers were used. The slope correction factor appeared to adequately adjust the critical values in the case of deformed channel beds. The scour potential, Ω, proved to be an extremely useful means of determining the tendency towards scour and deposition in the situation of a deformed bed.

It appears that the method developed in this thesis has the potential to predict scour and deposition in any situation given the correct boundary conditions. The main limitations at present are:

i) An inadequate free surface routine.

ii) The lack of an unstructured mesh in the CFD package to facilitate corrections to the boundary as scour and / or deposition takes place. In this thesis, only the initial and final states were modelled.

iii) No facility for the program to make continuous corrections to the boundary in response to the scour potential calculations without further input from the user.

iv) The limited capacity of the current generation of machines.

Part 4

Conclusions and recommendations

Chapter 10
Conclusions

At the beginning of this thesis, it was noted that scour and deposition do not simply cause major engineering problems, but they are also largely responsible for shaping the landmasses of the world. In spite of the availability of high-speed computers, most design is still based on empirical formulae or physical model studies. This is because scour and deposition are the results of the complex interaction of many physical factors that are not easily modelled numerically. Empirical formulae, however, have severe limitations. They usually only predict one parameter – the maximum scour depth – and the predicted value of this parameter varies over a large range depending on the formula that is used. Physical models are more reliable, provided that they are constructed at a sufficiently large scale. Physical models, on the other hand, are time consuming to construct and test, and are thus expensive.

The objective of this thesis was to construct a mathematical model of scour and deposition that would provide insight into the scour and deposition processes. To make the problem more tractable, the investigation concentrated on local clear-water scour in uniform, approximately spherical sand particles around structures of simple geometry.

The findings were as detailed below.

i) Although incipient motion – the conditions under which sediment movement commences – can be described in terms of flow velocity, bed shear stress, and stream power, these parameters are related. The first and last parameters can both be expressed in terms of the Movability Number (u_* / v_{ss}) where u_* is the shear velocity and v_{ss} is the settling velocity of the sediment particles in quiescent water. Meanwhile, since u_* is defined by Equation 2.13:

$$u_* = \sqrt{\frac{\tau_0}{\rho}} \tag{2.13}$$

where τ_0 is the bed shear stress and ρ is the density of water, the Movability Number is thus also proportional to the square root of the bed shear stress.

ii) Incipient motion is however something that is hard to define as it refers to some "threshold of motion" within what is actually a stochastic process. Analysis of sediment transportation data revealed that it is possible to link the "intensity of motion" to a Movability Number. This must be, however, adjusted for bed-slope and relative depth. The result is Equation 7.16 and Figure 7-3.

$$\frac{u_*}{v_{ss}} = \psi\left(0.2405 + 0.0066\ln(I) + 0.204\frac{d}{Y}\right) \tag{7.16}$$

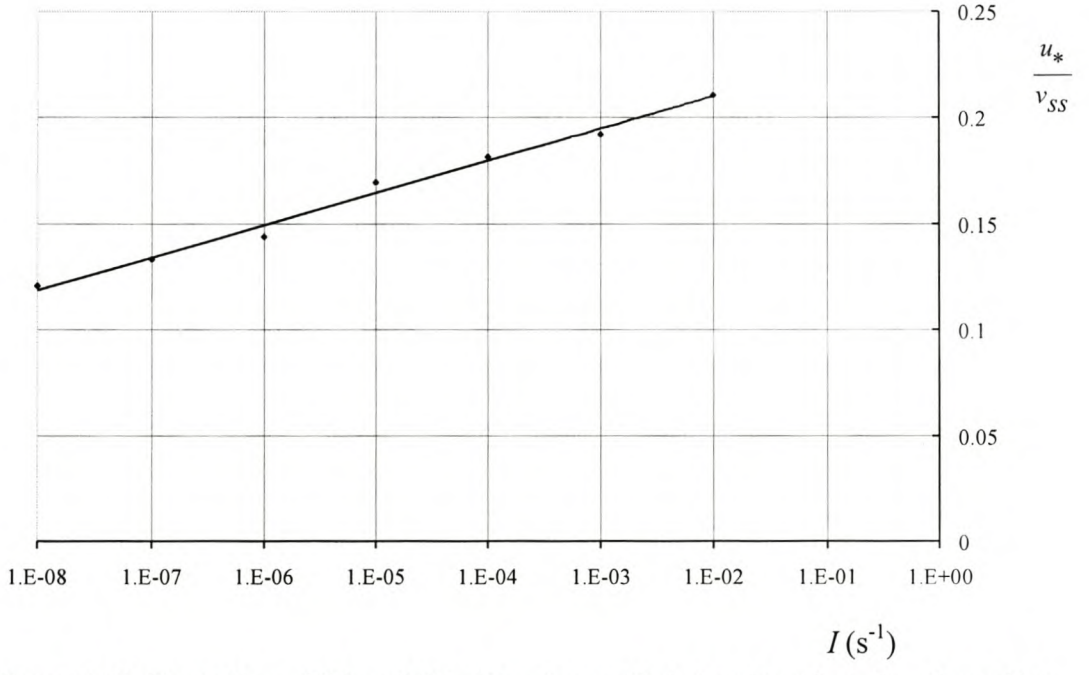

Figure 7-3: Variation of Movability Number with intensity of motion for a flat turbulent bed and zero relative roughness (Semi-logarithmic plot)

In Equation 7.16, I is the intensity of motion, d / Y is the relative depth (particle diameter divided by the water depth), and ψ is the slope correction factor given by Equation 6.18:

$$\psi = \sqrt{\cos\beta\left(1 - \frac{\tan\beta}{\tan\phi_r}\right)\cos\gamma\left(1 - \frac{\tan^2\gamma}{\tan^2\phi_r}\right)}^{1/2} \tag{6.18}$$

In Equation 6.18, β is the longitudinal bed-slope (in the direction of flow), and γ is the transverse bed-slope (normal to the direction of flow).

iii) Work carried out by Shvidchenko & Pender (2000) showed that the intensity of motion, I, can be directly equated to the dimensionless bedload parameter, q_b^*, i.e. Equation 7.12:

$$I = q_b^* \tag{7.12}$$

Equations 7.12 and 7.16 lead naturally to Equation 7.20, which could be used to determine the rate of scour:

$$q_b = \rho_s \sqrt{(s-1)gd^3}\, e^{\xi} \tag{7.20}$$

In Equation 7.20, q_b is the unit bedload transportation rate, ρ_s is the density of the sediment, s is the relative density of the sediment, g is gravitational acceleration, d is the diameter of the (uniform) sediment, and ξ is the exponent given by Equation 7.19:

$$\xi = \frac{1}{\psi}\frac{u_*}{v_{ss}} - 0.204\frac{d}{Y} - 0.2405 \tag{7.19}$$

iv) The analysis of transportation data revealed that there is no specific value of Movability Number at which movement can be said to have begun or ceased. For the purposes of the model presented in this thesis, however, Equations 7.21 and 7.22 can be used to describe the Movability Number criteria at which scour becomes appreciable (taken to be at an intensity of motion $I = 2 \times 10^{-5}$ s^{-1} in this thesis) on horizontal beds ($\psi = 1.00$). These equations are plotted in Figure 7-8:

$$\frac{u_*}{v_{ss}} = \frac{2.0}{Re_*} \quad \text{for } Re_* \leq 11.8 \text{ (laminar boundaries)} \tag{7.21}$$

$$\frac{u_*}{v_{ss}} = 0.17 \quad \text{for } Re_* > 11.8 \text{ (turbulent boundaries)} \tag{7.22}$$

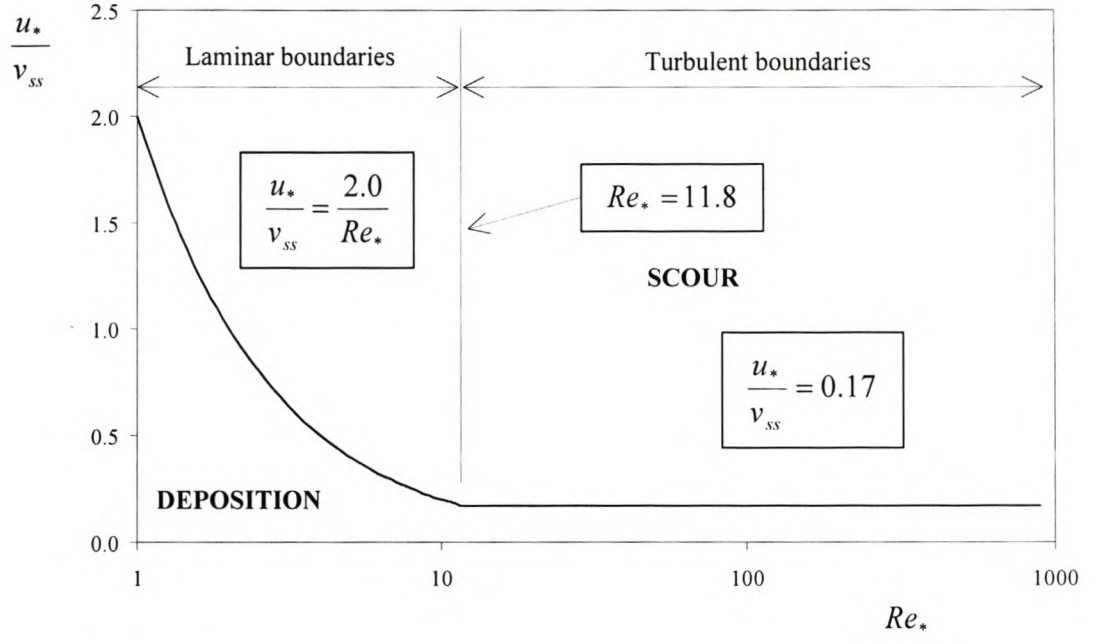

Figure 7-8: New criteria for predicting the onset of scour

If the bed is sloped, then Equation 6.17 is applicable:

$$\left.\frac{\mathbf{u}_*}{\mathbf{v}_{ss}}\right|_{\beta,\gamma} = \psi \left.\frac{\mathbf{u}_*}{\mathbf{v}_{ss}}\right|_{0} \tag{6.17}$$

In Equation 6.17, $\mathbf{u}_* / \mathbf{v}_{ss}$ is the Mobility Number vector having the direction of the shear velocity.

Consideration of Equations 7.21 and 7.22 or Figure 7-8 reveal that that relatively small changes in the flow conditions result in large changes in the intensity of motion.

v) Rooseboom (1992) showed that the unit stream power required to suspend a particle, P_r, could be related to the applied unit stream power, P_t. If η represents the ratio between the two, then this implies Equation 6.1:

$$P_t = \eta P_r \tag{6.1}$$

In Equation 6.1, P_t is the dissipation function, Φ, given by Equation 4.14:

$$\Phi = \tau_{ji} \frac{\partial u_i}{\partial x_j} \tag{4.14}$$

In Equation 4.14, τ_{ji} is the shear stress in the i-direction on a surface with a normal in the j-direction, u_i is the velocity component in the i-direction, and x_j indicates that the gradient is in the direction of the normal to the surface.

P_r is given by Equation 3.32:

$$P_r \approx (\rho_s - \rho) g v_{ss} \tag{3.32}$$

Closer examination of Equations 7.21 and 7.22 reveals that the ratio η is different for laminar boundaries, η_l = 1/6, and turbulent boundaries, η_t = 1/67. As a consequence, for the purposes of the scour model, the onset of scour can be described in terms of unit stream power as follows:

$$P_t \geq \frac{P_r}{6} \quad \text{for } Re_* \leq 11.8 \text{ (laminar boundaries)} \tag{7.24}$$

and,

$$P_t \geq \frac{P_r}{67} \quad \text{for } Re_* > 11.8 \text{ (turbulent boundaries)} \tag{7.25}$$

In the case of the unit stream power equations, correction for bed-slope can be made with the aid of Equations 6.19 or 6.20:

$$P_t = \psi^2 \eta_l P_r \quad \text{(Laminar boundaries)} \tag{6.19}$$

$$P_t = \psi^3 \eta_t P_r \quad \text{(Turbulent boundaries)} \tag{6.20}$$

The main drawback with the above is that unit stream power is a scalar variable, but the calculation of the longitudinal and transverse slopes demands a vector describing the direction of the flow.

vi) From the foregoing, a simple model of scour and deposition around a structure can be proposed (Section 6.4). The sediment transport through a hydraulic structure is determined mainly by the upstream and downstream conditions i.e. the supply and removal of sediment respectively. If the supply rate of sediment to the region around a structure exceeds the removal rate there is accretion at the structure. If the removal rate exceeds the supply rate there will be degradation. Sometimes, potential degradation in the vicinity of the structure is prevented by local conditions e.g. the structure may be founded on a rigid base.

Erosion and deposition around the structure will reach "equilibrium" at the point where the applied unit stream power, P_t, equals the value required for incipient motion. This is indicated by Equations 7.21 and 7.22, or 7.24 and 7.25 modified by Equations 6.17 or 6.19 and 6.20 if there is a non-zero bed-slope. If the unit stream power at the bed is greater than that required for incipient motion, there will be scour. If the unit stream power at the bed is less than that required for incipient motion, but the stream is conveying sediment, there will be nett deposition.

vii) McGahey (2001) tested out the proposed model with the flow parameters calculated with the aid of CFX Versions 4.3 and 4.4 using the k-ε turbulence model. The processor was a 667MHz Intel Pentium III processor (PC) with 256MB of RAM. The model appeared to give good results when applied to the prediction of scour upstream of a weir. The results were not as impressive when the model was applied to the prediction of scour around piers and abutments although the general scour pattern was clearly visible. This could be due in part to the free surface approximation that was implemented. Coding is now available that gives a better determination of the free surface, and that could lead to an improvement in the CFD modelling. The choice of the k-ε turbulence model also plays a role. The accuracy of the numerical model could be improved through the use of Direct Numerical Simulation (DNS) of the Navier-Stokes equations. It is, however, likely to be a very long time before computers are generally available that are capable of adequately modelling the scour

around engineering structures using DNS. The k-ε model is likely to be the best compromise for a while.

When the scour around a pier with a deformable boundary was modelled, the analysis showed that the final profile was consistent with the numerically generated bed conditions.

The unit stream power model presented in this thesis shows considerable promise for the prediction of scour and deposition, but extensive development will be required before the model will be able to solve the entire range of problems facing Engineers in this field.

Chapter 11
Recommendations for future work

i) Further work could be carried out to improve the accuracy of the calculations. The lack of a good free-surface routine undoubtedly had an impact of the results of the numerical analyses. It would be valuable to see what difference would be made if the analyses were repeated with a more advanced CFD package equipped with a good free surface routine. A faster machine with greater memory would also help to improve accuracy since the flow domain could be more finely discretised.

ii) Incipient motion on smooth and transitional channel beds requires more attention. The data presented in Figure 7-7 shows considerable scatter. A thorough examination and analysis of existing data should be carried out. The experiment (described in Section 7.3) could be repeated with measurements of the bed-load.

iii) The investigation should be extended to include cohesive materials and / or non-uniform materials, live-bed scour, and the impact of other types of structures e.g. drop structures, downstream of weirs or spillways etc.

iv) Equation 7.19 could possibly be used to estimate the rate of sediment deposition and scour-hole development. This should be investigated further. This could be carried out through its inclusion into the computational procedure. It could then be benchmarked against observed deposition and scour hole development. Scour-hole development should also be looked at in the context of flood flows. Flood flows are invariably unsteady and have short-durations.

v) The long-term goal is for the development of a software package capable of predicting scour and deposition around any obstacle. This should be extensively tested against both empirical and physical models to ensure that it provides a more accurate and / or cost-effective solution.

vi) The unit stream power method also has potential for application to related engineering problems, e.g. the design of improved sediment and / or litter traps,

and the transportation of sediments in pipes (stormwater pipes, sewer pipes, and hydrotransport). This should be investigated.

References

References

Ackers, P. & W. R. White (1973). "Sediment Transport: New Approach and Analysis." *J. Hydr. Div. ASCE,* Vol. 99, HY11, pp 2041 - 2060.

Ahmad, M. (1953). "Experiments on Design and Behavior of Spur Dikes." *Proc., Int. Hydr. Convention,* ASCE, New York, pp 145 – 159.

Allan A. F. & L. Frostick (1999). "Framework dilation, winnowing, and matrix particle size: the behavior of some sand-gravel mixtures in a laboratory flume." *Journal of Sedimentary Research*, Vol. 69, No. 1, pp 21 – 26.

Annandale, G. W. (1986). "Reservoir sedimentation: The stable non-equilibrium state." *The Civil Engineer in South Africa*, Vol. 28, No. 5, pp 169 – 174.

Ashworth, P. J., S. J. Bennett, J. L. Best & S. J. McLelland (1996) – editors. *Coherent Flow Structures in Open Channels*. John Wiley & Sons.

Babaeyan-Koopaei, Kourosh (1996). *A Study of Straight Stable Channels and their interactions with Bridge Structures*. PhD thesis, University of Newcastle upon Tyne, UK.

Bagnold, R. A. (1960). *Sediment Discharge and Stream Power*. U.S. Geol. Survey Circular 421, 23 pages.

Bagnold, R. A. (1966). "An Approach to the Sediment Transport Problem from General Physics." *U.S. Geol. Survey Professional Paper 422-I*, 37 pages.

Barton, J. R. & P. N. Lin (1955). "A Study of the Sediment Transport in Alluvial Channels." *Colorado A & M College*, Report No. 55JRB2.

Basson G. R. & A. Rooseboom (1997). *Dealing with Reservoir Sedimentation.* Report No. TT 91/97 of the Water Research Commission of South Africa.

Bennett, S. J. & J. L. Best (1996). "Mean Flow and Turbulence Structure over Fixed Ripples and the Ripple-dune Transition." *Coherent Flow Structures in Open Channels* edited by P. J. Ashworth, S. J. Bennett, J. L. Best & S. J. McLelland, John Wiley & Sons, pp 281 – 304.

Biglari, Bahram & Terry W. Sturm (1998). "Numerical Modelling of Flow around Bridge Abutments in Compound Channel." *J. Hydr. Engrg, ASCE,* Vol. 124, No. 2, pp 156 – 164.

Bonnefille, R. (1963). "Essais de synthese des lois de debut d'entrainment des sediments sous l'action d'un courant en regime uniform." *Bull. du CREC*, No. 5, Chatou.

Breusers, H. N. C. & A. J. Raudkivi (1991). *Scouring. IAHR Hydraulic Structures Design Manual 2.* A. A. Balkema.

Brooks, N. H. (1963) discussion of "Boundary Shear Stresses in Curved Trapezoidal Channels", by A. T. Ippen and P. A. Drinker. *J. Hydr. Engrg., ASCE,* Vol. 89, No. HY3, pp 327 – 333.

Cao, Z. (1997). "Turbulent Bursting-Based Sediment Entrainment Function." *J. Hydr. Engrg. ASCE* Vol. 123, No. 3, pp 233 – 236.

Cellino M, & W. H. Graf (2000). "Experiments on Suspension Flow in Open Channels with Bed Forms." *J. Hydr. Engrg.*, Vol. 38, No. 4.

CFX (1999). *CFX Version 4.3.* AEA Technology (includes Manual).

CFX (2001). *CFX Version 4.4.* AEA Technology.

Chadwick, Andrew & John Morfett (1998*). Hydraulics in Civil and Environmental Engineering, 3rd Edition.* E & FN SPON.

Chang, F. F. M. (1973). *A statistical summary of the cause and cost of bridge failures.* Federal Highway Administration, US Department of Transportation, Washington, D.C.

Chanson, H. (1999). *The Hydraulics of Open Channel Flow*. Arnold.

Chen, C. J., C. Shih, J. Lienau & R. J. Kung (1996). *Flow Modelling and Turbulence Measurements*. A. A. Balkema.

Cheng, D. H. & C. G. Clyde (1972). "Instantaneous Hydrodynamic Lift and Drag Forces on Large Roughness Elements in Turbulent Open Channel flow." *Sedimentation, Symposium to Honor H. A. Einstein*, pp 3-1 to 20.

Cheng, N. -S. (1997). "Simplified Settling Velocity Formula for Sediment Particle." *J. Hydr. Engrg. ASCE*, Vol. 123, No. 2, pp 149 – 152.

Cheng, N. -S. & Y. -M. Chiew (1998). "Pickup Probability for Sediment Entrainment." *J. Hydr. Engrg. ASCE* Vol. 124, No. 2, pp 232 – 235.

Cheng, N. -S. & Y. -M. Chiew (1999). "Analysis of Initiation of Sediment Suspension from Bed Load." *J. Hydr. Engrg. ASCE* Vol. 125, No. 8, pp 855 – 861.

Chepil, W. S. (1958). "The Use of Evenly Spaced Hemi-Spheres to Evaluate Aerodynamic forces on a Soil Surface." *Transactions, American Geophysical Union*, Vol. 39, No. 3, pp 397 – 404.

Chepil, W. S. (1961). "The Use of Spheres to Measure Lift and Drag on Wind Eroded Soil Grains." *Proceedings of Soil Science Society of America*, Vol. 25, No. 5, pp 343 – 345.

Chien, Ning & Zhaohui Wan (1999). *Mechanics of Sediment Transport*. ASCE Press.

Chiew, Yee-Ming & Gary Parker (1994). "Incipient sediment motion on non-horizontal slopes." *J. Hydraulic Research*, Vol. 32, No. 5, pp 649 – 660.

Chiew, Yee-Ming (1995). "Mechanics of Riprap Failure at Bridge Piers." *J. Hydr. Div. ASCE,* Vol. 121, No. 9, pp 635 – 643.

Colebrook, C. F. & C. M. White (1937). "Experiments with fluid friction in roughened pipes." *Proc. Roy. Soc. London*, Vol. A161, pp 367 – 381.

Coleman, N. L. (1972). "The Drag Coefficient of a Stationary Sphere on a Boundary of Similar Spheres." *La Houile Blanche*, No. 1 pp 17 – 21.

Dargahi, B (1987). *Flow field and local scouring around a cylinder. Bulletin TITRA-VBI-137*, Department of Hydraulics Engineering, Royal Institute of Technology, Stockholm, Sweden.

De Vries, M. (1975). "A morphological time scale for rivers." *Proceedings, IAHR Congress, Sao Paulo*, pp 17 – 23.

Defina, A. (1996). "Transverse Spacing of Low-speed Streaks in a Channel Flow over a Rough Bed." *Coherent Flow Structures in Open Channels* edited by P. J. Ashworth, S. J. Bennett, J. L. Best & S. J. McLelland, John Wiley & Sons, pp 87 – 99.

Delft Hydraulics (1972). *Systematic Investigation of Two-Dimensional and Three-Dimensional Scour*. Report M648/M863, Delft, The Netherlands.

Dey, Subhasish, Sujit K. Bose, & Ghandikota L. N. Sastry (1995). "Clear Water Scour at Circular Piers: A Model." *J. Hydr. Engrg. ASCE,* Vol. 121, No. 12, pp 869 – 876.

Dietz, J. W. (1969). Kolkbildung im feinen oder leichten Sohlmaterialien bei strömendem Abfluss. *T. U. Karlsruhe,* Mitteilungen Rehbock Flussbaulab., Heft 155, 1 – 119.

Egiazaroff, I. V. (1957). "L'Equation generale du transport des alluvions non cohesives par un courent fluide." *Paper D43, Proceedings of the 7th Congress, IAHR*, Lisbon, Portugal, pp 1 – 10.

Egiazaroff, I. V. (1965). "Calculation of Nonuniform Sediment Concentrations." *J. Hydr. Div. ASCE*, Vol. 91, No. HY4, Proc. Paper 4417, pp 225 – 247.

Einstein, H. A. & E. A. El-Samni (1949). "Hydrodynamic Forces on a Rough Wall." *Review of Modern Physics*, Vol. 21, No. 3, pp 520 – 524.

Einstein, H. A. (1950). *The bed load function for sediment transportation in open channel flows*. Tech. Bull. 1026, U.S. Department of Agriculture, Washington, D.C.

Einstein, H. A. & Ning Chien (1954). *Second Approximation to the Solution of Suspended Load Theory*. Univ. of California, Inst. Res., No. 3.

Einstein, H. A. & Ning Chien (1955). "Effects of Sediment Concentration Near the Bed on the Velocity and Sediment Distribution." *M.R.D. Sediment Series No. 8*. Missouri River Div., Corps Engrs..

Einstein, H. A. & H. Li (1958). "Secondary Currents in Straight Channels." *Transactions of American Geophysical Union*, Vol. 39.

Einstein, H. A. & F. M. Abdel-Aal (1972). "Einstein Bed Load Function at High Sediment Rates." *J. Hydr. Div. ASCE* Vol. 98, No. HY1, pp 137 – 151.

Engelund, F. & J. Fredsoe (1976). "A sediment transport model for straight alluvial channels." *Nordic Hydro*, 7, pp 293 – 306.

Ettema, R. (1980). *Scour at bridge piers*. School of Engineering Report No. 216, University of Auckland, New Zealand.

Ettema, Robert (1990). Discussion on B. W. Melville & A. J. Sutherland, "Design Method for Local Scour at Bridge Piers." *J. Hydr. Div. ASCE,* Vol. 116, No. 10, pp 1290 – 1292.

Ferguson, R. I., A. D. Kirkbride & A. G. Roy (1996). "Markov Analysis of Velocity Fluctuations in Gravel-bed Rivers." *Coherent Flow Structures in Open Channels* edited by P. J. Ashworth, S. J. Bennett, J. L. Best & S. J. McLelland, John Wiley & Sons, pp 165 – 183.

Fortier, S., & F. C. Scobey (1926). "Permissible Canal Velocities." *Trans. ASCE,* Vol. 89, pp 940 - 984.

Fredsoe, J. & R. Deigaard (1992). *Mechanics of coastal sediment transport.* World Scientific Publishing Co., River Edge, N.J.

French, R. H. (1994). *Open-Channel Hydraulics, International Edition.* McGraw-Hill Inc.

Friedman, G. M. (1962). "Comparison of Moment Measures for Sieving and Thin-Section Data in Sedimentary Petrological Studies." *Journal of Sediment Petrology*, Vol. 32, pp 15 – 25.

Froehlich, D. C. (1989). "Local Scour at Bridge Abutments." *Proc. ASCE Nat. Hydr. Conf.* ASCE, New York, pp 13 – 18.

Fujisaki, K., K. Tanaka & K Shiono (1999). "Concentration profile of suspended sediment in rectangular open channel flow." *Proc. IAHR Symposium on River, Coastal and Estuarine Morphodynamics*, Genoa, Italy, pp 55 – 64.

García, M., Y. Niño & F López (1996). "Laboratory Observations of Particle Entrainment into Suspension by Turbulent Bursting." *Coherent Flow Structures in Open Channels* edited by P. J. Ashworth, S. J. Bennett, J. L. Best & S. J. McLelland, John Wiley & Sons, pp 63 – 86.

Garde, R. J., K. Subramanya & K. D. Nambudripad (1961). "Study of Scour Around Spur Dikes." *J. Hydr. Div. ASCE,* Vol. 87, No. HY6, pp 23 – 37.

Garde, R. J. & S. Sethuraman (1969). "Variation of the Drag Coefficient of a Sphere Rolling down an Inclined Boundary of Closely Packed Spheres." *La Houille Blanche*, No. 7, pp 727 – 732.

Ghia, U., K. N. Ghia & C. T. Shin (1982). "High-*Re* Solutions for Incompressible Flow using the Navier-Stokes Equations and a Multi-grid." *Journal of Computational Physics,* Vol. 48, pp 387 – 411.

Gill, Mohammad Akram (1972). "Erosion of sand beds around spur dikes." *J. Hydr. Div. ASCE,* Vol. 98, No. HY9, pp 1587 – 1602.

Goncharov, V. N. (1962). *Basic River Dynamics*. Hydro-Meteorological Press, Leningrad (in Russian).

Gosman D. A. & W. M. Pun (1973). Lecture Notes for course entitled "Calculation of Recirculating Flow." *Report HTS/74/2,* Heat Transfer Section, Imperial College, London.

Govers, G. (1987). "Initiation of Motion in Overland Flow." *Sedimentology*, No. 34, pp 1157 – 1164.

Graf, W. H. (1998). *Fluvial Hydraulics: Flow and Transport Processes in Channels of Simple Geometry*. John Wiley & Sons.

Graf, W. H. & G. G. Pazis (1977). "Les Phenomenes de Deposition et D'Erosion dans un Canal Alluvionnaire." *J. Hydr. Res.*, Vol. 15, No. 2.

Graf, Walter Hans (1971). *Hydraulics of Sediment Transport*. McGraw-Hill, 513pp.

Grass, A. J. (1970). "Initial instability of fine bed sand." *J. Hydr. Div. ASCE,* Vol. 96, No. HY3, pp 619 – 632.

Grass, A. J. (1982). "The influence of boundary layer turbulence on the mechanics of sediment transport." *Proc. Euromech 156: Mech. of Sediment Transport*, Tech. Univ. of Istanbul.

Grass, A. J. & M. Mansour-Tehrani (1996). "Generalized Scaling of Coherent Bursting Structures in the Near-wall Region of Turbulent Flow over Smooth and Rough Boundaries." *Coherent Flow Structures in Open Channels* edited by P. J. Ashworth, S. J. Bennett, J. L. Best & S. J. McLelland, John Wiley & Sons, pp 41 – 61.

Hamil, Les (1999). *Bridge Hydraulics*. E & FN SPON, Routledge, 367 pp.

Hancu, S. (1971). "Sur le calcul des affouillements locaux dams la zone des piles de pont." *Proc. 14th IAHR Congr.*, Vol. 3, pp 299 – 313.

Harnett, B. R (1998). *Damming the River Sabie, South Africa: The sedimentation problem*. Internal Report, Centre for Water in the Environment, University of the Witwatersrand, South Africa.

HEC-18 (1995). *Evaluating Scour at Bridges, Third Edition. U.S. Department of Transportation, Federal Highway Administration Publication*, No. FHWA HI-96-031, Hydraulic Engineering Circular No. 18, 204 pages.

Hoffmans G. J. C. M. & H. J. Verheij (1997). *Scour Manual.* A. A. Balkema.

Hopkins, G. R., R. W. Vance & B. Kasraie (1980). *Scour around bridge piers*. U.S. Department of Transportation, Federal Highway Administration Publication, Rep. No. FHwA-RD-79-103.

Hjulström, F. (1935). "Studies of the Morphological Activity of Rivers as Illustrated by the River Fyris." *Bulletin of the Geological Institute of Uppsala*, Vol. 25, Chap. 3.

IDL (2000). "Interactive Data Language, Version 5.2." *Research Systems Inc* (RSI).

Jain, S. C., & E. E. Fischer (1979). *Scour around circular bridge piers at high Froude numbers*. U.S. Department of Transportation, Federal Highway Administration Publication, Rep. No. FHwA-RD-79-104.

Johnson, Peggy A. (1995). "Comparison of Pier-Scour Equations Using Field Data." *J. Hydr. Engrg. ASCE,* Vol. 121, No. 8, pp 626 – 629.

Jones, J. S. (1983). "Comparison of prediction equations for bridge pier and abutment scour." *Transp. Res. Rec. 950: Second Bridge Engrg. Conf.*, Vol. 2, Transp. Res. Board, Washington, D.C.

Julien, P. Y. (1995). *Erosion and Sedimentation.* Cambridge University Press, 280 pages.

Kandasamy, J. K. (1989). *Local scour at skewed abutments. Rep. No. 375*, School of Engineering, University of Auckland, New Zealand.

Kazanskij, I. (1981). "Über theoretische und praxisbezongene Aspekte des hydraulischen Feststofftransportes." University of Hannover, *Mitt. des Franzius-Inst.*, Vol. 52.

Kennedy, John, F. (1995). "The Albert Shields Story." *J. Hydr. Engrg. ASCE,* Vol. 121, No. 11, pp 766 – 772.

Knoros, V. S. (1958). "Non-scouring Velocity for Non-cohesive Soil and Its Application." *Proc. Soviet National Hydrology Institute*, Vol. 59 (in Russian).

Kramer, H. (1935). "Sand mixture and sand movement in fluvial model." *Trans. ASCE*, Vol. 100, pp 798 – 873.

Kwan, T. F. (1988). *A study of abutment scour.* Report No. 328, School of Engineering, University of Auckland, New Zealand.

Lane, E. W., et al. (1947). "Report of the Subcommittee on Sediment Terminology." *Transactions of the American Geophysical Union,* Vol. 28, No. 6, pp 936 – 938.

Lane, E. W. (1953). "Progress Report on Studies on the Design of Stable Channels by the Bureau of Reclamation." *Proc. ASCE*, Vol. 79, No. 280.

Laursen, E. M. (1958). *Scour at bridge crossings.* Bull. No. 8, Iowa Highway Research Board, Ames, Iowa.

Laursen, E. M. (1962). "Scour at bridge crossings." *Trans. ASCE*, Vol. 127, No. 1, pp 166 – 180.

Laursen, E. M. (1963). "Analysis of relief bridge scour." *J. Hydr. Div. ASCE,* Vol. 89, No. 3, pp 93 – 118.

Laursen, E. M. & A. Toch (1956). *Scour around bridge piers and abutments.* Bull. No. 5, Iowa Highways Research Board, Ames, Iowa.

Le Grange, A. du P. & A Rooseboom (1993). *The Development of a Model to Simulate Channel Deformation in Alluvial Rivers.* Report No. 236/1/93 of the Water Research Commission of South Africa.

Leiner, O. (1912). "Zur Erforschung der Geschiebe und Sinkstoff Bewegung." *Zeitschrift für Bauwesen*, 62, pp 490 – 515.

Levy, E. E. (1956). *River Mechanics*. National Energy Press, Moscow (in Russian).

Li, Baoru (1959). "Calculation of Threshold Velocity of Sediment Particles." *Journal of Sediment Research*, Vol. 4, No. 1, pp 71 – 77.

Lim, Siow-Yong (1997). "Equlibrium Clear-Water Scour around an Abutment." *J. Hydr. Engrg. ASCE,* Vol. 123, No. 3, pp 237 – 243.

Lim, Siow-Yong & Nian-Sheng Cheng (1998). "Prediction of Live-Bed Scour at Bridge Abutments." *J. Hydr. Div. ASCE,* Vol. 124, No. 6, pp 635 – 638.

Liu, Hsin-Kuan (1957). "Mechanics of Sediment-Ripple Formulation." *J. Hydr. Div. ASCE,* Vol. 83, No. HY2, 23 pages.

Liu, H.-K., F. M. Chang & M. M. Skinner (1961*). Effect of bridge construction on scour and backwater*. CER 60 HKL 22, Colorado State Univ., Civ. Engrg. Section, Ft. Collins, Colorado.

Lugt, H. J. (1983). *Vortex Flow in Nature and Technology*. John Wiley & Sons.

Massey, B. S. (1989). *Mechanics of Fluids, 6th Edition*. Chapman & Hall.

McGahey, Caroline (2001). *A computational fluid dynamics model for sediment movement based on the unit stream power approach.* MSc (Eng) thesis, University of Cape Town, South Africa.

Melville, B. W. (1992). "Local Scour at Bridge Abutments." *J. Hydr. Engrg. ASCE,* Vol. 118, No. 4, pp 615 – 631.

Melville, Bruce W. (1995). "Bridge Abutment Scour in Compound Channels." *J. Hydr. Engrg. ASCE,* Vol. 121, No. 12, pp 863 – 868.

Melville, Bruce W. (1997). "Pier and Abutment Scour: Integrated Approach." *J. Hydr. Engrg. ASCE,* Vol. 123, No. 2, pp 125 – 136.

Melville, B. W. & Y. -M. Chiew (1999). "Time Scale for Local Scour at Bridge Piers." *J. Hydr. Engrg. ASCE,* Vol. 125, No. 1, pp 59 – 65.

Midgley, Mark (2000). *Sediment movement around piers in open channel flow.* BSc(Eng) thesis, University of Cape Town, South Africa.

Mitchell, Alex (2000). *Sediment movement around abutments in open channel flow.* BSc(Eng) thesis, University of Cape Town, South Africa.

Molls, Thomas & M. Hanif Chaudhry (1995). "Depth-Averaged Open-Channel Flow Model." *J. Hydr. Engrg., ASCE*, Vol. 121, No. 6, pp 453 – 465.

Neill, C. R. (ed.) (1973). *Guide to bridge hydraulics.* University of Toronto Press.

Nikuradse, J. (1933). "Strömungsgesetze in rauhen Rohren." *Forschg. Geb. D. Ing.-Wessens,* Heft 361.

Olsen, Nils R. B. & Morten C. Melaaen (1993). "Three-Dimensional Calculation of Scour Around Cylinders." *J. Hydr. Engrg. ASCE,* Vol. 119, No. 9, pp 1048 – 1054.

Olsen, Nils R. B. & Hilde M. Kjellesvig (1998). "Three-dimensional numerical flow modeling for estimation of maximum local scour depth." *J. Hydr. Res.*, Vol. 36, No. 4, pp 579 – 590.

Ouillon, S & D Dartus (1997). "Three-dimensional Computation of Flow around a Groyne." *J. Hydr. Engrg. ASCE,* Vol. 123, No. 11, pp 962 – 970.

Parker, G., P. C. Klingeman & D. G. McLean (1982). "Bedload and size distribution in paved gravel-bed streams." *J. Hydr. Div., ASCE*, Vol 108, pp 544 – 571.

Potter, M. C. & D. C. Wiggert (1997). *Mechanics of Fluids, 2nd Edition.* Prentice Hall.

Prandtl, L. (1904). "Über Flüssigkeitsbewegung bei sehr kleiner Reibung." *Proc. 3rd Intern. Math. Congr. Heidelberg*, pp 484-491.

Prandtl, L. (1925). "Über die ausgebildete Turbulenz." *Z. Angew. Math. Mech.*, Vol. 5, pp. 136 – 139.

Prandtl, L. (1952). *Essentials of Fluid Dynamics*. Blackie & Son Limited.

Przedwojski, B., R. Blazejewski & K. W. Pilarczyk (1995). *River Training Techniques: Fundamentals, Design and Applications*, A. A. Balkema.

Raudkivi, A. J. (1986). "Functional trends of scour at bridge piers." *J. Hydr. Engrg. ASCE,* Vol. 112, No. 1, pp 1 – 13.

Raudkivi, A. J. (1998). *Loose Boundary Hydraulics*. A. A. Balkema.

Reynolds, A. J. (1974). *Turbulent Flows in Engineering*. John Wiley & Sons.

Richardson, E. V., D. B. Simons & P. Julien (1990). "Highways in the River Environment." *U.S. Department of Transportation, Federal Highway Administration Publication*, No. FHWA-IP-90-014.

Richardson, John E. & Vijay G. Panchang (1998). "Three-Dimensional Simulation of Scour-Inducing Flow at Bridge Piers." *J. Hydr. Engrg., ASCE*, Vol. 124, No. 5, pp 530 – 540.

River Study Group, WIHEE (1965). "Review on the Einstein Theory of Bed Load Motion and Discussion on Bed Load Motion." *Bulletin of Wuhan Institute of Hydraulic and Electric Engineering*, No. 4, pp 1 – 16 (in Chinese).

Roberson, J. A. & C. T. Crowe (1997). *Engineering Fluid Mechanics, 6th Edition*. John Wiley & Sons, Inc.

Rodi, W., R. N. Pavlovic & S. K. Srivatsa (1981). "Prediction of flow and pollutant spreading in rivers." *Transport models for inland and coastal waters.* Academic Press, Inc., New York.

Rooseboom, A. (1975). *Sediment Transport in Rivers and Reservoirs*. D. Eng dissertation, University of Pretoria, South Africa (in Afrikaans).

Rooseboom, A. (1992). *Sediment Transport in Rivers and Reservoirs – A Southern African Perspective*. Report No. 297/1/92 of the Water Research Commission of South Africa.

Rooseboom, Albert & Aldu le Grange (2000). "The hydraulic resistance of sand streambeds under steady flow conditions." *J. Hydr. Res.*, Vol. 38, No. 1, pp 27 – 35.

Rubey, W. W. (1933). "Settling velocities of gravel sand and silt particles." *American Journal of Science*, 5th Series, Vol. 25(148), pp 325 – 338.

Schiller, L. & A. Naumann (1933). "Über die grundlegenden Berechnungen bei der Schwerkraftaufbereitung."" *Zeitschrift der VHI*, Vol. 77.

Schlichting, H. (1979). *Boundary-Layer Theory, 7th Edition*. McGraw-Hill Book Company.

Shamov, G. E. (1952). "Formulas for Determining Near-Bed Velocity and Bed Load Discharge." *Proc. Soviet National Hydrology Institute*, Vol. 36 (in Russian).

Shen, H. W., V. R. Schneider & S. Karaki (1969). "Local scour around bridge piers." *J. Hydr. Div. ASCE,* Vol. 95, No. HY6, pp 1919 – 1940.

Shields, A. (1936). "Anwendung der Aenlichkeitsmechanik und der Turbulenzforschung auf die Geschiebebewegung." *Mitteilungen der Preussischen Versuchsanstalt für Wasserbau und Schiffbau*, Heft 26 (in German). (English translation by W. P. Ott and J. C. van Uchelen, *Hydrodynamics Laboratory Publication No. 167*, Hydrodynamics Lab. California Inst. Of Tech., Pasadena).

Shvidchenko, Andrey B. & Gareth Pender (2000a). "Flume study of the effect of relative depth on the incipient motion of coarse uniform sediments." *Water Resources Research*, Vol. 36, No. 2, pp 619 – 628.

Shvidchenko, A. B. & G. Pender (2000b). "Initial motion of streambeds composed of coarse uniform sediments." *Proc. Instn Civ. Engrs Water & Mar. Engng*, **142**, Dec., pp 217 – 227.

Shvidchenko, A. B. & G. Pender (2001). Personal communication with Dr Shvidchenko, University of Glasgow and Prof. G Pender, University of Heriot-Watt, UK.

Sicilian, J. M., C. W. Hirt & R. P. Harper (1987). "FLOW-3D: Computational modelling power for scientists and engineers." *Rep. FSI-87-00-1*, Flow Science, Los Alamos, N.M.

Simons, D. B. & Sentürk, F. (1977). *Sediment Transport Technology*. Water Resources Publications, Colorado.

Smith, C.R. (1996). "Coherent Flow Structures in Smooth-wall Turbulent Boundary Layers: Facts, Mechanisms and Speculation." *Coherent Flow Structures in Open Channels* edited by P. J. Ashworth, S. J. Bennett, J. L. Best & S. J. McLelland, John Wiley & Sons, pp 1 – 39.

Soltiropoulos, F. & Y. Ventikos (1996). "Assessment of some Non-linear Two-equation Turbulence Models in a 3D Shear Flow." *Flow Modelling and Turbulent Measurements*, pp 331 – 338.

Speziale, C.G. (1991). "Analytical Methods for the Development of Reynolds-stress Closures in Turbulence." *Annual Revision Fluid Mechanics*, Vol. 23, pp 107 – 157.

Streeter, Victor L. (1948). *Fluid Dynamics*. McGraw-Hill Book Company, Inc., New York.

Strickler, A. (1923). "Beiträge zur Frage der Geschwindigkeitsformel und der Rauhigkeitszahlen für Ströme, Kanäle und geschlossene Leitungen." *Mitt. des eidgenössischen Amtes für Wasserwirtschaft*, Bern, Switzerland.

Sumer, B. Mutlu (1973). "Simulation of Dispersion of Suspended Particles." *J. Hydr. Div. ASCE,* Vol. 99, No. HY10, pp 1705 – 1726.

Sumer, B. M. & B. Oguz (1978). "Particle motions near the bottom in turbulent flow in an open channel." *J. Fluid Mech.*, 86(1), pp 109 – 127.

Sumer, B. M. & R. Deigaard (1981). "Particle motions near the bottom in turbulent flow in an open channel, part 2." *J. Fluid Mech.*, 109, pp 311 – 337.

Talapatra, S. C. & S. N. Ghosh (1983). "Incipient Motion Criteria for Flow Over a Mobile Bed Sill." *Proc. 2nd International Symposium on River Sedimentation*, Nanjing, China, pp 459 – 471.

Taylor, B. D. (1971). *Temperature Effects in Alluvial Streams*. Report No. KH-R-27, W. M. Keck Laboratory of Hydraulics and Water Resources, California Institute of Technology, Pasadena, California.

Tingsanchali, T & S. Maheswaran (1990). "2-D Depth-averaged Flow Computation near Groyne, *J. Hydr. Engrg., ASCE*, Vol. 116, No.1, pp 71 – 86.

Tsujimoto, T. & T. Kitamura (1996). "Interaction Between Cellular Secondary Currents and Lateral Alternate Sorting." *Coherent Flow Structures in Open Channels* edited by P. J. Ashworth, S. J. Bennett, J. L. Best & S. J. McLelland, John Wiley & Sons, pp 359 – 374.

Unsöld, G. (1982). *Der Transportbeginn rolligem Sohlenmaterials in gleichförmigen turbulentem Strömungen: Eine kritische Überprüfung der Shields-Funktion und ihre experimentelle Erweiterung auf feinkörnige, nicht-bindige Sedimente*. Dissertation, Mathematische-Naturwissenschaftlichen Fakultät, Universität Kiel, Germany.

Van Rijn, L. C. (1987). *Mathematical modeling of morphological processes in the case of suspended sediment transport*. PhD Thesis, Delft University of Technology.

Van Rijn, L. C. (1993). *Principles of sediment transport in rivers, estuaries and coastal seas*. Aqua Publications, The Netherlands.

Vanoni, V. A. & G. N. Nomicos (1959). "Resistance Properties of Sediment-laden Streams." *J. Hydr. Div. ASCE,* Vol. 85, HY5, pp 77- 107.

Vanoni, V. A. & G. N. Nomicos (1960). "Resistance Properties of Sediment-laden Streams." *Trans. ASCE,* Vol. 125, pp 1140 - 1175.

Vanoni, V. A. (1975) – editor. *Sedimentation Engineering*. ASCE Press.

Ven te Chow (1959). *Open-Channel Hydraulics*. McGraw-Hill International Book Company.

Versteeg, H. K. & W. Malalasekera (1995). *An Introduction to Computational Fluid Dynamics*. Addison Wesley Longman Limited, Harlow, Essex, UK.

Watters, G. Z. & M. V. P. Rao (1971). "Hydrodynamic Effects of Seepage on Bed Particles." *J. Hydr. Div. ASCE,* Vol. 97, HY3, pp 421- 439.

White, Frank M. (1991). *Viscous Fluid Flow, 2nd Edition*. McGraw-Hill, Inc., New York.

Whitehouse, R. J. S. & J. Hardisty (1988). "Experimental Assessment of Two Theories for the Effect of Bed Slope on the Threshold of Bed Load Transport." *Marine Geology*, Vol. 79, pp 135 – 139.

Wilcox, D. C. (1993). *Turbulence Modelling for CFD*. DCW Industries, LaCanada, CA.

Wormleaton, P. R. (1996). "Floodplain Secondary Circulation as a Mechanism for Flow and Shear Stress Redistribution in Straight Compound Channels." *Coherent Flow Structures in Open Channels* edited by P. J. Ashworth, S. J. Bennett, J. L. Best & S. J. McLelland, John Wiley & Sons, pp 581 – 608.

Yalin, M. S. (1972). *Mechanics of Sediment Transport*. Pergamon Press.

Yang, C. T. (1972). "Unit Stream Power and Sediment Transport." *J. Hydr. Div. ASCE,* Vol. 98, HY10, pp 1805 - 1826.

Yang, C. T. (1973). "Incipient Motion and Sediment Transport." *J. Hydr. Div. ASCE,* Vol. 99, HY10, pp 1679 - 1703.

Yang, C. T. (1976). "Minimum Unit Stream Power and Fluvial Hydraulics." *J. Hydr. Div. ASCE,* Vol. 102, HY7, pp 919 - 934.

Yang, Chih Ted & Charles, C. S. Song (1979). "Theory of Minimum Rate of Energy Dissipation (1979)." *J. Hydr. Div. ASCE*, Vol. 105, HY7, pp 769 – 784.

Yang, C. T. (1996). *Sediment Transport: Theory and Practice*. McGraw-Hill.

Yang, C. T. & C. C. S. Song (1979). "Theory of Minimum Rate of Energy Dissipation." *J. Hydr. Div. ASCE,* Vol. 105, HY7, pp 769 - 784.

Yegiazapov, I. V. (1960). "Generalized Formula for Sediment-Carrying Capacity in Alluvial Rivers and Threshold Velocity." *Collection of the 3rd National Hydrological Conference*, USSR, Vol. 5, Leningrad, pp 117 – 132.

Young, Donald F., Bruce R. Munson & Theodore H. Okiishi (1997). *A Brief Introduction to Fluid Mechanics*. John Wiley & Sons, Inc., New York.

Zaghloul, N. & J. A. McCorquodale (1973). "A Numerical Model for Flow Past a Spur Dike." *Proc. First Canadian Hydraulic Conference*, Canadian Society for Civil Engineering.

Zanke, U. (1978). *Zusammenhänge zwischen Strömung und Sedimenttransport, Teil 1: Berechnung des Sedimenttransportes, -allgemeiner Fall-, Teil 2: Berechnung des Sedimenttransportes hinter befestigten Sohlenstrecken, -Sonderfall sweidimensionaler Kolk-.* Mitteilungen des Franzius-Instituts der TU Hannover, Heft 47, 48.

Zeng, Zhaozen & Shangyi Wang (1963). "Study on Threshold Criteria for Granular Sediment." *Journal of Tianjin University*, pp 19 – 40 (in Chinese).

Zhu, L. J. & N. S. Cheng (1993). *Settlement of sediment particles*. Res. Rep., Dept. of River and Harbour Engrg., Nanjing Hydr. Res. Inst., China (in Chinese).

Appendices

A. Incipient motion on turbulent beds (Shvidchenko & Pender, 2001)

A.1 Shvidchenko & Pender (2000)

Obtained using the 300 mm wide Armfield flume at the University of Glasgow, UK.

Run No.	Sediment d (mm)	Slope S x 10^3	Flow Q (l/s)	Depth Y (m)	Sampling Duration (min)	Bedload Yield (g)	Intensity I (s^{-1})	Water Temp. (^{o}C)	Froude Fr
U1-1	1.5	1.9	3.0	0.036	127	8.5	3E-05	20.0	0.48
U1-2		1.9	3.5	0.038	120	37.6	0.0001	19.5	0.51
U1-3		1.9	3.7	0.039	131	132.3	0.0003	19.8	0.52
U1-4		1.9	4.2	0.04	60	105.7	0.0006	18.8	0.56
U1-7	1.5	4.1	1.0	0.021	75	20.9	0.0001	16.2	0.36
U1-8		4.1	1.3	0.022	80	49.5	0.0003	17.1	0.42
U1-9		4.1	1.9	0.023	60	210.2	0.0015	18.0	0.57
U1-14	1.5	6.5	-	0.015	60	23.6	0.0001	19.0	n/a
U1-15		6.5	-	0.016	147	26.1	4E-05	20.2	n/a
U1-16		6.5	-	0.016	60	59.5	0.0003	19.2	n/a
U1-17		6.5	-	0.017	85	143.6	0.0005	19.0	n/a
U1-18		6.5	0.9	0.017	30	385.7	0.0019	19.3	0.42
U1-20	1.5	8.3	-	0.012	130	7.6	1E-05	17.6	n/a
U1-21		8.3	-	0.012	127	17.4	6E-05	19.2	n/a
U1-22		8.3	-	0.013	60	38.3	0.0004	18.4	n/a
U1-23		8.3	-	0.013	60	167.7	0.0008	19.4	n/a
U1-24		8.3	-	0.013	60	27.6	0.0003	18.8	n/a
U1-25		8.3	-	0.014	60	450.0	0.0013	19.1	n/a
U1-28	1.5	14.1	-	0.007	128	5.0	6E-06	18.8	n/a
U1-29		14.1	-	0.007	20	188.4	0.0007	19.0	n/a
U1-30		14.1	-	0.008	87	3.0	6E-06	19.5	n/a
U1-32		14.1	-	0.01	47	160.2	0.0004	20.5	n/a
U2-1	2.4	2.6	5.2	0.045	60	7.5	8E-06	17.2	0.58
U2-2		2.6	6.0	0.049	45	31.5	5E-05	17.8	0.59
U2-3		2.6	7.0	0.052	50	69.4	7E-05	17.4	0.62
U2-4		2.6	8.0	0.057	50	150.3	0.0002	17.3	0.63
U2-5		2.6	9.4	0.064	15	177.7	0.0008	17.6	0.62
U2-6		2.6	10.5	0.068	10	433.4	0.0028	18.4	0.63
U2-8	2.4	4.1	-	0.037	90	4.9	5E-06	22.7	n/a

Run No.	Sediment d (mm)	Slope S x 10^3	Flow Q (l/s)	Depth Y (m)	Sampling Duration (min)	Bedload Yield (g)	Intensity I (s^{-1})	Water Temp. (^{o}C)	Froude Fr
U2-9		4.1	-	0.039	120	37.9	7E-05	20.2	n/a
U2-10		4.1	-	0.043	90	83.9	5E-05	21.5	n/a
U2-11		4.1	-	0.043	123	573.2	0.0018	23.5	n/a
U2-13		4.1	-	0.046	65	765.6	0.0015	23.4	n/a
U2-14		4.1	-	0.047	60	519.9	0.0008	23.0	n/a
U2-15		4.1	-	0.049	30	1075.0	0.0038	23.0	n/a
U2-16		4.1	-	0.053	60	889.8	0.0019	23.0	n/a
U2-17		4.1	-	0.057	18	1636.5	0.019	23.2	n/a
U2-18		4.1	-	0.063	15	1186.9	0.009	23.2	n/a
U2-19		4.1	-	0.066	7	2014.4	0.0333	22.7	n/a
U2-20	2.4	6.5	-	0.024	60	3.0	5E-06	22.5	n/a
U2-21		6.5	-	0.027	60	4.3	8E-06	22.8	n/a
U2-22		6.5	-	0.028	60	10.3	2E-05	22.5	n/a
U2-23		6.5	-	0.029	90	49.9	0.0001	21.8	n/a
U2-24		6.5	-	0.03	60	31.1	8E-05	22.8	n/a
U2-25		6.5	-	0.031	91	425.5	0.0004	22.3	n/a
U2-26		6.5	-	0.032	60	670.4	0.0016	22.5	n/a
U2-27		6.5	-	0.033	60	1064.8	0.0014	22.5	n/a
U2-28		6.5	-	0.035	15	1531.3	0.015	24.0	n/a
U2-29		6.5	-	0.04	11	2268.6	0.03	23.3	n/a
U2-30		6.5	-	0.042	5	2333.4	0.069	23.8	n/a
U2-31	2.4	8.3	-	0.021	60	6.5	5E-06	23.2	n/a
U2-32		8.3	-	0.023	60	11.1	8E-06	23.1	n/a
U2-33		8.3	-	0.023	60	37.0	3E-05	21.7	n/a
U2-34		8.3	-	0.024	60	91.8	0.0002	22.5	n/a
U2-35		8.3	-	0.026	60	369.8	0.0004	22.7	n/a
U2-36		8.3	-	0.028	30	1374.8	0.009	22.5	n/a
U2-37		8.3	-	0.031	10	1370.3	0.02	24.1	n/a
U2-38		8.3	-	0.033	6	1992.4	0.068	24.0	n/a
U2-39		8.3	-	0.036	6	1819.5	0.056	22.7	n/a
U2-40		8.3	-	0.038	5	2144.8	0.061	24.4	n/a
U2-41	2.4	14.1	-	0.014	65	2.5	2E-06	20.2	n/a
U2-42		14.1	-	0.014	60	59.7	5E-05	20.6	n/a
U2-43		14.1	-	0.015	64	28.5	4E-05	19.4	n/a
U2-44		14.1	0.3	0.015	40	281.4	0.0003	20.5	0.17
U2-45		14.1	0.8	0.016	30	185.5	0.0006	20.8	0.42
U2-46		14.1	1.0	0.017	20.33	540.9	0.0048	19.5	0.49
U2-47		14.1	1.4	0.018	13	674.2	0.011	20.7	0.64

Run No.	Sediment d (mm)	Slope S x 10^3	Flow Q (l/s)	Depth Y (m)	Sampling Duration (min)	Bedload Yield (g)	Intensity I (s^{-1})	Water Temp. (^{o}C)	Froude Fr
U2-48		14.1	2.0	0.019	7	1071.0	0.023	20.2	0.83
U3-1	3.4	1.9	15.0	0.095	60	32.5	2E-05	19.0	0.54
U3-2		1.9	18.2	0.104	60	50.6	4E-05	18.5	0.58
U3-3		1.9	21.5	0.117	48	58.3	6E-05	18.8	0.57
U3-4		1.9	24.8	0.127	47	84.0	1E-04	20.2	0.58
U3-5		1.9	26.3	0.135	30	261.8	0.0004	20.4	0.56
U3-6	3.4	2.6	14.5	0.085	55	43.4	3E-05	18.6	0.63
U3-7		2.6	15.8	0.089	65	118.2	6E-05	19.1	0.63
U3-8		2.6	18.1	0.096	55	134.2	0.0001	20.0	0.64
U3-9		2.6	20.7	0.105	42	108.3	9E-05	19.7	0.65
U3-10		2.6	23.8	0.116	25	194.4	0.0004	19.6	0.64
U3-11		2.6	28.7	0.127	11	398.8	0.0013	19.6	0.68
U3-12	3.4	4.1	8.5	0.06	60	12.6	2E-05	15.5	0.62
U3-13		4.1	9.2	0.063	60	17.1	1E-05	16.0	0.63
U3-14		4.1	10.2	0.066	61	46.2	3E-05	18.5	0.65
U3-15		4.1	10.8	0.068	65	43.3	2E-05	19.1	0.64
U3-16		4.1	11.9	0.072	60	70.8	6E-05	20.0	0.65
U3-17		4.1	13.7	0.078	60	123.7	7E-05	20.8	0.67
U3-18		4.1	14.5	0.081	40	155.1	0.0002	18.5	0.67
U3-19		4.1	15.8	0.084	30	315.7	0.0003	19.5	0.69
U3-20		4.1	16.4	0.086	20	169.2	0.0004	19.8	0.69
U3-21		4.1	18.8	0.089	4	414.1	0.006	19.6	0.76
U3-22		4.1	17.8	0.089	6.5	127.8	0.0009	20.1	0.71
U3-23	3.4	6.5	5.4	0.041	65	16.3	1E-05	20.9	0.69
U3-24		6.5	6.7	0.045	60	33.0	3E-05	20.1	0.75
U3-25		6.5	7.5	0.048	70	140.1	6E-05	21.1	0.76
U3-26		6.5	8.0	0.05	60	144.8	0.0001	21.8	0.75
U3-27		6.5	8.6	0.052	40	202.3	0.0002	21.7	0.77
U3-28		6.5	9.4	0.054	25	335.3	0.0007	21.4	0.80
U3-29		6.5	9.8	0.056	17	331.5	0.001	21.8	0.79
U3-30		6.5	10.2	0.057	10	427.1	0.0016	20.9	0.79
U3-31		6.5	10.8	0.058	6	614.9	0.005	21.5	0.82
U3-32	3.4	8.3	4.2	0.033	61	12.2	6E-06	21.4	0.75
U3-33		8.3	5.1	0.036	60	32.4	3E-05	20.8	0.81
U3-34		8.3	5.6	0.039	63	106.5	7E-05	20.3	0.79
U3-35		8.3	6.0	0.04	60	180.2	1E-04	20.0	0.81
U3-36		8.3	6.3	0.041	60	200.8	0.0002	21.0	0.80

Run No.	Sediment d (mm)	Slope S x 10^3	Flow Q (l/s)	Depth Y (m)	Sampling Duration (min)	Bedload Yield (g)	Intensity I (s^{-1})	Water Temp. (^{o}C)	Froude Fr
U3-37		8.3	7.0	0.042	15	353.3	0.0007	20.7	0.85
U3-38		8.3	7.9	0.046	8	733.4	0.0027	20.2	0.85
U3-39		8.3	8.8	0.05	6	639.6	0.0057	21.5	0.84
U3-40	3.4	14.1	2.4	0.023	76	14.8	1E-06	20.6	0.75
U3-41		14.1	3.0	0.024	60	27.4	2E-05	22.0	0.86
U3-42		14.1	3.4	0.025	60	125.9	7E-05	21.1	0.92
U3-43		14.1	3.6	0.026	62	231.4	0.0001	20.6	0.89
U3-44		14.1	4.1	0.027	30	378.6	0.0006	20.6	0.97
U3-45		14.1	4.4	0.03	15	374.5	0.0019	21.0	0.92
U3-46		14.1	4.9	0.031	8	691.3	0.0029	20.6	0.96
U3-47	3.4	23.8	-	0.013	60	7.6	1E-05	18.6	n/a
U3-48		23.8	0.8	0.014	55	28.7	3E-05	18.1	0.51
U3-49		23.8	0.7	0.014	41	59.2	1E-04	18.5	0.43
U3-50		23.8	1.0	0.015	62	230.0	0.0002	18.6	0.56
U3-51		23.8	1.5	0.016	14	241.1	0.001	17.0	0.77
U3-52		23.8	1.8	0.019	10	758.9	0.0038	18.3	0.76
U4-1	4.5	2.6	21.0	0.114	45	5.2	8E-06	18.4	0.58
U4-2		2.6	24.5	0.118	45	27.4	3E-05	18.7	0.64
U4-3		2.6	29.3	0.136	40	179.6	0.0002	16.6	0.62
U4-4		2.6	29.3	0.136	46	38.3	5E-05	18.3	0.62
U4-5	4.5	4.1	15.0	0.083	60	25.9	1E-05	21.0	0.67
U4-6		4.1	19.2	0.094	60.2	237.6	9E-05	18.3	0.71
U4-7		4.1	23.1	0.109	68	222.5	6E-05	19.8	0.69
U4-8		4.1	29.0	0.122	33	391.3	0.0004	19.0	0.72
U4-9	4.5	6.5	10.2	0.061	67	66.9	1E-05	19.8	0.73
U4-10		6.5	11.2	0.063	60	168.8	7E-05	21.1	0.75
U4-11		6.5	-	0.066	63.5	347.0	0.0001	20.2	n/a
U4-12		6.5	13.3	0.068	60	334.2	0.0002	21.7	0.80
U4-13		6.5	14.7	0.071	22	411.2	0.0006	21.0	0.82
U4-14		6.5	15.8	0.073	16	505.2	0.001	21.1	0.86
U4-15		6.5	18.6	0.078	4	838.3	0.007	21.6	0.91
U4-16	4.5	8.3	7.7	0.047	66	106.4	3E-05	19.4	0.81
U4-17		8.3	8.4	0.05	65	129.6	7E-05	21.7	0.80
U4-18		8.3	9.8	0.054	51	252.0	0.0002	22.5	0.84
U4-19		8.3	10.5	0.055	26	402.6	0.0006	20.4	0.86
U4-20		8.3	11.0	0.057	21	520.3	0.0007	19.8	0.86
U4-21		8.3	11.6	0.059	11	404.7	0.0013	20.3	0.86

Run No.	Sediment d (mm)	Slope S x 10^3	Flow Q (l/s)	Depth Y (m)	Sampling Duration (min)	Bedload Yield (g)	Intensity I (s^{-1})	Water Temp. (^{o}C)	Froude Fr
U4-22		8.3	12.4	0.06	6	528.8	0.0036	20.6	0.90
U4-23	4.5	11.5	5.6	0.036	60	83.5	3E-05	21.7	0.89
U4-24		11.5	6.0	0.037	61	133.3	7E-05	21.3	0.90
U4-25		11.5	6.3	0.038	63	279.6	0.0002	22.1	0.90
U4-26		11.5	7.0	0.041	30	405.2	0.0005	22.0	0.90
U4-27		11.5	7.3	0.042	32	352.5	0.0005	21.5	0.91
U4-28		11.5	8.0	0.044	8	472.5	0.0021	21.9	0.93
U4-29	4.5	14.1	4.3	0.03	60	16.7	3E-05	16.5	0.90
U4-30		14.1	4.9	0.03	24	40.7	7E-05	20.2	0.98
U4-31		14.1	5.2	0.032	62	160.2	0.0002	18.1	0.98
U4-32		14.1	5.6	0.034	50	385.1	0.0003	18.7	0.97
U4-33		14.1	6.0	0.034	23	379.7	0.001	17.2	1.00
U4-34		14.1	6.5	0.036	17	549.5	0.0016	19.1	1.00
U4-35	4.5	28.7	0.9	0.017	46	20.0	1E-05	16.6	0.44
U4-36		28.7	1.2	0.018	55	89.8	9E-05	16.2	0.54
U4-37		28.7	1.6	0.018	30	256.8	0.0005	16.9	0.71
U4-38		28.7	1.8	0.019	11	318.1	0.0013	17.0	0.74
U4-39		28.7	2.8	0.022	6	1225.3	0.0067	16.8	0.93
U5-1	5.65	4.1	20.7	0.102	60	13.0	1E-05	22.7	0.68
U5-2		4.1	24.4	0.112	60	115.5	7E-05	21.5	0.69
U5-3		4.1	26.6	0.122	60	109.4	6E-05	22.7	0.67
U5-4		4.1	29.0	0.124	60	53.0	3E-05	23.8	0.71
U5-5	5.65	6.5	11.2	0.066	60	26.7	1E-05	17.7	0.70
U5-6		6.5	13.1	0.069	60	52.9	2E-05	19.2	0.77
U5-7		6.5	13.3	0.072	60	69.4	4E-05	22.6	0.74
U5-8		6.5	15.0	0.074	30	103.8	9E-05	21.2	0.79
U5-9		6.5	17.6	0.081	60	360.0	0.0001	17.2	0.82
U5-10		6.5	19.1	0.085	43	518.7	0.0002	20.1	0.82
U5-11		6.5	21.0	0.089	20	421.9	0.0003	20.5	0.84
U5-12		6.5	24.5	0.094	21	1449.5	0.0013	20.3	0.90
U5-14	5.65	8.3	9.6	0.056	60	38.5	3E-05	21.5	0.77
U5-15		8.3	11.2	0.06	60	135.8	3E-05	22.1	0.81
U5-16		8.3	12.2	0.062	60	254.2	9E-05	21.8	0.84
U5-17		8.3	13.0	0.065	60	318.6	9E-05	22.2	0.83
U5-18		8.3	14.3	0.069	30	530.8	0.0004	21.2	0.85
U5-19		8.3	15.0	0.07	20	475.8	0.0004	22.6	0.87
U5-20		8.3	16.1	0.072	15	848.1	0.0009	21.9	0.88

Run No.	Sediment d (mm)	Slope S x 10^3	Flow Q (l/s)	Depth Y (m)	Sampling Duration (min)	Bedload Yield (g)	Intensity I (s^{-1})	Water Temp. (^{o}C)	Froude Fr
U5-21	5.65	11.5	6.6	0.043	60	18.9	7E-06	21.7	0.79
U5-22		11.5	7.2	0.045	60	24.1	1E-05	21.6	0.81
U5-23		11.5	8.0	0.047	60	146.0	4E-05	20.3	0.85
U5-24		11.5	8.5	0.048	60	191.7	8E-05	21.4	0.87
U5-25		11.5	8.8	0.05	60	276.1	0.0001	22.3	0.85
U5-26		11.5	9.7	0.052	60	414.2	0.0002	22.5	0.88
U5-27		11.5	10.4	0.053	30	673.8	0.0004	22.5	0.91
U5-28		11.5	11.1	0.055	30	590.5	0.0004	22.2	0.92
U5-29		11.5	12.2	0.057	12	1001.9	0.0018	21.7	0.97
U5-30	5.65	14.1	5.9	0.038	60	28.0	9E-06	22.5	0.85
U5-31		14.1	6.2	0.04	60	46.0	5E-06	22.6	0.82
U5-32		14.1	6.5	0.042	60	92.9	1E-05	23.0	0.82
U5-33		14.1	7.4	0.043	60	156.2	9E-05	22.8	0.89
U5-34		14.1	8.0	0.044	30	455.6	0.0005	23.1	0.92
U5-35		14.1	8.1	0.046	30	292.6	0.0002	22.7	0.87
U5-36		14.1	8.4	0.047	20	450.7	0.0006	22.7	0.89
U5-37		14.1	9.1	0.048	15	691.2	0.0015	22.2	0.93
U5-38	5.65	15.7	5.0	0.033	60	37.9	1E-05	22.4	0.88
U5-39		15.7	5.1	0.035	60	24.4	1E-05	22.2	0.84
U5-40		15.7	5.4	0.036	60	16.2	7E-06	22.6	0.83
U5-41		15.7	5.6	0.037	60	21.4	1E-05	22.8	0.82
U5-42		15.7	6.6	0.039	60	278.4	8E-05	22.6	0.91
U5-43		15.7	6.9	0.04	60	387.6	0.0001	23.0	0.92
U5-44		15.7	7.2	0.041	33	260.2	0.0002	22.6	0.92
U5-45		15.7	7.8	0.042	14	635.5	0.0011	23.3	0.96
U5-46		15.7	8.1	0.043	9	528.8	0.0015	22.6	0.98
U6-1	7.15	4.1	28.0	0.121	60	43.0	1E-06	16.6	0.71
U6-2	7.15	6.5	22.4	0.092	56	61.0	9E-06	21.5	0.85
U6-3		6.5	-	0.096	65	181.2	2E-05	18.4	n/a
U6-4		6.5	26.2	0.1	55	413.4	3E-05	20.0	0.89
U6-5		6.5	26.8	0.103	35	484.9	0.0001	22.4	0.87
U6-6		6.5	28.0	0.106	25	832.1	0.0003	19.7	0.86
U6-7	7.15	8.3	16.0	0.071	65	96.7	5E-06	21.5	0.90
U6-8		8.3	18.7	0.078	55	104.4	3E-05	20.6	0.92
U6-9		8.3	21.0	0.082	65	765.2	9E-05	21.0	0.95
U6-10		8.3	23.1	0.087	66	929.3	0.0001	21.8	0.96
U6-11		8.3	25.2	0.092	47	1221.1	0.0003	22.4	0.96

Run No.	Sediment d (mm)	Slope S x 10^3	Flow Q (l/s)	Depth Y (m)	Sampling Duration (min)	Bedload Yield (g)	Intensity I (s^{-1})	Water Temp. (°C)	Froude Fr
U6-12		8.3	26.2	0.096	21	1177.8	0.0005	22.3	0.94
U6-13		8.3	28.0	0.105	20	949.3	0.0006	21.4	0.88
U6-14	7.15	11.5	10.8	0.054	40	39.0	7E-06	21.4	0.93
U6-15		11.5	11.9	0.056	65	249.3	3E-05	21.6	0.95
U6-16		11.5	13.0	0.06	57	197.9	2E-05	22.0	0.94
U6-17		11.5	13.5	0.061	60	480.7	8E-05	22.2	0.95
U6-18		11.5	14.2	0.064	46	753.3	0.0002	21.4	0.94
U6-19		11.5	15.4	0.067	30	1087.4	0.0005	20.8	0.95
U6-20		11.5	17.5	0.072	13	999.6	0.0009	21.9	0.96
U6-21		11.5	21.3	0.077	3	1683.7	0.009	21.9	1.07
U6-22	7.15	14.1	10.0	0.05	55	257.3	5E-05	21.4	0.95
U6-23		14.1	8.6	0.047	57	50.2	3E-06	22.3	0.90
U6-24		14.1	9.8	0.049	65	337.3	5E-05	21.4	0.98
U6-25		14.1	11.2	0.051	35	404.6	0.0001	22.4	1.02
U6-26		14.1	11.6	0.052	25	1036.9	0.0004	20.7	1.05
U6-27		14.1	12.5	0.056	17	1050.9	0.0007	20.9	1.01
U6-28		14.1	13.2	0.058	11	1077.9	0.0013	21.0	1.01
U6-29		14.1	14.3	0.06	6	1274.9	0.0027	21.8	1.05
U6-30	7.15	23.8	4.7	0.029	55	142.1	3E-06	19.4	1.01
U6-31		23.8	5.1	0.031	66	273.7	1E-05	19.2	0.99
U6-32		23.8	5.6	0.032	50	466.9	0.0001	18.6	1.04
U6-33		23.8	6.2	0.034	42	1198.0	0.0003	20.3	1.06
U6-34		23.8	7.2	0.035	21	882.2	0.0008	19.8	1.18
U6-35		23.8	7.7	0.038	5.5	1305.5	0.0043	17.8	1.13
U7-1	9	6.5	28.0	0.114	60	52.4	2E-05	18.9	0.77
U7-2	9	8.3	21.0	0.091	60	65.0	1E-05	20.6	0.81
U7-3		8.3	23.8	0.098	60	92.0	2E-05	21.9	0.83
U7-4		8.3	29.0	0.104	60	195.0	4E-05	22.0	0.92
U7-5	9	11.5	12.2	0.065	60	31.6	1E-05	22.8	0.78
U7-6		11.5	13.5	0.068	60	75.3	1E-05	23.4	0.82
U7-7		11.5	14.4	0.07	60	132.8	1E-05	22.3	0.84
U7-8		11.5	15.8	0.072	60	97.4	2E-05	23.2	0.87
U7-9		11.5	17.2	0.074	60	287.7	3E-05	23.2	0.91
U7-10		11.5	18.6	0.077	60	307.8	7E-05	23.8	0.94
U7-11		11.5	19.8	0.08	20	669.4	0.0003	23.2	0.94
U7-12		11.5	22.0	0.083	20	472.2	0.0003	24.3	0.99
U7-13		11.5	24.8	0.086	8	580.2	0.0009	23.8	1.05

Run No.	Sediment d (mm)	Slope S x 10^3	Flow Q (l/s)	Depth Y (m)	Sampling Duration (min)	Bedload Yield (g)	Intensity I (s^{-1})	Water Temp. (^{o}C)	Froude Fr
U7-14	9	14.1	10.8	0.058	60	45.4	2E-05	23.8	0.82
U7-15		14.1	12.2	0.06	60	196.9	3E-05	22.7	0.88
U7-16		14.1	13.3	0.062	60	236.0	3E-05	23.8	0.91
U7-17		14.1	14.5	0.064	60	221.7	4E-05	22.3	0.95
U7-18		14.1	15.0	0.066	40.3	644.7	9E-05	24.0	0.95
U7-19		14.1	16.1	0.068	25	453.9	0.0002	22.7	0.98
U7-20		14.1	18.2	0.071	15	626.6	0.0007	22.7	1.03
U7-21		14.1	21.0	0.075	4.5	1082.6	0.0037	23.7	1.10
U7-22	9	15.7	9.8	0.051	60	58.7	1E-05	21.9	0.92
U7-23		15.7	11.4	0.055	60	81.3	3E-05	22.1	0.95
U7-24		15.7	12.4	0.056	60	317.4	5E-05	21.6	1.01
U7-25		15.7	13.0	0.058	60	281.2	3E-05	21.8	1.00
U7-26		15.7	13.2	0.06	60	155.9	5E-05	21.8	0.97
U7-27		15.7	14.0	0.061	60	417.3	8E-05	22.1	0.98
U7-28		15.7	15.8	0.063	15	580.1	0.0007	22.7	1.08
U7-29		15.7	15.6	0.063	17	581.2	0.0003	21.8	1.05
U7-30		15.7	16.4	0.064	13	513.0	0.0007	22.6	1.07
U7-31		15.7	17.2	0.065	6	685.5	0.0011	22.9	1.12
U8-1	12	11.5	16.7	0.073	60	37.9	3E-06	13.3	0.90
U8-2		11.5	20.0	0.082	60	109.1	1E-05	16.0	0.91
U8-3		11.5	24.5	0.092	50	110.9	2E-05	17.2	0.94
U8-4		11.5	29.0	0.1	60	421.3	5E-05	18.7	0.97
U8-5		11.5	28.0	0.101	55	1241.8	0.0001	19.1	0.94
U8-6	12	14.1	21.0	0.079	60	403.9	4E-05	21.4	1.01
U8-7		14.1	22.0	0.083	60	237.8	2E-05	19.4	0.98
U8-8		14.1	24.6	0.084	60	770.7	6E-05	20.8	1.08
U8-9		14.1	25.4	0.086	57	837.0	0.0002	22.2	1.07
U8-10		14.1	26.6	0.089	23	1090.2	0.0004	22.1	1.07
U8-11		14.1	29.0	0.09	18	896.4	0.0003	22.6	1.14
U8-12		14.1	29.0	0.095	19	890.9	0.0003	20.4	1.05
U8-13	12	17.8	14.3	0.062	35	29.0	2E-05	20.3	0.98
U8-14		17.8	15.3	0.063	60	357.8	3E-05	20.8	1.03
U8-15		17.8	16.3	0.066	35	255.6	5E-05	21.3	1.03
U8-16		17.8	17.8	0.067	55	955.2	9E-05	21.2	1.09
U8-17		17.8	19.2	0.069	13	1440.4	0.0011	21.0	1.12
U8-18		17.8	18.8	0.072	21	614.2	0.0003	22.1	1.05
U8-19		17.8	21.7	0.074	6	1560.5	0.0018	21.4	1.16

Run No.	Sediment d (mm)	Slope S x 10^3	Flow Q (l/s)	Depth Y (m)	Sampling Duration (min)	Bedload Yield (g)	Intensity I (s^{-1})	Water Temp. (^oC)	Froude Fr
U8-20		17.8	20.0	0.074	17	1278.7	0.001	21.4	1.06
U8-21	12	28.7	7.8	0.043	60	305.9	1E-05	21.6	0.94
U8-22		28.7	10.2	0.044	27	1454.2	0.0004	20.6	1.17
U8-23		28.7	9.1	0.045	62	868.8	1E-04	21.4	1.03
U8-24		28.7	8.4	0.045	46	76.4	8E-06	22.5	0.94
U8-25		28.7	9.5	0.048	40	902.3	0.0002	22.6	0.96
U8-26		28.7	11.9	0.052	6	1782.2	0.0037	23.0	1.08
U8-27		28.7	13.0	0.055	5	1673.8	0.0067	23.1	1.09

A.2 Casey (1936)

Grain Size (mm)	Velocity (m/s)	Depth (m)	Width (m)	Slope (m/m)	Bedload Discharge (kg/s m)
2.46	0.483	0.1170	0.4	0.00125	0.00009
2.46	0.513	0.1283	0.4	0.00130	0.00039
2.46	0.533	0.1387	0.4	0.00130	0.00068
2.46	0.542	0.1475	0.4	0.00123	0.00070
2.46	0.558	0.1567	0.4	0.00120	0.00070
2.46	0.582	0.1655	0.4	0.00119	0.00099
2.46	0.625	0.1759	0.4	0.00120	0.00206
2.46	0.650	0.1826	0.4	0.00123	0.00351
2.46	0.652	0.1875	0.4	0.00119	0.00355
2.46	0.676	0.1942	0.4	0.00125	0.00617
2.46	0.679	0.2063	0.4	0.00129	0.00830
2.46	0.659	0.2192	0.4	0.00128	0.00790
2.46	0.657	0.1871	0.4	0.00140	0.00381
2.46	0.558	0.1814	0.4	0.00125	0.00096
2.46	0.514	0.1448	0.4	0.00126	0.00018
2.46	0.454	0.1167	0.4	0.00121	0.000001
2.46	0.438	0.0530	0.4	0.00250	0.00007
2.46	0.477	0.0582	0.4	0.00251	0.00007
2.46	0.489	0.0628	0.4	0.00250	0.00026
2.46	0.539	0.0668	0.4	0.00250	0.00146
2.46	0.518	0.0738	0.4	0.00251	0.00305
2.46	0.538	0.0771	0.4	0.00245	0.00452
2.46	0.546	0.0796	0.4	0.00248	0.00495
2.46	0.563	0.0835	0.4	0.00248	0.00637
2.46	0.573	0.0872	0.4	0.00249	0.00833
2.46	0.595	0.0920	0.4	0.00251	0.01186
2.46	0.610	0.0951	0.4	0.00256	0.01326
2.46	0.637	0.0981	0.4	0.00290	0.01962
2.46	0.564	0.0789	0.4	0.00240	0.00550
2.46	0.556	0.0796	0.4	0.00253	0.00530
2.46	0.569	0.0887	0.4	0.00249	0.00875
2.46	0.599	0.0960	0.4	0.00252	0.01413
2.46	0.619	0.0985	0.4	0.00250	0.02607
2.46	0.671	0.1219	0.4	0.00250	0.01820
2.46	0.749	0.1378	0.4	0.00250	0.05836
2.46	0.448	0.0335	0.4	0.00499	0.00002

Grain Size (mm)	Velocity (m/s)	Depth (m)	Width (m)	Slope (m/m)	Bedload Discharge (kg/s m)
2.46	0.480	0.0360	0.4	0.00499	0.00008
2.46	0.474	0.0354	0.4	0.00494	0.00008
2.46	0.496	0.0384	0.4	0.00491	0.00155
2.46	0.537	0.0427	0.4	0.00496	0.01517
2.46	0.568	0.0466	0.4	0.00505	0.01892
2.46	0.606	0.0515	0.4	0.00498	0.01320
2.46	0.631	0.0582	0.4	0.00500	0.03525
2.46	0.694	0.0677	0.4	0.00509	0.05950
2.46	0.588	0.0472	0.4	0.00506	0.01237
2.46	0.565	0.0415	0.4	0.00502	0.00197
2.46	0.530	0.0378	0.4	0.00509	0.00784
2.46	0.478	0.0323	0.4	0.00498	0.00152
2.46	0.439	0.0271	0.4	0.00496	0.00091

A.3 Bogardi & Yen (1939)

Grain Size (mm)	Velocity (m/s)	Depth (m)	Width (m)	Temp (°C)	Slope (m/m)	Bedload Discharge (kg/s m)
6.849	0.738	0.0506	0.823	19	0.0148	0.00120
6.849	0.692	0.0402	0.823	19	0.0143	0.00018
6.849	0.820	0.0738	0.823	19.8	0.0145	0.02192
6.849	0.921	0.0567	0.3	19.8	0.0141	0.00614

A.4 Ho (1939)

Grain Size (mm)	Velocity (m/s)	Depth (m)	Width (m)	Temp (°C)	Slope (m/m)	Bedload Discharge (kg/s m)
6.01	0.691	0.1094	0.4	10.8	0.00333	0.00010
6.01	0.773	0.1448	0.4	11.0	0.00335	0.00072
6.01	0.810	0.1658	0.4	11.5	0.00334	0.00094
6.01	0.935	0.174	0.4	11.7	0.00333	0.00319
6.01	0.824	0.100	0.4	12.2	0.005	0.00059
6.01	0.929	0.135	0.4	12.6	0.005	0.01442
6.01	1.020	0.157	0.4	12.9	0.00501	0.02706

A.5 Paintal (1971)

Grain Size (mm)	Velocity (m/s)	Depth (m)	Width (m)	Slope (m/m)	Bedload Discharge (kg/s m)
2.5	0.59	0.109	0.914	0.00134	0.00016123
2.5	0.50	0.095	0.914	0.00138	0.00000909
2.5	0.73	0.122	0.914	0.00163	0.00661440
2.5	0.66	0.101	0.914	0.00144	0.00004547
2.5	0.61	0.102	0.914	0.00172	0.00103350
2.5	0.49	0.082	0.914	0.00153	0.00000384
2.5	0.62	0.113	0.914	0.00152	0.00075859
2.5	0.73	0.158	0.914	0.00158	0.01368354
2.5	0.65	0.148	0.914	0.00140	0.00797862
2.5	0.76	0.167	0.914	0.00163	0.02893800
2.5	0.42	0.042	0.914	0.00140	0.00000003
2.5	0.40	0.050	0.914	0.00145	0.00000020
2.5	0.43	0.057	0.914	0.00159	0.00000035
2.5	0.44	0.042	0.914	0.00167	0.00000003
2.5	0.50	0.067	0.914	0.00153	0.00000072
2.5	0.51	0.083	0.914	0.00162	0.00001951
7.95	0.76	0.081	0.914	0.00487	0.00001170
7.95	0.53	0.054	0.914	0.00470	0.00000012
7.95	0.72	0.086	0.914	0.00468	0.00000378
7.95	0.60	0.068	0.914	0.00490	0.00000156
7.95	0.70	0.098	0.914	0.00480	0.00004444
7.95	0.65	0.044	0.914	0.00487	0.00000013
7.95	0.71	0.065	0.914	0.00480	0.00000057
7.95	0.86	0.109	0.914	0.00453	0.00002067
7.95	0.67	0.077	0.914	0.00453	0.00000030
7.95	0.74	0.090	0.914	0.00455	0.00000165
7.95	0.84	0.103	0.914	0.00520	0.00014469
7.95	0.88	0.112	0.914	0.00520	0.00049608
7.95	0.91	0.123	0.914	0.00470	0.00017280
7.95	0.85	0.116	0.914	0.00450	0.00002005
7.95	0.74	0.046	0.914	0.00572	0.00000023
7.95	0.90	0.124	0.914	0.00529	0.00179002
7.95	0.98	0.134	0.914	0.00535	0.00206700
7.95	0.57	0.057	0.914	0.00478	0.00000020
7.95	0.53	0.053	0.914	0.00487	0.00000002
22.2	1.17	0.158	0.914	0.00910	0.00003183

Grain Size (mm)	Velocity (m/s)	Depth (m)	Width (m)	Slope (m/m)	Bedload Discharge (kg/s m)
22.2	1.24	0.163	0.914	0.00914	0.00007978
22.2	1.27	0.171	0.914	0.00915	0.00008102
22.2	1.29	0.183	0.914	0.00905	0.00014882
22.2	1.33	0.187	0.914	0.00912	0.00017486
22.2	1.38	0.203	0.914	0.00912	0.00043818

A.6 Ikeda (1983)

Grain Size (mm)	Velocity (m/s)	Depth (m)	Width (m)	Temp (°C)	Slope (m/m)	Bedload Discharge (kg/s m)
6.5	1.21	0.248	4	22.7	0.00254	0.0462
6.5	1.05	0.186	4	23.5	0.00228	0.0037
6.5	1.17	0.211	4	23.0	0.00248	0.0337
6.5	1.33	0.278	4	24.2	0.00261	0.0943
6.5	1.37	0.313	4	24.3	0.00269	0.1689
6.5	1.08	0.189	4	23.5	0.00241	0.0031
6.5	1.06	0.171	4	24.0	0.00250	0.0015
6.5	0.99	0.154	4	24.0	0.00247	0.00030
6.5	1.37	0.219	4	26.0	0.00544	0.2472
6.5	1.07	0.135	4	25.5	0.00485	0.0169
6.5	1.14	0.159	4	25.7	0.00515	0.0779
6.5	1.36	0.179	4	25.1	0.00472	0.1308
6.5	1.52	0.198	4	24.2	0.00494	0.2544

A.7 Bathurst et al. (1984)

Grain Size (mm)	Velocity (m/s)	Depth (m)	Width (m)	Temp (°C)	Slope (m/m)	Bedload Discharge (kg/s m)
11.5	1.005	0.166	0.6	19.0	0.005	0.0046375
11.5	1.092	0.183	0.6	19.5	0.005	0.0231875
11.5	1.173	0.199	0.6	20.0	0.005	0.0706667
11.5	1.301	0.218	0.6	19.5	0.005	0.1395667
11.5	1.047	0.127	0.6	18.0	0.0075	0.0048142
11.5	1.134	0.147	0.6	17.0	0.0075	0.0311817
11.5	1.150	0.174	0.6	20.0	0.0075	0.0848
11.5	1.280	0.182	0.6	20.0	0.0075	0.1210167
11.5	0.992	0.102	0.6	18.0	0.01	0.0016695
11.5	1.034	0.113	0.6	18.5	0.01	0.0060508
11.5	1.158	0.129	0.6	19.5	0.01	0.0697833
11.5	1.222	0.150	0.6	19.0	0.01	0.14575
11.5	1.308	0.166	0.6	19.5	0.01	0.2486583
11.5	1.416	0.176	0.6	20.0	0.01	0.3581917
22.2	1.155	0.216	0.6	21.5	0.01	0.0150773
22.2	1.372	0.243	0.6	22.0	0.01	0.1319267
22.2	1.640	0.254	0.6	22.5	0.01	0.6853333
22.2	1.032	0.079	0.6	18.5	0.03	0.0007667
22.2	1.139	0.088	0.6	18.5	0.03	0.0108797
22.2	1.186	0.091	0.6	21.0	0.03	0.0441183
22.2	1.130	0.105	0.6	19.5	0.03	0.0396208
22.2	1.390	0.097	0.6	18.0	0.03	0.2128817
22.2	1.400	0.110	0.6	18.0	0.03	0.37265
22.2	1.250	0.133	0.6	17.0	0.03	0.6853333
22.2	0.997	0.058	0.6	18.0	0.05	0.0445467
22.2	0.934	0.071	0.6	18.0	0.05	0.2000317
22.2	0.974	0.077	0.6	17.5	0.05	0.3538033
22.2	1.246	0.067	0.6	18.0	0.05	0.5054333
22.2	1.380	0.072	0.6	17.0	0.05	0.9808833
22.2	1.730	0.077	0.6	17.0	0.05	2.2187667
22.2	2.000	0.083	0.6	17.5	0.05	3.66225
22.2	0.749	0.044	0.6	17.5	0.07	0.003401
22.2	0.909	0.046	0.6	17.5	0.07	0.3666533
22.2	0.942	0.053	0.6	17.5	0.07	0.7538667
22.2	1.160	0.057	0.6	17.5	0.07	1.7047667
22.2	1.250	0.067	0.6	18.0	0.07	2.4929

Grain Size (mm)	Velocity (m/s)	Depth (m)	Width (m)	Temp (°C)	Slope (m/m)	Bedload Discharge (kg/s m)
22.2	1.650	0.061	0.6	13.5	0.07	3.4480833
22.2	1.490	0.067	0.6	16.5	0.07	3.6708167
22.2	1.420	0.082	0.6	16.0	0.07	4.6688333
44.3	1.407	0.130	0.6	18.0	0.03	0.0075167
44.3	1.486	0.146	0.6	17.0	0.03	0.0098083
44.3	1.534	0.163	0.6	17.0	0.03	0.1219167
44.3	1.639	0.173	0.6	18.5	0.03	0.1659167
44.3	1.842	0.172	0.6	18.5	0.03	0.495
44.3	1.012	0.082	0.6	16.5	0.05	0.0022
44.3	1.169	0.100	0.6	17.5	0.05	0.0260792
44.3	1.228	0.095	0.6	18.0	0.05	0.0103583
44.3	1.365	0.110	0.6	17.5	0.05	0.116875
44.3	1.489	0.123	0.6	13.5	0.05	1.0725
44.3	1.415	0.153	0.6	13.5	0.05	1.8975
44.3	1.646	0.152	0.6	16.0	0.05	3.3870833
44.3	1.059	0.079	0.6	15.0	0.07	0.0295167
44.3	1.066	0.109	0.6	16.0	0.07	0.59125
44.3	1.235	0.121	0.6	17.0	0.07	2.5758333
44.3	1.303	0.141	0.6	16.0	0.07	4.5008333

A.8 Graf & Suszka (1987)

Grain Size (mm)	Velocity (m/s)	Depth (m)	Width (m)	Slope (m/m)	Bedload Discharge (kg/s m)
12.2	1.012	0.163	0.6	0.0050	0.00085
12.2	1.038	0.175	0.6	0.0050	0.00158
12.2	1.063	0.185	0.6	0.0050	0.00296
12.2	1.103	0.195	0.6	0.0050	0.00521
12.2	1.135	0.207	0.6	0.0050	0.01236
12.2	1.167	0.217	0.6	0.0050	0.02743
12.2	1.203	0.223	0.6	0.0050	0.03286
12.2	1.252	0.229	0.6	0.0050	0.03639
12.2	1.289	0.238	0.6	0.0050	0.06030
12.2	1.315	0.242	0.6	0.0050	0.07116
12.2	1.328	0.251	0.6	0.0050	0.08773
12.2	1.340	0.255	0.6	0.0050	0.11462
12.2	1.058	0.189	0.6	0.0050	0.00397
12.2	1.114	0.211	0.6	0.0050	0.01575
12.2	1.159	0.230	0.6	0.0050	0.02879
12.2	1.224	0.245	0.6	0.0050	0.05486
12.2	0.918	0.118	0.6	0.0075	0.00022
12.2	0.954	0.124	0.6	0.0075	0.00058
12.2	0.985	0.132	0.6	0.0075	0.00067
12.2	1.019	0.139	0.6	0.0075	0.00356
12.2	1.054	0.147	0.6	0.0075	0.00714
12.2	1.097	0.155	0.6	0.0075	0.01255
12.2	1.097	0.161	0.6	0.0075	0.01841
12.2	1.121	0.162	0.6	0.0075	0.02303
12.2	1.154	0.169	0.6	0.0075	0.03531
12.2	1.188	0.174	0.6	0.0075	0.04400
12.2	1.200	0.182	0.6	0.0075	0.05160
12.2	1.224	0.192	0.6	0.0075	0.08420
12.2	1.260	0.201	0.6	0.0075	0.12276
12.2	1.276	0.209	0.6	0.0075	0.15210
12.2	1.306	0.217	0.6	0.0075	0.17790
12.2	1.346	0.229	0.6	0.0075	0.24172
12.2	1.384	0.236	0.6	0.0075	0.27975

Grain Size (mm)	Velocity (m/s)	Depth (m)	Width (m)	Slope (m/m)	Bedload Discharge (kg/s m)
23.5	1.318	0.153	0.6	0.015	0.0089
23.5	1.356	0.161	0.6	0.015	0.0134
23.5	1.389	0.168	0.6	0.015	0.0215
23.5	1.392	0.182	0.6	0.015	0.0487
23.5	1.350	0.179	0.6	0.015	0.0350
23.5	1.426	0.187	0.6	0.015	0.0944
23.5	1.482	0.190	0.6	0.015	0.1300
23.5	1.539	0.196	0.6	0.015	0.1866
23.5	1.500	0.210	0.6	0.015	0.2695
23.5	1.381	0.187	0.6	0.015	0.0670
23.5	1.337	0.167	0.6	0.015	0.0254
23.5	1.300	0.159	0.6	0.015	0.0083
23.5	1.236	0.151	0.6	0.015	0.0032
23.5	1.173	0.125	0.6	0.020	0.0061
23.5	1.138	0.123	0.6	0.020	0.0064
23.5	1.238	0.136	0.6	0.020	0.0235
23.5	1.288	0.141	0.6	0.020	0.0539
23.5	1.370	0.146	0.6	0.020	0.1185
23.5	1.394	0.153	0.6	0.020	0.2088
23.5	1.379	0.168	0.6	0.020	0.3529
23.5	1.492	0.162	0.6	0.020	0.3912
23.5	1.046	0.094	0.6	0.025	0.0012
23.5	1.083	0.100	0.6	0.025	0.0024
23.5	1.122	0.104	0.6	0.025	0.0124
23.5	1.131	0.109	0.6	0.025	0.0342
23.5	1.176	0.112	0.6	0.025	0.0512
23.5	1.243	0.114	0.6	0.025	0.0785
23.5	1.243	0.122	0.6	0.025	0.1746
23.5	1.331	0.119	0.6	0.025	0.2216
23.5	1.421	0.129	0.6	0.025	0.5144

B. Incipient motion on laminar and transitional beds

dmin (mm)	*dmax* (mm)	B_f (m)	Bed (mm)	Surface (mm)	*T* (Celsius)	Gauge (mm)	*Q* (*l*/s)	*Y* (mm)
0.150	0.300	0.610	69.1	152.8	16.7	541.2	12.30	83.7
0.150	0.300	0.610	69.1	139.8	16.8	527.2	9.66	70.7
0.150	0.300	0.610	69.1	127.8	16.9	516.6	7.91	58.7
0.150	0.300	0.610	69.1	118.1	17.1	502.3	5.87	49.0
0.150	0.300	0.610	69.1	106.6	17.2	486.7	4.05	37.5
0.150	0.300	0.610	69.1	89.7	17.3	463.9	2.08	20.6
0.300	0.425	0.610	69.0	181.6	17.2	573.5	19.92	112.6
0.300	0.425	0.610	69.0	171.6	17.5	567.3	18.29	102.6
0.300	0.425	0.610	69.0	162.1	17.6	557.1	15.78	93.1
0.300	0.425	0.610	69.0	165.8	17.1	549.1	13.96	96.8
0.300	0.425	0.610	69.0	146.0	17.7	538.4	11.74	77.0
0.300	0.425	0.610	69.0	134.7	17.8	528.9	9.96	65.7
0.300	0.425	0.610	69.0	120.8	17.9	517.3	8.01	51.8
0.300	0.425	0.610	69.0	109.4	18.0	502.6	5.91	40.4
0.300	0.425	0.610	69.0	96.1	18.1	487.6	4.14	27.1
0.300	0.425	0.610	69.0	88.0	17.0	463.7	2.06	19.0
0.425	0.500	0.610	69.5	180.6	18.1	573.8	20.00	111.1
0.425	0.500	0.610	69.5	166.3	18.2	566.7	18.13	96.8
0.425	0.500	0.610	69.5	156.8	18.3	558.9	16.20	87.3
0.425	0.500	0.610	69.5	147.9	18.4	549.9	14.14	78.4
0.425	0.500	0.610	69.5	139.4	18.5	540.7	12.20	69.9
0.425	0.500	0.610	69.5	127.0	18.6	529.4	10.05	57.5
0.425	0.500	0.610	69.5	115.9	18.7	515.7	7.77	46.4
0.425	0.500	0.610	69.5	104.6	18.8	502.6	5.91	35.1
0.425	0.500	0.610	69.5	89.1	18.8	487.1	4.09	19.6
0.500	0.600	0.610	68.8	175.1	19.0	573.2	19.84	106.3
0.500	0.600	0.610	68.8	163.4	19.0	565.1	17.73	94.6
0.500	0.600	0.610	68.8	151.9	19.0	557.7	15.92	83.1
0.500	0.600	0.610	68.8	143.8	19.0	550.7	14.32	75.0
0.500	0.600	0.610	68.8	131.4	19.0	539.2	11.90	62.6
0.500	0.600	0.610	68.8	121.2	19.1	530.1	10.17	52.4
0.500	0.600	0.610	68.8	107.8	19.1	514.0	7.51	39.0
0.500	0.600	0.610	68.8	99.4	19.1	501.3	5.74	30.6
0.500	0.600	0.610	68.8	89.6	19.1	487.9	4.17	20.8
0.500	0.600	0.610	68.8	82.8	19.1	467.3	2.32	14.0
0.600	0.850	0.610	71.4	142.1	18.0	539.4	11.94	70.7
0.600	0.850	0.610	71.4	131.0	18.0	528.1	9.82	59.6

dmin (mm)	*dmax* (mm)	B_f (m)	Bed (mm)	Surface (mm)	*T* (Celsius)	Gauge (mm)	*Q* (*l*/s)	*Y* (mm)
0.600	0.850	0.610	71.4	125.0	18.1	516.8	7.94	53.6
0.600	0.850	0.610	71.4	116.2	18.1	506.7	6.46	44.8
0.600	0.850	0.610	71.4	100.2	18.2	488.7	4.26	28.8
0.600	0.850	0.610	71.4	86.1	18.2	466.0	2.22	14.7

C. Flowchart for the numerical modelling of scour and deposition (McGahey, 2001)

McGahey (2001) presents the following flowchart for the numerical modelling of scour and deposition described in Chapter 9

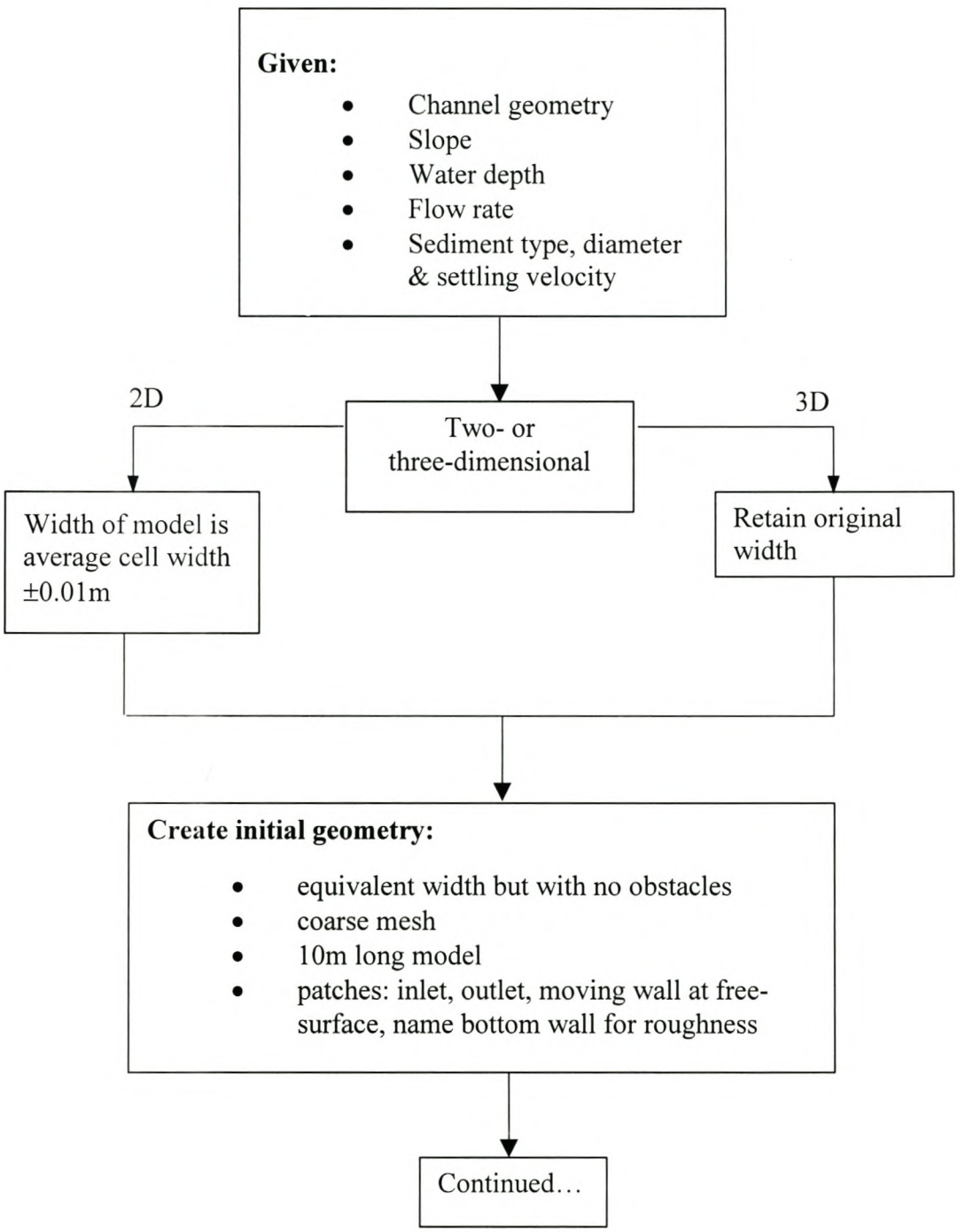

From previous page…

Create command file:

- 2D or 3D
- Rectangular grid
- Cartesian co-ordinates
- Turbulent flow
- Heat transfer
- Buoyancy
- Incompressible flow
- Steady state
- No. user scalars
- Fortran routines: USRBCS,USRWTM
- Name user scalars
- Differencing scheme: QUICK all variables except k-ε use HYBRID
- Wall treatments: no-slip, logarithmic
- Standard fluid water: density 1000, viscosity 0.001, temperature 293 K
- Turbulence model: k-ε model (2D), Low Reynolds Number k-ε model (3D)
- Gravity vector (accounts for slope)
- Solver data: no. of iterations, mass source tolerance
- Pressure correction : SIMPLEC (variable)
- Solver: STONE u,v,w ICCG p – 2D
  BLOCKSTONE u,v,w ICCG p – abutment
  BLOCKSTONE u,v,w AMG p - pier
- Boundary conditions: inlet – average velocity, turbulent intensity, dissipation length scale, 'dummy' moving-wall velocity

Continued…

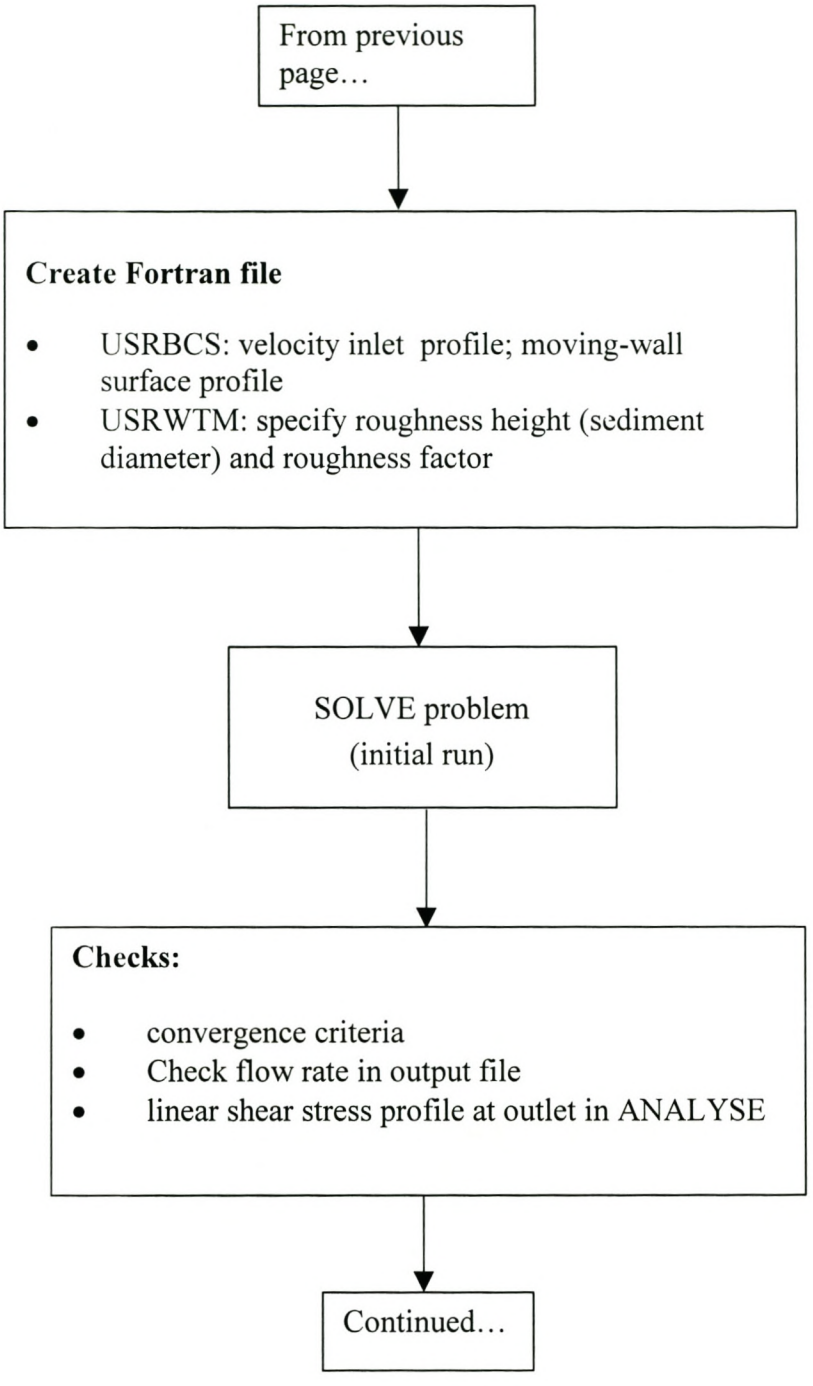

From previous page…

Save data and open in Microsoft EXCEL:

- Plot k and ε variations with depth at outlet. Find best-fit polynomials to represent these curves. For 3D case, plot k and ε variations with width at mid-height as well. Hence find equation to approximate surface distribution of k and ε.
- Find depth of the laminar sub-layer (equation 2.28 & 2.24) using the shear stress and hence the depth of the minimum cell.

Second geometry:

- Build the actual geometry, refining the mesh at the boundary (according to sub-layer thickness and sediment height) and adjacent to the obstacle. Create user 2D and 3D patches where necessary.

Update command file:

- Add user routine USRTRN

Update Fortran file:

- Add k and ε distributions to USRBCS.
- Program power equations, Movability Number, slope adjustment function etc. in USRTRN.

Continued…